Investigation of Fluid Flow in Grinding Using LDA Techniques and CFD Simulation

Hui Wu

A thesis submitted in partial fulfilment of the requirements of Liverpool John Moores University for the degree of Doctor of Philosophy

September 2009

Abstract

This research aimed to establish the requirements for effective fluid flow in grinding and to improve the efficiency of the fluid delivery system (fluid delivery optimization). Highly efficient fluid delivery will lower grinding temperatures, reduce the risk of thermal damage and reduce wheel wear. The thesis describes the work completed in the investigation of the complex fluid flow that occurs in the region close to the grinding contact zone between the wheel and workpiece and the boundary layer phenomena around the periphery of the rotating grinding wheel. Studies on air scraper and shoe nozzle application are also presented.

Laser Doppler Anemometry (LDA) was employed to obtain a basic understanding of the flow velocity profile in the region close to the grinding contact zone in a low speed grinding system and key characteristics of the fluid flow under varying grinding conditions were identified.

The mathematical formulae describing the air velocity distribution around the wheel have been derived from theory based on Newton's laws. Air boundary layer flow around the rotating grinding wheel was studied using LDA measurements and Computational Fluid Dynamics (CFD) simulation to get the air velocity distribution in varying conditions. The experimental results and the investigation made clear the contradictory knowledge relative to this issue and gave a full understanding of the air boundary layer flow.

Air scrapers are used to reduce the effects of the air boundary layer. The effects of the size and position of the different scrapers on the air flow velocity and pressure distribution was investigated using CFD simulation. The research work provides a comprehensive assessment of the ability of the air scraper to reduce the intensity of the air boundary layer. The upper surface of the shoe nozzle can be regarded as an air scraper used to interrupt the air flow. Three different shoe nozzles were applied to investigate the fluid delivery situation using CFD simulation. Results from preliminary studies are presented for the shoe nozzle application. The effects of input fluid velocity, gap size and wheel speed on the pressure distribution along the arc of the gap are reported.

Acknowledgements

I would like to thank my director of studies, Dr. M.N. Morgan for his invaluable help throughout the course of the work.

Gratitude is also due to Dr. Y.D. Tridimas, Professor W.B. Rowe and Dr. Rui Cai whose invaluable assistance throughout the project has been vital to the author. Particular thanks go to Dr Andre Batako for his guidance and encouragement to complete this work.

I would also like to thank the technical staff without whom none of this work could have been accomplished. Particular thanks go to Mr Paul Wright, Mr John Carrier, Mr Peter Moran, Mr Mick Noord, Mr Brian Gray, Mr Thomas Scargill, Mr Dave Winsor and Ms Helen Pottle for their support throughout my time at AMTReL.

I wish to thank the University and the General Engineering Research Institute (GERI) the financial support they gave me, as well as the EPSRC for the funding they provided and industrial sponsors of the project.

Finally, I would like to thank my family and friends who have provided critical emotional support and guidance throughout the course of this endeavour.

Contents

List of Figures

List of Tables

Nomenclature

Symbol	Meaning	Units
a	Acceleration	m/s^2
A	Cross-sectional area perpendicular to the flow	m^2
C	Coefficient, log-layer constant	-
C_D	Drag coefficient	-
C'	Abbreviation of $\frac{2C}{m}$, Drag coefficient	-
f	Frequency of signal	Hz
	Focal length (Ch.3)	mm
f_D	Frequency of an LDA signals	Hz
F_D	Drag force	N
d	Diameter of sphere body	mm
D	Diameter of wheel	mm
h	Height of fluid film	mm
h_c	Clearance between the wheel and the workpiece	mm
$\overline{h}$	Value of h at which $dp/dx = 0$	-
i	Number of samples	-
k	Drag coefficient (constant);	-
	Turbulent kinetic energy per unit mass	-
k'	Abbreviation of $\frac{k}{m}$	-
k^*	Coefficient	-
l	Length;	mm
	Beam separation (Ch. 3)	mm
m	Mass	kg
M_f, M_a	Momentum of stream of fluid	kg·m/s
n	Wheel speed (rev/min)	-
p	Pressure	pa
p_{abs}	Absolute Pressure in CFX	pa
p_{ref}	Reference Pressure in CFX	pa
P_{stat}	Static pressure in CFX	pa
p_{tot}	Total pressure in CFX	pa
p^*	Non-dimensional pressure	-
Q_{CL}	Quantity of the coolant	m^3/s

R	Radius of the wheel	mm
Re	Reynolds number	-
R_t	Grinding wheel surface roughness	mm
s	Distance	mm
Δt_i	Transit time of i^{th}	s
T	Temperature	K
u	Fluid velocity	m/s
u_τ	Shear stress velocity	-
u^*	Dimensionless velocity near the wall	-
U	Free stream velocity	m/s
U_i	Velocity of i^{th} particle	m/s
V	Volt	W
V_f	Fluid velocity	m/s
v	Velocity	m/s
v_0	Initial velocity	m/s
v_r, Vr	Radial velocity	m/s
v_s	Wheel speed	m/s
v_t, Vt	Tangential velocity	m/s
Vz	Axial velocity	m/s
y^*	Dimensionless wall distance	-

Greek symbols

δ	Fringe spacing	mm
y^*	Boundary thickness	mm
θ	Angle	degree
κ	Karman constant	-
λ	Wavelength of the laser light	nm
μ	Fluid dynamic viscosity	$g \cdot cm^{-1} \cdot s^{-1}$
υ	Kinematic viscosity	$cm^2 \cdot s^{-1}$
ξ	Non-dimensional form of coordinate x Coefficient	-
ρ	Fluid density	kg/m^3
σ	RMS velocity	m/s
τ_w	Shear stress	N/m^2
ϕ	Diameter	mm

Chapter 1 Introduction

1.1 Background

Grinding is a major manufacturing process that accounts for some 20-25% of the total expenditure on machining operations in industrialized countries (Malkin, 1989). It is traditionally regarded as a final machining process in the production of components requiring smooth surfaces and fine tolerance. There is no process which can compete with grinding for most precision machining operation. Another area where grinding is virtually unchallenged is for machining of materials which, because of their extreme hardness or brittleness, cannot be efficiently shaped by other methods.

Although grinding is a fundamental manufacturing process important for achievement of low geometric tolerances and a high quality workpiece finish, the specific energy associated with grinding is relatively high compared with other material removal processes (Guo & Malkin, 1992 A). For conventional grinding, specific energy is typically of the order 20 J/mm^3 to 100 J/mm^3 depending on material removal rate, wheel condition, fluid employed and workpiece material (Kim, et al., 1997). Virtually all of this energy is converted to heat, which is concentrated within the grinding zone. The high temperatures produced can cause various types of thermal damage to the workpiece, such as burning, phase transformations, softening of the surface layer with possible rehardening, unfavourable residual tensile stresses, cracks, and reduced fatigue strength. It can also accelerate wheel wear. Furthermore, thermal expansion of the workpiece during grinding contributes to inaccuracies and distortions in the final product. The production rates which can be achieved by grinding are often limited by grinding temperatures and their deleterious influence on workpiece quality (Guo & Malkin, 1994).

In order to limit these high temperatures and consequent thermal damage and wheel wear, grinding fluid is applied at the grinding zone (Howes, 1990; Bauer, et al., 2005). Grinding fluid plays a crucial role in grinding, and the basic requirements of the fluid include lubrication, bulk cooling and transport of debris from the cutting zone. Grinding

fluids help to reduce the amount of heat generated by direct cooling of the workpiece by convection and flush the chips away to prevent wheel loading which would otherwise lead to increased friction and wastage of power.

For a grinding fluid to be effective as a lubricant and coolant, it must be delivered in sufficient quantity to the grinding zone. There are two main methods of grinding fluid delivery: low pressure (flood) and high pressure (jet) by means of nozzles (Krishnan, et al., 1995; Webster & Cui, 1995; Kovacevic & Beardsley, 1997). With high-speed grinding a boundary layer of air develops around the periphery of the wheel. In a low-pressure system, the velocity of the fluid may be insufficient for the fluid to penetrate this layer, thereby the air layer will prevent the fluid from reaching the grinding zone (Davies & Jackson, 1981; Gong, et al., 2004). Aside from using high pressures, one simple solution to this problem is to break up the air film by positioning a scraper plate close to the wheel surface at a location just ahead of where the fluid hits the wheel (Anon, 1974). Environmental concerns are another reason to improve the efficiency of the grinding delivery system (Howes, et al., 1991; Oliveira & Alves, 2006).

1.2 Problem definition

There are conflicting recommendations for the design of fluid application systems and a lack of knowledge concerning the principles of fluid delivery into the grinding contact (Webster, et al., 1995; Gao, et al., 2003; Babic, et al., 2005). In consequence, fluid burn-out is common, grinding quality suffers and substantial energy is usually wasted in larger production grinding systems (Axinte, et al., 2003). This is principally because very little supplied flow reaches inside the grinding contact zone (Jin, et al., 2003). As a result, industry has consistently requested research on fluid delivery.

The deleterious effect of ineffective fluid delivery raises a question concerning the magnitude of flowrate that is required to achieve the maximum quantity of flow that can pass through the grinding contact zone (Guo & Malkin, 1992 A). A significant factor is the flow mechanism in the contact zone between the workpiece and the wheel (Gviniashvili, et al., 2004). The region of pre-contact in grinding presents the condition of a large diameter disk rotating at high speed, a converging gap and a pressure decrease in the flow direction. As a result, there are effects of turbulent behaviour and boundary layer separation.

The grinding wheel rotating at relatively high speed carries on its surface a layer of air flow (air boundary layer flow), which at sufficient high wheel speed may divert the stream of grinding fluid. Therefore, the fluid must penetrate the air layer developed around the periphery of the rotating wheel surface to achieve effective grinding fluid delivery. This has aroused research interest and has led to studies of the air boundary layer flow around the rotating grinding wheels (Davies & Jackson, 1981). However, due to the different measurement instruments used by the researchers, results are often contradictory and no comprehensive understanding of the air boundary layer flow has been achieved (Kaliszer & Trmal, 1975; Sven & Johansson, 1996). This work attempts to clarify issues concerning air boundary layer flow in order to improve the efficiency of the flow delivery in grinding.

Air scrapers are frequently used in industry to reduce the effects of the air boundary layer on opposing fluid delivery; however, the understanding of air scraper effects remains incomplete (Campbell, 1995; Catai, et al., 2006). This work provides a comprehensive assessment of the ability of the air scraper to reduce the intensity of the air boundary layer.

An efficient alternative, even for lower grinding fluid flowrate, is the shoe nozzle. The upper surface of the shoe nozzle can be regarded as an air scraper, used to interrupt the air flow. Therefore, fluid will flow more easily under this "air scraper", the grinding wheel is wetted and the wheel surface pores can be filled with coolant immediately prior to penetrating the grinding contact zone. The application of shoe nozzles in grinding requires further research and results from preliminary studies are presented.

In this thesis, it is proposed to investigate (i) the complex fluid flow that occurs in the region of the initial contact between the wheel and workpiece and (ii) the boundary layer phenomena around the rotating grinding wheel. Air scraper and shoe nozzle application are also to be studied.

1.3 Aims and objectives

The aim of the research was to establish requirements for effective fluid flow and improve the efficiency of the fluid delivery in the grinding situation (fluid delivery optimization).

Objectives of this research were:

1. To investigate the velocity profile of the fluid in the grinding contact entry region with Laser Doppler Anemometry (LDA) for different fluid types, fluid delivery conditions and grinding conditions in a conventional speed grinding system.
2. To investigate the velocity profile of the air boundary layer that develops around a rotating grinding wheel.
3. To develop an analytical model to describe the physics of fluid flow around the rotating grinding wheel.
4. To analyze the application of an air scraper in grinding.
5. To provide initial guidance on shoe nozzle application.

1.4 Scope

The work was confined to plane surface operations. Water and neat oil were employed in the fluid flow mapping experiments. The Laser Doppler Anemometry (LDA) and Computational Fluid Dynamics (CFD) were employed for these studies. The workpiece material was ferrous and the abrasive material was aluminium oxide. Other laboratory facilities were also employed for all experimental tests. CFD Simulations was undertaken using the ANSYS CFX proprietary software.

Chapter 2 Literature Review

2.1 Introduction

In this Chapter, basic grinding technology is introduced and grinding fluid application reviewed. The major problems associated with grinding fluid application are identified and described.

2.2 Overview of the grinding process

Grinding is a material removal process that employs an abrasive grinding wheel rotating at high speed to remove material from a softer material. In modern industry, grinding technology is highly developed according to particular product and process requirements. Advances in productivity have relied on increasing sophistication in the application of abrasives (Marinescu, et al., 2007).

New grinding fluids and methods of delivering grinding fluid have also been an essential feature in achieving high removal rates while maintaining quality (Brinksmeier, et al., 1999). Developments in fluid delivery systems include high-velocity jets, shoe nozzles and neat mineral oils. The new technology of minimum quantity lubrication (MQL) is claimed to provide an alternative to flood and jet delivery methods and is aimed at environmentally friendly manufacturing. Further studies on the applicability of MQL are required to establish its effectiveness on improved machining performance (Weinerta, et al., 2004).

Grinding is not a process without its share of problems. Problems experienced may include thermal damage, rough surfaces, vibrations, chatter, wheel glazing and rapid wheel wear. Overcoming these problems quickly and efficiently is helped by a correct understanding of the interplay of factors in grinding.

2.2.1 Grinding processes

There are many types of grinding operation: 'precision' and 'rough', internal, external, surface, centreless; using wheels or belts; and conventional or 'super' abrasive.

However, they all act in generally the same manner. When a moving abrasive surface contacts a workpiece, if the force is high enough, material will be removed from the part and abrasive wear will result.

Figure 2-1 illustrates a typical reciprocating surface grinding operation. The five main elements are the grinding wheel, the workpiece, the grinding fluid, the atmosphere, and the grinding swarf. The grinding wheel is composed of abrasives and performs the machining of the workpiece. The interaction of the abrasives with the workpiece wears the grinding wheel. The grinding swarf can be considered an undesirable outcome of the process, although it is not necessarily valueless. The grinding fluid serves to lubricate, cool and flush the contact region (Marinescu, et al., 2004).

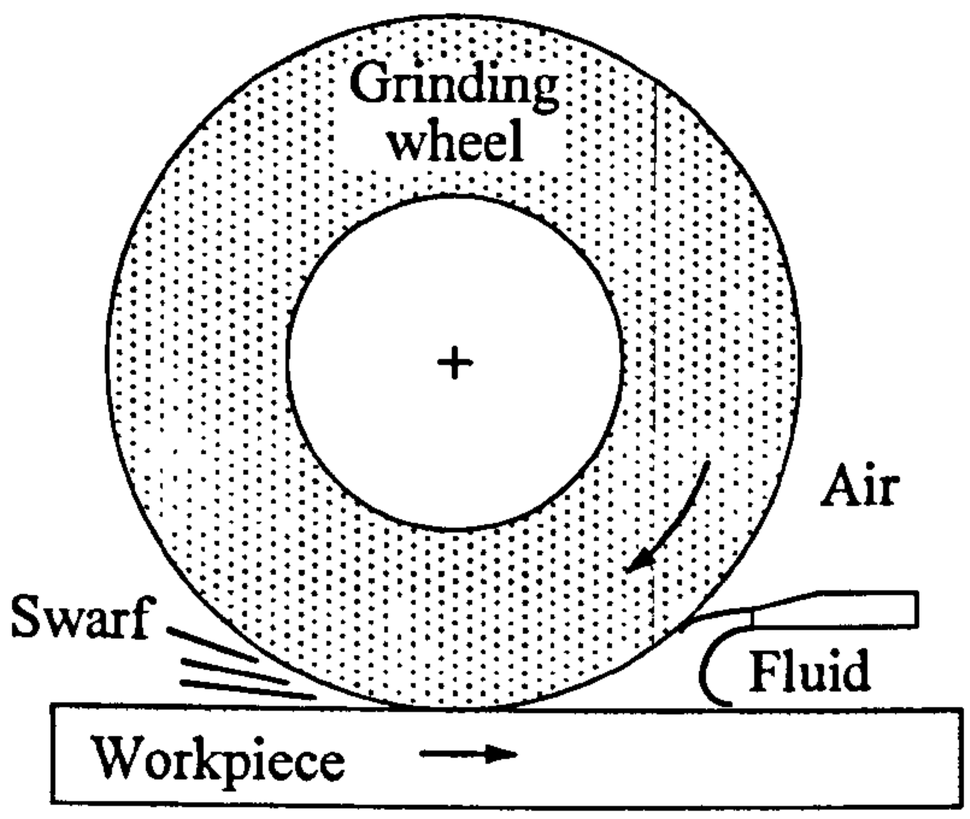

Figure 2-1 Grinding operation

There are three stages of material deformation as a grain interacts with a workpiece: firstly rubbing, then ploughing, and finally cutting. In rubbing, the force on each grain is too small to cause large penetration of the workpiece. Elastic deformation and some plastic deformation take place. Ploughing occurs when the penetration of the grains is increased. In the ploughing stage, scratch marks become evident and ridges are formed at the sides of the scratches. As the penetration of the grains is further increased, material removal occurs and chips are produced.

2.2.2 Grinding wheel

Grinding wheels consist of hard abrasive grains or grits, which do the cutting, that are held in a weaker bonding matrix. Depending on the particular type of bond, the space between the abrasive particles may be partially filled – leaving gaps and porosity – or completely filled with binder. The properties and performance of grinding wheels is dependent on the type of abrasive grain material, the size of the grit, the bond material, the properties of abrasive and bond, and the porosity in addition to machine settings of wheelspeed, workspeed and infeed rate.

Grinding wheels are made from many types of different grit in a wide range of sizes, in conjunction with many bond materials and compositions. 'Conventional' wheels in common use contain either aluminium oxide or silicon carbide abrasive with vitrified or resinoid bonds. 'Superabrasive' wheels with diamond and cubic boron nitride (cBN) abrasives are produced with vitrified, resin, and metal bonds. The different types of grinding wheels, together with the requirements of a wide variety of wheel shapes and sizes to fit all the diverse grinding machines and jobs to be done, lead to an almost endless diversity of grinding wheels.

2.2.3 Grinding temperature and thermal damage

The grinding process requires an extremely high input of energy per unit volume of material removed. Virtually all of this energy is converted to heat which is concentrated within the grinding zone. The high temperatures produced can cause various types of thermal damage to the workpiece, such as burning, phase transformations, softening of the surface layer with possible rehardening, unfavourable residual tensile stresses, cracks, and reduced fatigue strength. Furthermore, thermal expansion of the workpiece during grinding contributes to inaccuracies and distortions in the final product. The production rates which can be achieved by grinding are often limited by grinding temperatures and their deleterious influence on workpiece quality (Jin, et al., 2002).

2.3 Grinding fluid application

The grinding fluid, often referred to as coolant, plays an important role in the grinding process. The development of methods and systems to ensure correct application of fluid remains a significant subject in grinding research. The mechanisms of cooling and

lubricating in grinding are not understood completely and there remains a lack of knowledge concerning principles of fluid delivery into the grinding contact zone (Osman & Malkin, 1972; Chang, 1997). Lubrication and cooling can be enhanced if fluid flow through the grinding zone reaches the useful flowrate; and many recent experimental works have been undertaken to establish this value quantitatively (Vries & Murray, 1994).

2.3.1 Grinding fluid function

The use of a grinding fluid may be essential for one or more reasons related to the various properties of the fluid. The grinding fluid has wider functionality than cooling. The main functions in shallow grinding are flushing, bulk cooling, and lubrication. In creep grinding, the additional function of process cooling is important. In general, the functions of grinding fluid include (Marinescu, et al., 2004):

- Mechanical lubrication of the abrasive contacts;
- Chemo-physical lubrication of the abrasive contacts;
- Cooling in the contact area, particularly in creep grinding;
- Bulk cooling outside the contact area;
- Flushing or transport the swarf away from the abrasive process;
- Transport of abrasive to a loose abrasive process;
- Entrapment of abrasive dust and metal process vapours.

In grinding, fluid in the contact zone influences the chip formation process by building up a lubricant film, thus lowering the friction forces, and cooling the material and tool surfaces. As the lubrication effect increases, there is a corresponding increase in elastic-plastic deformation under the cutting edge of the abrasive grain, resulting in a decrease in workpiece roughness. Meanwhile, by reducing friction forces, friction heat is reduced and therefore also the total process heat. Another important influence of grinding fluid on lubrication is the lowering friction along the chip flow line, i.e. between the chip, the grain cutting edge and the grinding wheel bond. This reduces bond abrasion and grinding wheel wear (Schumack, et al., 1991).

A plentiful channel of grinding fluid on and around the workpiece achieves bulk cooling and flushing of the swarf. This is essential even if very little fluid enters the contact zone between the grinding wheel and workpiece. Lubrication does not necessarily require a large volume of fluid to achieve a significant reduction in wheel wear, but lubrication will be ineffective if no fluid enters the grinding zone at all. Even small quantities of fluid entering the contact zone can be beneficial to process efficiency, and there have been reported trends towards minimum quantity lubrication (MQL) as a means of reducing environmental and disposal costs (Marinescu, et al., 2004). Air sometimes also can be seen as the coolant (dry grinding), but the grinding results are not satisfactory compared with using grinding fluid (Choi, et al., 2001; Nguyen & Zhang, 2003).

2.3.2 Grinding fluid types

Cooling and lubrication requirements differ in every application and mainly depend on grinding conditions (Monici, et al., 2006). Coolants should ideally be composed to suit each specific case. Every coolant consists of a basic fluid, to which are added other products such as anti-wear, anti-corrosion or emulsifying agents. Brinksmeier, et al. (1999) divide coolants into oil-based and water-based types according to the German standard.

In order to decrease friction, high pressures and temperatures during machining, it is necessary to create separation films between the surfaces of the tool and the workpiece. Oil-based coolant normally consists of 80-95% basic oil and normally provides enhanced corrosion resistance and lubrication in comparison with water-based coolant. Low viscosity oils have a better crack penetration ability in comparison to higher viscosity oils. Higher viscosity oils adhere more strongly and produce less oil mist.

For high cooling efficiency and flushing capabilities, water-based emulsions or solutions are employed. Their main disadvantage is susceptibility to leakage oils and microorganisms making high maintenance costs unavoidable. Furthermore, the water and oil phase must be separated before disposal. Water-based solutions consist of inorganic and/or organic substances and water and very seldom contain mineral oils. High chemical stability and transparency are further advantages in high cooling

efficiency and washing away capability. Water-based emulsion concentrates contain 20-70% basic oil (mostly mineral oil). For metal grinding operations, oil-in-water emulsions are common; the mount of oil determines the lubrication ability of the emulsion. Common oil concentrates in emulsions for grinding operations are between 2 and 15%. Water-based coolants contain up to 20 components in which, each of the components can themselves be multicomponent mixtures (Brinksmeier, et al., 1999).

Additives are added to basic fluids to optimise the particular types of production process; each one is aimed at improving specific coolant properties. During metallic solid body frictional contact, certain additives form highly stable compounds either due to their charge polarity or due to chemical reactions at the metal surface. These reactions take place within defined temperature ranges, so the process temperature is an important influencing factor in the effectiveness of the additive.

2.3.3 Fluid delivery methods

It is not only the coolant type and composition, but also the effectiveness of the supply of coolant to the contact zone by nozzles and diffusers that governs the efficiency of the cooling and lubrication in respect of the workpiece quality. It is critically important that the coolant is forced into the contact zone or at least available to be transported through the zone as in the shoe nozzle applications or submerged grinding situations (Brinksmeier & Minke, 1993; Tomita & Eda, 1997).

The design of the fluid supply system and the feed parameters selection must meet the specific technological demands of the grinding process. The coolant system is required to accomplish several different tasks during the machining process. First of all, it has to provide a continuous coolant flow to the grinding contact zone to execute the job of cooling, lubricating, flushing, and the chip transport. Moreover, it is required to store and transport the cooling lubricant, maintaining a constant quality and temperature and with a sufficient quantity to execute the job of cooling, lubricating, flushing, and swarf transporting. In addition to economic requirements, some further requirements must be met including operating safety (Stephenson, 2005).

Traditional delivery of the coolant to slow-speed abrasive machining processes is simple low-pressure feed, which is typically supplied from a pump with less than 0.1 MPa pressure. However, the requirements for modern high-speed abrasive processes need careful planning to obtain the benefits of optimal lubrication, cooling, and wheel cleaning (Ramesh, et al., 2004). Large flowrate and high-energy consumption is the price sometimes paid to achieve a satisfactory fluid delivery.

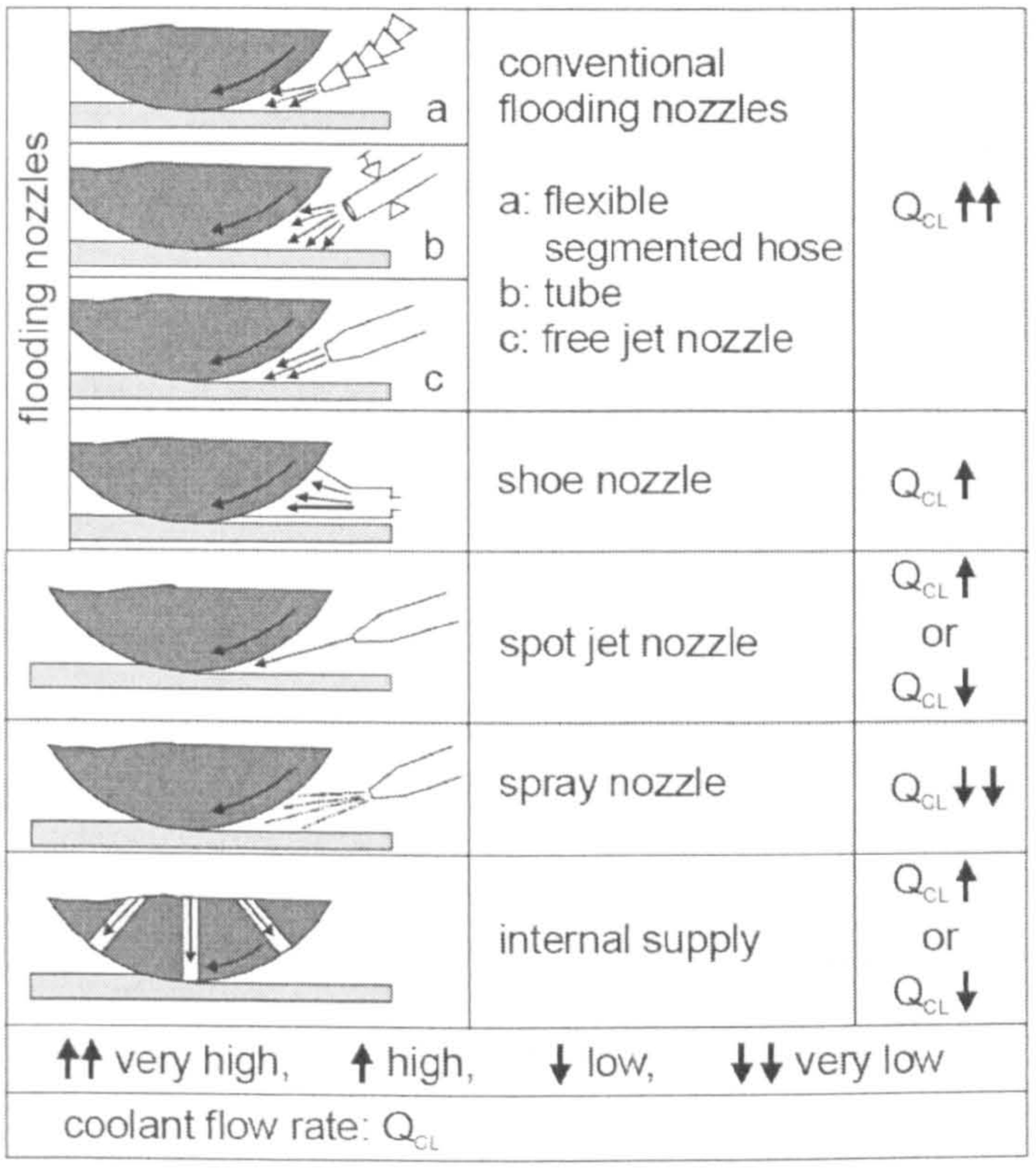

Figure 2-2 Examples of fluid delivery in grinding (Brinksmeier, et al., 1999)

The performance and characteristics of the nozzle for the supply coolant have a major influence on the grinding result. Different nozzles have been developed in order to meet the requirements of various applications (Figure 2-2). Generally, there are three ways to distinguish between types of nozzle systems:

- By function (flooding, not flooding)
- By focusing (free jet nozzle, point nozzle, swell nozzle, spray nozzle)
- By nozzle geometry (squeezed pipe, needle nozzle, shoe nozzle)

The primary task of all nozzles is the distribution of coolant to the grinding contact zone. The free jet nozzles as well as the shoe nozzle, both belonging to the group of flooding nozzles, are most common. During supply with a conventional flooding free jet nozzle or with a spot jet nozzle, the coolant jet is pointed tangentially at the grinding contact zone.

A different concept of lubricant distribution is the supply of cooling lubricant from the interior of the grinding wheel or the grinding layer. The fluid is fed into a chamber of the wheel body allowing the centrifugal force to distribute it through radial channels to the grinding layer (Graham & Whiston, 1978).

2.3.4 Useful flow through the grinding zone

A key objective of fluid delivery research is to deliver to industry the knowledge to achieve optimal useful flow, i.e. the amount of grinding fluid, which passes through the grinding zone. Many factors affect the flowrate of fluid through the grinding contact region. Most studies indicate that an increase of coolant flowrate with otherwise identical process parameters in flooding, gives enhanced surface quality of the workpiece and reduced residual stress (Kovacevic & Mohan, 1995; Wang & Kou, 1997; Hryniewicz, et al., 2000). Above a certain flowrate, saturation takes place. Accordingly, excess coolant is rejected resulting in a reduction of usefully delivered coolant.

An experimental test rig was developed by Engineer, et al, (1992) to measure the amount of grinding fluid, which flows through the grinding zone in straight plunge grinding with flood application. The percentage of fluid utilization was found to significantly increase with wheels that are more porous and a closer positioning of the nozzle to the grinding zone. Wheel dressing had only a secondary influence on the percentage utilization, which was attributed to its influence on near-surface wheel porosity. Workpiece speed and wheel depth of cut had virtually no effect on the percentage utilization.

A theoretical model of fluid flow in grinding had been developed by an analysis of fluid flow through a porous medium by Guo and Malkin (1992 B). The results indicated that

the nozzle velocity, effective wheel porosity, and the nozzle position were the main factors, which influenced the useful flowrate.

Schumack, et al. (1991) modelled fluid flow under a grinding wheel using a perturbation scheme. Experiments showed that nozzle jet velocity, nozzle angle, volumetric flowrate, and surface tension all affect flow behaviour.

Chang, et al. (1996) constructed another predictive model for calculating the flowrate of the grinding fluid through the grinding zone. Both hydrodynamics and ram pressure effects on flow through a porous wheel were considered in this model. The results show that the main parameters influencing the flowrate though the grinding zone are the wheel porosity, the wheel peripheral velocity, the applied flowrate and the wheel permeability.

Therefore, parameters that determine the quantity of fluid flow passing through the grinding contact zone include nozzle jet velocity, nozzle position, volumetric flowrate, wheel velocity, wheel porosity, the parameters of secondary influence include wheel dressing, and workpiece speed and wheel depth of cut, though these are reported to have very little influence.

The different nozzle angles and positions can result in different cooling effectiveness. Delivering the grinding fluid as near to tangential to the grinding wheel as possible, is a common approach with the cutting fluid directed straight towards the grinding zone. However, this is contrary to investigations, which have suggested the nozzle to be positioned at an angle to the wheel periphery (Gviniashvili, et al., 2004; Krishnan, et al., 1995; Webster, et al., 1995).

Ebbrell, et al. (2000) applied a jet of water-based fluid at three different heights and angles to the wheels surface. At the lowest height with a near tangential jet, the recirculating air obstructed the jet. At an increased height corresponding to 90° around the wheel from the grinding contact position with a jet inclined at 15° to the wheel radius, the jet stream was entrained, but became separated from the wheel surface within 45° around the periphery. Varying the position of the jet around the periphery, the best result was achieved with a jet inclined at 56° to the wheel radius and located

about 34° ahead of the contact area. From measurements of the useful flowrate, the best grinding results were obtained when the maximum useful flowrate was achieved.

Increasing coolant jet velocity can lead to a digressive incline of the heat transfer coefficient and therefore to a lower cooling efficiency. This is due to a geometrical limitation of the flowrate through the grinding arc. It was assumed that the volume of fluid supplied should depend on the grinding power, since power is related to temperature rise in the grinding zone. Matching nozzle jet velocity to wheel speed roughly matches spindle power and fluid delivery power. It is concluded that this condition approximately maximises useful flowrate and prevents total power for the fluid from becoming greatly excessive. The outcome of these tests show that the higher the jet speed the better the overall grinding results become with lower forces and an improvement in the surface finish (Gviniashvili, et al., 2004).

Different investigations have offered conflicting optimum angles at which to position the nozzle. This disparity may be due to the viscosity of the cutting fluid and its velocity at nozzle exit (Campbell, 1995). Until now, there has been no practical, economic method of quantifying how effectively the coolant is being applied.

2.4 Air boundary layer

The grinding process is a high speed machining operation and consequently brings about unique phenomena influencing grinding fluid delivery. The main factor is the presence of a boundary layer of air, which develops around the rotating wheel (Akiyama, et al., 1984).

Flood delivery of a grinding fluid typically delivers large volumes of cutting fluid at low velocity. Engineer, et al. (1992) suggested this method was ineffective, especially under high-speed grinding conditions where the energy of the fluid is not sufficient to penetrate the boundary layer of air surrounding the wheel. Even jet delivery via a nozzle, is not believed to fully penetrate this boundary layer and, thus, the majority of the cutting fluid is deflected away from the grinding zone.

Ebbrell, et al. (2000) investigated the effects of the air boundary layer on grinding fluid application through experiment and modelling and how it can be used to aid delivery by

increasing flowrate beneath the wheel. The experiments show that the effects of boundary layer reversal approaching the grinding zone inhibit the flow of cutting fluid delivered under flood conditions. A very interesting and clear example of this occurring is shown in Figure 2-3.

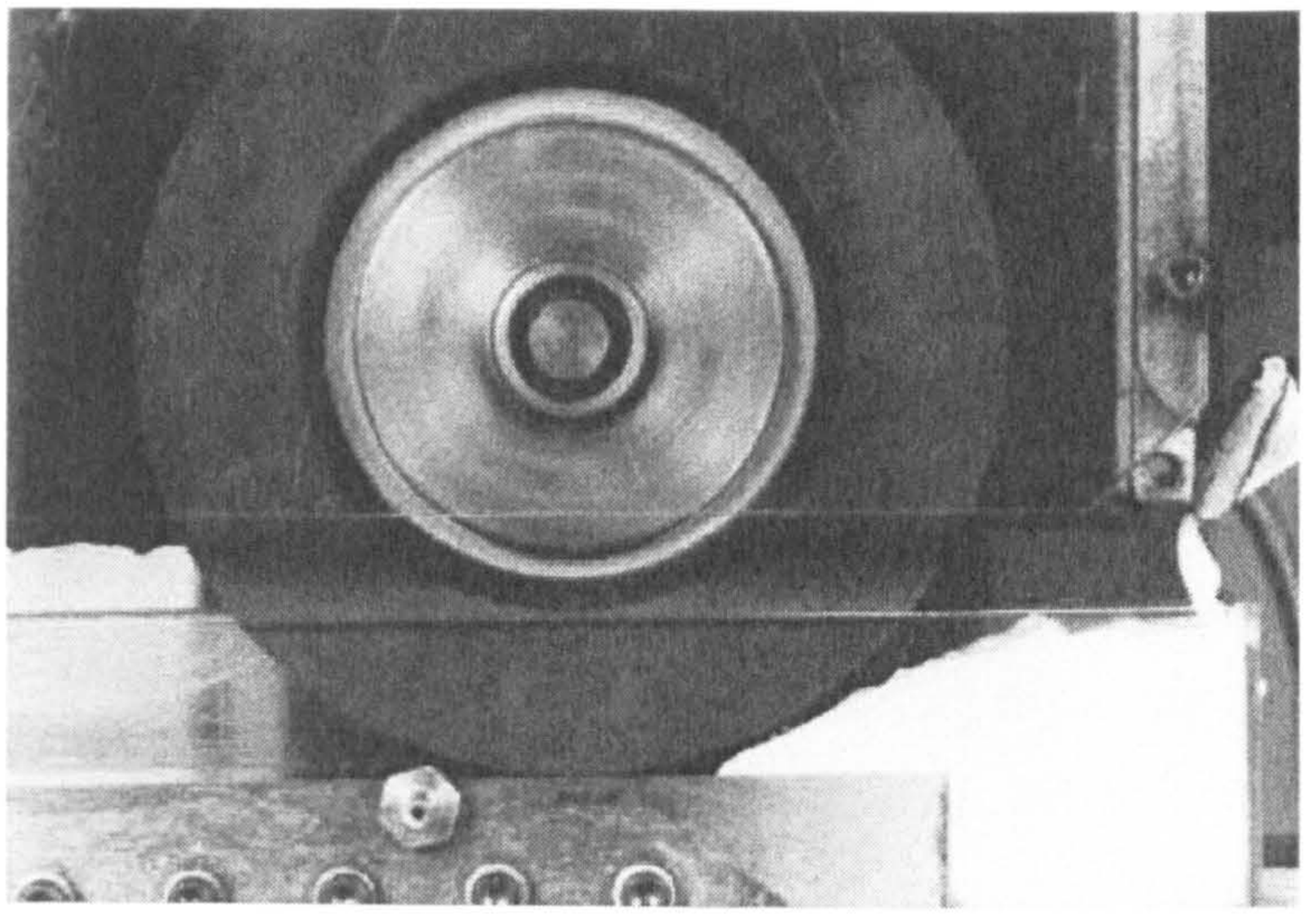

Figure 2-3 Cutting fluid backing up due to boundary layer effects (Ebbrell, et al., 2000)

Webster, et al. (1995) have carried out research into the effects of a coherent jet as opposed to a dispersed jet of grinding fluid upon exit from the nozzle. The need for high fluid velocities to penetrate the air boundary layer make the application of water based cutting fluids much more difficult in terms of a coherent jet. Through measuring the grinding temperature, Webster, et al. showed that when a coherent jet is maintained, the grinding temperature is reduced compared with a dispersed jet.

The work by Kovacevic and Mohan (1995) showed that the effectiveness of grinding fluid performance could be increased if it is supplied at a speed higher than the peripheral velocity of the wheel so it could overcome the centrifugal force and penetrate the surrounding air boundary layer. However, this can be costly in terms of pump and power requirements.

Since the air boundary layer flow can have sufficient energy to prevent the fluid reaching the wheel surface and the grinding contact zone, this has aroused interest that has led to the studies of the air boundary layer flow around the rotating grinding wheel.

2.5 Air scraper

Usually, an air scraper is employed to interrupt the air boundary layer and hence help facilitate fluid delivery to the grinding contact region. As the grinding wheel velocities increase, the effect of the air boundary layer becomes more pronounced (Davies & Jackson, 1981)

Scraper plates of various shapes and dimensions were investigated by previous researchers. Use of a scraper plate was shown to improve delivery and hence the cooling efficiency even at low coolant velocity, because it obstructs the air flow layer and allows the coolant to approach the wheel surface (Shigeki, et al., 1993).

In one work, the employment of a scraper gave a reduction in the cutting force values of 5.5% and grinding wheel radial wear by 5.5% (Catai, et al., 2006). Therefore, the use of a scraper system is often a good choice for operations where improved quality of surface finish with less tool wear is desirable. When the gap between the wheel and the scraper plate reduces, the action of the cutting fluid improves. However, a small gap may require frequent adjustment due to the wheel wear and therefore may not be very practical in actual industrial conditions (Kaliszer & Trmal, 1975).

2.6 LDA application in grinding

The Laser Doppler Anemometer (LDA) technique is a new technique applied in grinding research. Ebbrell, et al. (2000) undertook fluid flow research using LDA and the velocity of the air boundary layer entrained around the grinding wheel was measured using one component LDA. Measurements were made in the area near the minimum gap where previous experimental work had shown reversal to take place. The results showed that this became more pronounced as the minimum gap was reduced. The greatest velocity in the reversed flow occurred just above the workpiece surface. The LDA work presented in this thesis focuses on the air boundary layer and air scraper flows.

Chapter 3 LDA Measurements

3.1 Introduction

Laser Doppler Anemometry (LDA) is a well-established and efficient method of non-intrusive measurement; it is a technique used to measure velocities of flows or more specifically of small particles in flows. Since Yeh and Cummins devised a method of using lasers with consideration to the Doppler Effect to measure flow velocities in 1964, the basic principles have been adapted through the years and to the present day where LDA system is used for accurate measurements (Ainsworth, et al., 1997). The special advantages of the laser Doppler anemometer include: non-intrusive measurements, which do not disturb the flow; high temporal and spatial resolution; no need for calibration; up to three velocity components; velocity range zero to supersonic. Moreover, it is the ideal measurement technique for the non-intrusive investigation of liquid flows. The limit of this measurement method is the need for a transparent flow through which the light beams can pass, and seeding of the flow with particles.

3.2 LDA system

The LDA technique is based on the measurement of laser light scattered by particles that pass through a series of interference fringes. There are many types of LDA systems. The LDA system used in this work was a Dantec high-accuracy argon-ion Laser Doppler anemometry system. This is a two-component dual-beam LDA system operating in back scatter mode. 'Two-component' implies the measurement of two orthogonal velocity components. 'Dual beam' refers to two laser beams of equal intensity.

3.2.1 LDA theory and principles

The basic configuration of the LDA is shown in Figure 3-1. It consists of:

- A continuous wave laser
- Transmitting optics, including a beam splitter and a focusing lens

- Receiving optics, comprising a focusing lens, an interference filter and a photomultiplier
- A signal conditioner and a signal processor

The transmitting optics split the single laser beam into two beams, which are focused using a lens. The lens also changes the direction of the beams causing them to cross at the point where they are focused. The region where the beams intersect is where the velocity measurement is made. It is called the measurement volume.

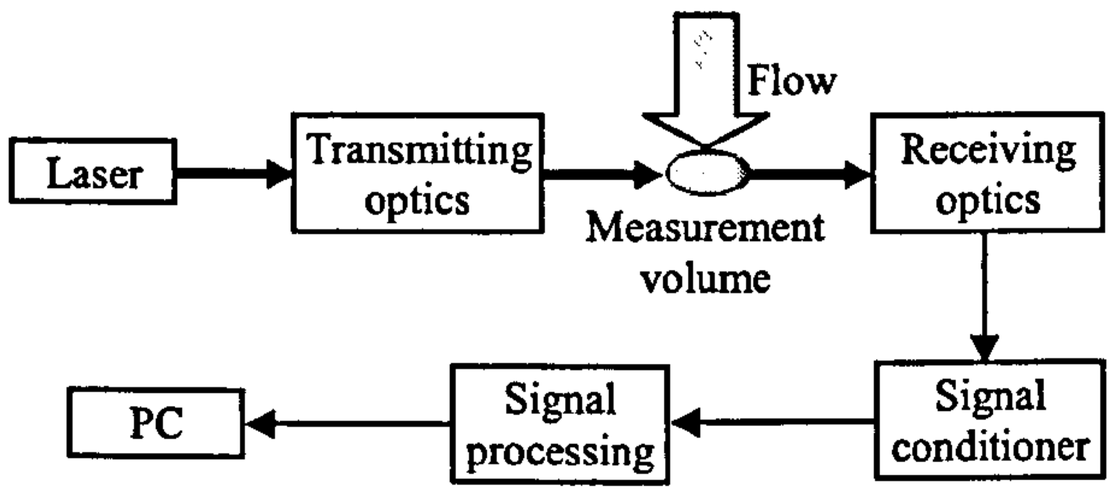

Figure 3-1 Schema of configuration of an LDA system (Dantec Dynamics)

Figure 3-2 shows the enlarged measurement volume schematically and the arrangement of the light waves within the two beams. The waves are represented by lines showing where the peaks are. The interference of the light beams in the measurement volume creates a set of equally spaced fringes (light and dark bands). Since laser light is monochromatic and coherent, it can be seen that the bright and dark fringes form in lines parallel to the bisector of the beams.

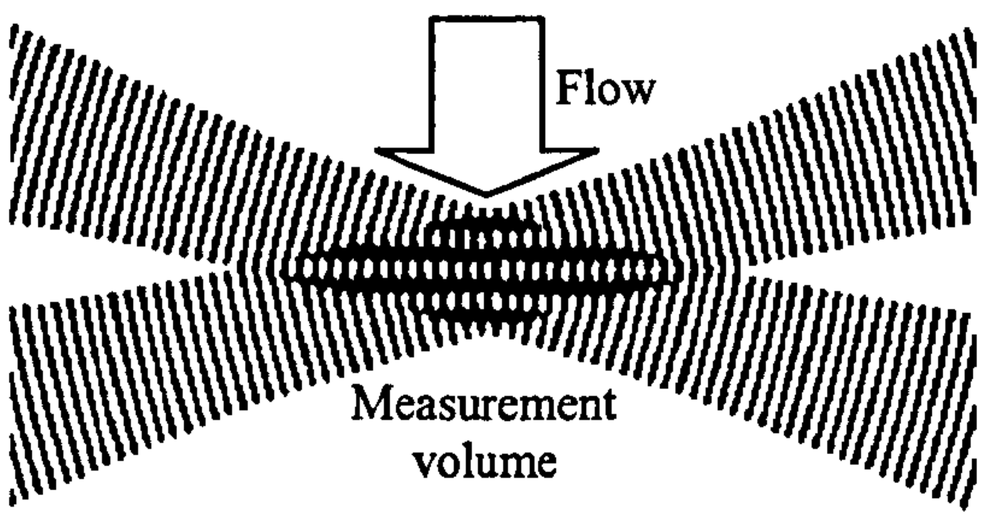

Figure 3-2 Detail of the measurement volume showing the formation of fringes (Lines represent the peaks of the light)

A velocity measurement is made when a tiny particle being carried by the flow passes through these fringes. As it does so the amount of light received by the particle

fluctuates with its position in the fringes, the amount of light scattered by the particle therefore also fluctuates. The frequency of this fluctuation is proportional to the velocity of the particle normal to the fringes. The light scattered by the particle is collected by the receiving optics and focused onto a photomultiplier, which converts the fluctuations in light intensity into fluctuations in a voltage signal. An electronic device, known as a signal processor, is then used to determine the frequency of the signal and therefore the velocity of the flow (Devenport, 2002). In the experiments, two 'Burst Spectrum Analysers (BSA1and BSA2) were used to process the signal. The software 'BurstwareTM' running in the PC was used to operate the signal processing.

If the wavelength of the laser light λ and the angle between the beams θ are known, the velocity of particles moving with the flow can be calculated. Considering the enlarged part of measurement volume, as shown in Figure 3-3, adjacent bright fringes and light waves form an isosceles triangle of angle θ. Using trigonometry, the fringe spacing δ is can be calculated as,

$$\delta = \frac{\lambda}{2\sin(\theta/2)} \tag{3.1}$$

With the fringe spacing known, the relationship between the velocity of the particle and the frequency it generates can be determined.

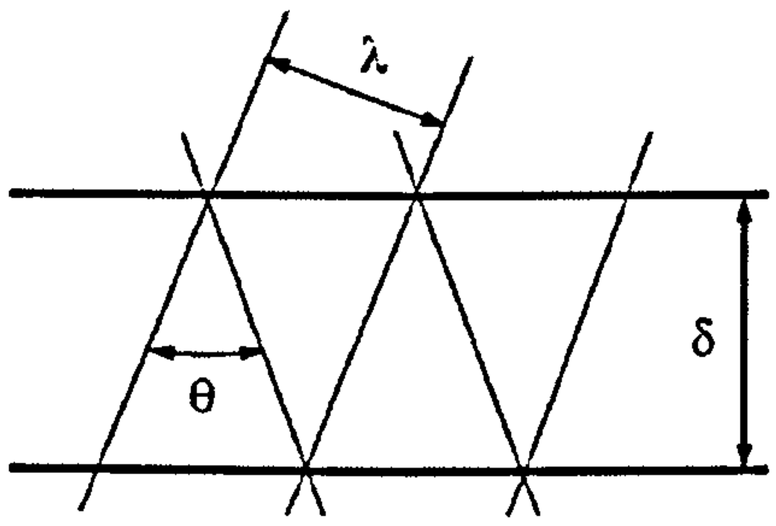

Figure 3-3 Relationship between fringe spacing, light wavelength and the angle between beams

If the fringes are a distance δ apart and the velocity component of the particle normal to the fringes and in the plane of the beams is u, then the particle will generate a signal of frequency f,

$$f = \frac{u}{\delta} = \frac{u \sin(\theta/2)}{\lambda/2} \tag{3.2}$$

This important expression, known as the LDA equation, relates the frequency of the LDA signals, f_D, to the velocity of the flow, u.

$$u = f_D \frac{\lambda/2}{\sin(\theta/2)} \tag{3.3}$$

The explanation given of how a laser Doppler anemometer works, in terms of particles passing through equally spaced fringes, is known as the fringe model (Dantec Elektronik, User's Guide).

3.2.2 The LDA optical system

The Dantec Argon-ion Laser Doppler anemometry system is made up of three main components: the Laser optical System, the Burst Spectrum Analyzers (BSA) and the PC (shown in Figure 3-4). With this LDA system, two components of velocity can be measured simultaneously.

The Laser optical System includes:

- Reliant Series Laser system (Laser generator, 500mw maximum output)
- Dantec 60x40 Transmitter (The Bragg Cell)
- Dantec 60x24 Manipulator
- Dantec 55x35 Color Separator
- Dantec 60x11 FiberFlow Probe
- The fibre cable
- The photomultipliers

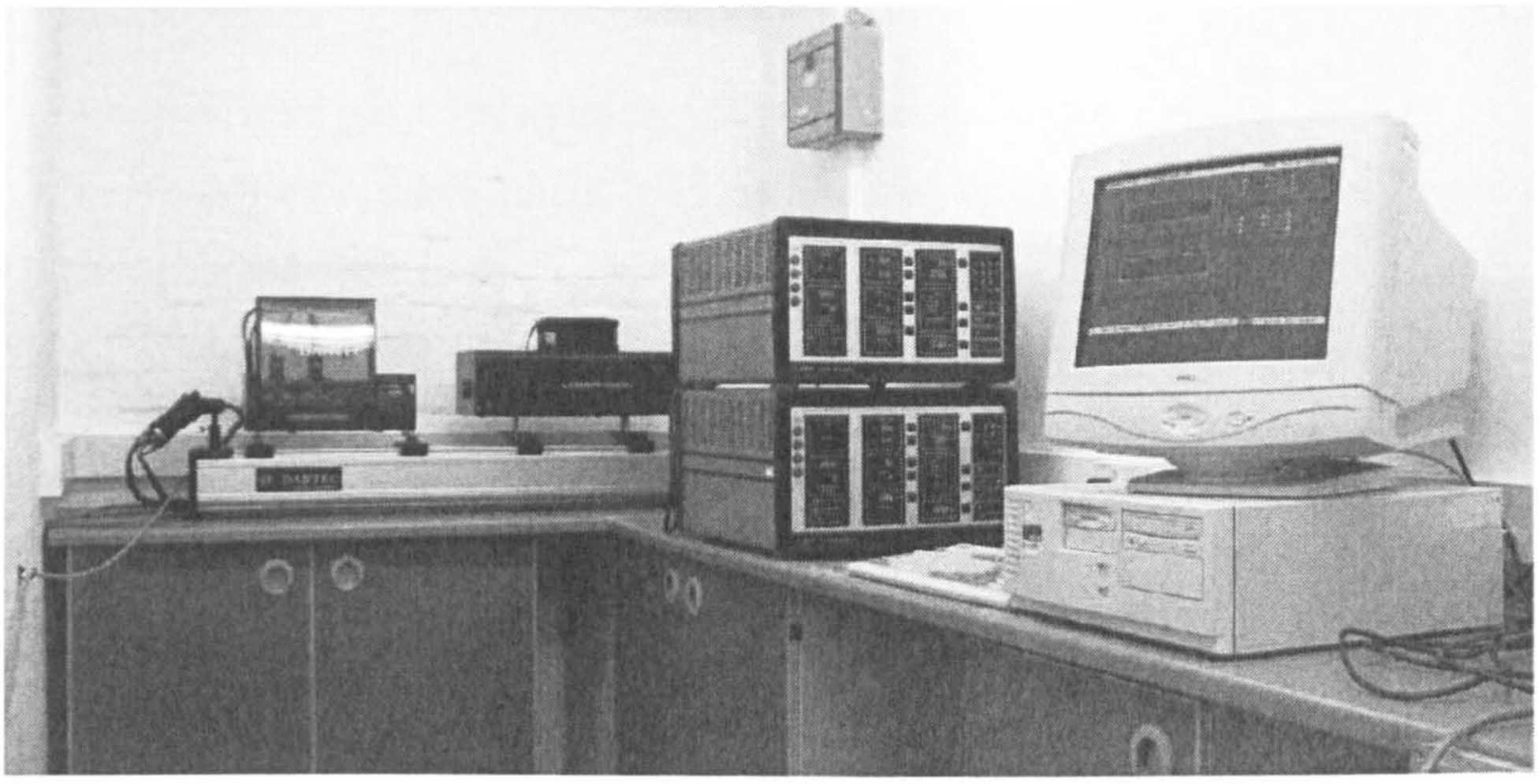

Figure 3-4 Laser Doppler Anemometry measuring system setup

The Reliant Series Laser system is a coherent light source capable of generating laser radiation at a number of discrete wavelengths within the 457 nm to 514.5 nm range.

The basic modules of the Transmitter are the beam splitter (includes Bragg Cell) and an achromatic lens. The beam splitter can divide the laser beam into two beams: one is a direct laser beam, the other is a frequency shifted laser beam generated by the Bragg cell. With frequency shifting, low velocities and the flow direction can be distinguished.

Each laser beam is separated into two colours by the Colour Separator:

- Green laser: $\lambda = 514.5$ nm
- Blue laser: $\lambda = 488$ nm

Each colour is used for measuring one velocity component. Thus, the transmitter can be used for 2D measurements.

The Manipulator centres and directs the laser beam so as to obtain the maximum amount of light into the thin single mode optical fibres of the FibreFlow probe. One manipulator is used for each output beam from the transmitter. Thus, for a 2D system four manipulators are needed.

The Dantec 60x11 2D FiberFlow Probe comprises

- Four fibre plugs for coupling with the manipulators
- Four single mode fibers (one for each of the transmitted beams, cased in an enforced cable hose)
- One multimode fibre used as receiving fibre in backscatter mode, cased in the same hose
- The probe house
- One of several front lenses

The Probe, comprising a focusing lens, can focus the laser beams into a point; thus, measurement volume is formed. The Probe also collects the scattered laser light (backscatter mode), and focuses it onto a photomultiplier via the multimode fibre cable (Figure 3-5).

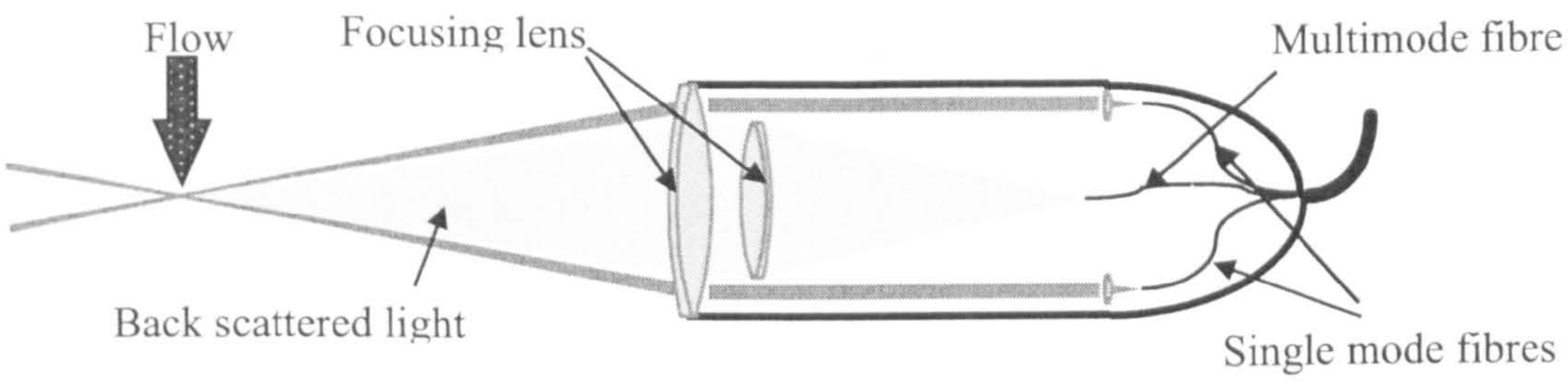

Figure 3-5 Schematic illustration of fibre flow laser probe

The parameters of the Probe used in the experiments are

- Probe dimensions: ϕ 60 x 275 mm
- Beam diameter: 1.35 mm
- Beam spacing: 38 mm (distance between pair of laser beams at the front lens)
- Focal length: 160 mm (transmitting lens focal length)
- Laser wave length: 488 nm (blue beam); 514.5 nm (green beam)
- Transmission fibres: Polarization preserving single-mode
- Receiving fibres: Multi-mode

The photomultipliers convert the light intensity fluctuations to electrical signals, which are in turn converted to velocities by the Burst Spectrum Analyser (BSA). There are two burst spectrum analysers used as signal conditioners and signal processors.

3.2.3 Burst Spectrum Analyzer (BSA)

The BSA uses a sophisticated technique to extract the Doppler frequencies from the Fourier Transform of the Doppler bursts. This is different to the method employed by counters and tracker processors. Two Dantec 57N10 BSA were used in this work. The BSA can handle signals with very low Signal to Noise Ratios (SNR), which means that reflections from nearby surfaces will not interfere with the measurement. The BSA is fully computer controlled, i.e. both the measurement data transfer and the parameter setup can be performed from a host computer via an IEEE 488 interface.

It is important to track the optimal parameters in the measurement for the best signal results. The following parameters are the major measurement parameters:

Centre Frequency and Bandwidth:

The Centre frequency and Bandwidth define the measuring range. If the mean velocity of the flow is known, the centre velocity should be set to a value just above the known value. The span should be as large as possible. If the velocity is not known, the setting should be as large as possible. By watching the Doppler signal output at the front panel and/or by observing the bar graph with the measured frequencies through the monitor, the frequency and the span are adjusted downwards to achieve the highest validation and the highest data rate.

Signal Gain:

The signal gain is the amplification of the input signal, and is defined as the ratio between the voltages at the Doppler out monitor and the PM in (photodetector input). It can be changed in steps of 1 dB (decibel) to determine the amplification of the input signal. The range depends on the centre frequency and the span selected. When a new signal gain value is entered, the BSA automatically selects the nearest value it can realize according to the centre frequency and the span.

High Voltage:

The dynodes of the Photomultiplier require a High Voltage. The Burst Spectrum Analyzer supplies this voltage, in steps of 8 V from 0 V to 2040 V.

The signal gain and the High Voltage to the PM tube are used in combination to obtain the best possible signal for the processor. The data rate may be increased, by adjusting the signal gain and/or the High Voltage to the Photomultiplier to the point where the anode current limiter becomes active. Another important restriction is that the noise-level must not be amplified to such a degree that it triggers the burst detector. The validation will decrease when this happens. Through the experiments, the signal gain was set to between 20-35 dB and the High Voltage set to about 1400 V for optimum signal.

Record Length:

It is defined as the number of samples per digitized burst. The record length can be 8, 16, 32, or 64. The number describes how many samples a record will contain. It was usually set between 8 and 32 in the experiments.

The record length and the selected span define the record interval. The interval should be as close as possible to the shortest of the Doppler bursts (to prevent noise from being picked up in the record after the burst has been collected, and thus reduce the validation percentage). When the record length is adjusted, the data rate and the validation percentage increase immediately.

The burst processing mode is chosen as the data collection mode. For burst processing data collection mode, the BSA performs one measurement per burst. The measured parameters are frequency, arrival time, and transit time.

The software (Dantec BURSTware version 3.11) running in the PC was used to operate the signal conditioning and processing. It supported the 55X Modular LDA Optics, 60X FiberFlow Probe with any BSA signal processor or combinations of them in 2D configuration. Communications between the PC and the BSA were based on the GPIB board from National Instruments. Vertical and horizontal velocity components of fluid flow could be obtained from BSA1 and BSA2 respectively.

When the optimal parameters are found, the measurements can be carried out.

3.3 Seeding requirements

It is important that tiny particles must be present in the flow for a measurement to be made. These are referred to as seeding particles. These particles should be small enough to follow accurately all the movements of the flow. That way, when the velocity of the particles is measured, the velocity of the flow is also measured. The particles form only a minuscule fraction of the volume of the fluid, even in well-seeded flows. Therefore, they have no significant effect upon the flow.

Numerous properties of the particle material have to be taken into consideration when selecting the appropriate seeding medium for a particular measurement task. Mean particle size is only one of the parameters. Other parameters of interest include specific gravity, particle shape, particle size distribution, surface characteristics, and refractive index. The choice of the right seeding material to scatter light from the laser beams or a light sheet can be crucial to the acquisition of successful experimental data. Usually, one-micron diameter particles are small enough, and such particles are present naturally in tap water.

In order to satisfy seeding requirements, the Dantec Polyamid Seeding Particles (PSP-20) were used (Table 3-1) for the fluid velocity measurement. For air velocity measurement, the SAFEX Fog Generator 2001 was employed to produce seeding particles, using the fog fluid SAFEX Inside Fog Fluid Blitz. This generated a white, quickly disappearing fog, and the mean diameter of the fog droplet was about 1μm to 1.5μm.

Table 3-1 Specification of PSP-20 particle

Mean particle size	Size distribution	Density (g/cm3)	Melting point (°C)	Refractive index	Material	Particle shape
20μm	5 - 35 μm	1.03	175	1.5	Polyamide 12	non-spherical but round

3.4 Signal processing and signal characteristics

The electronic signal given out by the photomultiplier contains periods of silence when there are no particles in the measurement volume, randomly interspersed with bursts of signal when a particle passes through the measurement volume. Figure 3-6 shows an idealized signal burst. The shape of the burst is a consequence of the fact that the beam light intensity is greater at the centre than at the edges. As the particle passes through the edge of the measurement volume where the fringes are weakly illuminated the signal fluctuations are also weak. As the particle passes through the centre of the measurement volume; the signal fluctuations become larger and then decay again.

The signal can be split into two parts - a low frequency part called the 'pedestal', and a high frequency part that contains the Doppler signal.

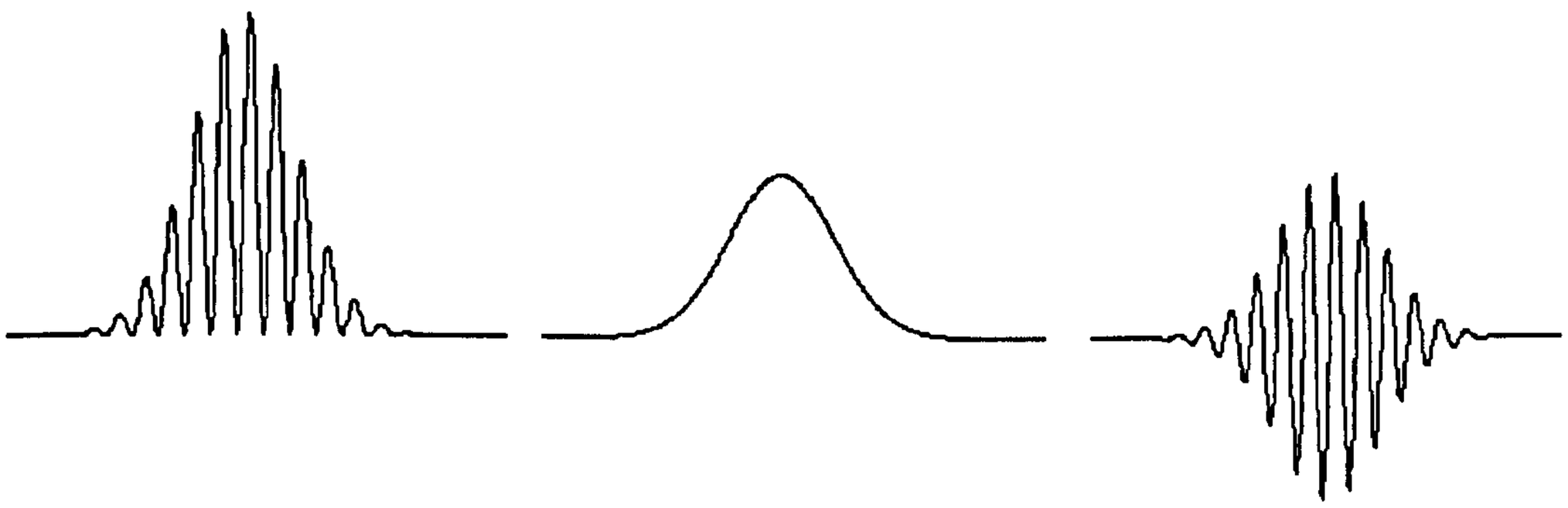

a. Burst b. Pedestal c. Doppler signal

Figure 3-6 Components of an LDA signal burst

The signal processors use digital technology to analyze each burst and extract the frequency and thus velocity at that instant. Typically, such processors have 'burst-detection' circuits to tell them when there is a signal. They then digitize that signal and determine its frequency. 'Burst Spectrum Analyzers' utilise the Fourier spectrum of the signal in order to determine its frequency.

In the fluid dynamics community, LDA is considered as an absolute flow measurement method. Knowing the laser wavelength and the intersection angle between the laser beams, the calibration constant or fringe spacing can be calculated easily. However, as

with any other measurement technique, there are always some noise signals can affect LDA measurements. The main sources of noise in LDA measurements are:

- Photomultiplier shot noise
- Secondary electronic noise, thermal noise from preamplifier circuit
- Optical noise
- Light scattered from outside the measurement volume, dirt, scratched windows, ambient light, multiple particles, etc.
- Unwanted reflections (windows, lenses, mirrors, etc)

Although some sources of noise cannot be eliminated, measures may be taken in order to maximize the signal to noise ratio (SNR):

- Optimizing the seeding: it is best to arrange the seeding so that there is never more than one particle in the measurement volume at any given time. If multiple particles are present then the signals they produce will, most likely, cancel out.
- Avoiding light scattered from outside the measurement volume to get into the receiving lens. It is good practice to paint the wheel and the wall of tank opposite the laser probe black.
- Keeping the laser power moderate (three quarter of maximum output in experiments)
- Choosing the optimal parameters when changing the experimental conditions
- Reducing the preamplifier level when the SNR is very low

Chapter 4 Fluid velocity mapping

4.1 Introduction

The main aim of this preliminary study was to acquire a basic understanding of the flow velocity profile in the region close to the grinding contact zone and to determine the basic characteristics of the fluid flow under varying grinding conditions. Additionally, the tests were used to establish that the LDA system is a suitable measurement tool to be used in grinding research and to assess its performance and capability for future measurements.

In this context, the experiments were undertaken to measure the fluid velocity distribution. The gap of separation between the wheel and workpiece was varied to permit study of the flow in the region of interest. Fluid levels comparable to those encountered in a shoe nozzle type system were used. This arrangement avoided potentially extensive, time-consuming experiments on a CNC machine tool and unnecessary fabrication of jigs and fixtures. The arrangement served as the close to a match of the grinding situation without high costs. i.e. a low cost intermediate solution.

The experiments also provided data used to validate theoretical models of fluid flow conditions in grinding, aided analysis of the fluid chamber system and gave insight into the requirements of a shoe nozzle system.

4.2 Experimental arrangement

In order to simplify the measurement of fluid velocity in grinding and to aid the development of a robust reliable experimental technique for future measurements, a surface grinding arrangement was established prior to the experiments undertaken. This took the form of a modified bench grinder, shown in Figure 4-1.

The wheel diameter D, was 200 mm, and the wheel bore was 20 mm. The wheel speed v_s was 1.4 m/s, which could not be changed due to the grinder specification. This is not

a practicable speed, however it provides for analysis of the profiles. After dressing, the wheel width was 38 mm.

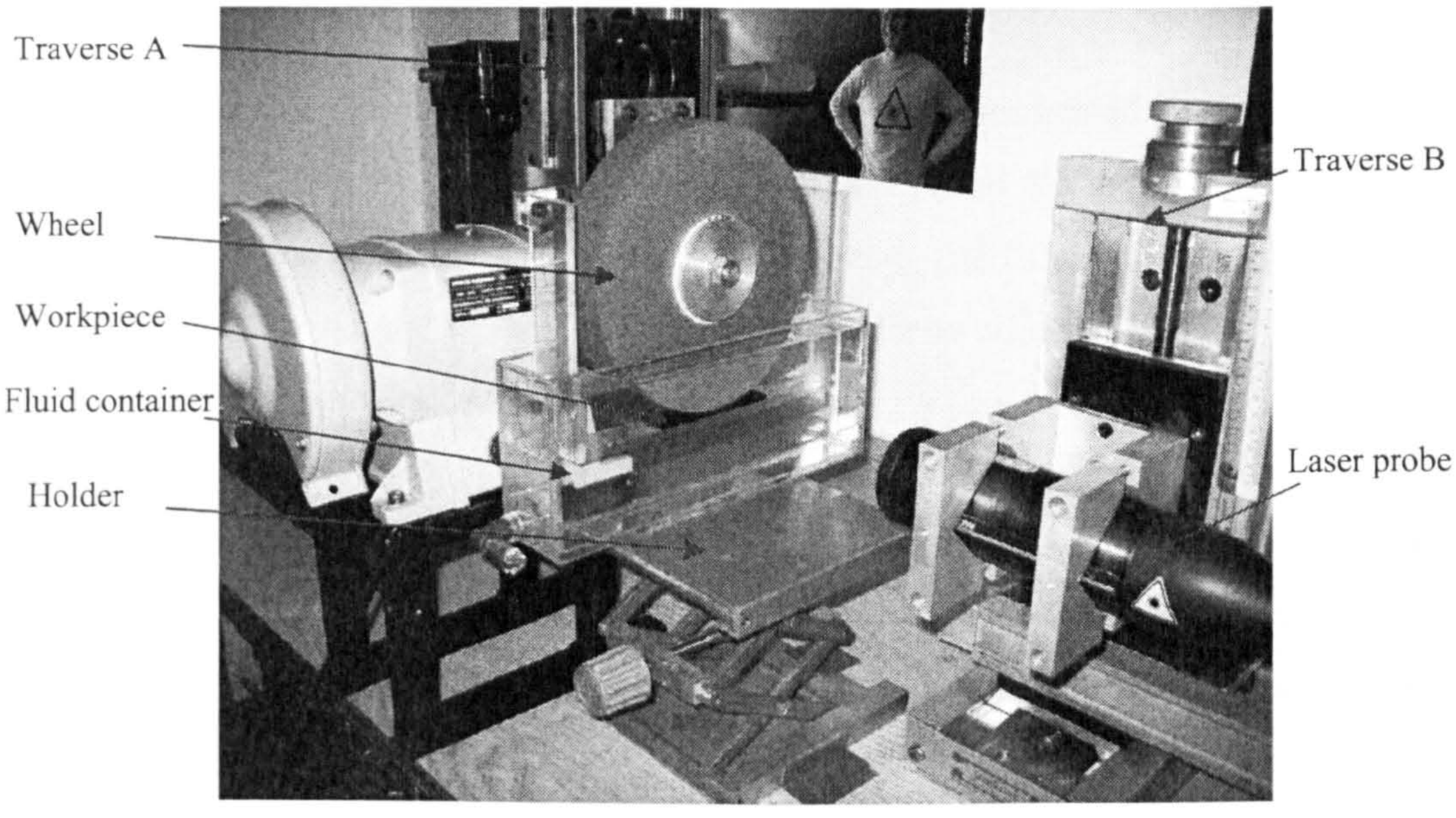

Figure 4-1 Experimental arrangement

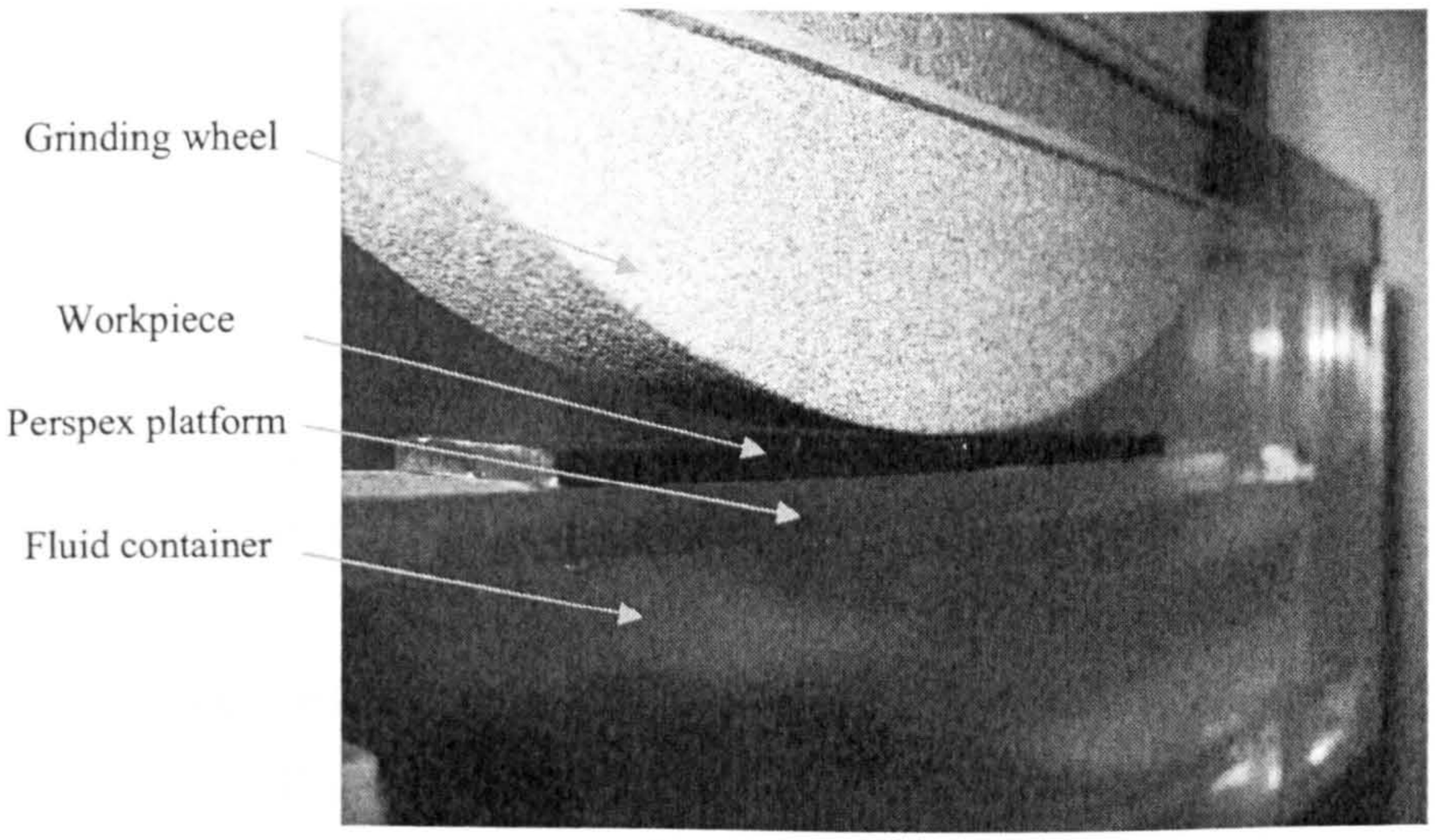

Figure 4-2 Wheel and workpiece arrangement

The workpiece was made of aluminium, and its width was the same as the width of the grinding wheel, Figure 4-2. The length and thickness were 100 mm and 3 mm

respectively. The workpiece was painted black in order to avoid laser scattering, and it was attached on the Perspex platform, which could be adjusted in the vertical direction by Traverse A, Figure 4-1. This provided simple adjustment of the distance between the wheel and the workpiece during the experiments.

Part of the wheel and the whole of the workpiece were immersed in fluid inside a Perspex container. Water or oil was used as the grinding fluid as the LDA system is not as effective in an emulsion due to its poor transparency. The fluid container was placed on a holder, and the height of the fluid container could be adjusted enabling the water level to be changed when needed.

The LDA probe was placed toward the measuring area between the grinding wheel and the workpiece. It was mounted on a 3D traversing mechanism (Traverse B), with a distance resolution of 0.01 mm, which make possible accurate positioning of the measuring point.

4.3 Basic flow characteristic measurement

The velocity profiles under the immersed wheel arrangement were studied in the first instance. This study helped determine the basic characteristics of the fluid flow under varying grinding conditions and the profile of the velocity distribution in the region close to the grinding contact zone.

4.3.1 Method of experiment

Three parameter sets were applied in the experiments to obtain the fluid velocity profile between the grinding wheel and the workpiece. The following procedure was employed:

1. Tests with two different gaps: Gap a=1 mm and Gap b=0 mm (shown in Figure 4-3). The gap is defined as the distance of the wheel surface to the workpiece upper surface.
2. Tests with two fluid levels: Level A=40 mm and Level B=20 mm (shown in Figure 4-3). The height of the water levels was from the workpiece surface to the water surface level in the container.

3. Tests with two different measuring sections along the laser beam direction: (section I (side section) and section II (middle section), which are parallel to the wheel side surface, shown in Figure 4-4 and Figure 4-5). Section I is 2 mm from the right side surface of wheel, and Section II is the middle section of the wheel.

Figure 4-3 and Figure 4-4 show a schematic of the measurement area (front view and side view). The

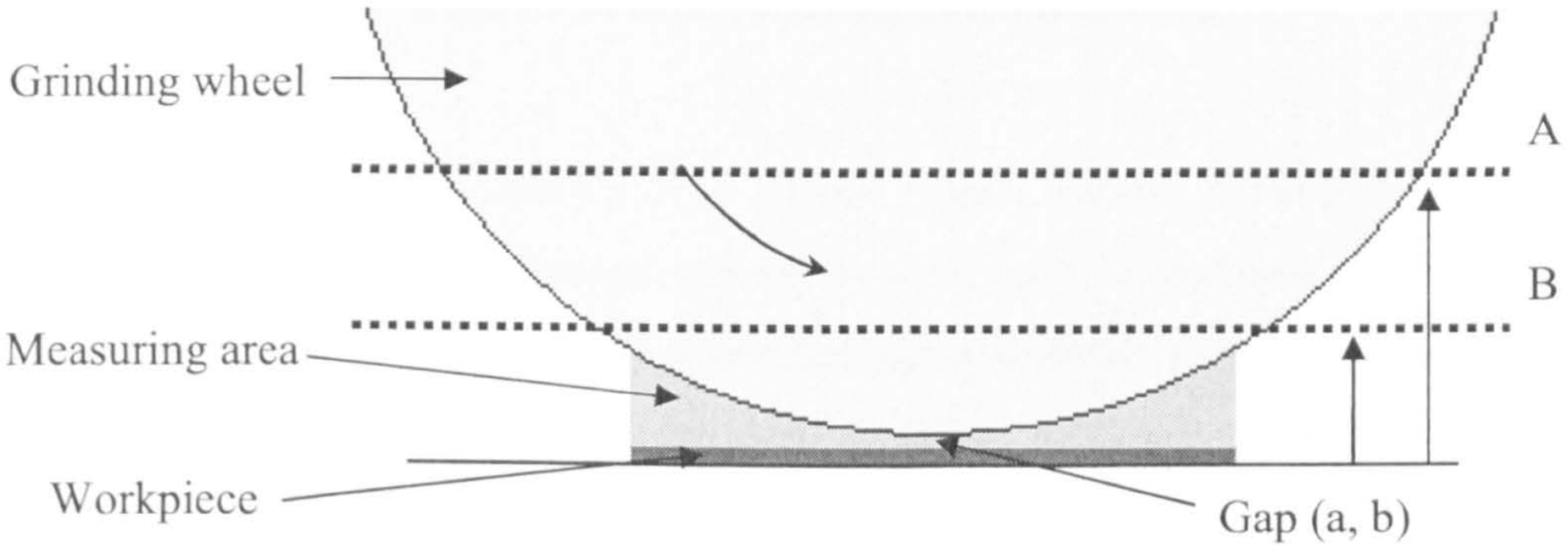

Figure 4-3 Schematic illustration of measurement area (front view)

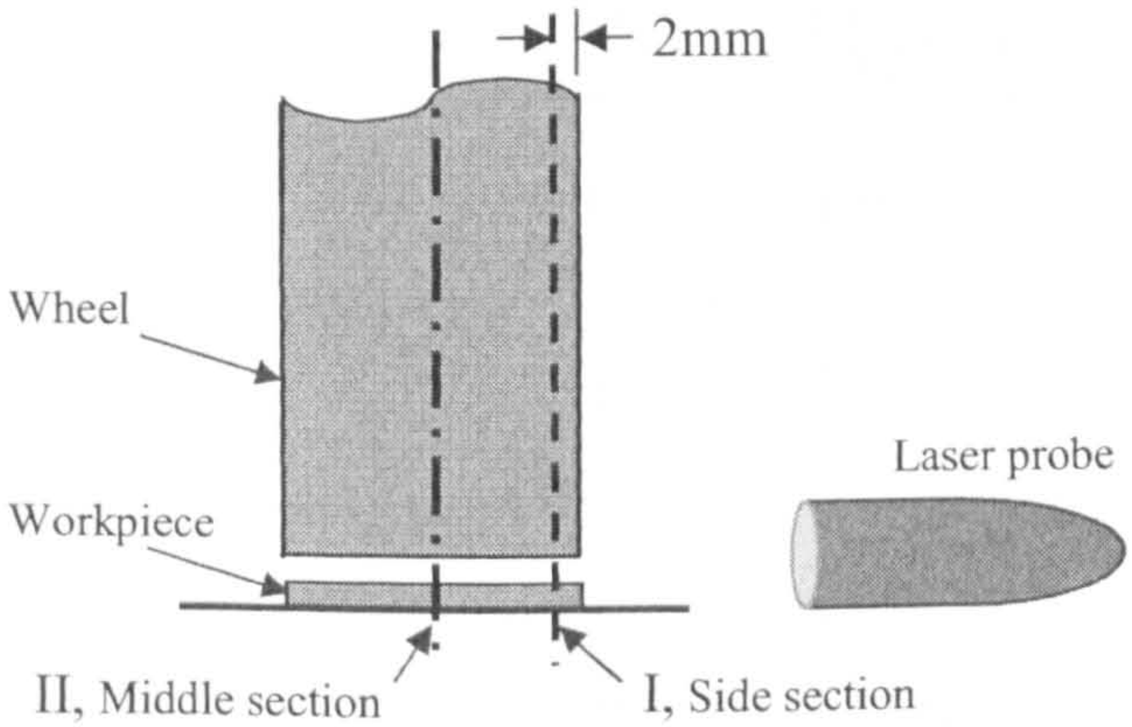

Figure 4-4 Schematic illustration of measurement area (side view)

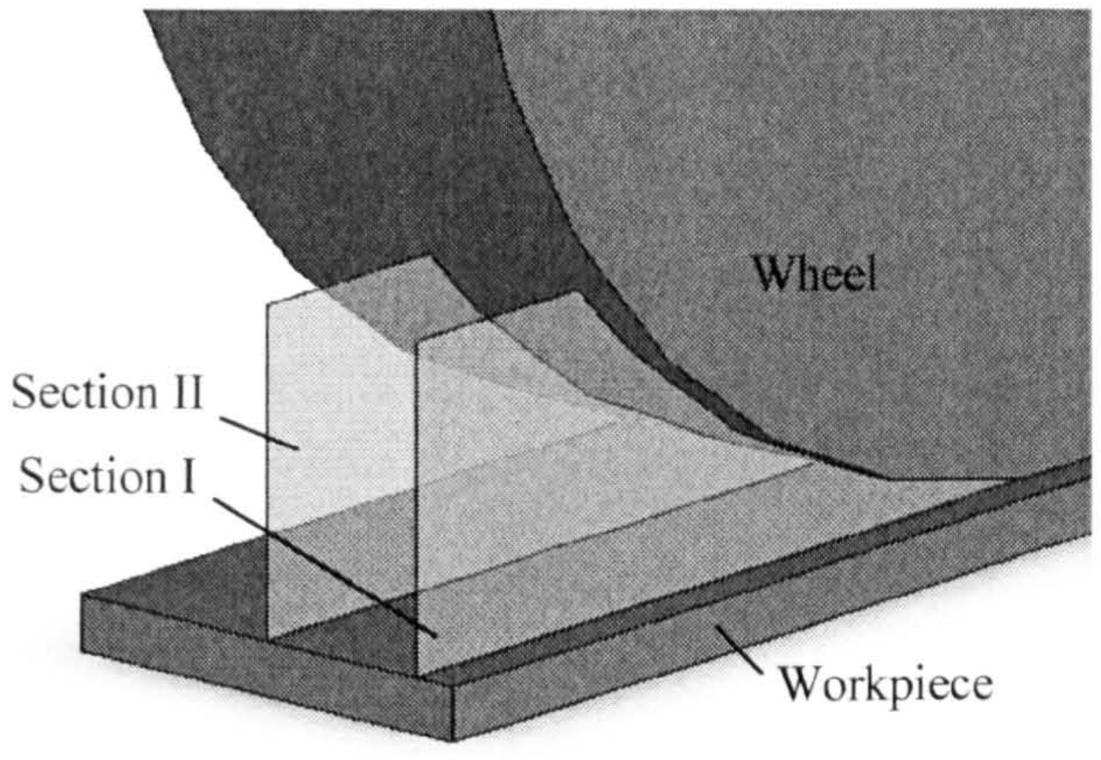

Figure 4-5 Position of the measurement section

The different settings provided for eight groups of data, shown in Table 4-1. In each set of experiments, a series of LDA measurements were made, allowing a matrix to be built up covering the area of the grinding contact entry and exit regions. These two areas were the wedge shape just close to the minimum gap, as shown in Figure 4-6. In order to determine the resultant velocity at a particular point, the vertical and horizontal components of velocity are required.

Table 4-1 Eight groups' data measured in experiments

Data group	Water level		Gap		Measuring section	
	A=40 mm	B=20 mm	a=1 mm	b=0 mm	I section	II section
1	√		√		√	
2	√		√			√
3	√			√	√	
4	√			√		√
5		√	√		√	
6		√	√			√
7		√		√	√	
8		√		√		√

The coordinate system is shown in Figure 4-6. The point on the wheel edge, which is nearest to the workpiece surface and the laser probe, is the origin. The x-axis is parallel

to the workpiece top surface, and the y-axis is perpendicular to the workpiece top surface.

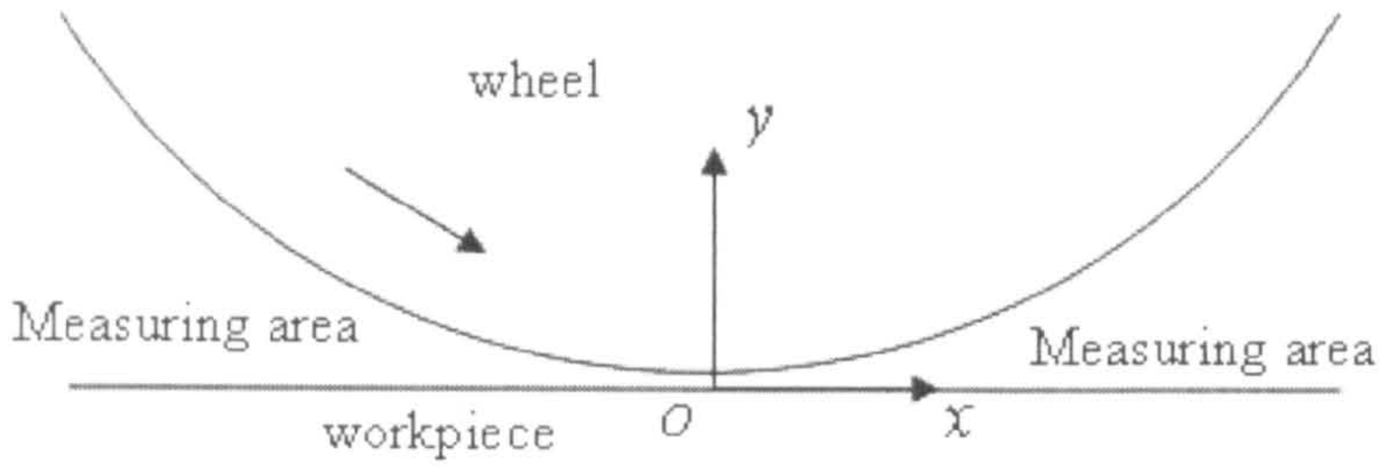

Figure 4-6 Coordinate system in the measurement area

The laser was first set at the origin. After the fluid velocity was measured at this point, the beams were moved to a neighbouring measurement point. This procedure was repeated at numerous points to provide data for one velocity distribution map. The measurement range was from -50 mm to +50 mm along the x-axis with intervals of 5 mm in the horizontal direction; in the vertical direction, measurements were made between the wheel and the top surface of the workpiece.

All measurement results were exported to Excel and processed with Matlab. The vector plots of the resultant velocity are given in the following sections.

4.3.2 Measurement limitations

This limitation occurred where the beams were too close to the wheel or workpiece surface, i.e. both the wheel and workpiece could interrupt the laser beams to cross in the measurement points since the beams were not parallel to the wheel surface or the workpiece surface. For example, the LDA is shown schematically in Figure 4-7. In the measurement of the vertical component velocity should the position of the laser probe be too high, the upper beam would be broken by the wheel, while if the laser probe position was too low, the bottom beam would be broken by the workpiece. Hence, the area very near the wheel or the workpiece could not be measured. The dimension of the area can be calculated according to the position of measurement section and parameters of the laser probe.

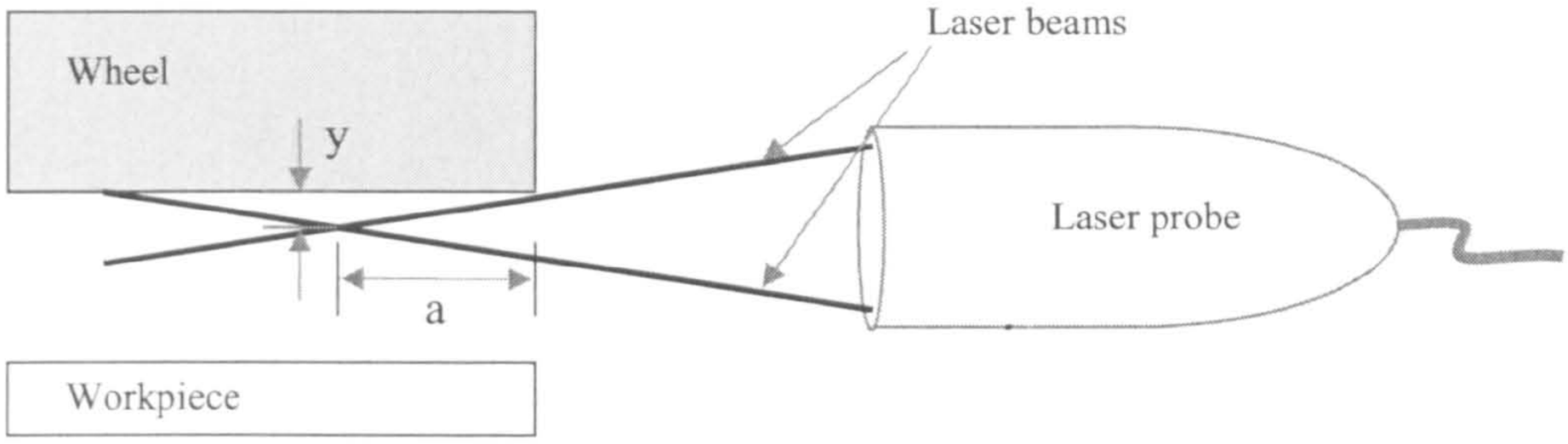

Figure 4-7 LDA measurements between wheel and workpiece

If the distance from the right side surface of the wheel to the measurement section is a, and the distance from the measurement point to the wheel cylindrical surface is y, then:

$$\frac{y}{a} = \frac{l/2}{f} \tag{4.1}$$

where beam separation l = 38 mm and focal length f = 160 mm,

$$\text{therefore} \quad y = \frac{l/2}{160} a = \frac{19}{160} a \tag{4.2}$$

If the measurement section is further away from the right side surface of the wheel, more of the area near to the wheel cannot be measured. Therefore, the LDA cannot obtain the vertical component velocity in the measurement section II (middle section of the wheel), if the measurement point was less than 2.26 mm (when a = 19 mm, half wheel width).

4.3.3 Results and discussion

There are eight groups of data obtained for different gaps, fluid (water) level and measuring section.

The vector velocity profiles of the fluid flow were obtained for each case (shown in Figure 4-8 to Figure 4-15).

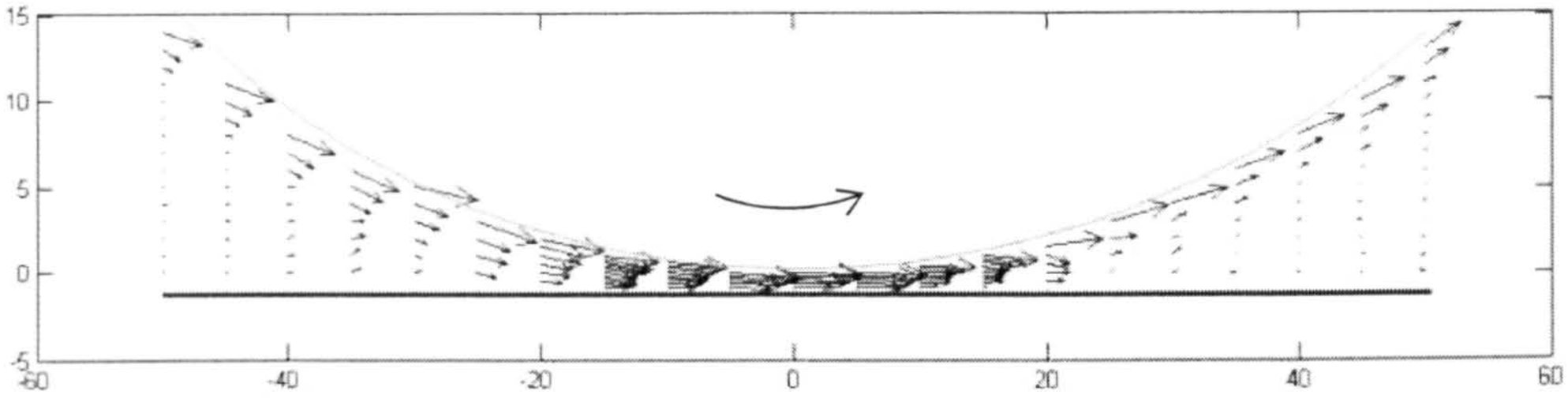

Figure 4-8 Velocity profile 1 (Data group 1: water level 40 mm; gap 1 mm; Side section)

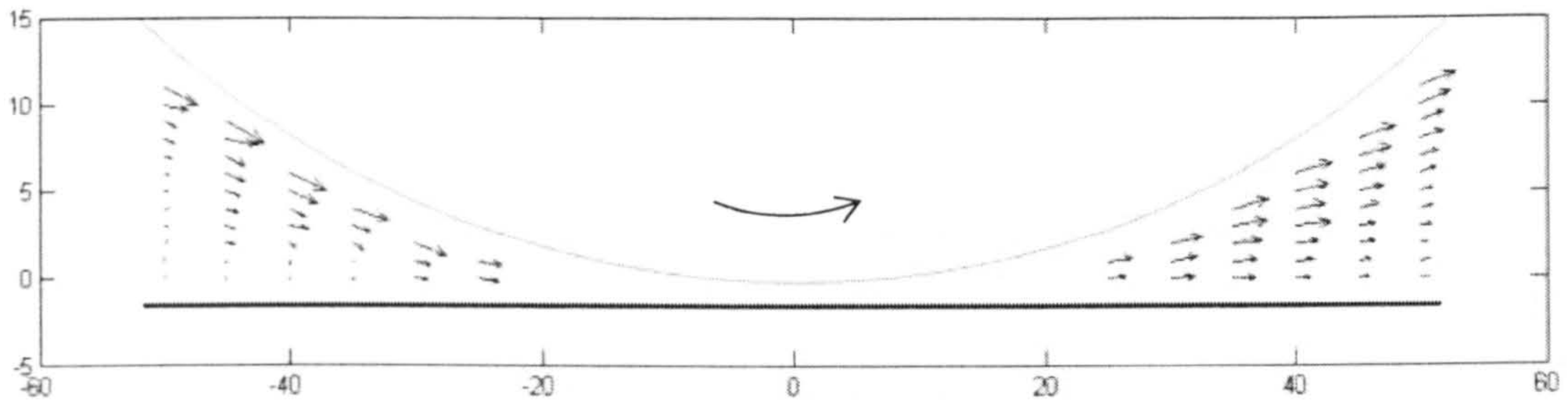

Figure 4-9 Velocity profile 2 (Data group 2: water level 40 mm; gap 1 mm; Middle section)

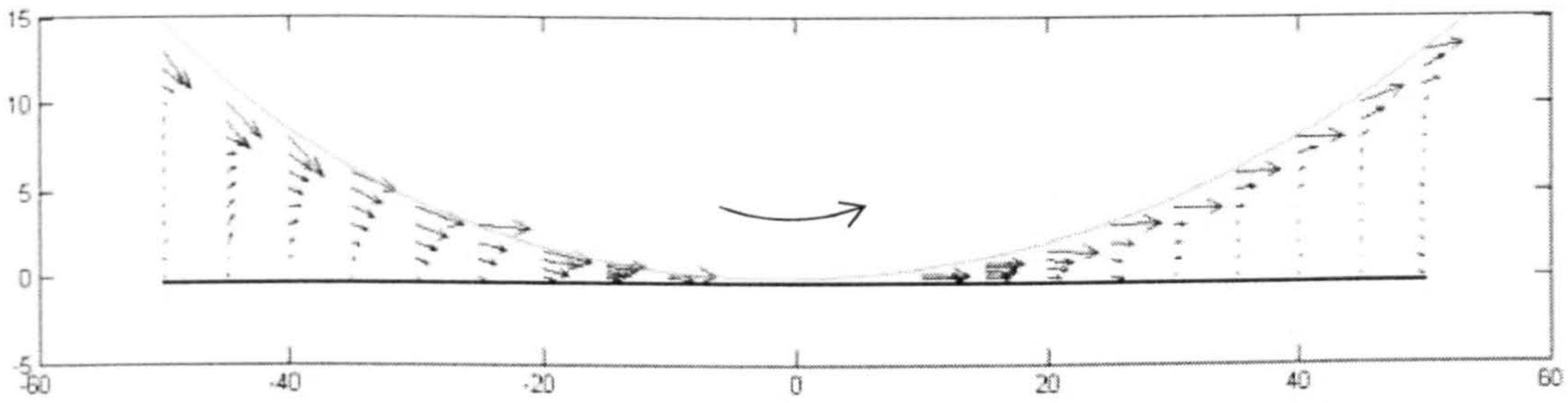

Figure 4-10 Velocity profile 3 (Data group 3: water level 40 mm; gap 0 mm; Side section)

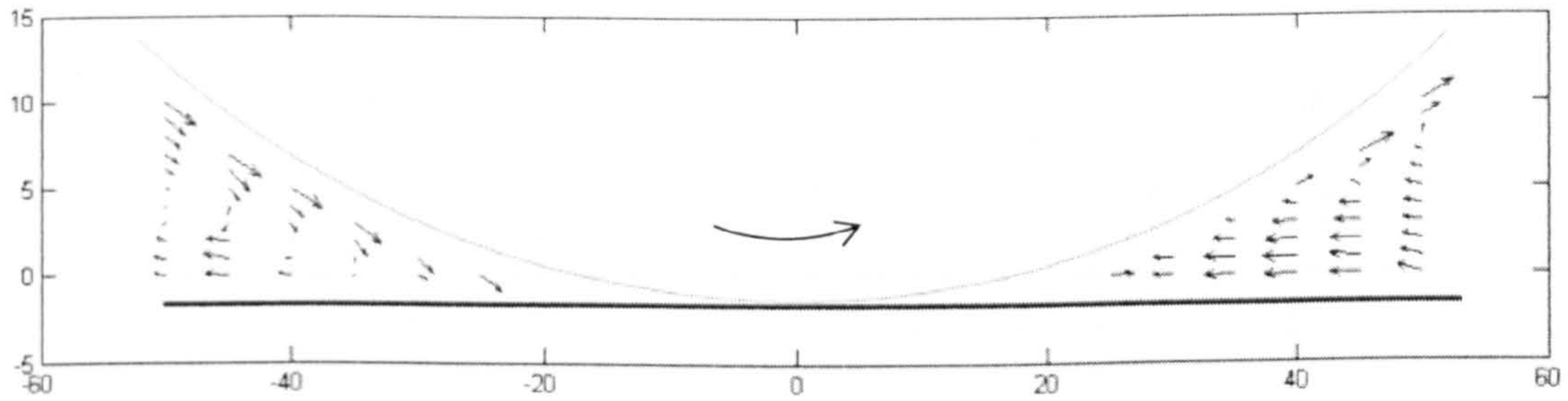

Figure 4-11 Velocity profile 4 (Data group 4: water level 40 mm; gap 0 mm; Middle section)

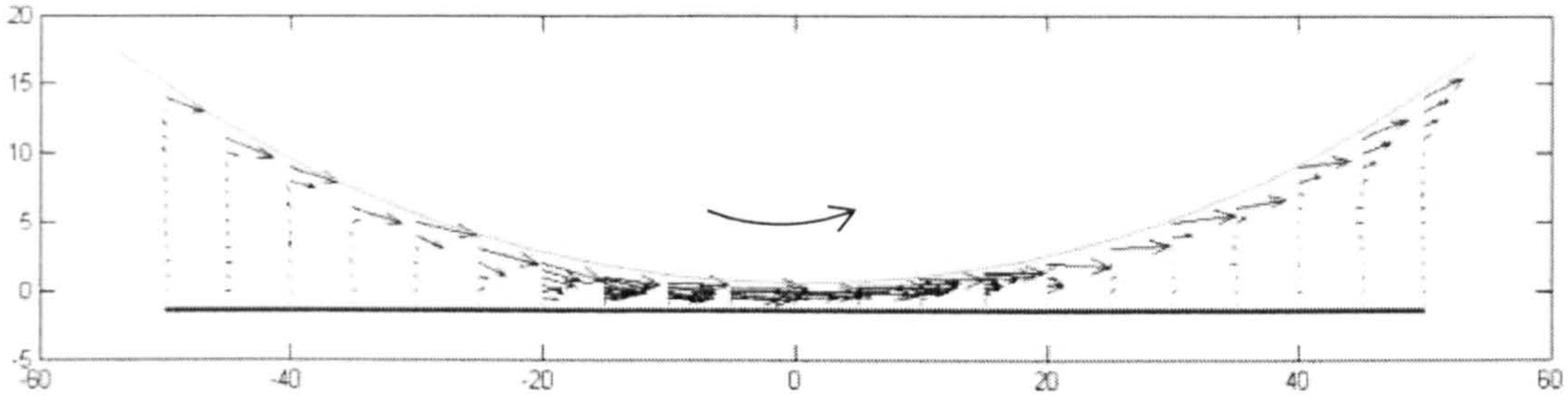

Figure 4-12 Velocity profile 5 (Data group 5: water level 20 mm; gap 1 mm; Side section)

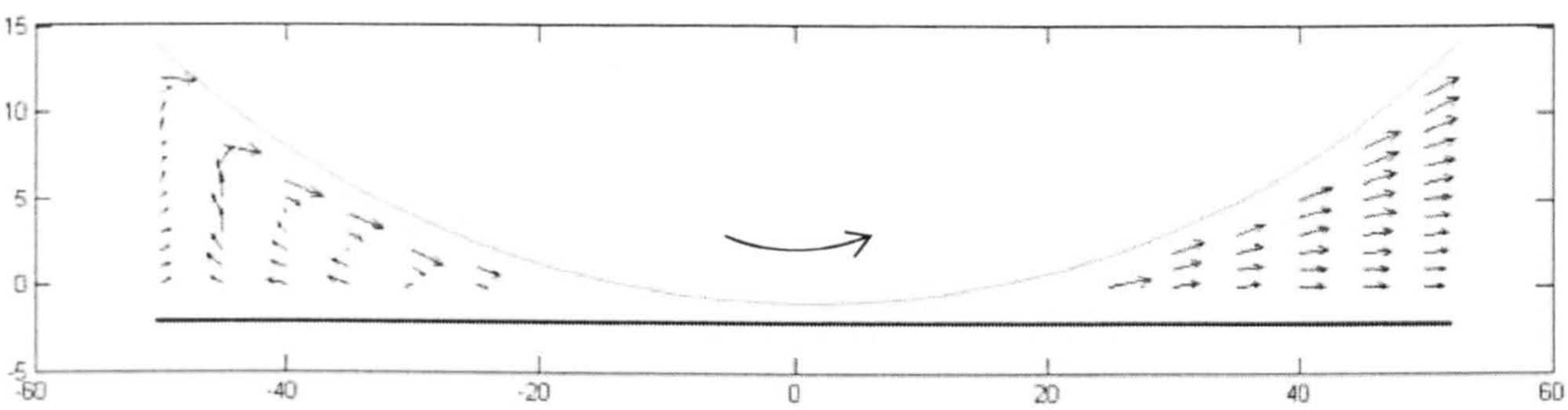

Figure 4-13 Velocity profile 6 (Data group 6: water level 20 mm; gap 1 mm; Middle section)

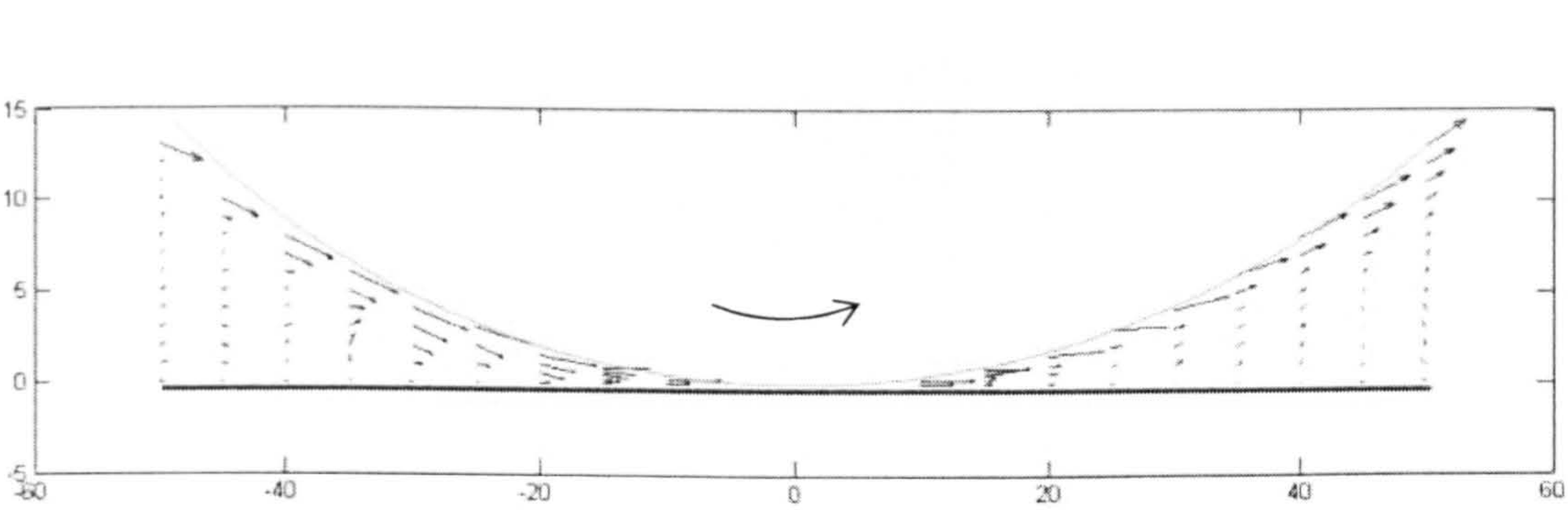

Figure 4-14 Velocity profile 7 (Data group 7: water level 20 mm; gap 0 mm; Side section)

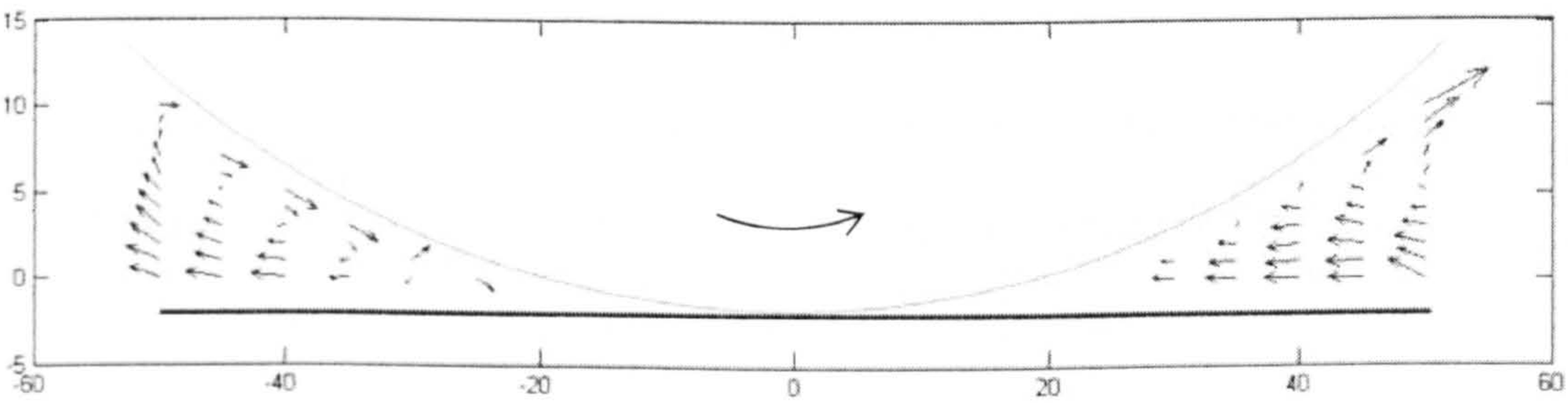

Figure 4-15 Velocity profile 8 (Data group 8: water level 20 mm; gap 0 mm; Middle section)

In order to aid discussion of the velocity maps, the fluid flow following the rotation of the wheel was termed: 'boundary layer flow'; the fluid flow passing through the gap

was termed: 'contact zone flow'. In practice, there would be fluid opposing the direction of the wheel rotation both in the entry region and in the exit region of the gap. These flows were termed: 'reverse flow in the entry region' and 'reverse flow in the exit region' respectively. Because of the limited size of the gap and also the inertia of the fluid flow, not all the fluid could pass through the gap or reverse from the contact zone, so some fluid would pass on either side of the contact zone, and this flow was termed 'side flow'. The side flow could be observed during the experiment.

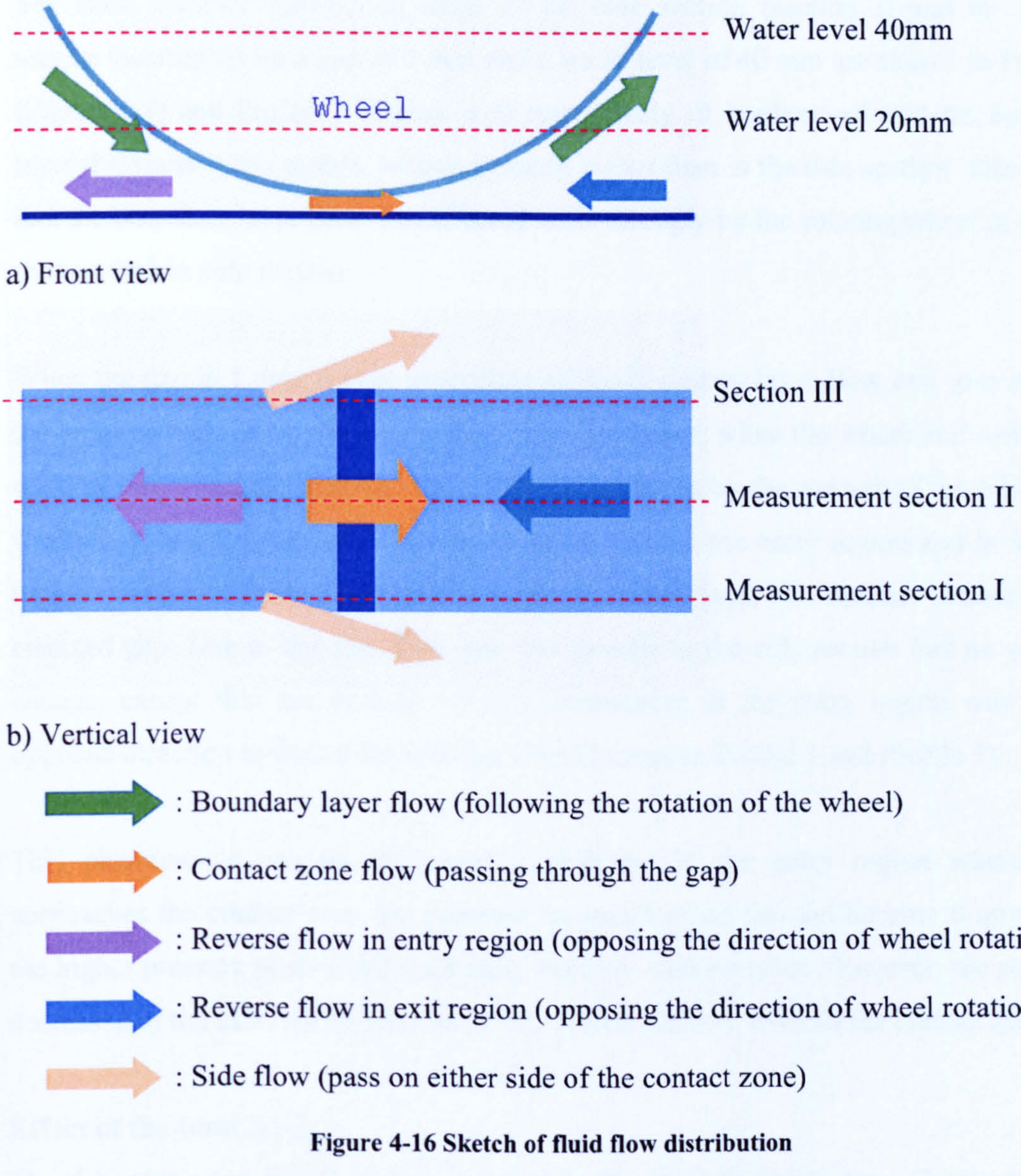

a) Front view

b) Vertical view

Figure 4-16 Sketch of fluid flow distribution

The named fluid flow distributions between wheel and workpiece are shown schematically in Figure 4-16. Because of the bilateral symmetry, the fluid flow

distribution on the side - Section III, which is opposite to the section I, was assumed equal (Figure 4-16b).

It is evident from the velocity profile maps that generally, the velocity of the boundary layer flow was the highest in the measurement area. The thickness of boundary layer flow in the exit region was smaller than that in the entry region.

Effect of the gap size:

The fluid velocity distribution maps of the side section (section I) and the middle section (section II) for a gap of 1 mm and a water level of 40 mm are shown in Profile 1 (Figure 4-8) and Profile 2 (Figure 4-9) respectively. It is observed that the boundary layer thickness in the middle section is much higher than in the side section. This shows that the boundary layer flow was affected more strongly by the rotating wheel in middle section than in side section.

When the gap is 1 mm, a high proportion of the boundary layer flow can pass through the gap and there is no obvious reverse flow. However, when the wheel and workpiece were in contacted, the boundary layer flow was broken by the contact of the wheel and workpiece, and the reverse flow was observed both in the entry region and in the exit region (compare Profile 2 and Profile 4); the boundary layer also became thinner by the changed gap. Due to the side flow, the flow profile in the side section had no obvious change, except that the vertical velocity component in the entry region was in the opposite direction to that of the rotating wheel (compare Profile 1 and Profile 3).

This phenomenon can be explained as follows: in the entry region where fluid approaches the contact area, the pressure increased when the gap became 0 mm, thus, the higher pressure pushed the fluid away from the contact zone. However, the pressure decreased in the exit region, and this is why the fluid flows towards the contact zone.

Effect of the fluid level:

The different water levels could also change the fluid flow situation. Comparing the fluid flow profile of each pair with the same gap and measurement section (Profile 1 and Profile 5, Profile 2 and Profile 6, Profile 3 and Profile 7, Profile 4 and Profile 8), the

major differences were in the entry region, and there were no obvious changes in the exit region.

When the water level was 20 mm, and the gap was 1 mm, the thickness of the boundary layer in the entry region became smaller than for the 40 mm water level. This can be explained: when the water level was low, the length of the contact arc between wheel and fluid became smaller; therefore, the fluid had not enough time to form the large flow following the rotating wheel in the entry region. This phenomenon could also be seen throughout the measurements.

In the middle section, the fluid flow reversed both in the horizontal direction and in the vertical direction, but at the area where x = - 50 mm, some fluid began to flow towards the contact zone again (Profile 6). The fluid formed a circular flow in the entry region. The reason is that: once the wheel began to rotate, the fluid was entrained by the wheel and caused a low-pressure region into which the surrounding fluid flowed, and this caused the pressure difference with the high pressure in the area very close to the grinding contact zone.

When the gap became 0 mm, a larger volume of fluid reversed in the entry region, and the velocity of the reverse flow became higher.

The velocity distribution of fluid flow is summarised in Table 4-2.

Table 4-2 Velocity map results summary

Flow types	Experimental conditions			
	A, a	A, b	B ,a	B, b
Boundary layer flow	High	Medium	High	Low
Contact zone flow	High	Low	High	Low
Reverse flow in entry region	No	Medium	Medium	High
Reverse flow in exit region	No	High	No	High
Side flow	Low	High	Low	High

A: water level 40 mm; B: water level 20mm

a: gap 1 mm; b: gap 0 mm

4.3.4 Conclusions

The fluid flow and boundary layer phenomena occurring in the entry and exit region of the contact zone were investigated using Laser Doppler Anemometry. The velocity maps in the above-mentioned region were obtained for different conditions.

The experimental results show that:

1. The velocity of the boundary layer flow was highest among all the measurement areas. The thickness of the boundary layer in the exit region was thinner than in the entry region because of the gap's size.

2. The fluid flow in the middle section was affected by the rotating wheel more either in the entry region or in the exit region. Boundary layer thickness in the middle section was much larger than in the side section.

3. When the gap became narrower, reverse flow appeared both in the entry region and in the exit region. When the wheel and workpiece contacted, the thickness of the boundary layer became smaller. The fluid flow profile in the side section showed no obvious change, but in the middle section, there was a large flow reversal in both the entry region and the exit region.

4. The water level can also affect the fluid flow situation. When the water level was low, there was not enough time for the fluid to form the large flow following the rotating wheel in the entry region, and the thickness of the boundary layer became thinner than when the water level was 40 mm in the entry region. In the middle section, the fluid formed a rotating flow in the entry region. When the gap became 0 mm, more fluid reversed in the entry region.

The velocity maps help to understand the boundary layer phenomena around the wheel surface, and determine the basic characteristics of the fluid flow. They will be helpful to establish requirements for effective fluid penetration in the grinding contact entry region and in future research work. They will also provide a guide for fluid delivery nozzle design. Therefore, they will help to acquire, evaluate and deliver the understanding needed to apply optimised useful fluid delivery.

4.4 Suggestions to theoretical analysis on fluid delivery

4.4.1 Reason to use theoretical analysis

For the grinding fluid to be effective as a lubricant and coolant, it must be delivered in sufficient quantity to the grinding zone. However, there is a lack of knowledge concerning the principles of fluid delivery into the grinding contact and these results in conflicting recommendations for the design of fluid application systems. Previous research has attempted to analyse the behaviour of coolant passing through the grinding contact zone using fluid dynamics theory, and the analyses have included parameters such as the pressure, the fluid velocity, the useful flow. Fluid dynamics and lubrication theory have been applied in this research; however, a comprehensive flow model has yet to be developed although this study has provided important insight into the nature of flow beneath a grinding wheel.

4.4.2 Theoretical models developed and their limitations

Simplified physical and geometrical models were developed in order to apply the fluid theories for the grinding fluid flow research. Schumack, et al. (1991) applied the Reynolds equation to analyse the bulk fluid behaviour and pressure distribution under conditions similar to surface grinding on a two-dimensional formulation. In this model, they concentrated on flow under a smooth wheel with a small clearance between the wheel and workpiece, and the effects of viscosity were ignored as well. The critical assumption used was that the wheel was held stationary while the table moved at the peripheral wheel speed. This had the effect of translating the wheel instead of rotating it. Guo and Malkin (1992 A) predicted the useful flow through the gap between a porous wheel and the workpiece theoretically. Their model also considered the flow to be two dimensional, because they argued that the width of grinding in the axial direction was generally much higher that the interconnecting porosity and grit spacing in the wheel and hence fluid penetration depth. Developing upon Guo's model, Chang, et al. (1996) and Chang (1997) replaced the grit covered grinding wheel with a porous outer layer. This allowed the flowrate to be predicted with Reynolds equation. Hryniewicz, et al. (2001) investigated a fluid flow in grinding with lubrication theory, and they proposed a model of fluid flow in grinding with a smooth wheel and rough wheel

respectively. It was assumed that the grinding entry region was flooded with fluid. The method by which fluid was delivered was not considered. There was a small gap between the surfaces of wheel and workpiece. Klocke, et al. (2000) described a physical model with the Navier-Stokes equation that simulated coolant induced forces during high-speed grinding. The gap between the wheel and the workpiece was chosen such that the wheel grit dimensions were essentially neglected.

To summarize, the theoretical models above have the following characteristics (Figure 4-17):

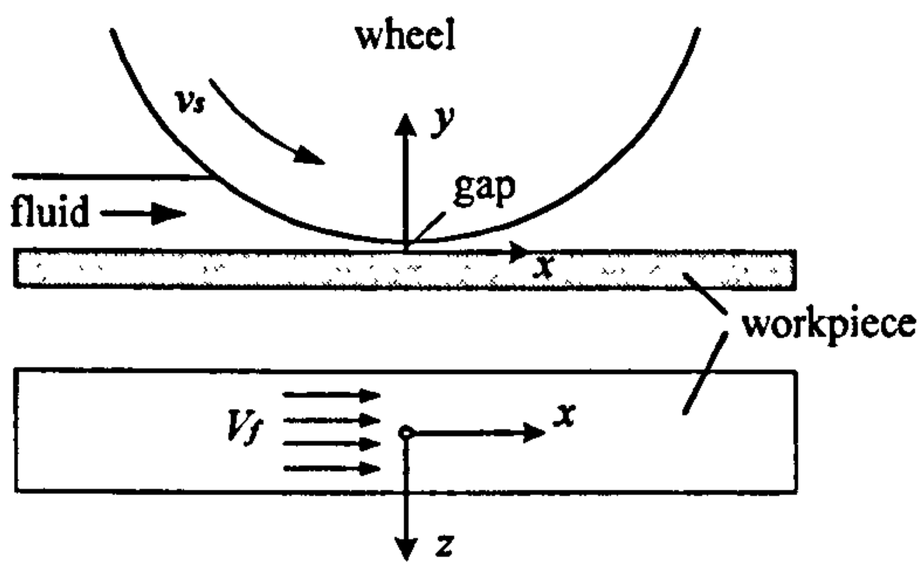

Figure 4-17 Common geometric grinding model based on previous theoretical analyses

Some or all of the following assumptions were always made to the grinding fluid in the model:

- Fluid motion is characterized by average velocity to transfer the turbulent flow to laminar flow.
- No side flow in the axial direction of the wheel, all flow takes in two-dimensional plane.
- There is a gap between wheel and workpiece to allow the fluid passing through; or the wheel surface is covered with grits or porous layer.
- Usually, the behaviour for bulk fluid delivery is analysed, and fluid viscosity is neglected.

Because a grinding wheel consists of abrasive grains of irregular shapes, bond material, and pores, the grinding fluid flow is very complex in grinding, so the simplified models

will invariably not include some important characteristic of the flow and result in models that do not explain the true phenomena or necessarily agree with experimental data accurately. It is therefore important to understand more fully the fluid motion in grinding.

4.4.3 Validation tests for theoretical models

The Laser Doppler Anemometry (LDA) measurement results can improve the understanding of fluid flow in grinding. The experimental work will help to verify current theoretical predictions and determine parameters necessary to refine and develop new models. The measurements described may be helpful to other researchers. The fluid velocity maps within different conditions measured using LDA in this section were shown in the previous section in this chapter.

The LDA measurements were made in the grinding contact entry region (the wedge area formed by the wheel and workpiece, approaching the grinding contact zone, shown in Figure 4-18). The experimental method was similar to that used in Chapter 4.3, and measurements were made in two measurement sections (shown in Figure 4-5), but measurements were only made when the workpiece and wheel were in contact, i.e. gap = 0 mm. The fluid level was set at 7 mm from the workpiece top surface in this test. This level compares with the setup in the theoretical model of other researchers'. Water and oil were used as the fluid to investigate the effect of fluid viscosity. Because the vertical component changed little in the different conditions could be ignored, only the horizontal component velocity was measured in the test. The measurement coordinate system is shown in Figure 4-17.

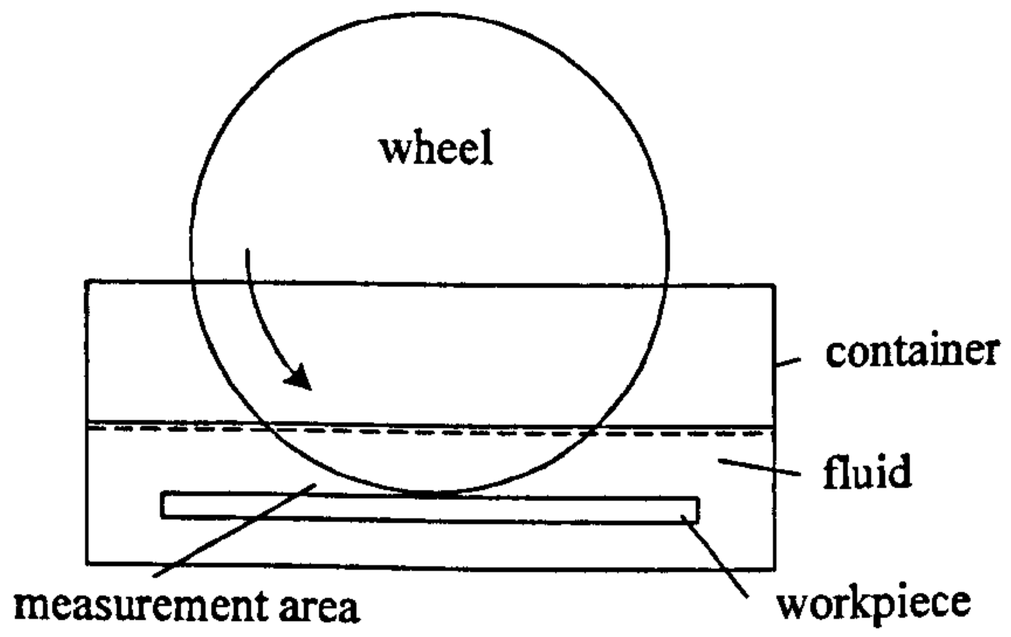

Figure 4-18 Schema of the experimental configuration

There are four fluid velocity maps presented below (Figure 4-19):

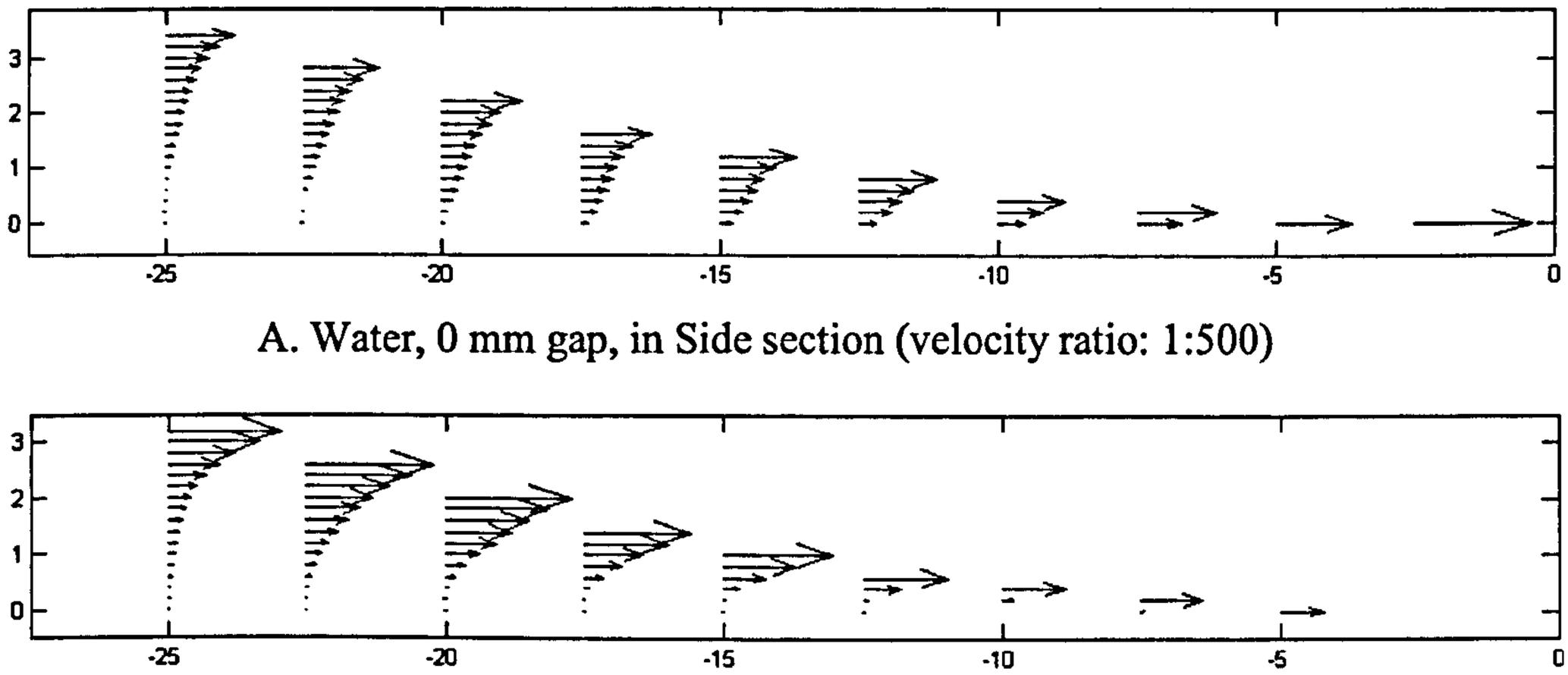

A. Water, 0 mm gap, in Side section (velocity ratio: 1:500)

B. Oil, 0 mm gap, in Side section (velocity ratio: 1:500)

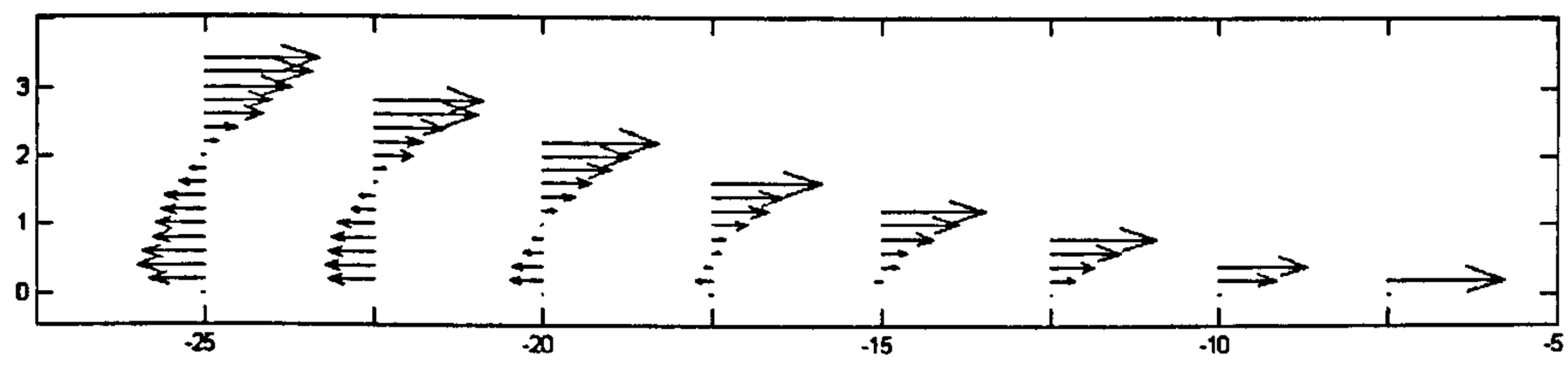

C. Water, 0 mm gap, in Middle section (velocity ratio: 1:250)

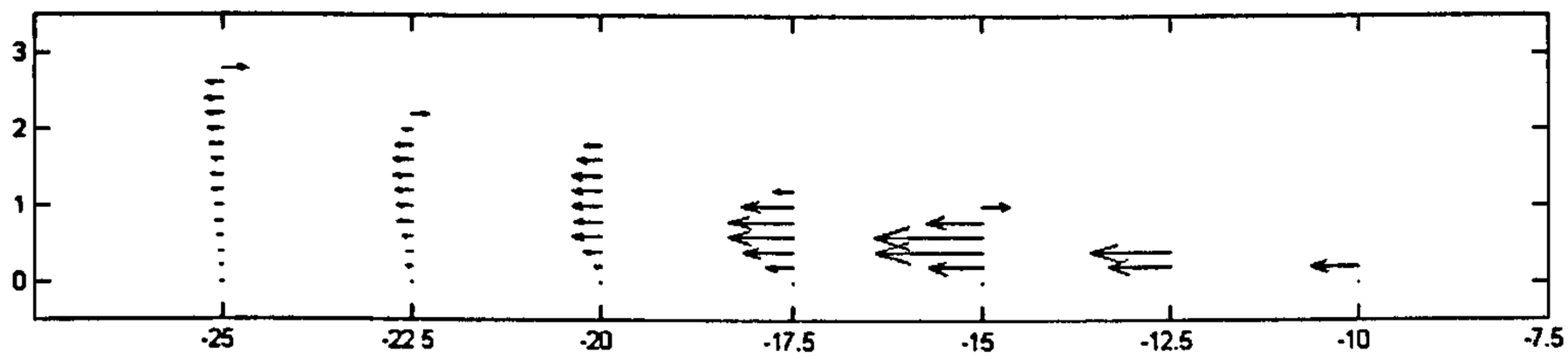

D. Oil, 0 mm gap, in Middle section (velocity ratio: 1:250)

Figure 4-19 Velocity maps with different fluids

In each map, the axes represent the x and y coordinates, and the units are in mm. Each arrow is a fluid velocity vector. The "velocity ratio" is the ratio of an arrow vector's length to the real velocity vector value. The ratios are different in order allow for a more effective display of the velocity vectors.

Normally, it is hard to say that the velocity in the wheel width direction is the same. This phenomenon can be seen through comparing Figure 4-19A and Figure 4-19C, or Figure 4-19B and Figure 4-19D. Actually in different measurement sections, the fluid velocity distribution varies, so it is not 2D flow. It was observed during the experiments that the fluid pressures in the side section were not sufficient to reverse flows. This was due to significant volumes of fluid exiting the contact zone as side flow.

There is a small difference between the velocity map for the water and for the oil in side section, but quite different in the middle section through comparing Figure 4-19A and Figure 4-19B, Figure 4-19C and Figure 4-19D. The boundary layer thickness of the water is larger than that of oil and the reverse flow appeared in a different area. The difference in fluid viscosity is responsible for the different experimental results.

Figure 4-20 shows the particles' velocity distribution in one measurement cycle (15 seconds). It can be seen from the distribution that, the velocities of these particles are not the same, so the flow is not laminar in the measurement area.

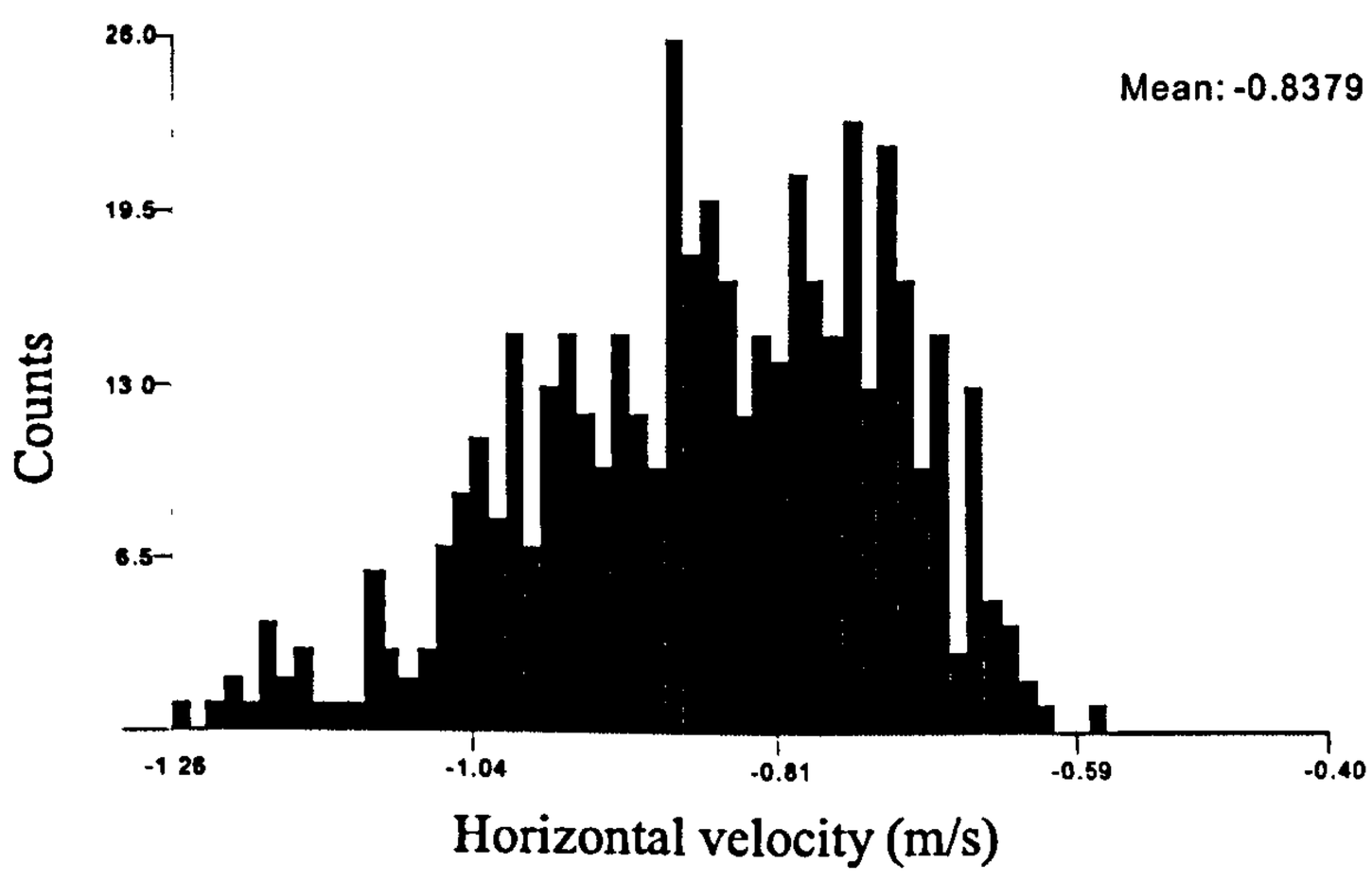

Figure 4-20 Particles velocity distribution in one measurement

The above experimental results clearly show the characteristics of fluid flow in the grinding contact entry region. There is significant conflict between the main assumptions that exist with current theoretical models and experimental results presented, and one concludes that present two-dimensional analyses inadequately

explain the mechanism of the fluid in the grinding zone. Only a model based on the full three-dimensional Navier-Stokes equations will more accurately predict the grinding fluid motion. However, the governing Navier-Stokes equations are difficult to solve for the three-dimensional turbulent motion, especially in complex fluid flows. Because of these limitations, it is proposed that 3-D Computational Fluid Dynamics (CFD) simulations could prove helpful in future investigations.

Chapter 5 Theories of Fluid Flow

5.1 Introduction

In this chapter, some concepts of the fluid dynamics which are relevant to the experimental work and the simulation work in this thesis, are explained. Two theories are introduced, one is concerned with air flow movement around the rotating wheel, and the other is concerned with the pressure distribution under the grinding wheel in the longitudinal direction of the workpiece surface. The theories provide insight into the fluid phenomena and help explain the experimental results. Since the fluid flow around the grinding wheel is a three-dimensional movement, traditional fluid mechanics cannot give exact solutions. However, the theory developed by application of Newton's laws of motion can be seen as an empirical formula. The pressure distribution under the grinding wheel is explained using lubrication theory and the case of non-dimensional pressure distribution.

5.2 Some concepts of fluid flow

5.2.1 Boundary layer flow

Since the investigation of the fluid flow around the rotating wheel is one of the main aims in this thesis, it is necessary to be clear on what is understood by the term 'boundary layer'. At the interface between a fluid and a surface in relative motion a condition known as 'no slip' dictates an equivalence between fluid and surface velocities. Away from the surface the fluid velocity changes rapidly; the zone in which this occurs is known as the boundary layer and its definition is fundamental to all calculations of surface drag and viscous force (Douglas, et al., 2005). The drag on a body passing through a fluid flow may be considered to be made up of two components: the form drag, which is dependent on the pressure forces acting on the body and the skin friction drag, which depends on the shearing forces acting between the body and the fluid. Therefore, the fluid adhering to the body of a surface should also be affected by the form drag and the skin friction drag, according to the Newton's third law: the law of reciprocal actions.

Normally, fluid boundary layer thickness is defined as that distance from the surface where the local velocity equals 99 per cent of the free stream velocity. With a stationary boundary and free fluid stream, the boundary thickness is

$$\delta = y_{(u=0.99U)}, \tag{5.1}$$

where U is the free stream velocity.

For a moving boundary in a stationary fluid, the boundary layer thickness is defined as the distance from the where the longitudinal fluid velocity reduce to 0.01 of the moving boundary velocity, that is

$$\delta = y_{(u=0.01U)}, \tag{5.2}$$

where U is the velocity of the moving surface.

However, the thickness of the air boundary layer around rotating grinding wheel is very big if using this definition and any thickness calculation is pointless. Therefore, the boundary layer thickness was not explicitly specified for the investigation of the fluid around the rotating wheel.

5.2.2 Reynolds number

The Reynolds number (Re) $\rho lu/\mu$ is a fundamental characteristic of the flow. The length l and velocity u are selected naturally and affect the numerical value of Re but they do not affect its fundamental significance (Massey, 1989). In many applications, convention has standardized the length and the velocity to be considered.

Reynolds number is essentially a means of comparing one flow with another. If corresponding lengths and corresponding velocities are compared in the two flows, the particular choices of length and velocity do not matter. Reynolds number concerns only the forces due to viscosity and inertia. i.e.

$$\text{Reynolds number} = \frac{\text{inertia force}}{\text{viscous force}} \tag{5.3}$$

A high value of Re indicates that inertial forces dominate the flow while viscous forces play only a small part; when Re is small in value, the viscous forces have the upper hand and inertia forces take second place.

5.2.3 Laminar flow and turbulent flow

Observation shows that two entirely different types of fluid flow exist: laminar flow and turbulent flow. The laminar flow is the flow wherein particles of fluid move in an orderly manner and retain the same relative position in successive cross-sections; turbulent flow is the flow wherein the particles of fluid no longer move in an orderly manner but occupy different relative positions in successive cross-sections (Douglas, et al., 2005).

When the motion of a fluid particle in a stream is disturbed, its inertia will tend to carry it on in the new direction, but the viscous forces due to the surrounding fluid will tend to make it conform to the motion of the rest of the stream. In viscous flow, the viscous shear stresses are sufficient to eliminate the effects of any deviation, but in turbulent flow, they are inadequate. The criterion, which determines whether flow will be viscous or turbulent, is therefore the ratio of the inertial force to the viscous force acting on the particle.

For the flow past a given cylinder, the Reynolds number is directly proportional to the velocity, and it can be defined in the following

$$\mathrm{Re} = \frac{\rho U d}{\mu} \tag{5.4}$$

where, ρ is the fluid density;

U is the flow velocity;

d is the diameter of the cylinder;

μ is the viscosity of the fluid.

If this definition is applied to the air flow around the rotating grinding wheel, and it is assumed that the air flow velocity is the same as the wheel tangential speed, the value of Reynolds number can be calculated. By the way of example, the density ρ of air is

$1.293(kgm^{-3})$ and the viscosity μ of air is $17.05\times10^{-6}(kgm^{-1}s^{-1})$ at the condition of $p=1\ atm$ and $T=273\ K$. If the air velocity U is 30 m/s (same to wheel speed) and the wheel diameter d is 0.18 m:

$$\mathrm{Re}=\frac{1.293kgm^{-3}\times30ms^{-1}\times0.18m}{17.05\times10^{-6}kgm^{-1}s^{-1}}=4.095\times10^{5}$$

Since up to $\mathrm{Re}=2\times10^{5}$ the boundary layer on the cylinder is laminar (Douglas, et al., 2005), then air flow around the wheel is turbulent.

The critical value of the Reynolds number for the onset of turbulence may be considerably reduced if the surface is rough. The presence of a pressure gradient can also be a major factor affecting the critical value of Reynolds number. Since the topography of the wheel surface is very complex, the flow close to the wheel surface should be turbulent flow. On the other hand, the air flow around the grinding wheel is driven by the wheel surface, so the flow condition is not completely the same as the flow over a cylinder because of the centrifugal effect. This phenomenon will be further discussed and reported in the following chapters.

5.2.4 Motion of a fluid particle in fluid

Any particle or element of the fluid will obey the normal laws of mechanics in the same way as a solid body. When a force is applied, its behaviour can be predicted from Newton's laws. The motion of the air element around the rotating wheel is not rotational, but centrifugal and diverging motion. Therefore, this motion cannot be solved by the general fluid dynamics theory. However, it can be calculated if some assumptions are given.

5.2.5 Drag effect

In general, when a body is immersed in a fluid and is in relative motion with respect to it, the drag is defined as that component of the resultant force acting on the body, which is in the direction of the relative motion.

Considering the case of drag on a sphere of diameter d moving at a speed U through a fluid of density ρ and viscosity μ, the drag force can be written as

$$F_D = f(d, U, \rho, \mu) \tag{5.5}$$

At small values of Reynolds numbers, the inertia forces in the equations of motion must become negligible, and the drag force approaches a linearly proportional relationship to the speed U; this is frequently called the Stokes law of resistance. At the opposite extreme, i.e., at large values of Reynolds numbers, the viscosity has only an indirect influence on the flow. The overall flow is controlled by inertia force alone, and μ does not feature in the equation at this limit. The drag force is proportional to U^2 for high Reynolds (Kundu and Cohen, 2001).

In summary, for small values of the Reynolds number (laminar flow), the drag coefficient is inversely proportionally to the velocity. This means that the drag is only proportional to the body's velocity

$$F_D = kU \ , \tag{5.6}$$

When the flow is turbulent the Reynolds number is large, and the drag coefficient C_D is approximately constant. This is the quadratic model of fluid resistance, in that the drag force is dependent on the square of the velocity

$$F_D = \frac{1}{2} C_D A \rho U^2 \ , \tag{5.7}$$

C_D = Drag coefficient,

A = Cross-sectional area perpendicular to the flow,

ρ = Density of the medium,

U = Velocity of the body relative to the medium.

5.3 Air element motion around rotating wheel

The air element is considered to be the air layer in proximity to the wheel surface. When the wheel is rotating, the air element will be driven by the wheel surface. This is due to the effect of the skin frictional force of the abrasive grain and the viscous forces of air in the porous wheel. Except for the very thin layer very close to the wheel surface, the air element will move away from the wheel by the centrifugal force after having achieved some particular velocity. It is normally thought that the velocity of this air element is the same as the wheel surface tangential speed. After moving away from the wheel surface, the velocity of this air element will reduce because the air viscous force, i.e. the effect of air drag force.

In this section, the motion of the air element around the rotating wheel will be analyzed and predicted using the Newton's laws. This analysis is based on the two dimensional model. The work aims to describe the relation of the air velocity with the distance from wheel surface in order to compare with the results of experiment and simulation.

5.3.1 Assumptions

Assumptions were made to simplify the model of the air element motion:

1. The motion of the air element is thought as the motion of the solid body, no mass loss and shape change.
2. The air element is seen as very small, thus, the volume can be ignored.
3. The initial velocity is same to the wheel tangential speed.
4. The motion of the air element obeys the normal laws of mechanics in the same way as a solid body.
5. The air element moves away from the wheel surface with an initial velocity along the wheel tangential direction, and the direction of movement is not changed during motion. Here, the sub-layer very close to the wheel surface is ignored, where the air can partly follow the rotating wheel.
6. The only force on the air element is the drag force (see 5.2.5 Drag effect) during motion.
7. The width of the wheel is looked upon as sufficient to enable the three-dimensional effect to be ignored.

5.3.2 Model derivation

A simple schematic of the situation shown in Figure 5-1 accordance with the previous assumptions, when the wheel is rotating with wheel speed v_s, an air element will begin to move away from Point A on the wheel surface with an initial velocity v_0 ($v_0 = v_s$). From Point A to Point B (the distance is s), the velocity of the air element will decrease due to the air drag force. v_t and v_r are the tangential velocity and the radial velocity of the air element at Point B. The distance to the wheel surface is l at Point B. The radius of the wheel is R.

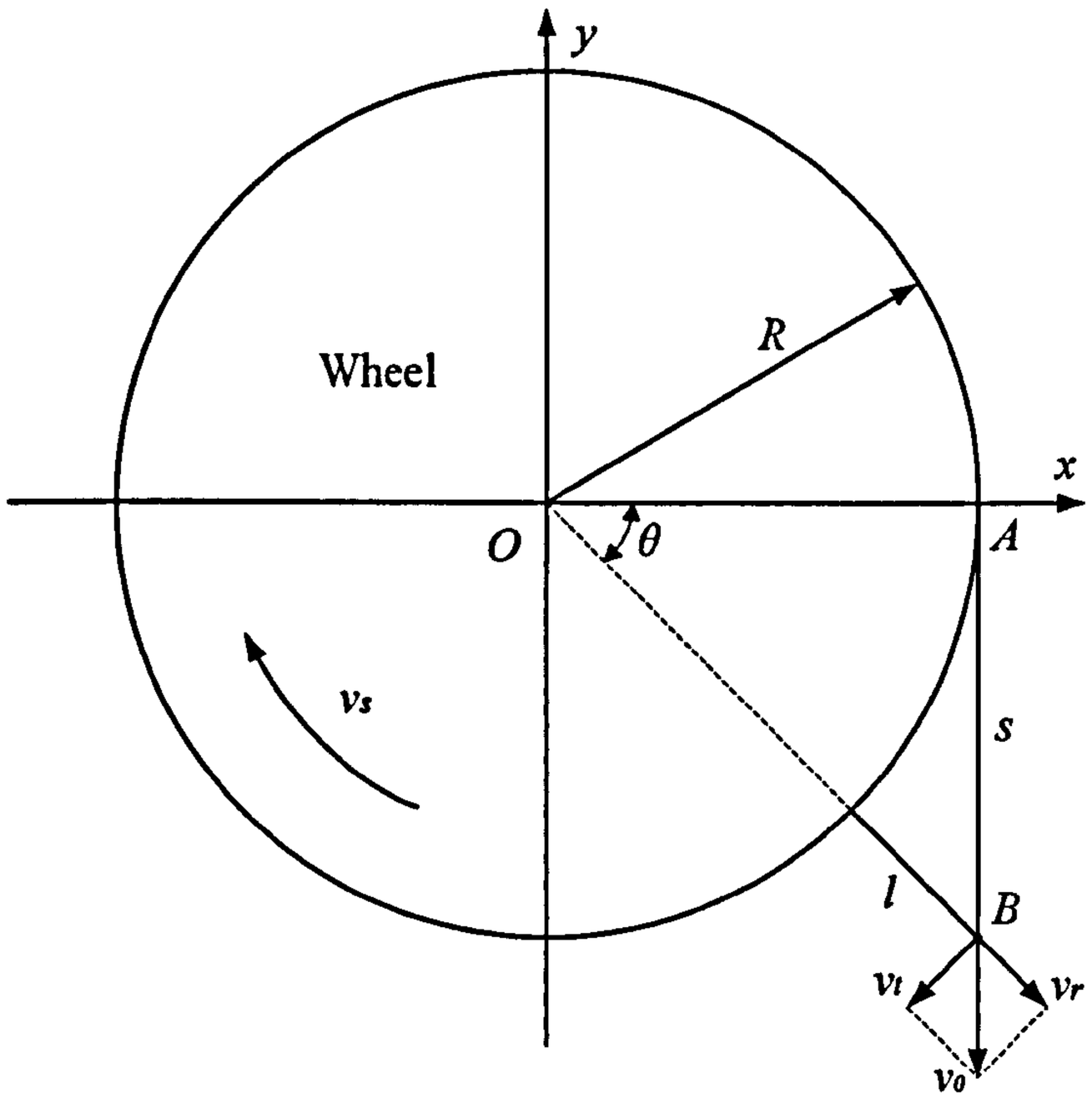

Figure 5-1 Sketch of the motion of the air element from wheel surface

Since the air motion is very complex, equation (5.6) was used in the first instance to calculate the air drag force on the air element. The initial velocity is assumed to be very high.

The drag force on the air element is (from equation 5.6)

$$F_D = -kv, \tag{5.8}$$

Where k is the drag coefficient and the negative sign implies that it is always directly opposes the velocity. Clearly, when k increases the drag force increases.

If the mass of the air element is m, the acceleration a can be calculated by the Newton's second law

$$F_D = -kv = ma$$

Therefore, $a = -\frac{k}{m}v$. (5.9)

To simplify the equation derivation, $\frac{k}{m}$ can be written as k'.

From Point A to Point B, there is the relationship between the initial velocity v_0, final velocity v and the distance s:

$$v^2 = v_0^2 + 2as \tag{5.10}$$

Substituting equation (5.9), then

$$v^2 = v_0^2 - 2k'vs \tag{5.11}$$

Therefore, the relationship between v and s can be calculated from the follow equation

$$v = \sqrt{v_0^2 + k'^2 s^2} - k's\,. \tag{5.12}$$

At Point B, the tangential velocity of the air element is

$$v_t = v\cos\theta = v\frac{R}{R+l}, \tag{5.13}$$

and the radial velocity is

$$v_r = v\sin\theta = v\frac{s}{l}. \tag{5.14}$$

Because

$(l+R)^2 = R^2 + s^2$,

s can be calculated from

$$s = \sqrt{(l+R)^2 - R^2}, \tag{5.15}$$

Combining equation (5.12), (5.13) and (5.14), the relationship of the air tangential velocity v_t with the distance l is obtained

$$v_t = \sqrt{v_0^{\,2} + k'^2(l^2+2lR)}\frac{R}{R+l} - k'\sqrt{l^2+2lR}\frac{R}{R+l} \tag{5.16}$$

Similarly, the relationship of the air radial velocity v_r and the distance l is obtained as

$$v_r = \sqrt{v_0^{\,2} + k'^2(l^2+2lR)}\frac{\sqrt{l^2+2lR}}{R+l} - k'\frac{l^2+2lR}{R+l} \tag{5.17}$$

Equation (5.16) and equation (5.17) can be termed as 'Theory 1' for the purpose of simplification in later discussion.

For high Reynolds flow, the air drag force is shown in equation (5.7)

If the term $\frac{1}{2}C_D A\rho$ is written as C, the drag force can be simplified to

$$F_D = -Cv^2. \tag{5.18}$$

Clearly, again when C is larger, the drag force is higher.

Using the same approach as used previous, the relationship of the air tangential velocity v_t and the distance l is

$$v_t = \frac{v_0}{\sqrt{1+\frac{2C}{m}\sqrt{l^2+2lR}}} \cdot \frac{R}{l+R}. \tag{5.19}$$

For further simplification, $\frac{2C}{m}$ is written as C'.

Therefore,

$$v_t = \frac{v_0}{\sqrt{1+C'\sqrt{l^2+2lR}}} \cdot \frac{R}{l+R}. \tag{5.20}$$

Similarly,

$$v_r = \frac{v_0}{\sqrt{1+C'\sqrt{l^2+2lR}}} \cdot \frac{\sqrt{l^2+2lR}}{l+R}. \tag{5.21}$$

The equation (5.20) and equation (5.21) can be termed as 'Theory 2' for the purpose of simplification in later discussion.

There is a coefficient k' in Theory 1 and coefficient C' in Theory 2. k' and C' are not non-dimensional parameters and they relate to the properties of air, that is: the viscosity, density, mass, initial velocity and other quantities. Within the different situations, the values of k' and C' are different, however their values can be confirmed from the boundary condition through using the results of experiments and simulations. Therefore, the above equations can be seen as the empirical formulas. Furthermore, these equations provide the two dimensional flow analyses, so they have limited use in their application to the air velocity around the grinding wheel (three-dimensional motion). However, they can be used to describe the air velocity distribution in the middle section of the wheel.

5.3.3 Velocity distribution profile using derived theories

The air velocity distribution profiles obtained using the Theory 1 and Theory 2 are shown in Figure 5-2. The wheel speed is 30 m/s and the wheel diameter is 180 mm. The profile length was 40 mm distance from wheel surface.

Both the tangential velocity and the radial velocity of the air flow are shown using Theory 1 and Theory 2. According to the experimental results, the value of coefficient k' in Theory 1 was estimated as 1000, and the value of coefficient C' in Theory 2 was estimated as 0.35. The results calculated from theory using these values most closely to match the experimental results.

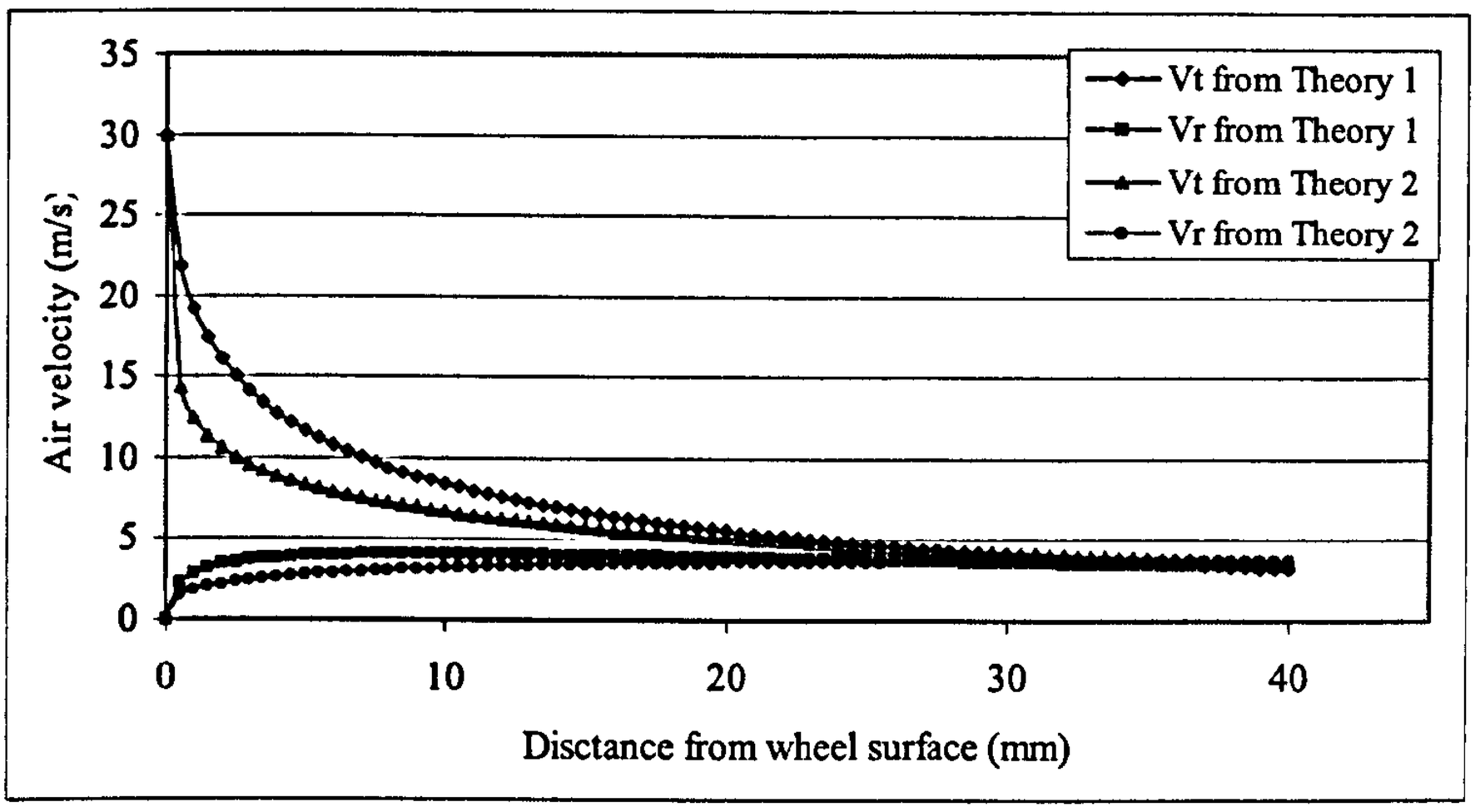

Figure 5-2 Air velocity distribution using the derived theories

It can be seen from Figure 5-2 that the values of the air velocities computed from Theory 2 decrease faster than those from Theory 1. This is because the greater drag force used in Theory 2. However, by comparing the experimental results, the velocity profile obtained using Theory 1 more closely matches the experimental results. Further discussion will be given in a later chapter.

5.4 Fluid velocity near the wall

The velocity of the fluid flow near a wall is commonly analysed using the 'Law of the Wall'. 'Law of the wall' is the forceful name for finding that, with certain assumptions, the mean velocity in constant-property turbulent flow near a smooth impermeable solid

surface of negligible curvature can be correlated in terms of the shear stress at the surface, the distance from the surface, the fluid density and fluid kinematic viscosity (Bradshaw and Huang, 1995). The 'Law of the Wall' for the inner part of a turbulent shear flow over a solid surface is one of the cornerstones of fluid dynamics, and one of the very few pieces of turbulence theory whose results include a simple analytic function for the mean velocity distribution, the logarithmic law. Although the law was normally derived with the model of flow near the flat wall, it is still valid for the turbulent flow around a rotating cylinder in a quiescent fluid (Dierich, et al., 1998).

5.4.1 Formula of 'Law of the Wall'

The simple equation of the 'Law of the Wall' gives:

$$\frac{U}{u_\tau} = f\left(\frac{u_\tau y}{\upsilon}\right), \tag{5.22}$$

where $u_\tau = \sqrt{\tau_w / \rho}$ is the shear stress velocity,

τ_w is the shear stress,

ρ is the fluid density,

U is the mean velocity of the flow,

y is the distance from the surface,

υ is the kinematic viscosity.

The mathematical derivation, has the final formula (Bradshaw and Huang 1995):

$$\frac{U}{u_\tau} = \frac{1}{\kappa}\ln\left(\frac{u_\tau y}{\upsilon}\right) + C, \tag{5.23}$$

where κ is the Karman constant is universal and has the generally accepted value 0.41,

C is a log-layer constant, and related to the increase in U across the viscous wall region.

5.4.2 Application of the 'Law of the Wall' in CFD

Near a no-slip wall, there are strong gradients in the dependent variables. In addition, viscous effects on the transport processes are large. Assuming that the logarithmic profile reasonably approximates the velocity distribution near the wall, it provides a means to compute numerically the fluid shear stress as a function of the velocity at a given distance from the wall. This is known as a 'wall function' and the logarithmic nature gives rise to the 'law of the wall.' Wall functions are the most popular way to account for wall effects.

The wall function method uses empirical formulae that impose suitable conditions near to the wall without resolving the boundary layer, thus saving computational resources. The major advantages of the wall function approach is that the high gradient shear layers near walls can be modelled with relatively coarse meshes, yielding substantial savings in CPU time and storage. It also avoids the need to account for viscous effects in the turbulence model (ANSYS CFX-Solver Modelling Guide, Release 11.0).

Equation (5.23) can also be written as the following:

$$u^* = \frac{U}{u_\tau} = \frac{1}{\kappa}\ln\left(y^*\right) + C, \tag{5.24}$$

where $y^* = \left(\frac{u_\tau y}{\upsilon}\right)$ is the dimensionless wall distance,

u^* is the dimensionless velocity near the wall.

The above wall function equations are appropriate when the walls can be considered as hydraulically smooth, for rough walls, the logarithmic profile still exists, but moves close to the wall. Roughness effects are accounted for by modifying the expression as follows

$$u^* = \frac{1}{\kappa}\ln\left(\frac{y^*}{1+0.3k^*}\right) + C, \tag{5.25}$$

where k^* is a coefficient, which is relative to sand grain roughness, the density and the viscosity of the fluid and the velocity near the wall.

5.5 Pressure distribution under the wheel (Lubrication Theory)

The studies of the grinding fluid in the region between a grinding wheel and workpiece have only touched upon the aspects of the flow mechanisms under a grinding wheel; no one has yet developed a comprehensive flow model.

In this section, the analysis was restricted to the fluid pressure distribution between the grinding wheel and workpiece. The basic lubrication theory was applied under the conditions similar to surface grinding. It is a one-dimensional formulation where, the fluid flow in wheel axial direction was ignored. Using this analysis, the pressure distribution of the fluid as well as the air under the grinding wheel zone can be estimated.

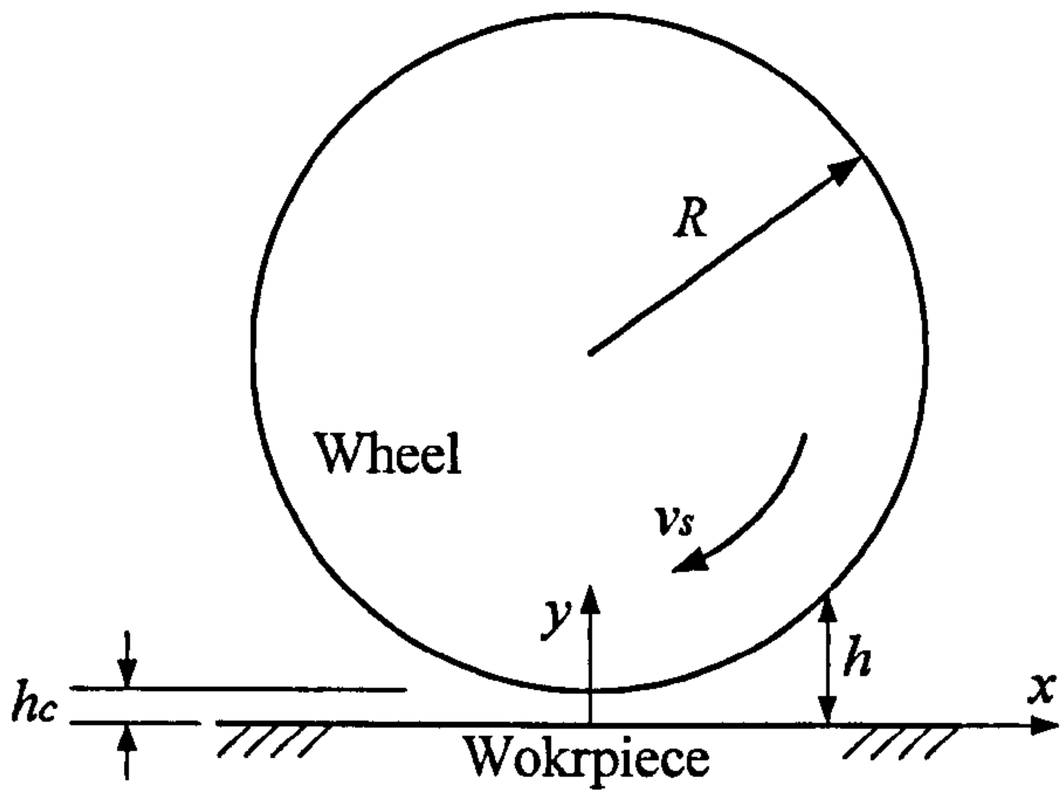

Figure 5-3 Geometry of the model

Figure 5-3 shows is simple form, the geometry of the model: the grinding wheel radius is R with wheel speed v_s; the h_c is the clearance at the point of closet approach between the wheel and the workpiece, and it is generally very small in comparison with the radius. The gap between the wheel and the workpiece is filled with fluid. The wheel can draw the fluid into the gap, thus the velocity $\bar{U}$ of entrained fluid can be seen as:

$$\bar{U} = \frac{v_s}{2}. \tag{5.26}$$

The thickness of the fluid film h between the wheel and workpiece can be calculated from:

$$h = h_c + R - \sqrt{R^2 - x^2} = h_c + R - R\left[1 - \left(\frac{x}{R}\right)^2\right]^{1/2} \tag{5.27}$$

The last term on the right side of equation (5.27) can be expressed in terms of series as (Hamrock, 1994)

$$h = h_c + R - R\left[1 - \frac{1}{2}\left(\frac{x}{R}\right)^2 - \frac{1}{8}\left(\frac{x}{R}\right)^4 - \frac{1}{16}\left(\frac{x}{R}\right)^8 - \cdots\right] \tag{5.28}$$

or

$$h = h_c + \frac{1}{2}\left(\frac{x^2}{R}\right)\left[1 + \frac{1}{4}\left(\frac{x}{R}\right)^2 + \frac{1}{8}\left(\frac{x}{R}\right)^4 + \cdots\right]. \tag{5.29}$$

Because in the film region $x \ll R$ so that $\frac{x^2}{R^2} \ll 1$, and this equation reduces to:

$$h = h_c + \frac{x^2}{2R}. \tag{5.30}$$

Within the fluid the pressure will satisfy the one-dimensional Reynolds equation (Williams, 2005):

$$\frac{dp}{dx} = -12\mu\bar{U}\frac{h - \bar{h}}{h^3} \tag{5.31}$$

where, μ is fluid dynamics viscosity, $\bar{h}$ is the value of h at which $dp/dx = 0$.

Integration of this Reynolds equation gives estimates of the pressure p when the variation in film thickness h is given. It need to specify some suitable boundary condition to estimate the pressure, that is, values of the origin the pressure in the film must fall to zero, but it is not obvious at what values of the x-coordinate this can be

taken to have occurred. Perhaps the best initial estimate is to take p as zero at very large distances from the point of closet approach of the surfaces, that is, to put $p=0$ where $x=\pm\infty$. This choice is known as the 'full Sommerfeld condition' and leads to a neat solution of the Reynolds equation, which is consistent with the wheel profiles, namely that:

$$p=4\frac{\bar{U}\mu x}{h^2} \tag{5.32}$$

This can be expressed conveniently in a non-dimensional form. In this case, the non-dimensional pressure p^* is best defined by:

$$p^*=-\frac{ph_c^2}{12\bar{U}\mu\sqrt{2Rh_c}}, \tag{5.33}$$

and ξ is the non-dimensional form of the position coordinate x, defined by:

$$\xi=\frac{x}{\sqrt{2Rh_c}} \tag{5.34}$$

Therefore, the variation of pressure through the contact then becomes

$$p^*=\frac{\xi}{3\left(1+\xi^2\right)^2} \tag{5.35}$$

This distribution is plotted in Figure 5-4, it is immediately obvious from this that this full Sommerfeld pressure distribution is anti-symmetrical about the position axis, the negative pressure curve being exactly the reverse image of the positive. The maximum value of p^* occurs when $\xi=1/\sqrt{3}$ and p^* is then of magnitude $\sqrt{3}/16=0.1083$. At this point the local film thickness is equal to $\frac{4}{3}h_c$.

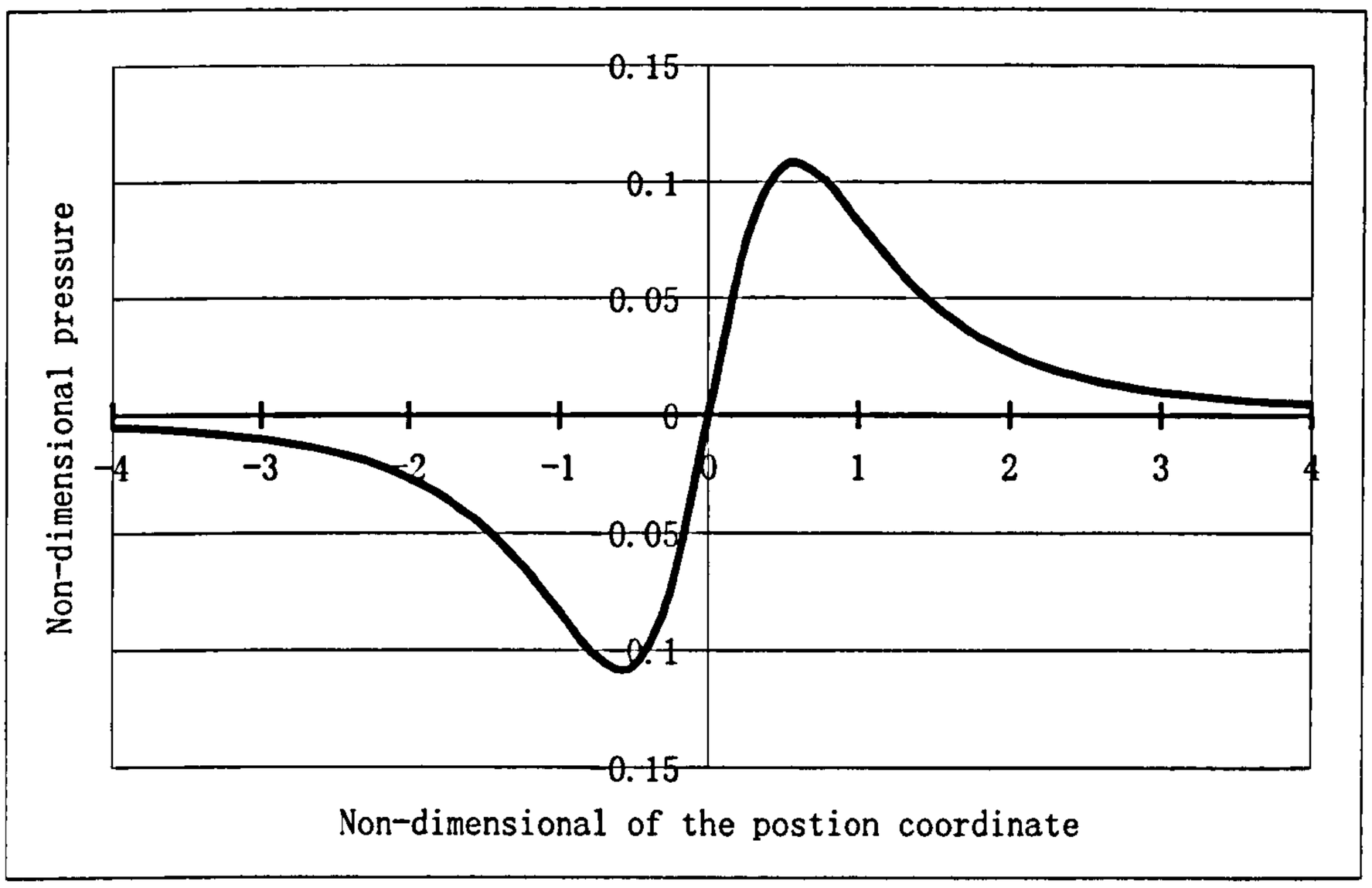

Figure 5-4 Pressure distribution through the wheel-workpiece

In grinding, it can be seen that the fluid pressure becomes highest at the area approaching the contact zone. Just after the contact zone, the pressure decreases to the lowest value. This theory can also explain the pressure of the air boundary layer near the grinding contact zone when fluid is not applied.

5.6 Summary

Some of the fundamental theory of fluid mechanics has been introduced and discussed in the context of the grinding situation. The air flow movement around the rotating wheel has been derived from Newton's laws, and the air flow velocity profile was estimated from this analysis. The 'Law of the Wall' was also introduced to help explain the flow phenomena and will be shown to be an important theory in the CFD simulations.

The introduction of these theories can help with the analysis and explanation of the boundary flow phenomena and experimental results.

Chapter 6 Experiments of Air Boundary Layer

6.1 Introduction

The grinding wheel rotating at relatively high speed carries on its surface the air boundary layer flow, which at sufficient high wheel speed may divert the stream of grinding fluid. A consequence is that as wheel speed increases, the pressure and velocity of the air boundary layer also increase, and the amount of grinding fluid delivered to the grinding zone decreases. Therefore, the grinding fluid can only reduce the bulk temperature of the workpiece without having any significant affect upon the grinding process itself (Kaliszer & Trmal, 1975). For very high wheel speeds, almost all of the cutting fluid may be prevented from penetrating the grinding zone and the grinding may become dry. In addition, air friction is an additional reason for high losses of grinding capacity. Ebbrell, et al. (2000) showed that the air barrier around the rotating grinding wheel could prevent the grinding fluid from entering the grinding contact zone even at relatively low wheel speeds.

Since the air boundary layer flow can prevent the fluid reaching the wheel surface and the grinding contact zone, the fluid must penetrate the air layer developed around the periphery of the rotating wheel surface to get effective grinding fluid delivery. This has aroused interest that has led to the studies of the air boundary layer flow around the rotating grinding wheels (Davies & Jackson, 1981). However, the use of the different experimental measurement methods has caused conflicting experimental results in previous investigations. With those measurement instruments, usually, only one component velocity of the air flow has been obtained, and the positive and the negative velocity values cannot be distinguished. Furthermore, most of the previous measurements are intrusive and not sensitive enough to measure the low velocity air flow. Accordingly, most researchers only measured the tangential component velocity of the air boundary layer around the grinding wheel, so they have not obtained a comprehensive understanding of the air boundary layer flow.

With the development of measurement technologies and techniques, the Laser Doppler Anemometry (LDA) obviously represents the most effective tool in the fluid velocity

measurements among a number of measurement instruments, which makes it an ideal measurement technique for the investigation of fluid velocity. This chapter will describe the LDA experiments, which was applied in order to improve understanding of the air flow motion around the rotating grinding wheel.

6.2 Review of previous studies of the air boundary layer

When the grinding fluid exits the nozzle, it collides with the air flow around a grinding wheel. The following happen to the fluid stream (Akiyama, et al., 1984):

i) It is deflected outward completely by the wall of the air flow.
ii) It is diffused in the air to form gas-liquid two-phase flow and rotates with the wheel periphery.
iii) It sticks to the peripheral wheel surface after penetrating the air flow.

The ideal fluid delivery should be as I (iii) above. The air boundary layer can also consume the extra power when grinding. An estimate using simple formulations from fluid dynamics revealed that air friction losses increase approximately by a power of 2.8 as a result of the speed, and by a power of 4.6 as a result of the grinding wheel diameter (Klocke, et al., 1997). Therefore, it is important to understand the air flow movement and its characteristics to achieve more effective fluid delivery and to reduce the air friction caused by the air flow layer.

6.2.1 Air flow velocity measurement

For measurement of air flow velocity in grinding, the most popular measurement instrument is the Pitot tube. The hot-wire anemometer can be also used for measuring both the air velocity as well as its percentage turbulence (Shibata, et al., 1982). Recently, the PIV (Particle Image Velocimetry) method was employed in the air boundary layer investigation (Gong, et al., 2006; Oliveira, et al., 2006). Video camera has also been used to record the transport of air in Sven and Johan's experiment (1996).

Typically, air velocities measured with a Pitot tube used a tube outer diameter of 1 mm, and air velocities below 1 m/s could not be measured, so only tangential air velocity (parallel to the wheel circumference) profiles were obtained with different radial distance from the wheel surface across the entire wheel width. No radial air velocity

component could be measured with the Pitot tube method (Sven and Johan, 1996; Ramesh, 2001). The experimental result obtained by other measurement methods did not give a full understanding of the air boundary layer flow.

6.2.2 Air flow velocity distribution

The state of the air flow has been illustrated conceptually by Shibata, et al. (1982) and is shown as Figure 6-1.

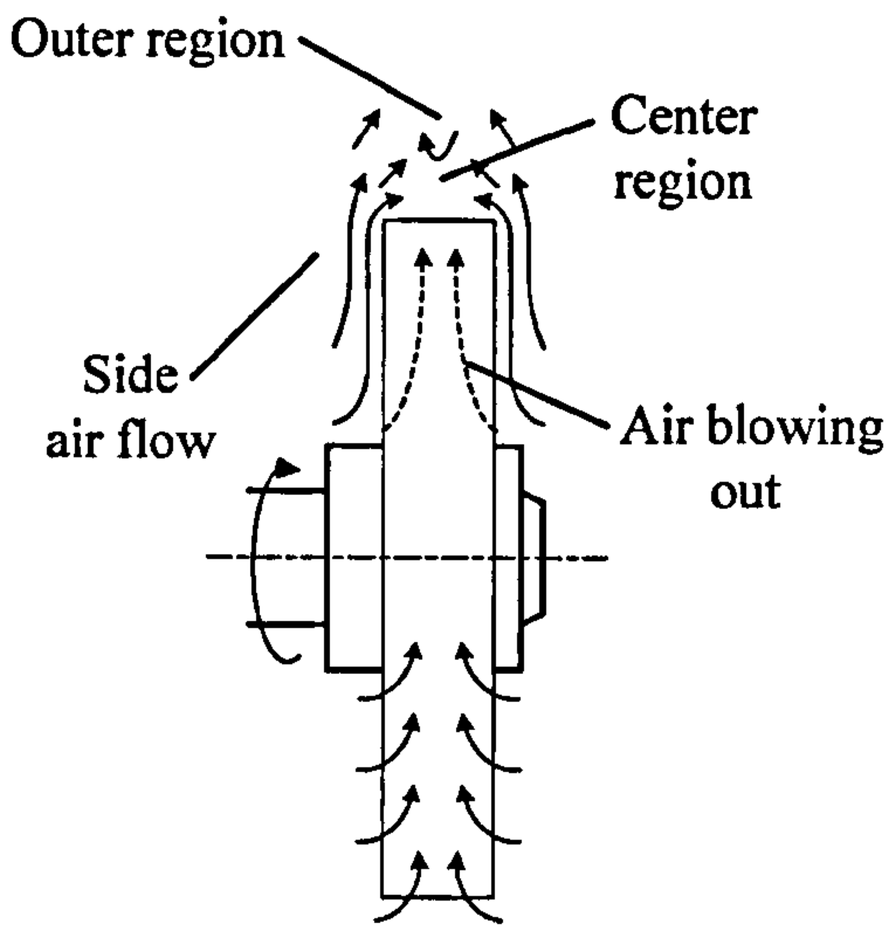

Figure 6-1 Shibata's conceptually illustration for the air flow around a grinding wheel

The layer of air immediately surrounding a rotating grinding wheel is carried on the wheel's surface, because of the friction of the wheel surface on the air and is simultaneously driven outwards by the centrifugal force. Consequently, an air flow toward the middle of the wheel width from the both sides would be induced to replace it. This suggests that the peripheral air flow would be affected significantly by the side air flow forced radially outwards along both sides of the grinding wheel. Then it might be considered that the layer of peripheral air flow basically consists of two regions: a central region situated near the middle of the wheel width and adjacent to the wheel surface; an outer region surrounding the central region. In the former region, the air flow is relatively stable and depends considerably on the peripheral surface topography. While in the latter region, the air flow is remarkably turbulent and depends on the side face topography of the wheel.

Shibata's experimental results show that, two-dimensional distribution pattern of air velocity is non-uniform over the wheel width. In the air layer near the wheel surface, there appear two peaks of air velocity around both sides of the wheel. These two peaks tend to shift toward the centre of the wheel width with the distance radially outwards from the wheel surface. The intensity of air velocity distribution is relatively small in the central region, whereas it is large in the outer region. The similar behaviour of the air flow was also pointed out in earlier work (Kaliszer & Trmal, 1975; Radhakrishnan & Rahman, 1977). In Trmal's results (1976), the air velocity changes along the wheel width reaching the minimum value in the middle section of the wheel. However, Sven and Johan (1996) presented an air boundary layer profile with a central maximum; Radhakrishnan obtained contrary results (central minimum). It shows that the air flow in the central region was more stable than in the outer region from Shibata's experimental results. According to the literature review, quite a few experimental results show that the distribution of air velocity in the radial direction decreases exponentially with the distance from the wheel periphery (Kaliszer & Trmal, 1975; Davies & Jackson, 1981; Sven & Johan, 1996).

Radhakrishnan, et al. presented graphs of air velocities and derive an empirical formula for the air velocity (1977):

$$V = 0.116 v^{1.05} \frac{0.215 R_t}{t^{0.220}} \tag{6.1}$$

V = Air velocity around grinding wheel surface, ms^{-1}

t = Distance from grinding wheel surface, mm

v = Peripheral velocity of grinding wheel, ms^{-1}

R_t = Grinding wheel surface roughness, mm

6.2.3 Air flow mechanics and the effecting factors

The work of previous research led to the conclusion that when a wheel made of porous material such as a vitrified grinding wheel rotating at high speed, the air contained in the wheel pores is forced out through the wheel body by centrifugal force. Hence, it is compared to a pumping action; this was demonstrated experimentally by showing how

the air velocity reduced when the wheel faces were covered with the protective paper. In Kaliszer and Trmal's review (1975), it is stated that the air velocity is greater for a porous wheel than in the case of a wheel with an average structure. For wheels of resinoid bonding with almost no pores, Khudobin states that 'the air stream will be significantly smaller as compared to wheels on ceramic bonding'. However, the experimental works show that the wheel surface drag forms and affects the air boundary layer. Air velocity increases with wheel abrasive grain size. Anon (1974) found from experiments that the air blowing out has little effect on the air flow around the grinding wheel. However, Shibata, et al. (1982) observed that the side air flow plays an important part and can not be disregarded from the aspect of air flow around the wheel.

Generally, the air boundary layer velocity is determined by factors such as wheel structure and topography, the wheel speed in grinding, the wheel guard, and so on (Kaliszer & Trmal, 1975; Rahman & Radhakrishnan, 1980; Gong, et al. 2006). Only the difference of the surface roughness of the wheel sides could cause the air velocity to change remarkably. The smoother the wheel periphery is, the lower the air velocity is. In the neighbourhood of the wheel surface, air velocity could be expected from the boundary layer theory (Shibata, et al., 1982). Most investigators agree that the velocity of the air boundary layer increases almost proportionally with the wheel speed according to Kaliszer's review. The wheel guard in which the grinding wheel is enclosed also plays an important part for the air velocity. The average dynamic pressure when the wheel rotates inside the guard is approximately 50% higher as compared with the wheel rotating without the guard (Trmal & Kaliszer, 1976).

6.2.4 Critical fluid velocity

It was argued that above a critical grinding wheel rotational speed, the air boundary layer developed around the grinding wheel would prevent coolant from entering the grinding zone. According to Fisher's results (1965), a grinding wheel rotating at a speed of v_s = 33 m/s has entrains an air flow belt with a proximately the same air velocity as the wheel speed.

Trmal and Kaliszer (1976) proposed that a critical fluid velocity exists, above which the fluid penetrates the air boundary layer and sticks to the wheel. Their analysis was based

on the assumption that the grinding fluid applied to the periphery of a stationary grinding wheel is divided into two streams -- one in the upwards direction, and one downwards (Figure 6-2).

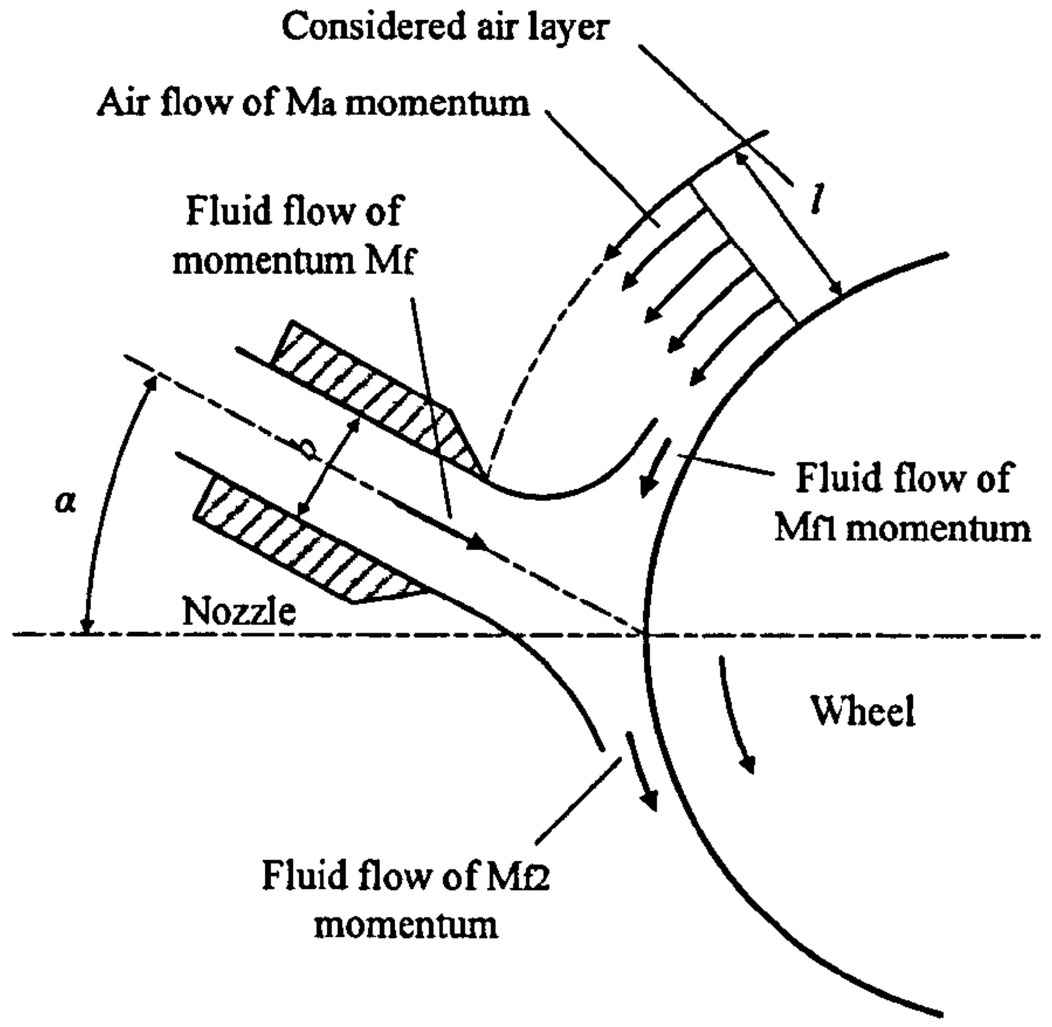

Figure 6-2 Mechanics of interaction between air boundary layer and fluid flow (v_s=0) (Trmal and Kaliszer, 1976)

The determination of a critical fluid velocity was based on the following assumption: if the momentum of flux of the layer is higher than the momentum of flux of fluid in the upwards direction, the fluid will not penetrate the air layer. If the fluid momentum is higher, the air layer will be diverted. For the critical value when the momentum of the air layer is bigger than the momentum of the upward stream of fluid $M_{fl}>M_a$, the cutting fluid can penetrate the air boundary layer and stick to the wheel. The critical velocity can be calculated out by consideration of the momentum of the main fluid flow M_{fl}. The agreement between theoretical and experimental results was surprisingly good. However, the wheel was assumed stationary in this theoretical study. The scraper can affect the critical wheel speed. The critical wheel speed achieved with the air scrapper was 22% greater than achieved without the air scrapper. The percentage increase in the coolant flow was calculated as 16% (with the air scraper).

6.3 Experiment arrangement and method

This section describes the experimental apparatus and the methodology used to undertake the experimental tests. The tests focused on measurement of the air boundary layer flows.

6.3.1 Grinding machine and LDA system

The grinding machine used in experiments was the Abwood Series 5020 surface grinding machine (Figure 6-3). This machine provides a relatively high spindle power and wheel speed. The spindle motor power is 2.2 kW (continuous power) – 8 kW (instantaneous power). The spindle speed is up to 6000 rev/min.

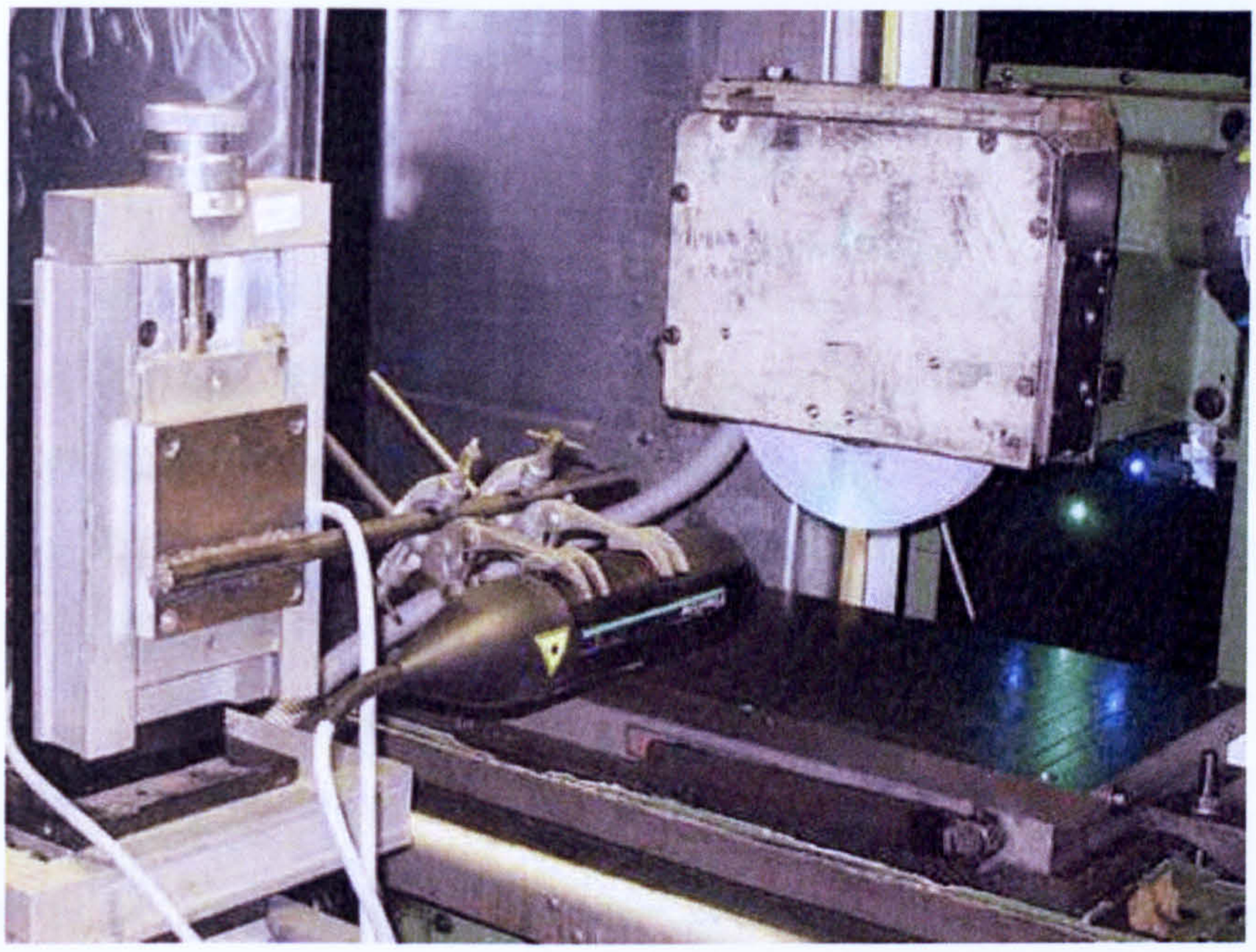

Figure 6-3 Experimental arrangement of air boundary layer investigation

The LDA measurement system was the Dantec Argon+-ion Laser Doppler Anemometry system based on burst spectrum analysis. It is a two-component dual-beam LDA system in back-scatter mode, and the blue/green laser combinations make it suitable for measuring the orthogonal velocity components of air flows simultaneously. The SAFEX Fog Generator 2001 was employed to apply the seeding particle for the LDA measurement (Figure 6-4), and the fog fluid is the SAFEX Inside Fog Fluid Blitz. The system can generate a white, quickly disappearing fog.

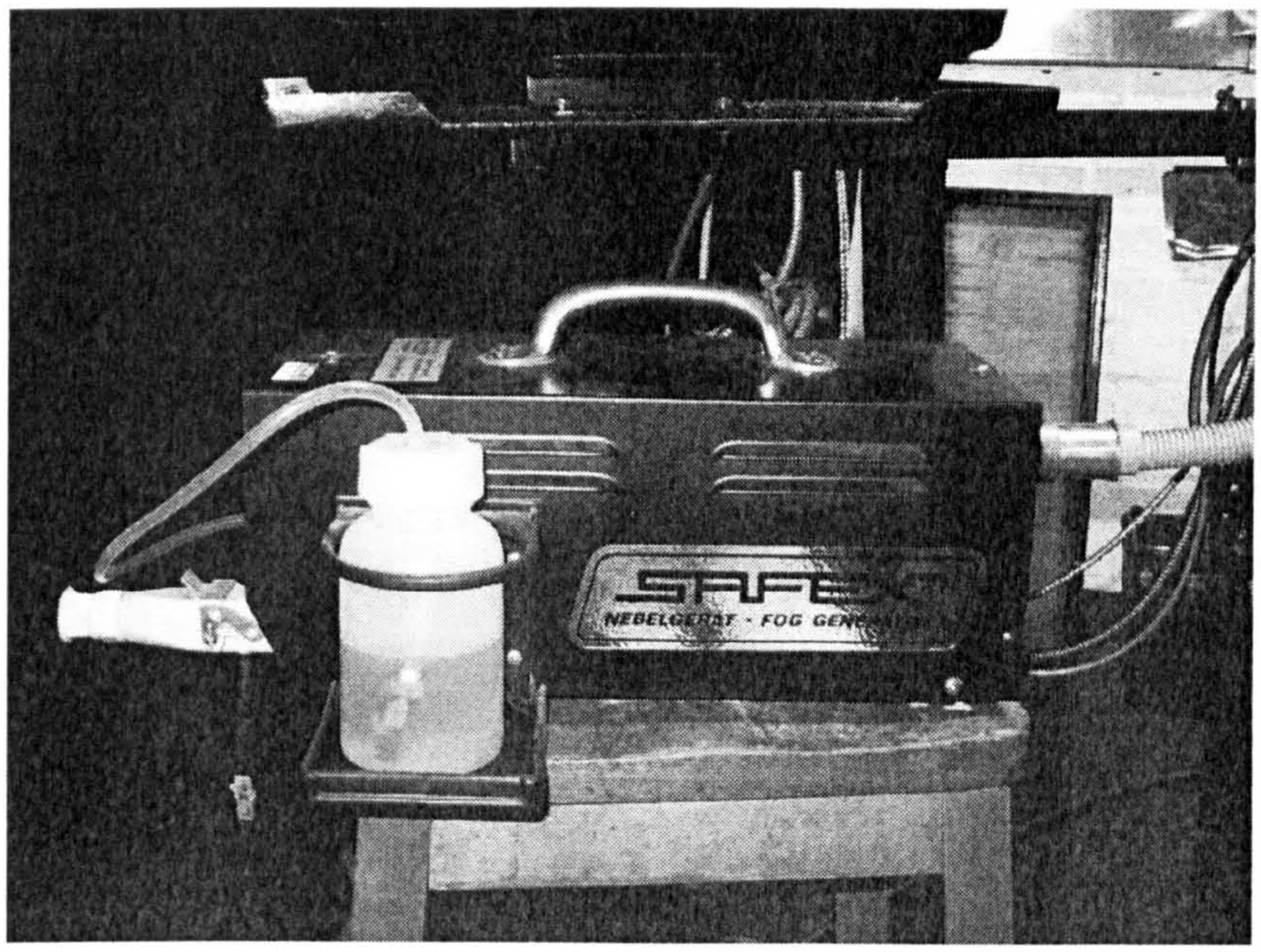

Figure 6-4 SAFEX Fog Generator 2001 and the Fog fluid

The diameter of the wheel was 182.5 mm after dressing; the wheel width was 25 mm. The value R_t of the wheel was measured to be approximately 2 mm (maximum height of the grain). The probe of the LDA was mounted on a traverse axis. With the help of this traverse, a three-dimensional movement of the laser probe was facilitated with a distance resolution of 0.02 mm.

6.3.2 Methodology

In the interest of safety, the wheel guard was not removed, and the air boundary layer velocity was measured in the area beneath the grinding wheel, as this area was the most readily accessible (shown in Figure 6-5). The measurement coordinate system is shown in Figure 6-6. There are three coordinate directions: x, tangential to the wheel cylindrical surface and parallel to the worktable surface; y, normal to the wheel cylindrical surface and perpendicular to the worktable surface; z, in the axial parallel to the wheel spindle. The three velocity components of air flow are tangential velocity V_t, radial velocity V_r, and the axial velocity V_z, which are along the x, y, and z axes respectively. The origin in the y direction is defined: by the position of a laser beam in the axial direction which contacts the wheel at its lowest point and half of it is blocked by the wheel (Figure 6-7). Therefore, because of this configuration and the dimension of

the laser beam, the velocity of air flow in the area very close to the wheel surface, cannot be measured. This distance is about 0.6 mm from the wheel surface.

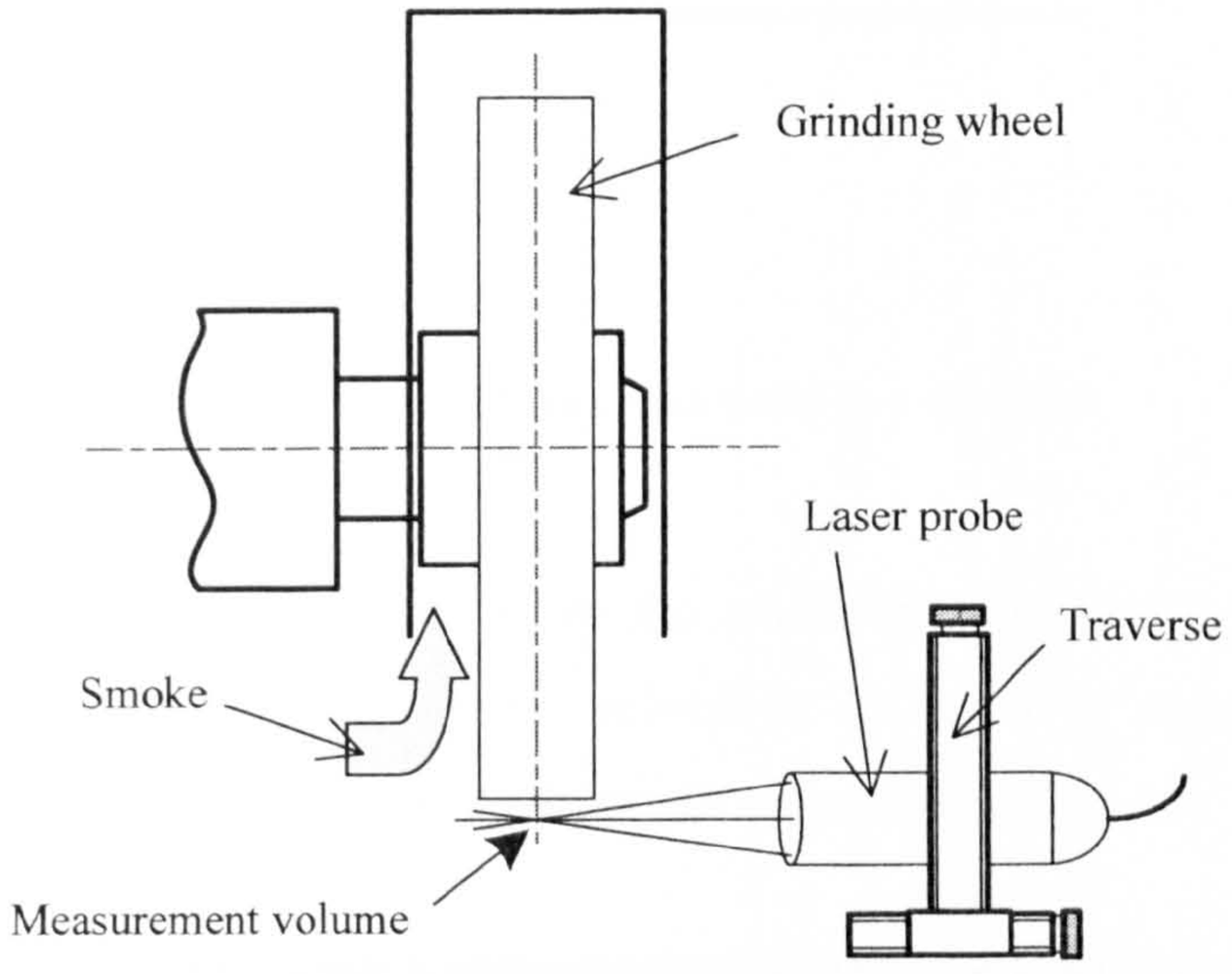

Figure 6-5 Schema of the configuration

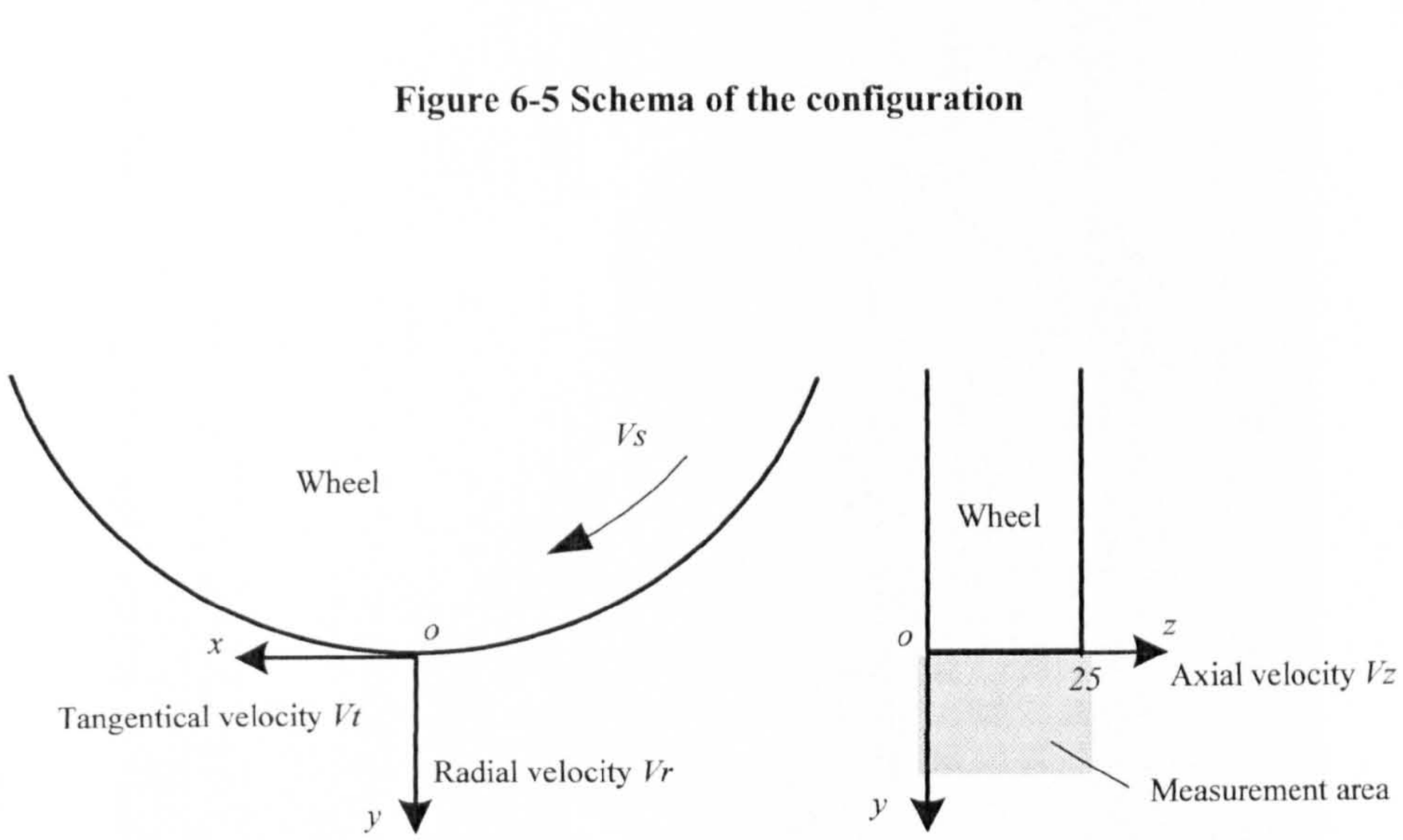

Figure 6-6 Measurement coordinate system and measurement area

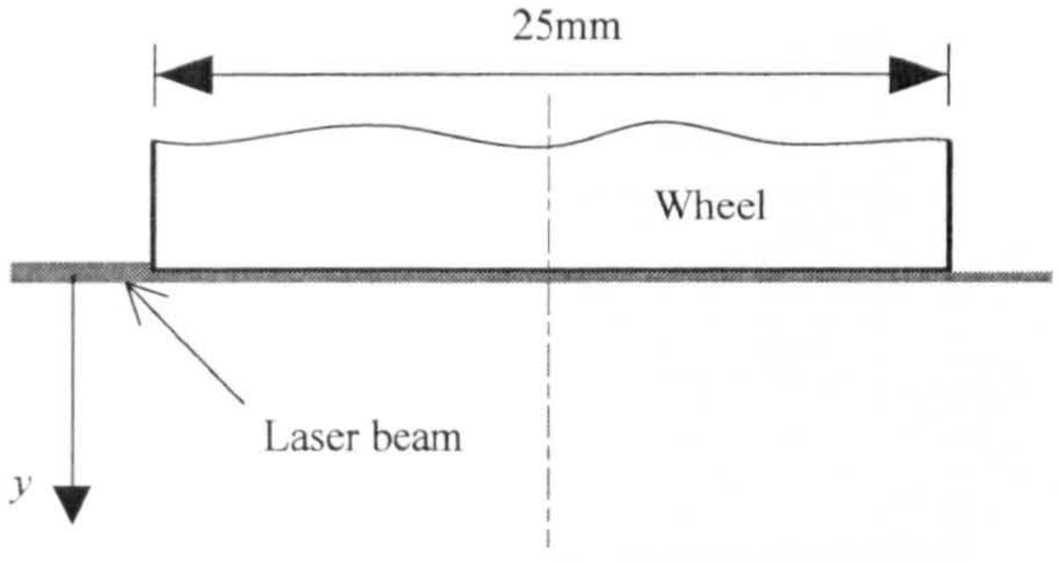

Figure 6-7 Definition of the origin point in y direction

When the laser probe was placed parallel to the wheel spindle (Figure 6-5) the LDA could measure the tangential and normal velocities. In order to measure the axial velocity V_z, the laser probe was placed as shown in (Figure 6-8).

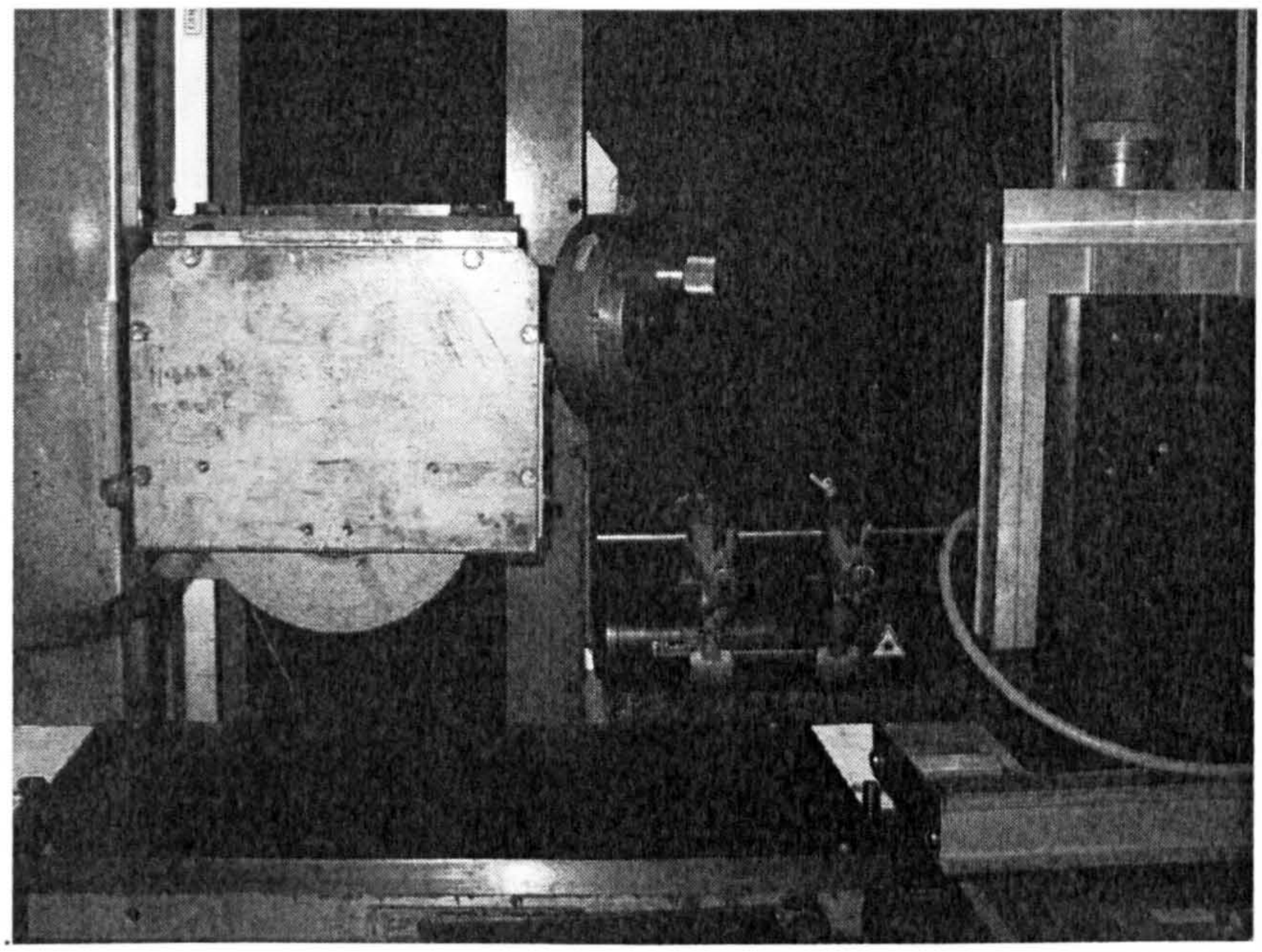

Figure 6-8 Laser probe position to measure axial velocity V_z

The probe was fixed on a traverse, and with the help of this traverse, three-dimensional movement was facilitated with a distance resolution of 0.02 mm.

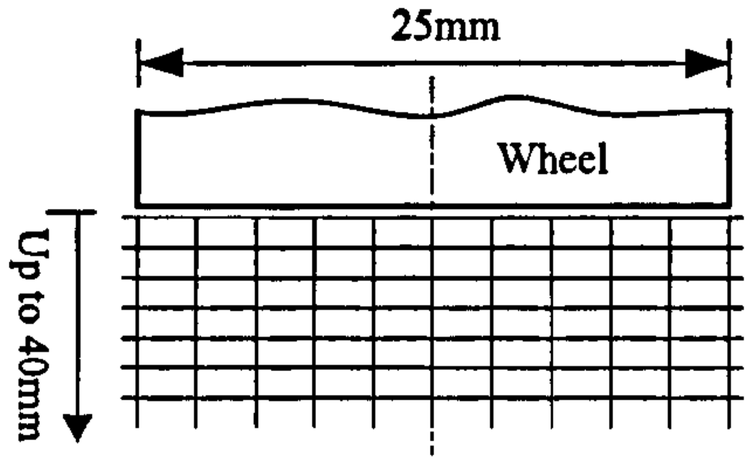

Figure 6-9 Lattice of measurement points

In the measurement area, the measurement points make up the dot lattice (Figure 6-9). The distance between the neighbouring measurement points is 0.5 mm or 1 mm in the y direction; the distance between the neighbouring measurements points is 2.5 mm, 5 mm or 7.5 mm in the z direction; the different distances being dependent on the different measuring demands.

The measurements were incremented from the wheel cylindrical surface of the wheel up to a distance of 40 mm radially outwards. At each measurement point, two velocity components were measured, i.e. the tangential velocity and the radial velocity.

The following experimental measurements were carried out:

1. The tangential velocity V_t map with the wheel speeds 20 m/s, 30 m/s and 40 m/s;
2. The radial velocity V_r map with the wheel speeds 20 m/s, 30 m/s and 40 m/s;
3. The tangential and radial velocity turbulence value map with wheel speed 30 m/s;
4. The axial velocity V_z map with wheel speed 30 m/s;
5. The tangential and radial velocity profile within the wheel speed range;
6. The tangential velocity with different wheel surface roughness;
7. The tangential velocity with different wheel configuration.

Due to the importance of the tangential velocity, most of the measurements concerned the tangential velocity.

6.4 Experimental results and discussion

6.4.1 Tangential velocity distribution

In order to analyze the tangential air velocity distribution in the y-z measurement plane, the experimental data were processed into velocity contour maps using Matlab. Three tangential velocity contours were obtained with the wheel speed of 20 m/s, 30 m/s and 40 m/s (Figure 6-10, Figure 6-11 and Figure 6-12 respectively).

These contour maps clearly show the tangential air velocity distribution in the y-z measurement area. The highest V_t value appears in the narrow area close to the wheel surface. In this area, V_t changes very little in the axial direction. With increasing distance away from the wheel surface, V_t is decreasing; it decreases more quickly close to the wheel edge area. (This phenomenon can also be seen in Figure 6-13, where z is the coordinate of the measurement line in the y-z plane, when the wheel speed is 20 m/s). The largest velocity value measured is only about 75% of the wheel speed (Figure 6-14). It appears that the velocity peaks near the middle of the wheel. Close to the wheel edges, the gradient of V_t is highest, and in the area far from the wheel surface, the tangential velocity shows no great change. Finally, the air tangential velocity decreases exponentially with distance from the wheel surface. This air velocity profile in the wheel radial direction agrees with results reported by some researchers: the air velocity in the radial direction changes exponentially decreasing with the distance from the wheel periphery (Kaliszer & Trmal, 1975).

No matter what the wheel speed is, the tangential velocity distribution is similar in the measurement area as can be seen in the three contour maps (Figure 6-10, Figure 6-11 and Figure 6-12). Generally, the air tangential velocity increases with wheel speed and this is shown clearly in Figure 6-14, where the three tangential velocity profile are along the wheel centre line in the y-z plane (z = 12.5 mm) are shown.

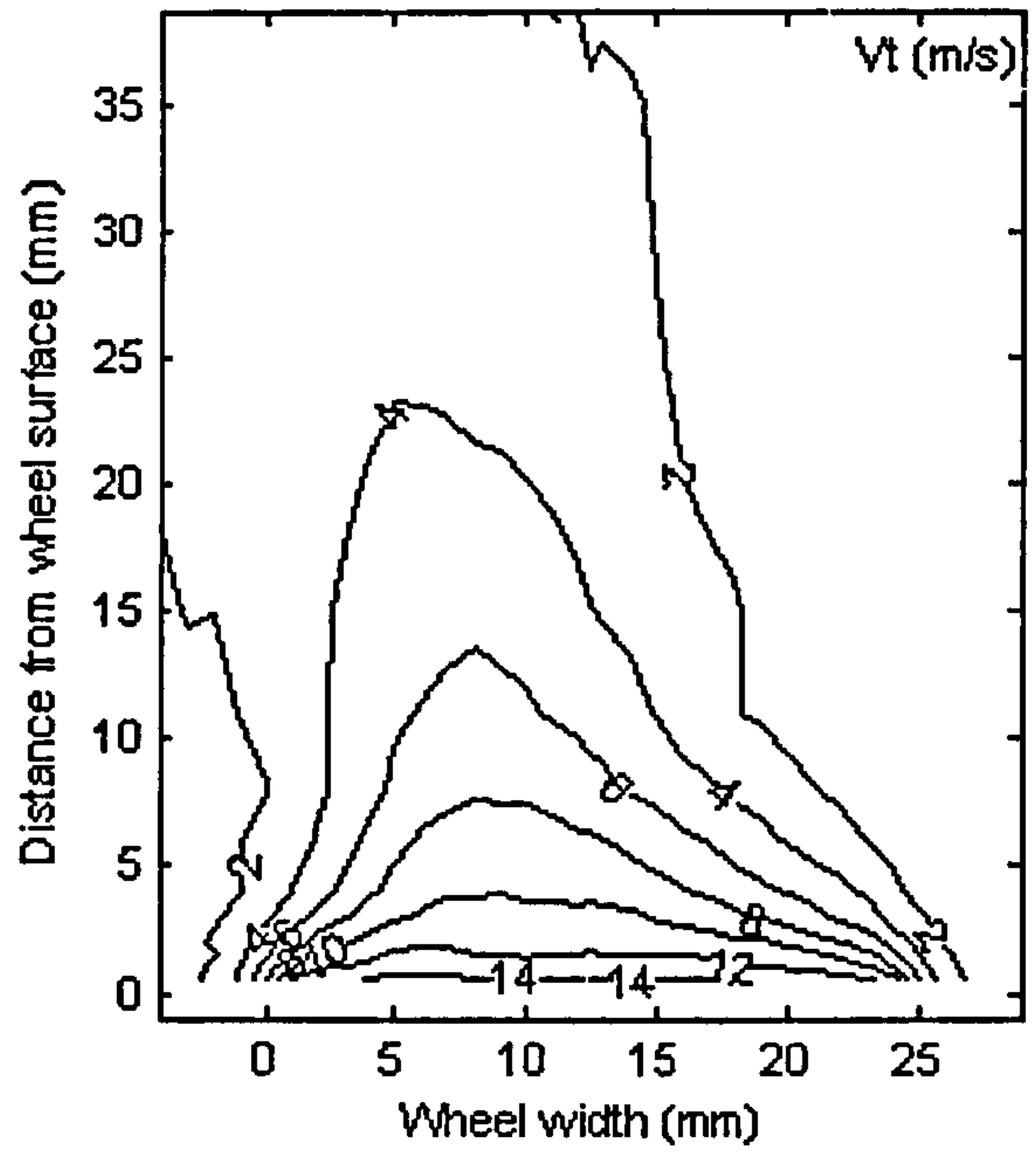

Figure 6-10 Air tangential velocity V_t contour (wheel speed = 20 m/s)

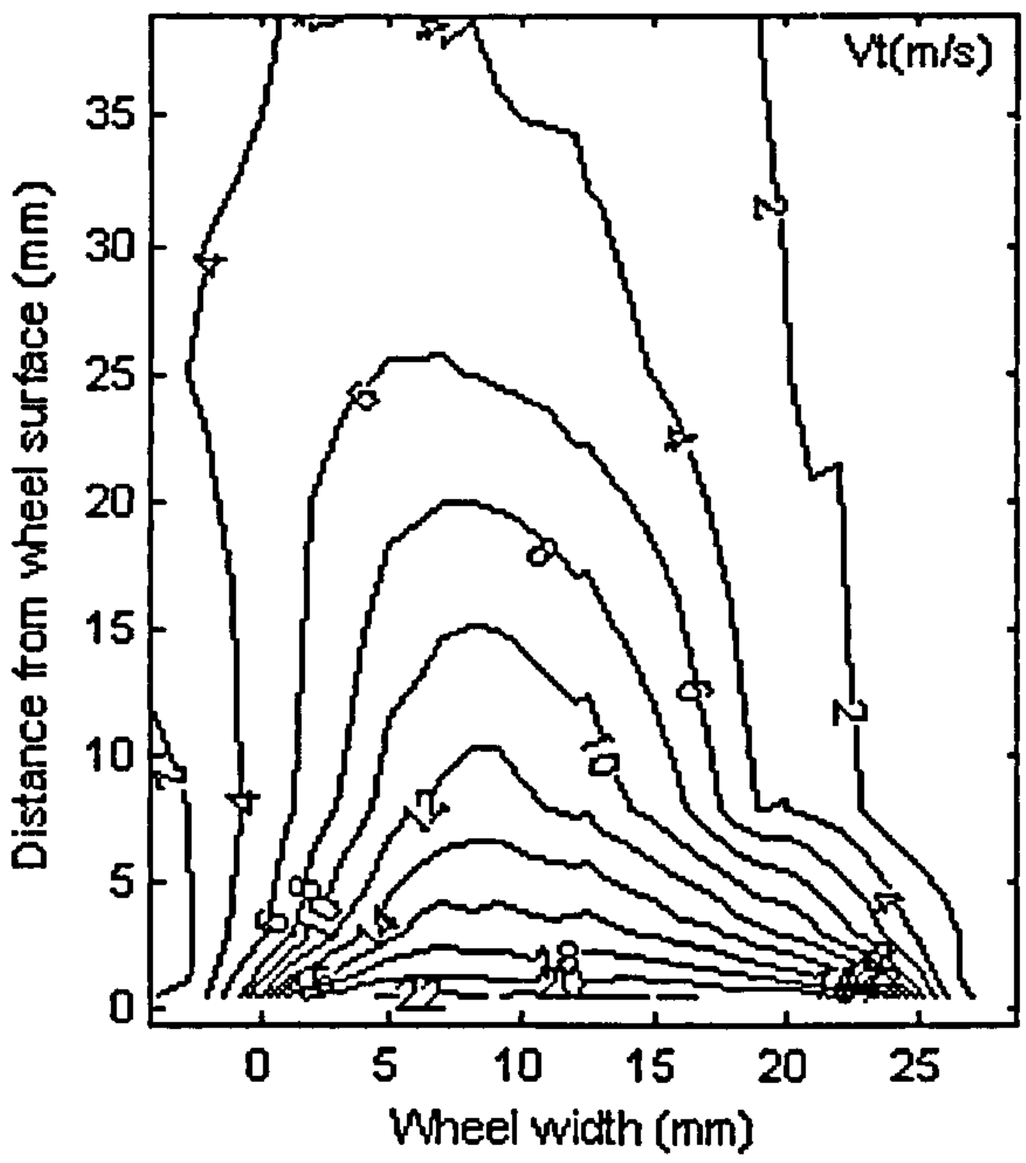

Figure 6-11 Air tangential velocity V_t contour (wheel speed = 30 m/s)

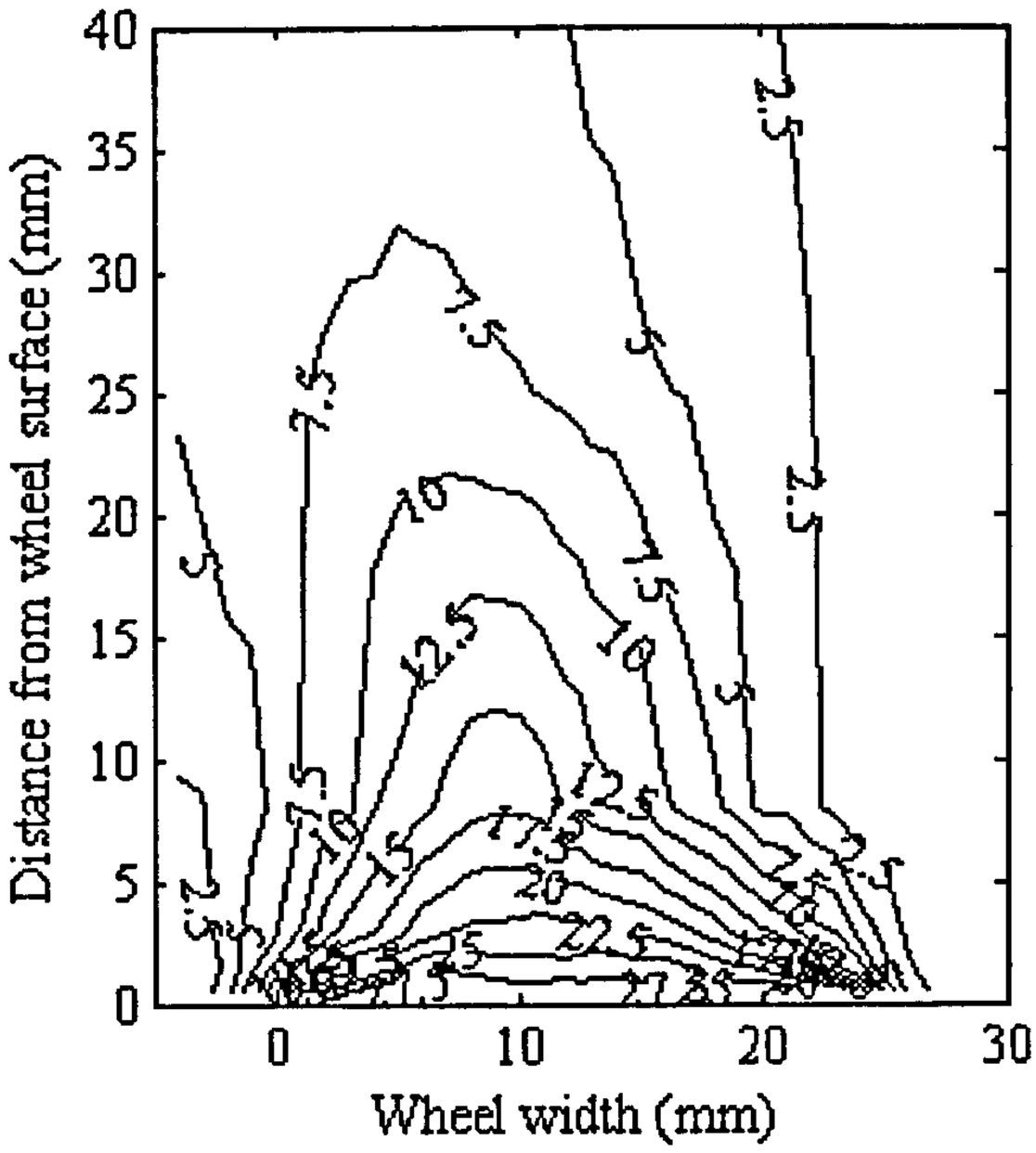

Figure 6-12 Air tangential velocity V_t contour (wheel speed = 40 m/s)

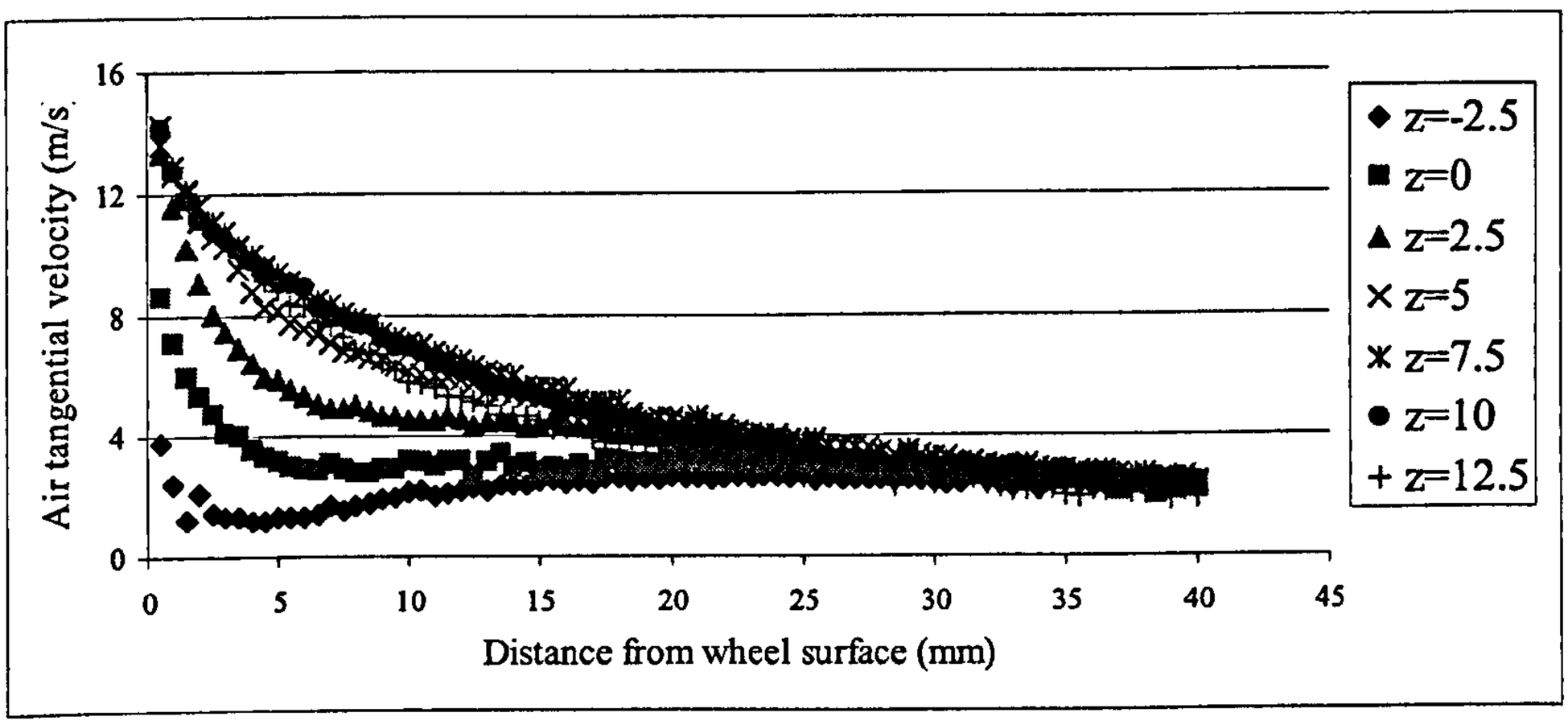

Figure 6-13 Air tangential velocity profile along the measurement lines

(z: Axial coordinate of the line)

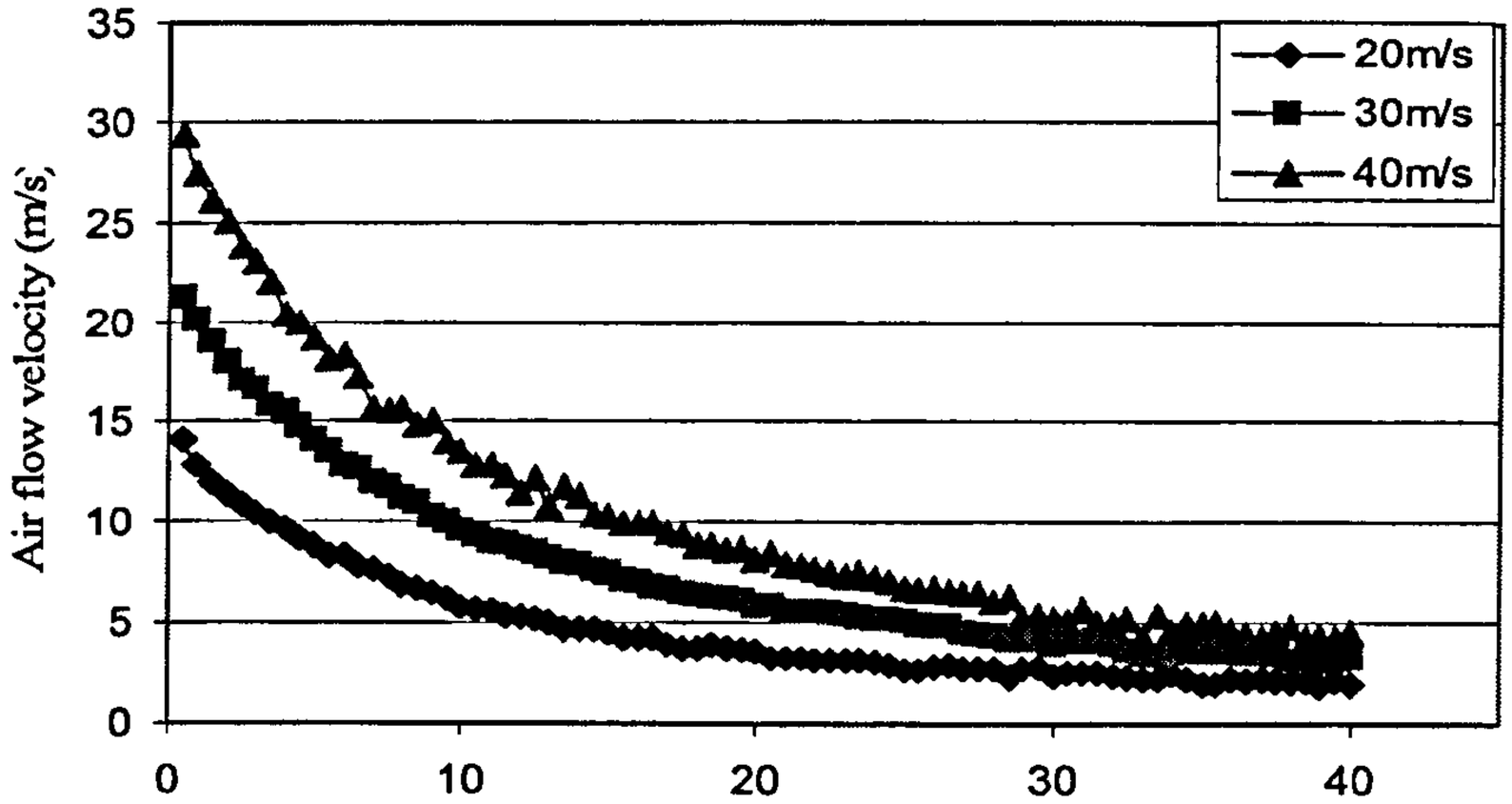

Figure 6-14 Profile of V_t with different wheel speed
(Measurement line is along the y direction, z=12.5 mm)

6.4.2 Radial velocity distribution

As in the case of the tangential velocity measurements, three radial velocity contour maps were obtained in the y-z measurement plane with the wheel speed 20 m/s, 30 m/s and 40 m/s (Figure 6-15, Figure 6-16 and Figure 6-17 respectively). Due to the laser beam, the radial velocity could not be measured in the area very close to the wheel surface.

The highest V_r value appears in the wheel middle, between 15 mm to 30 mm away from the wheel surface, and this can be observed in Figure 6-18.Further away the velocity begins to decrease. Therefore, it appears that velocity is maximum in the middle area. The radial velocity also increased with wheel speed (Figure 6-18).

Finally, the absolute value of the radial velocity is much smaller than that of the tangential velocity (Figure 6-19). The two velocity components became similar in value after 30 mm away from the wheel surface. Therefore, the air boundary layer velocity is mainly made up of the tangential velocity.

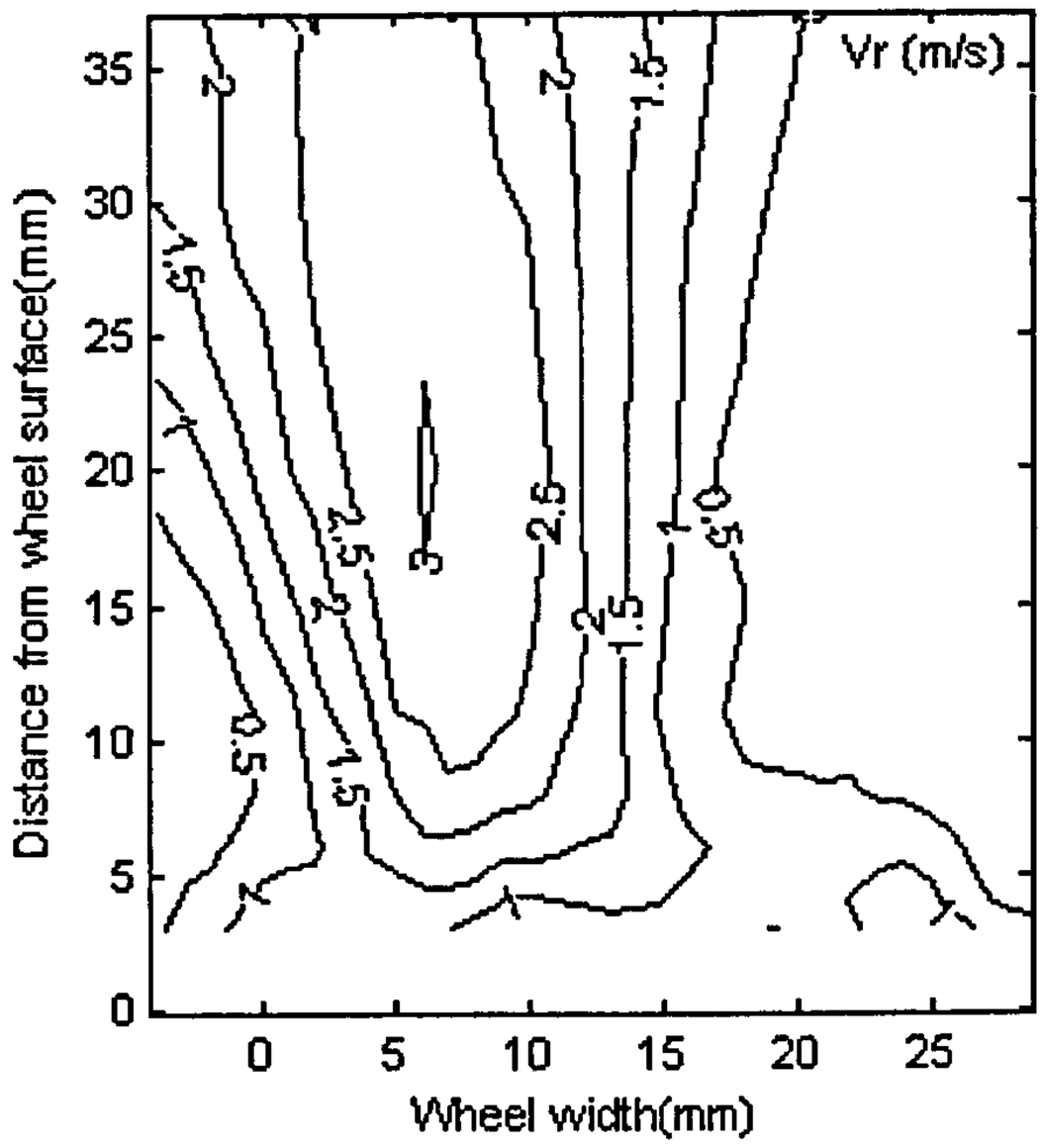

Figure 6-15 Air radial velocity V_r contour (wheel speed = 20 m/s)

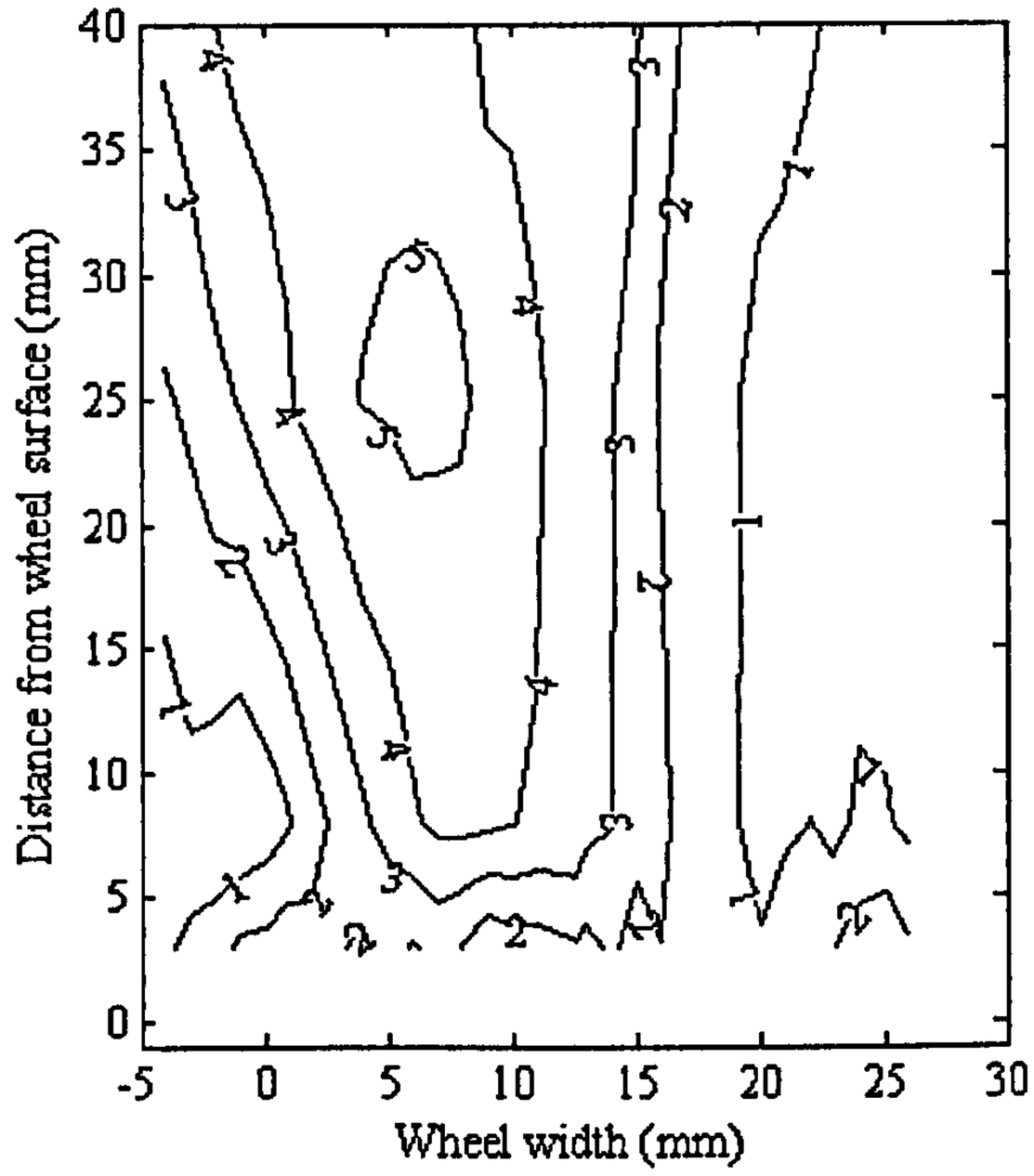

Figure 6-16 Air radial velocity V_r contour (wheel speed = 30 m/s)

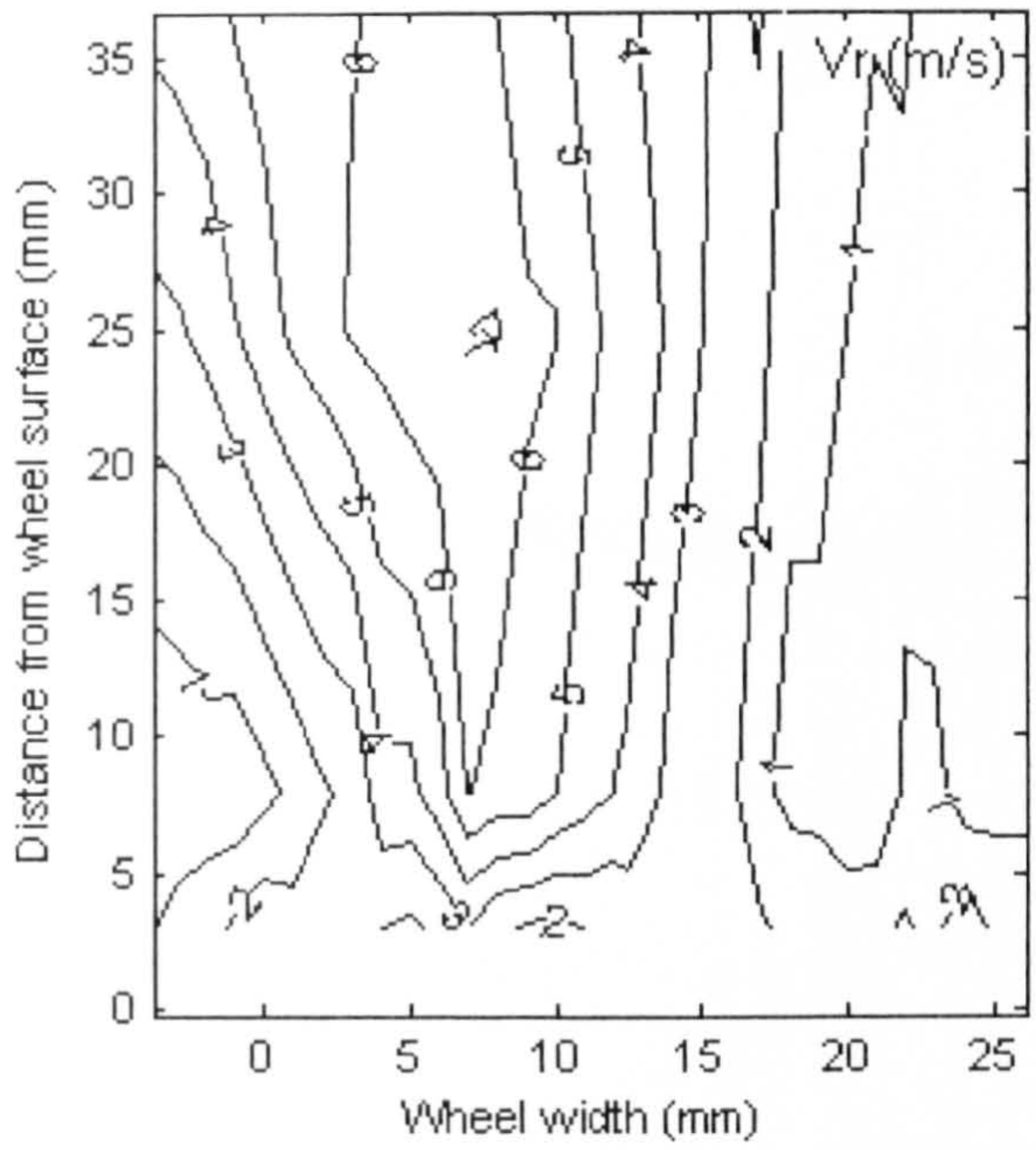

Figure 6-17 Air radial velocity V_r contour (wheel speed = 40 m/s)

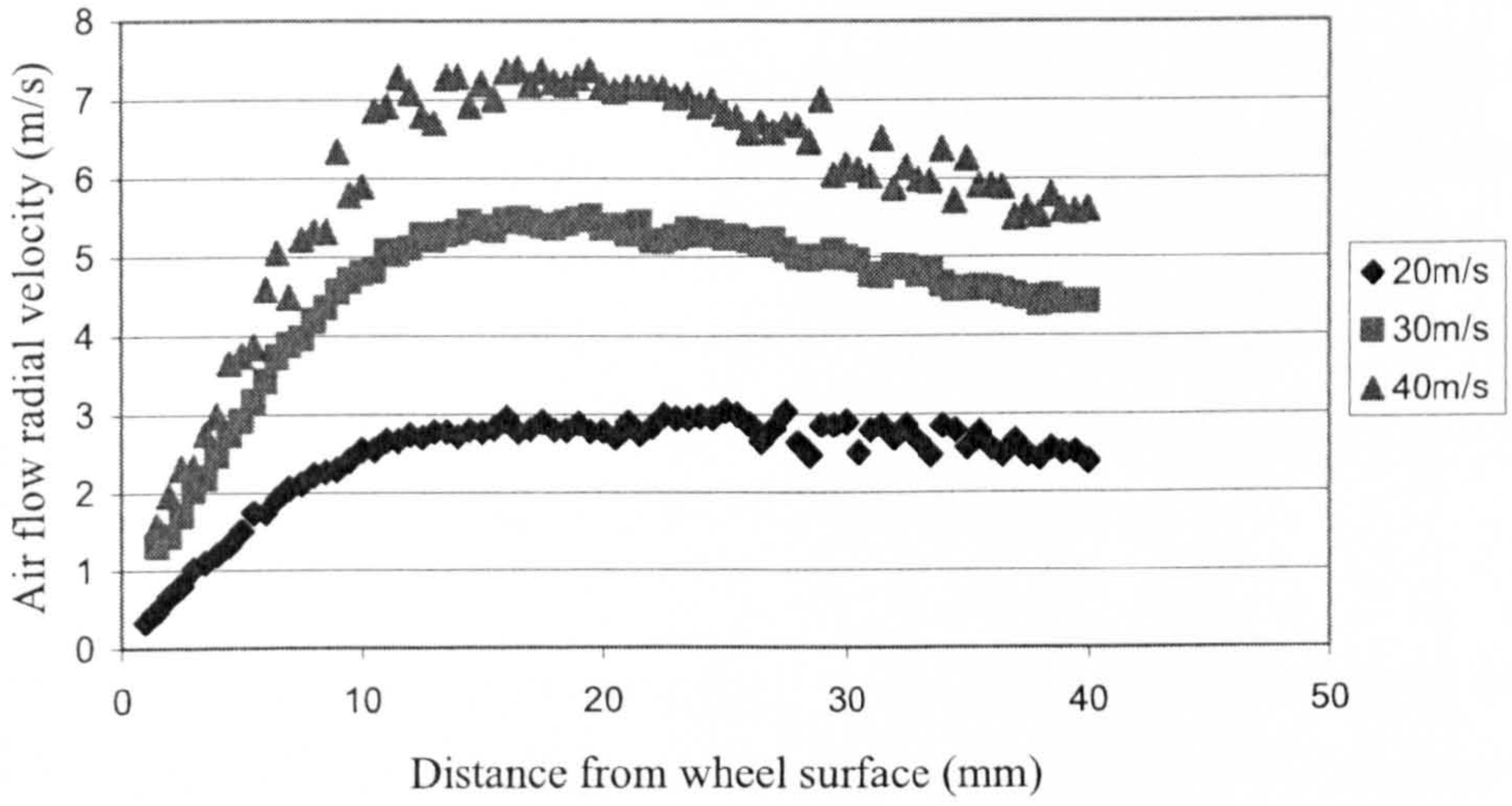

Figure 6-18 Profile of V_r with different wheel speeds

(Measurement line is along the y direction, z=7.5 mm)

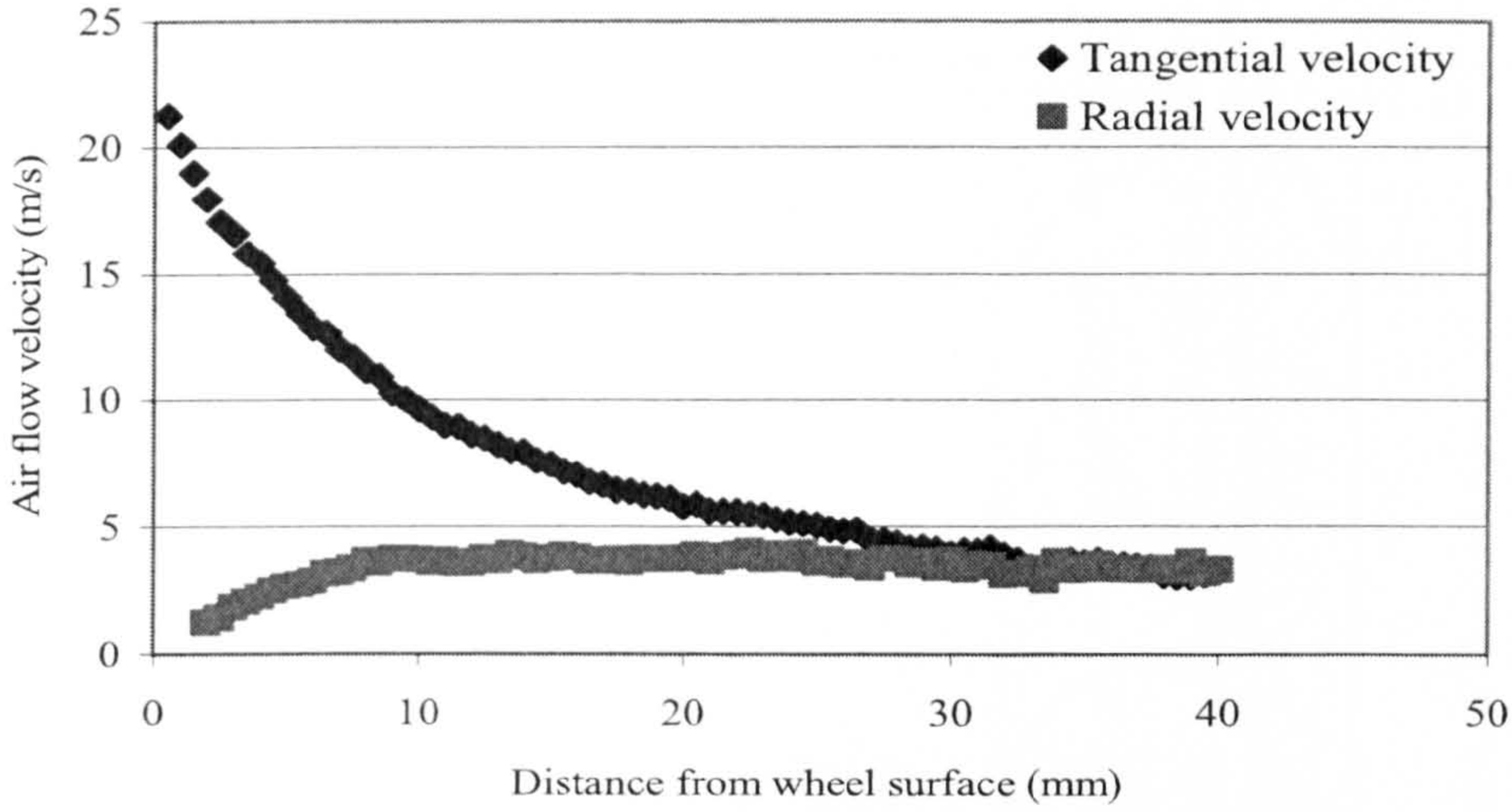

Figure 6-19 Comparison of V_t and V_r (wheel speed = 30 m/s)

6.4.3 Axial velocity distribution

The axial velocity distribution, V_z is shown in Figure 6-20. The largest absolute velocity value appears close to the wheel edge; at the middle section of the wheel, V_z becomes zero. Therefore, the results show that the air is flowing from the two sides of the wheel into the central area in the wheel axial direction. This can be explained as follows: the air surrounding the rotating wheel is driven outwards by the centrifugal force, and consequently air flows towards the middle of the wheel from both sides to replace it. Shibata et al (1982) forecast this phenomenon. The air flow velocity in the wheel axial direction has not been measured before, since it is very small and very turbulent, but it will affect the direction of the air flow rotating around the wheel.

The air velocity distribution is not completely symmetrical about the centre of the wheel width. This phenomenon is caused by the asymmetric structure of the experimental arrangement.

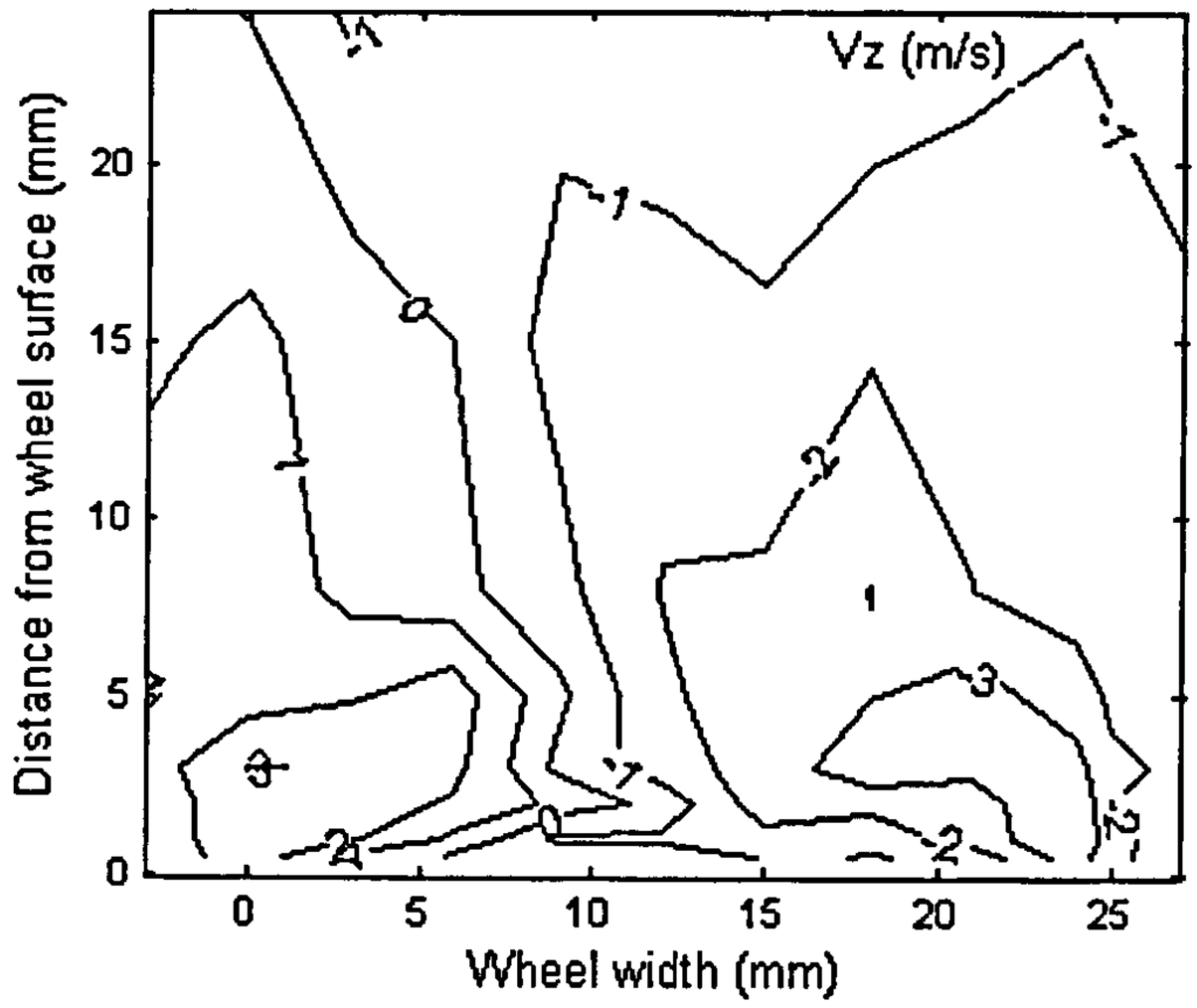

Figure 6-20 V_z distribution of air flow (wheel speed = 30 m/s)

6.4.4 Turbulent intensity

Using the LDA, the turbulent intensity value of velocity in one measurement point can be measured simultaneously when measuring the velocity. The air turbulent intensity value is the percentage of the RMS velocity value divided by the local mean velocity value.

Mean velocity is defined by the equation

$$\bar{U} = \frac{\sum U_i \Delta t_i}{\sum \Delta t_i} \tag{6.2}$$

U_i, velocity of i^{th} particle

Δt_i, transit time of i^{th}

$i = 1, 2, 3, ...N$, number of samples

RMS velocity value is defined by the equation

$$\sigma = \sqrt{\frac{\sum_i (U_i - \bar{U})^2 \Delta t_i}{\sum_i \Delta t_i}} \tag{6.3}$$

As shown in Figure 6-21, the smallest turbulence intensity value of V_t is at the centre position along wheel width direction in the area close to the wheel surface. It means that the air velocity is steadier in this area. However, the smallest turbulent value of V_r is at the centre area along wheel width as well as that of V_r, and not close to the wheel surface. The turbulence intensity contours are similar to the velocity contours. However, the higher velocity occurs always where the lower turbulence intensity value is observed.

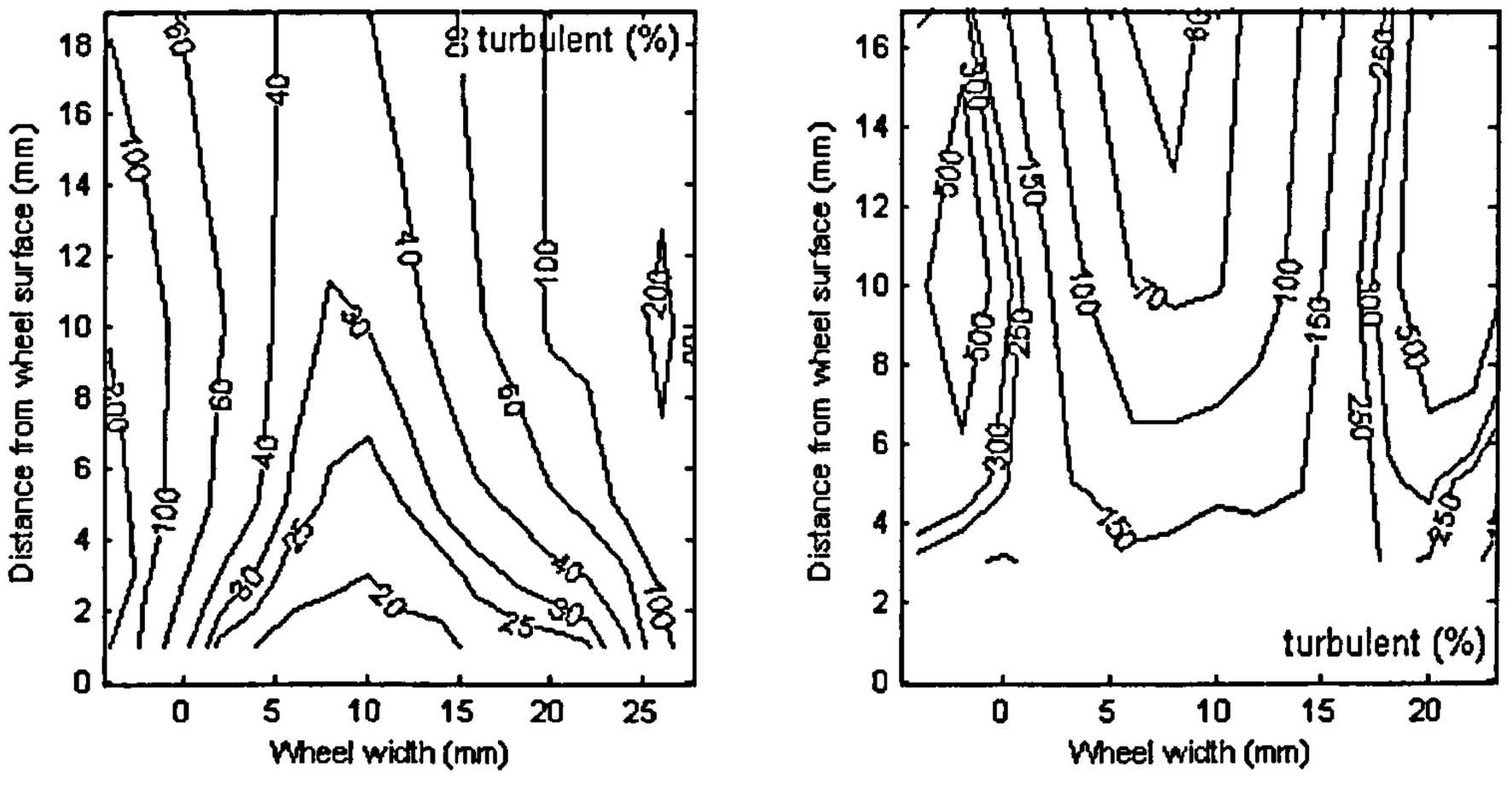

Figure 6-21 V_t (left) and V_r (right) Percent Turbulent distribution of air flow (wheel speed=30 m/s)

6.4.5 Air velocity VS wheel Speed

Three points were randomly selected to measure the air tangential velocity; the coordinates (x, y, and z) of these points are shown at the right bottom corner in Figure 6-22. In each point, the tangential velocity was found to be proportionally to the wheel speed from 20 m/s to 50 m/s.

If this trend is still true with wheel increasing speed, the tangential velocity distribution should be the same as the measured velocity (Figure 6-10, Figure 6-11 and Figure 6-12). Because of the limit in wheel speed, the experiments at high speed were not carried out. However, the simulation in Chapter 7 can verify this conclusion.

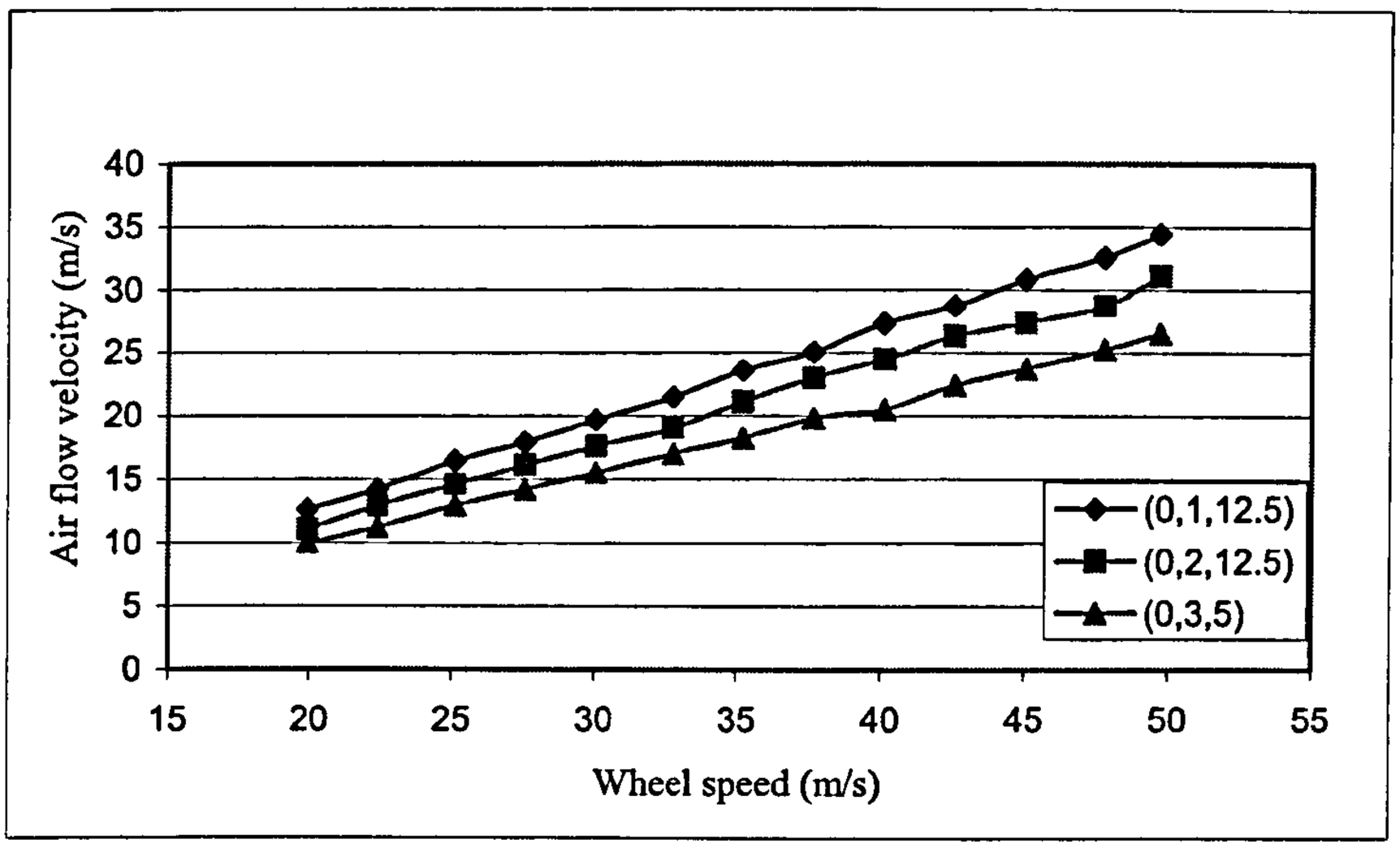

Figure 6-22 Relation between air velocity (tangential direction) and wheel speed for three different position

6.4.6 Air velocity VS wheel surface roughness

Three different grain size wheels were used to measure the air velocity in order to test the effect of wheel roughness. Two wheels were Aluminium Oxide wheels with grain size 60 and 30; the third wheel was the same size to the wheel with grain size 30, but the surfaces of the wheel were covered by plastic tape to make the wheel surface smooth. The velocity measurement were along the y direction in the wheel middle section (z = 12.5 mm), and the wheel velocity was 30 m/s.

The experimental results are shown in Figure 6-23 (tangential velocity) and Figure 6-24 (radial velocity). It is clearly shown that, no matter what the wheel surface roughness is, the air velocity profile is similar along the measurement line but the velocity values are different. Both the tangential velocity and the radial velocity decreased with decreasing wheel surface roughness.

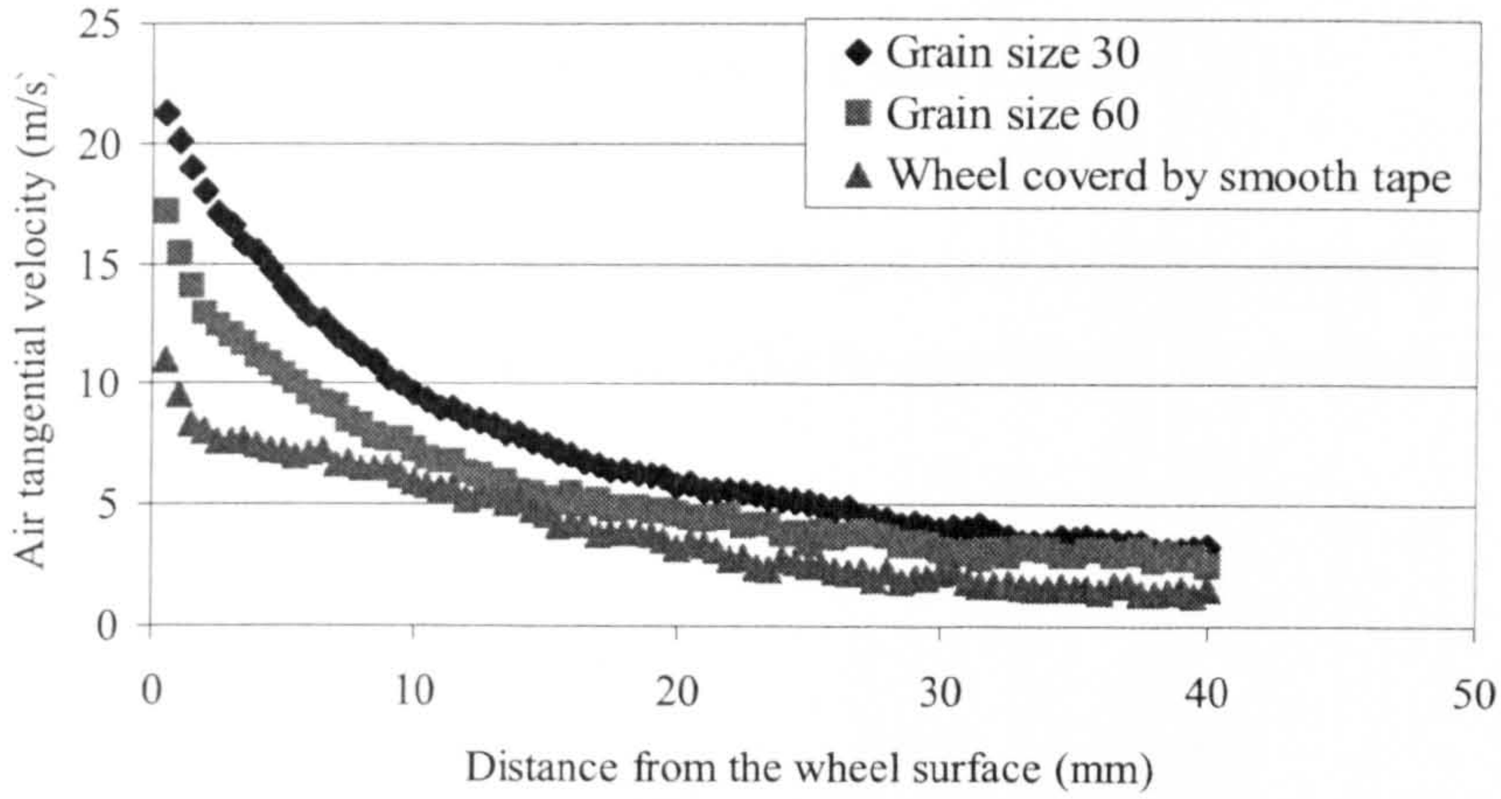

Figure 6-23 Air tangential velocity VS the wheel surface roughness

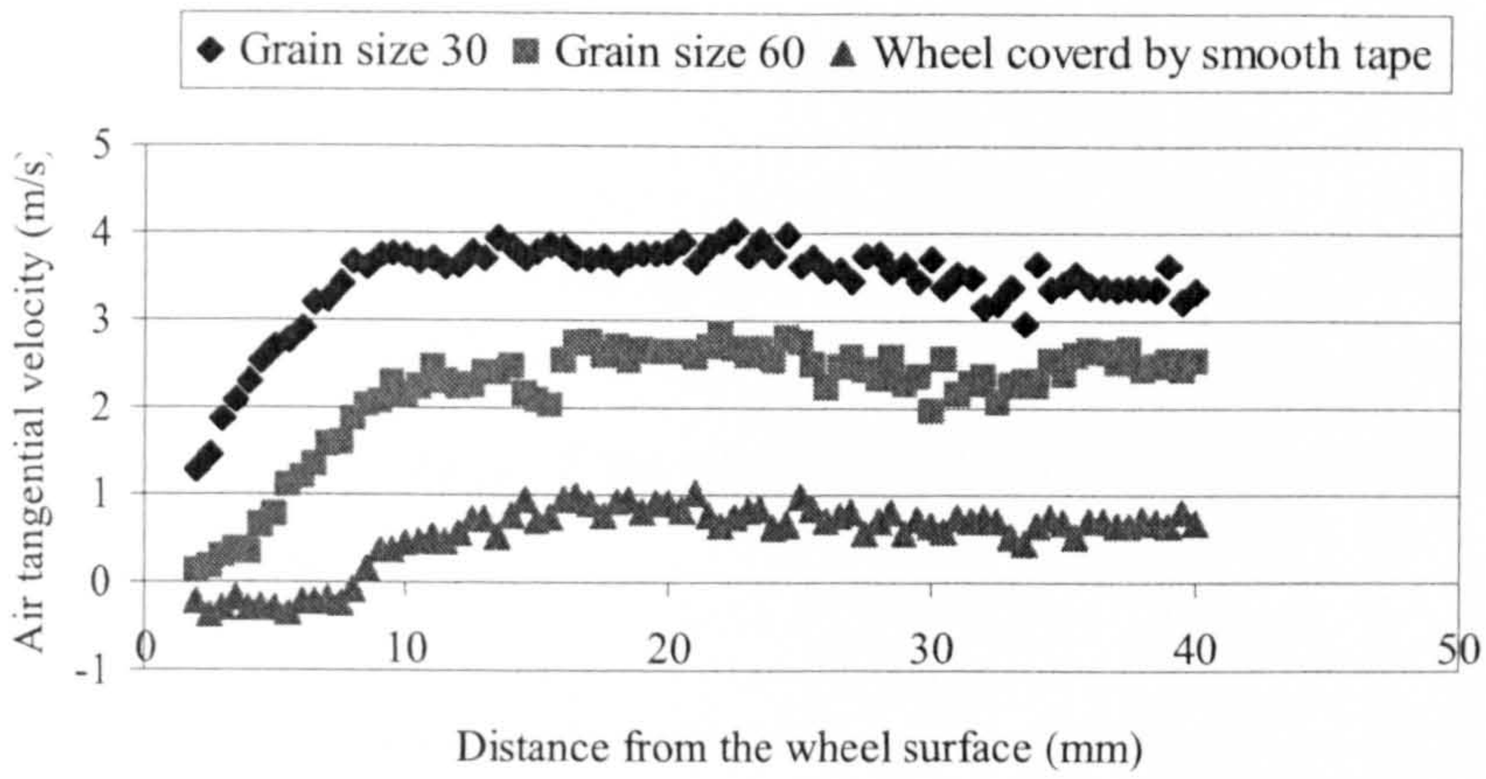

Figure 6-24 Air radial velocity VS wheel surface roughness

6.4.7 Air velocity VS wheel structure

In order to investigate the effect of the wheel porosity and wheel surface roughness on formation of the air boundary layer, four groups of experiments were carried out with different wheel surface combinations. One aluminium oxide wheel of grain size 30 was used for this measurement; the wheel diameter was 182 mm; the width was 25 mm. To obtain a smooth wheel surface without porosity, the selected surfaces of the wheel were covered by smooth tape, that producing four configurations were obtained:

- Rough cylindrical surface and rough flanks Figure 6-25 A;
- Rough cylindrical surface and smooth flanks Figure 6-25 B;

- Smooth cylindrical surface and rough flanks Figure 6-25 C;
- Smooth cylindrical surface and smooth flanks Figure 6-25 D.

Two velocity components were measured along a line in the y direction in the wheel middle section (z = 12.5 mm). The wheel velocity was 30 m/s for the four tests.

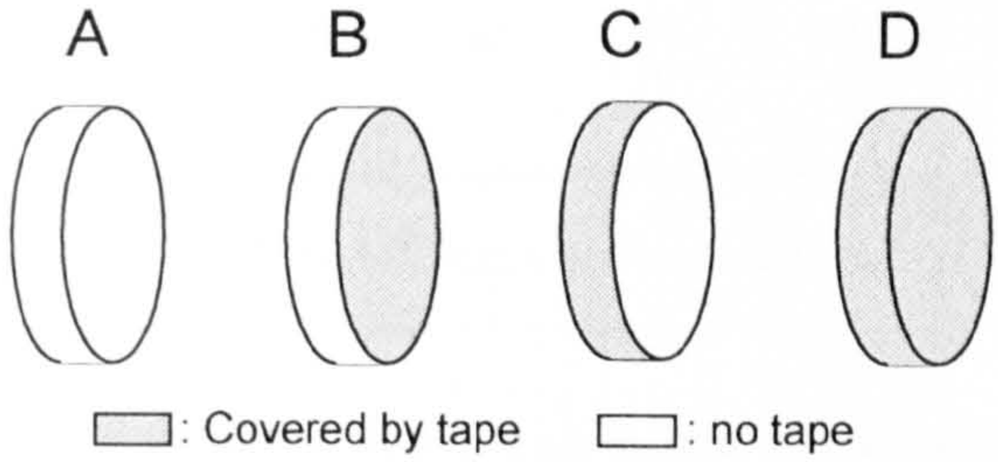

Figure 6-25 Four wheel surface combinations

The experimental results are shown in Figure 6-26 and Figure 6-27. They show that, the main factor affecting the velocity of the air flow is the roughness of the wheel cylindrical surface. The roughness of the wheel flanks can also affect the velocity of air flow, but to a lesser extent.

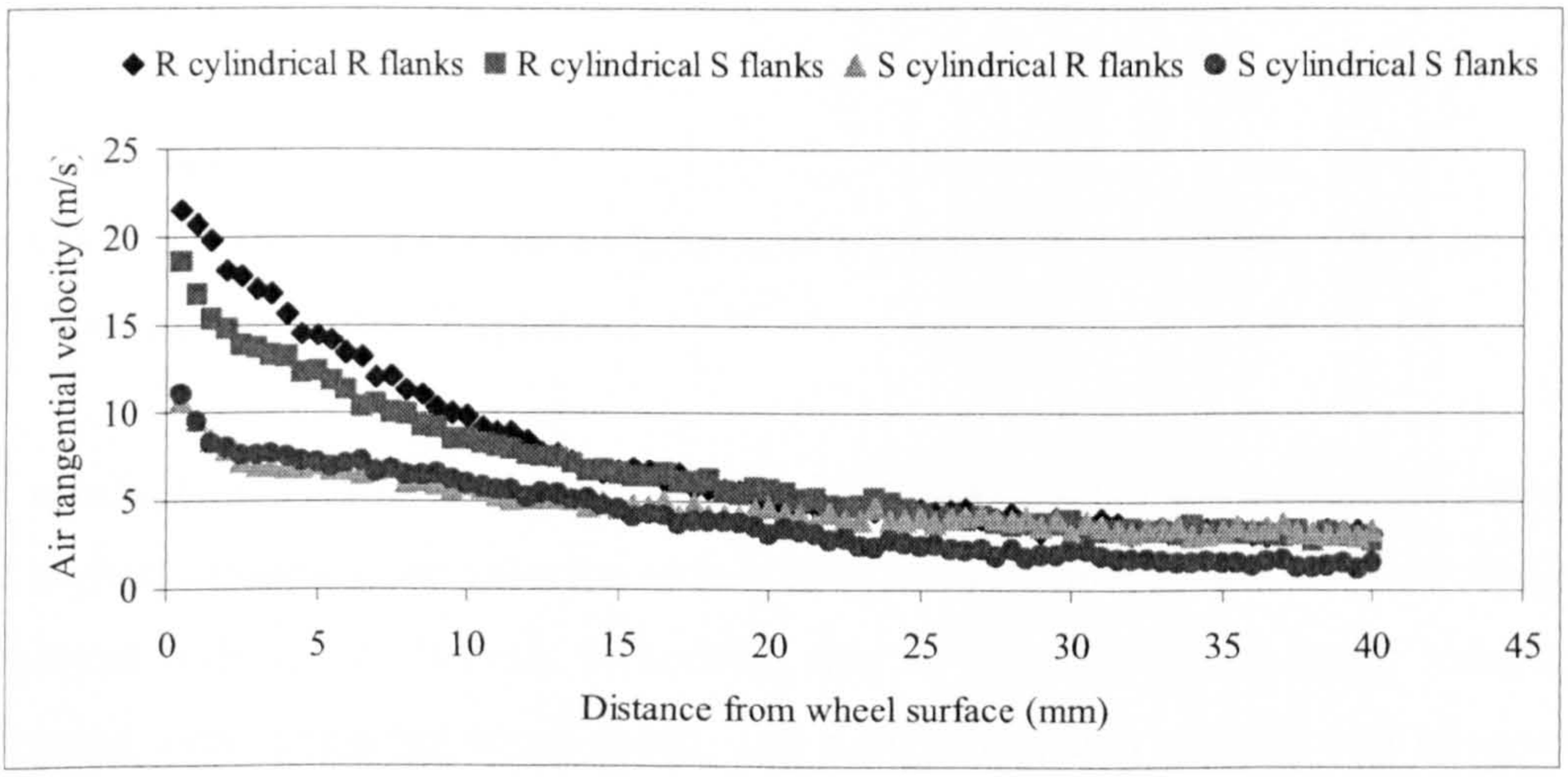

Figure 6-26 Tangential velocity of the air in four wheel configuration

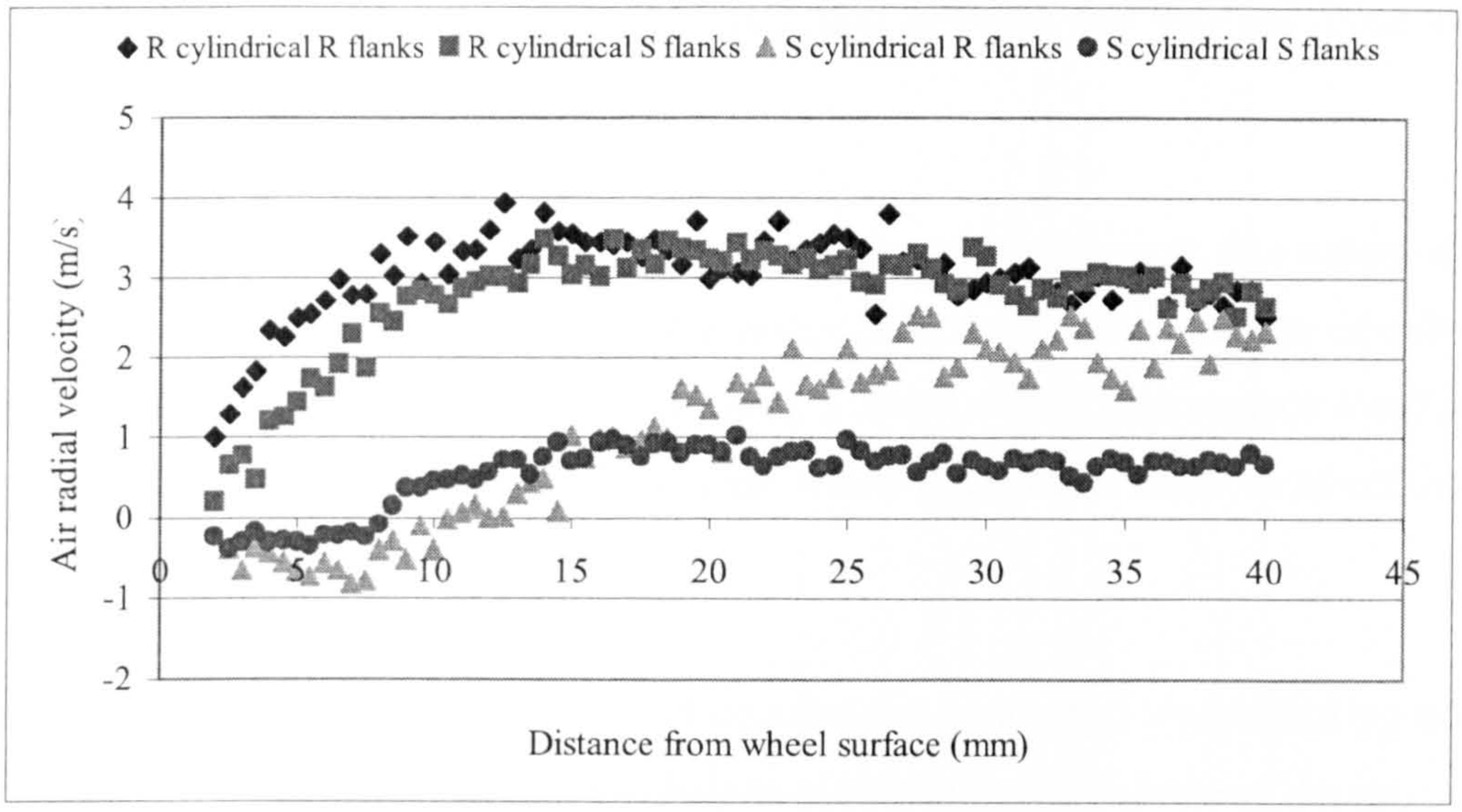

Figure 6-27 Radial velocity of the air in four wheel configuration

It is stated in the literature that when a wheel is made of porous material, the air contained in the wheel pores is forced out by the centrifugal force might possibly blow out through the wheel body. If the wheel surface was covered by the tape, the surface would be not porous. The centrifugal force effect can be seen in Figure 6-27. It is noted that the direction of the radial velocity is toward the wheel the wheel is covered by tape. This is because there is no air blowing out from inside of the wheel. However, the air blowing outward has not significant effect on the air flow around the grinding wheel.

6.5 Conclusions

The velocity distributions in the air boundary layer around the rotating wheel have been fully investigated in this Chapter.

The results have clearly shown the velocity distributions and the turbulence intensity. The highest tangential air velocity occurs only in the wheel middle section along the cylindrical side of the wheel. Generally, the air tangential and radial velocity is increasing with increasing wheel speed. The maximum radial velocity was observed at about 25 mm from the wheel surface in the wheel middle section.

The smallest turbulent value of tangential velocity is in the centre of the wheel width close to the wheel surface. The smallest turbulent value of radial velocity is in the centre

of the wheel width as well as that of the tangential velocity, but it is not close to the wheel surface.

The axial component of the air flow was also measured. Although this value of the velocity is much smaller than the tangential component, it can determine the air velocity direction. The air velocity increased when using a wheel with a high surface roughness. The roughness of the cylindrical surface of the wheel is the main factor to affect the air flow.

In summary, the experimental results and conclusions give a full understanding of the air boundary layer velocity and this will help to optimize the fluid delivery design.

Chapter 7 Simulation of Air Boundary Layer

7.1 Introduction

Computational Fluid Dynamics (CFD) is a computer-based tool for simulating the behaviour of systems involving fluid flow, heat transfer, and other related physical processes. It works by solving the equations of fluid flow (in a special form) over a region of interest, with specified (known) conditions on the boundary of that region.

The set of equations, which describe the processes of momentum, heat and mass transfer, are known as the Navier-Stokes equations. These partial differential equations have no known general analytical solution but can be discretized and solved numerically. There are a number of different solution methods, which are used in CFD codes. The most common is known as the finite volume technique. In this technique, the region of interest is divided into small sub-regions, called control volumes. The equations are discretized and solved iteratively for each control volume. As a result, an approximation of the value of each variable at specific points throughout the domain can be obtained. In this way, one derives a full picture of the behaviour of the flow. ANSYS CFX is based on the finite volume technique, and it was used for the simulation work in this research.

CFD Methodology includes the following steps: the first step is to identify the region of interest; then the geometry of the region of interest is defined. The mesh is then created. After importing the mesh into the CFD pre-processor, other elements of the simulation including the boundary conditions (inlets, outlets, etc.) and fluid properties are defined. The flow solver is run to produce a file of results that contains the variation of velocity, pressure and any other variables throughout the region of interest. The results can be visualized and provide an understanding of the behaviour of the fluid throughout the region of interest. In this case, the air boundary layer around the rotating wheel can be modelled and analyzed by simulation. The results of simulations can be compared with the LDA measurements and insight into the flows obtained. If the results of the two methods correlate well then the effect of changes to the system can be assessed readily

from the simulation, rather than having to undertake further time consuming experiments.

The CFX simulation of the air boundary layer was undertaken in this chapter. The parameter setup for the initial simulations were the same to the parameter setup in the experiments, therefore, this work can be used to evaluate previous experimental results and understand the existing knowledge of the air boundary layer. The following simulations were developed for the air flow layer velocity research in cylindrical grinding and internal grinding, which give greater understanding for different grinding conditions. The CFD software package used in this study is ANSYS CFX 10.0.

7.2 ANSYS CFX Structure

ANSYS CFX consists of five software modules that pass the information required to perform a CFD analysis, shown as in Figure 7-1:

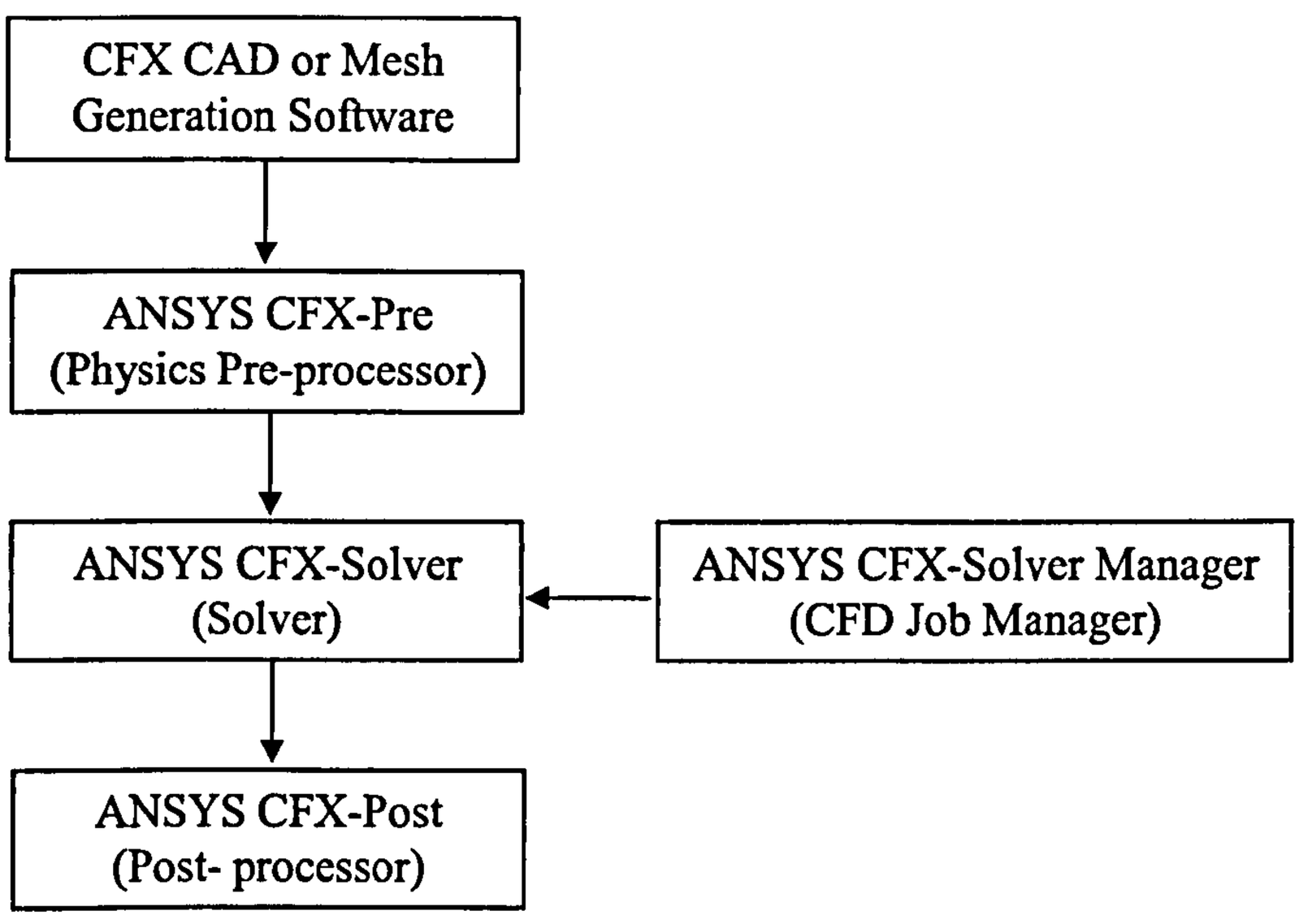

Figure 7-1 Structure of ANSYS CFX consists

ANSYS CFX-Pre allows multiple meshes to be imported, allowing each section of complex geometries to use the most appropriate mesh. Flow physics, boundary conditions, initial values and solver parameters are specified in ANSYS CFX-Pre. A full range of boundary conditions, including inlets, outlets and openings, together with

boundary conditions for heat transfer models and periodicity, are all available in ANSYS CFX through ANSYS CFX-Pre.

ANSYS CFX-Solver solves all the solution variables for the simulation for the problem specification generated in ANSYS CFX-Pre. ANSYS CFX uses the coupled solver, which is faster than the traditional segregated solver and fewer iterations are required to obtain a converged flow solution.

The ANSYS CFX-Solver Manager module provides greater control to the management of the CFD task. Its major functions are:

- Specify the input files to the ANSYS CFX-Solver.
- Start/stop the ANSYS CFX-Solver.
- Monitor the progress of the solution.
- Set up the ANSYS CFX-Solver for a parallel calculation.

ANSYS CFX-Post provides state-of-the-art interactive post-processing graphics tools to analyze and present the ANSYS CFX simulation results.

7.3 CFX simulation model setup

This section gives the fundamental process of the air boundary layer simulation. More simulations in this Chapter are based on this model including the dimensions of the model, the physics definitions, the boundary definitions, the solver control settings, and so on.

7.3.1 Geometry

The geometry of the simulation model is shown in Figure 7-2, and it was created in DesignModeler within ANSYS Workbench. The dimensions of the geometry are:

- Cuboid Length: 500 mm, in x direction;
- Cuboid Height: 250 mm, in y direction
- Cuboid Width: 150 mm, in z direction;
- Wheel Diameter: 182 mm;
- Wheel Width: 25 mm

The wheel, which rotates around the z aixs, is fixed in the centre of the cuboid, and its dimensions were the same as those of the wheel used for the experiments. The wheel speed in the simulation can be changed from low speed to high speed with the parameters setup. In order to be able to compare results of simulation with the experimental results, the wheel speed was set the same as in the experiment. In the simulation, the wheel is solid a rough surface, and the rest of the space within the cuboid is filled with air.

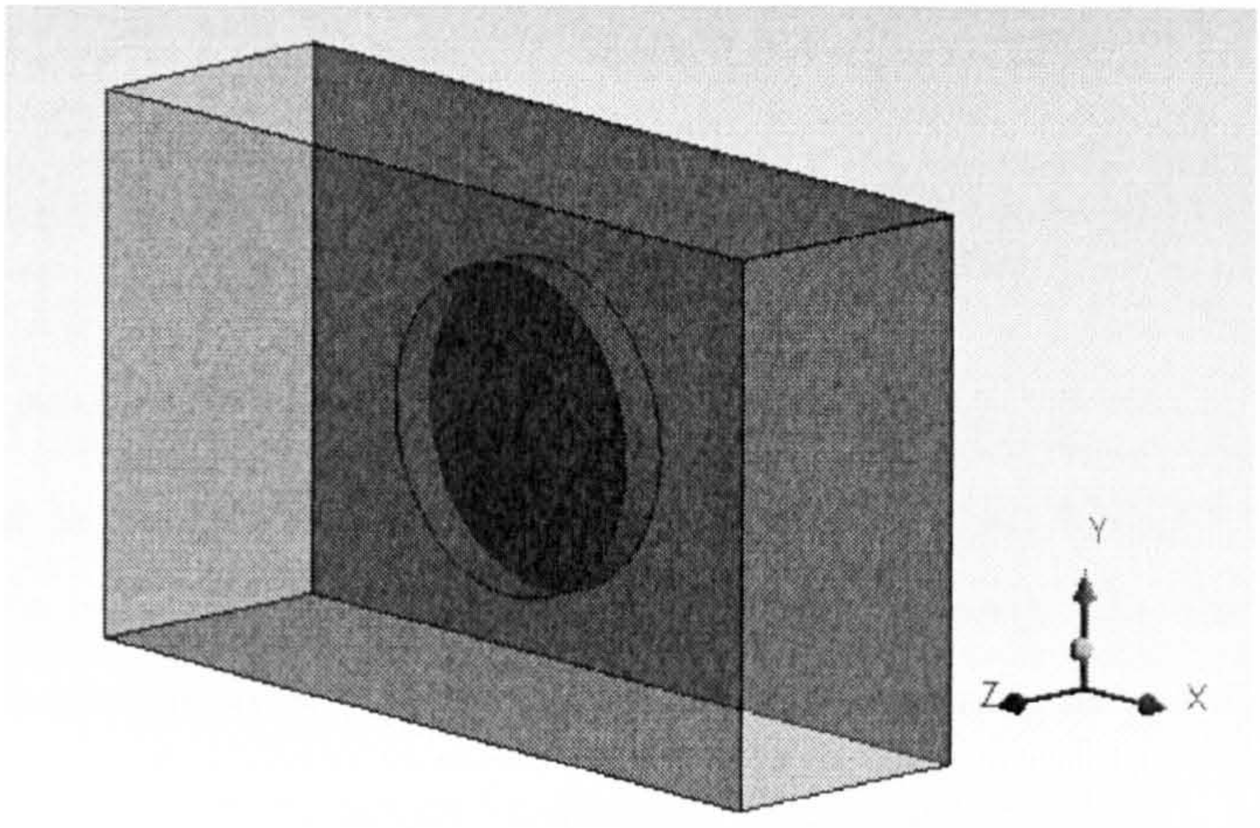

Figure 7-2 Schematic of the model geometry

7.3.2 Mesh

The mesh was generated using a CFX-Mesh method. It was refined by mesh control settings, especially in the area approaching the wheel surfaces. The surface mesh is shown in Figure 7-3. There were 1311080 elements in the volume mesh.

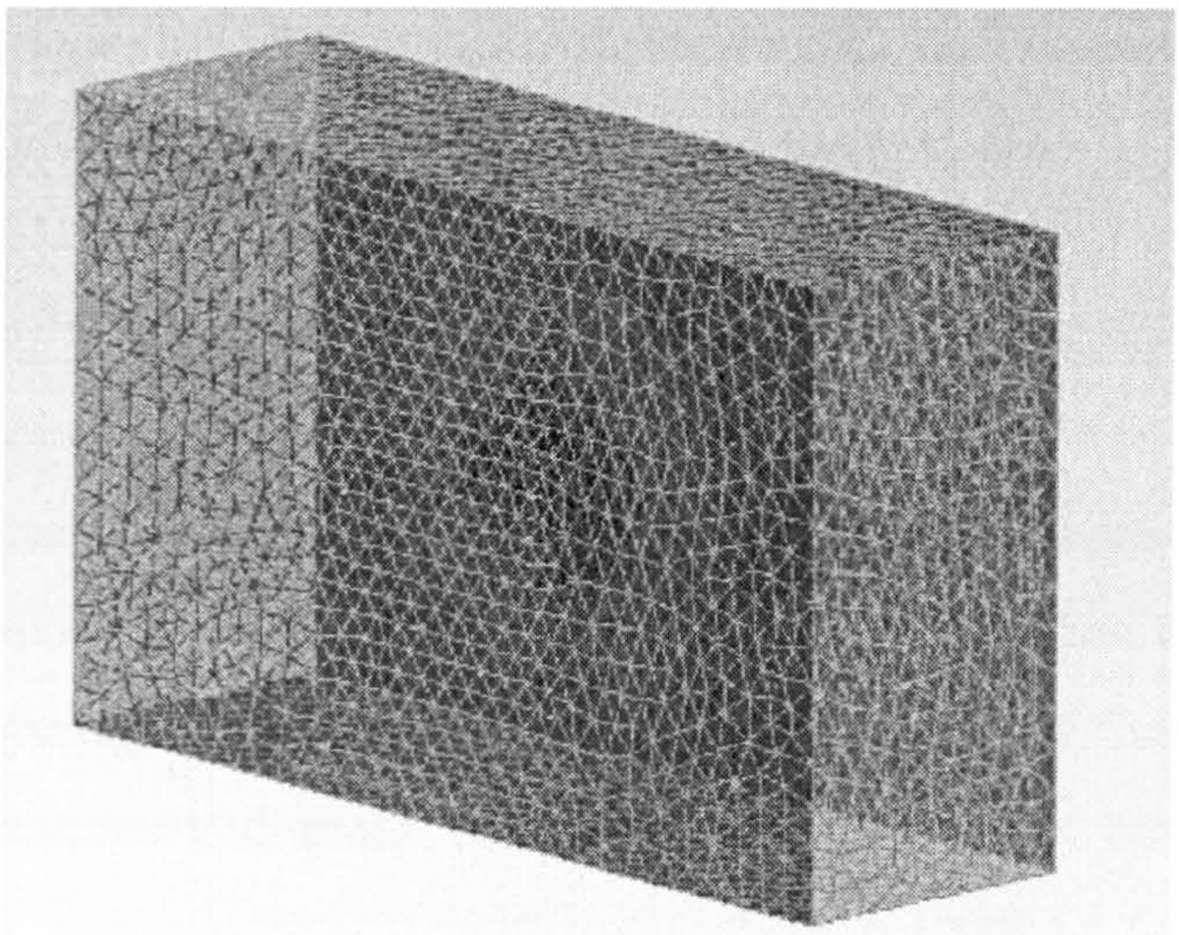

Figure 7-3 Surface mesh of the geometry

7.3.3 CFX-Pre parameters setup

ANSYS CFX-Pre is the physics definition pre-processor for ANSYS CFX that allows the easy definition of a simulation. After importing the mesh file, the following setup could be carried out in the CFX-Pre. The main parameters were set as shown in Table 7-1, and other parameters were set as the default values in CFX-Pre.

Table 7-1 Simulation parameters setup

Component	**Feature**	**Details**
Simulation	Type	Steady State
Domain	Domain Type	Single fluid domain
	Domain Motion	Stationary
	Reference Pressure	1 atm
	Fluid type	Air at 25°C
	Turbulence Model	k-Epsilon
Boundary condition	Wheel	No Slip; Rotating wall: 3175 rev/min; Rotation Axis: z Axis; Wall roughness: 1 [mm]
	Opening wall	Relative Pressure is 0 [Pa]

Steady state simulations are those whose characteristics do not change with time and whose steady conditions are assumed to have been reached after a relatively long time interval.

Regions of fluid flow and/or heat transfer in ANSYS CFX are called domains, in which the equations of fluid flow are solved. The type of the fluid can be defined within the region. In this simulation, the space between the wheels surface and the cuboid surfaces is defined as the domain. Single domain means only one type of fluid is defined in the simulation. The stationary domain is not permitted to move relative to the local boundary frame.

The Reference Pressure is the absolute pressure datum from which all other pressure values are taken. All relative pressure specifications in ANSYS CFX are relative to the Reference Pressure. It was set to be 1 atm in this simulation. Due to the air boundary layer simulation, the fluid in the domain was specified as the air at 25°C. The fluid turbulence model was the k-Epsilon turbulence model, a commonly used model, suitable for a wide range of applications.

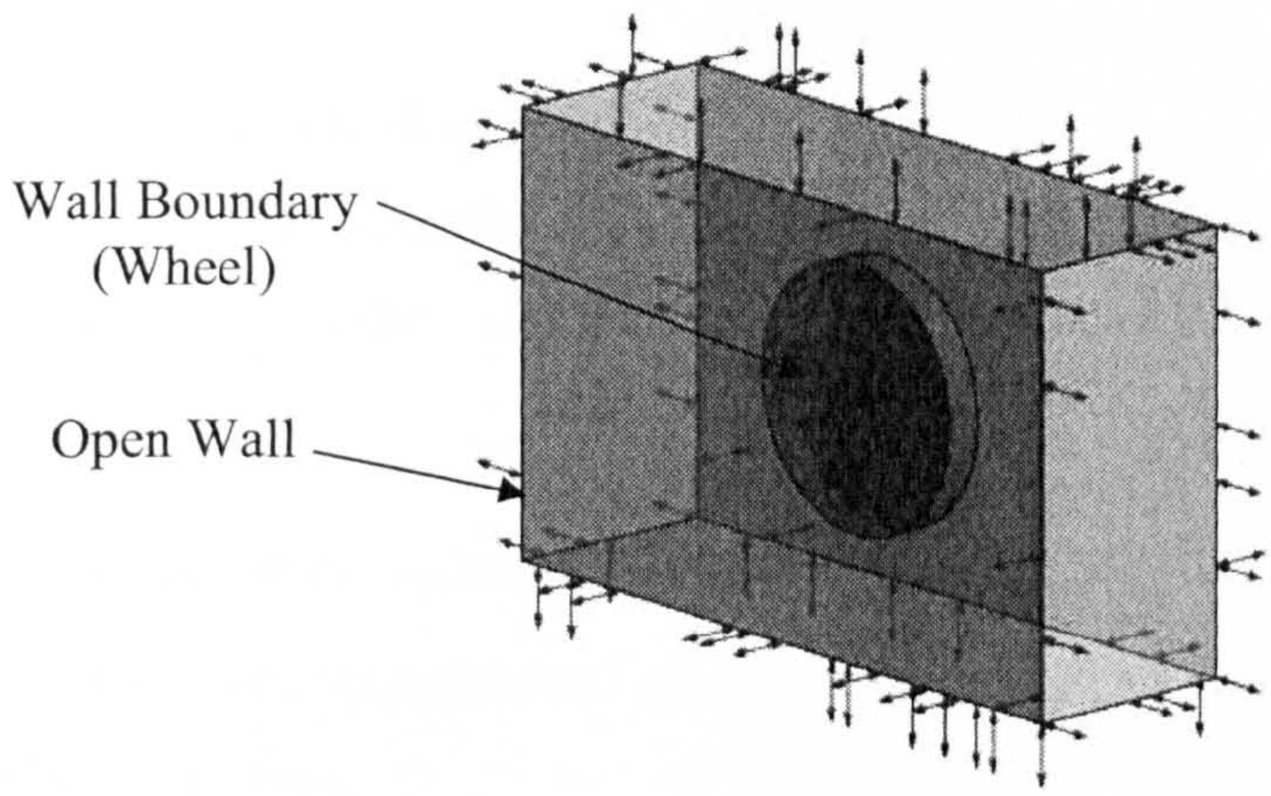

Figure 7-4 Boundary setup

Boundary conditions must be applied to all the bounding regions of the domain. Boundary conditions can represent inlets, outlets, openings, walls and symmetry planes. In this simulation, the Boundary condition setup is show in Figure 7-4. Two types of boundaries were defined: Wall and Opening wall. The Boundary types for the three

wheel surfaces were defined as rotating Walls; the six surfaces of the cuboid were defined as Opening Wall.

An Opening boundary condition allows the fluid to cross the boundary surface in either direction. The Wall boundary is an impenetrable boundary to fluid flow.

The 'No Slip' boundary condition means that the fluid at the wall boundary moves at the same velocity as the wall. The wheel speed was set to be 3175 rev/min in this simulation, the same as in the experiments.

The roughness height specified is the equivalent sand-grain roughness; this is not exactly equal to the real roughness height of the surface under consideration. Wall friction depends not only on roughness height but also on the type of roughness (shape, distribution, etc.), therefore, the appropriate equivalent sand-grain roughness needs to be determined by the experience.

After the CFX-Pre parameters are set up, the CFX-Pre file can be imported to the CFX-Solver to solve for all the solution variables of the simulation.

7.4 Simulation results and discussion

This section describes the simulation results of the air boundary velocity. These results (including the pictures and other data) were extracted from ANSYS CFX-Post.

7.4.1 Three components air velocity distributions

The simulation results and experimental results on the air boundary velocity distribution are compared in this section.

The velocity contours of the tangential velocity are shown in Figure 7-5. The cut areas of simulation are the same as those in the experiments. Comparison with experimental results, i.e. Figure 6-10, Figure 6-11, and Figure 6-12, shows that the simulation results are close to the experimental ones.

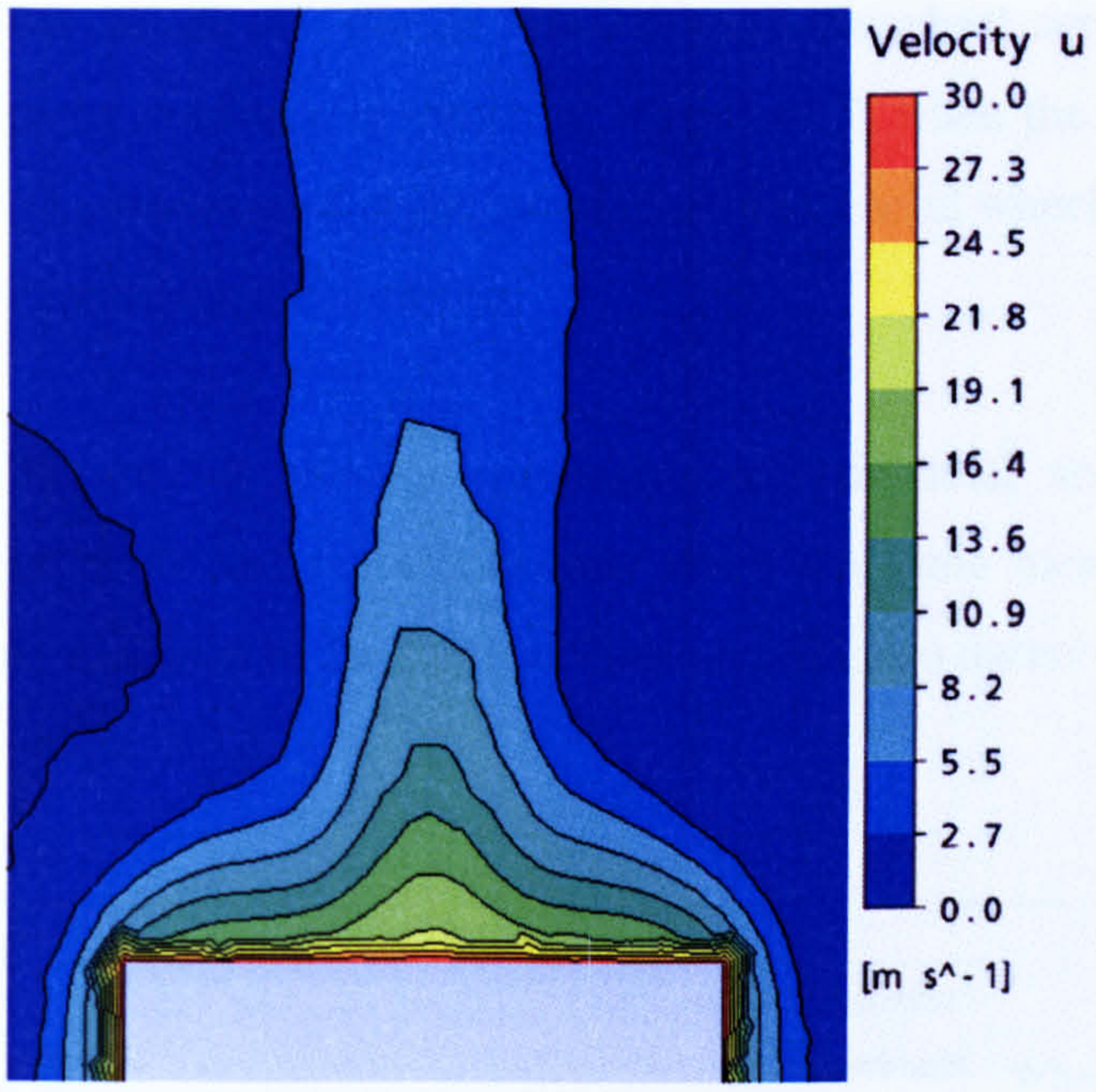

Figure 7-5 V_t simulation velocity contour (wheel speed = 30 m/s)

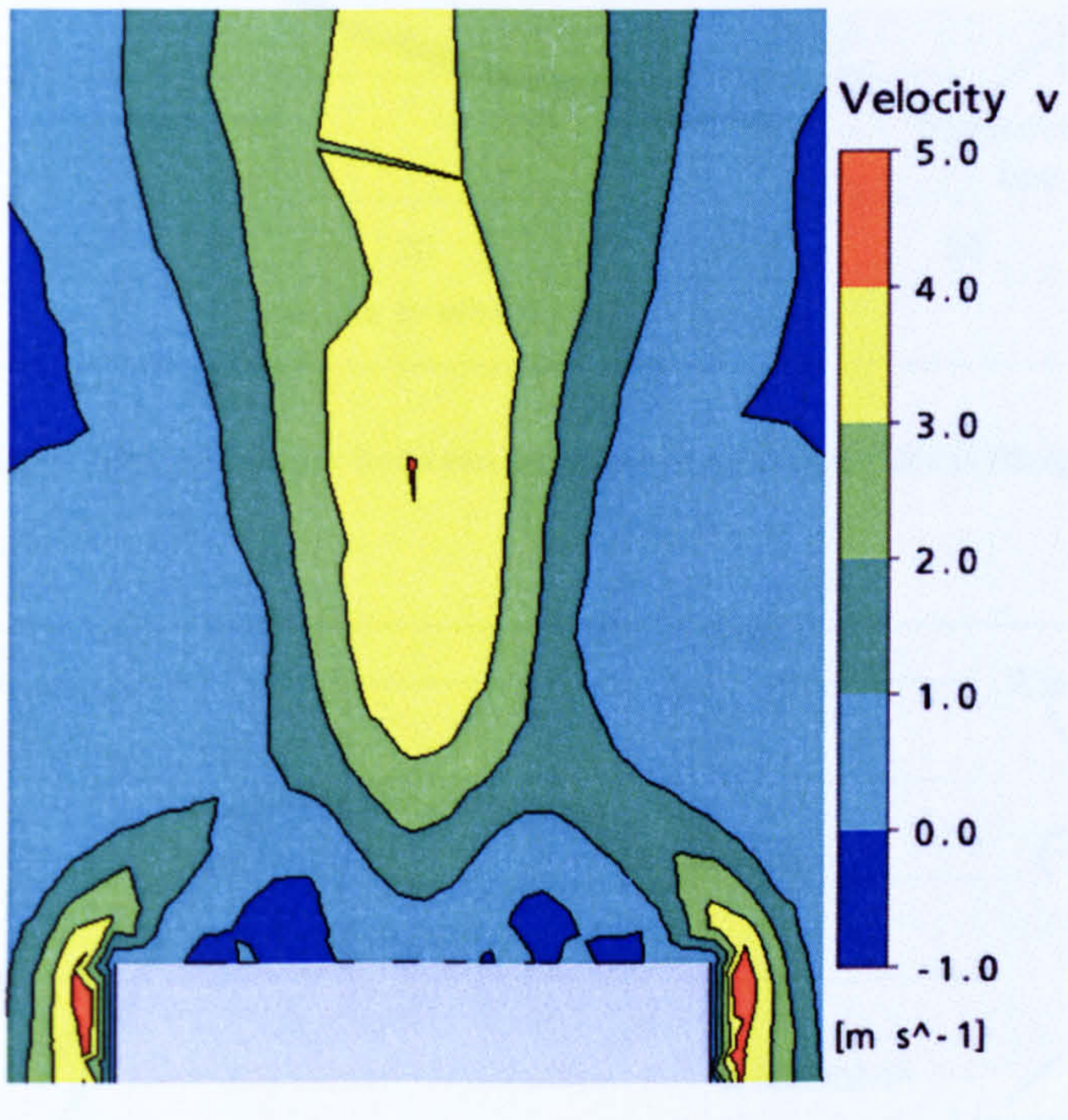

Figure 7-6 V_r simulation velocity contour (wheel speed = 30 m/s)

The radial velocity contour plot is shown in Figure 7-6. This result agrees well with the experimental results shown in Figure 6-15, Figure 6-16, and Figure 6-17. It needs to be pointed out that, the value of the radial velocity is negative in some areas close to the

wheel surface. This means that the air flows toward the wheel surface. This result is similar to the experimental results shown in Figure 6-27, when the wheel surface was covered by tape. The wheel used in the simulation was a solid wheel, so the situation is very close to the experimental conditions.

Figure 7-7 and Figure 7-8 show a comparison of tangential and radial velocities between the experiments and the simulations along the same measurement line (the position of the line is shown in the figures. These results also agree with the theoretical results shown in section 5.3.3.

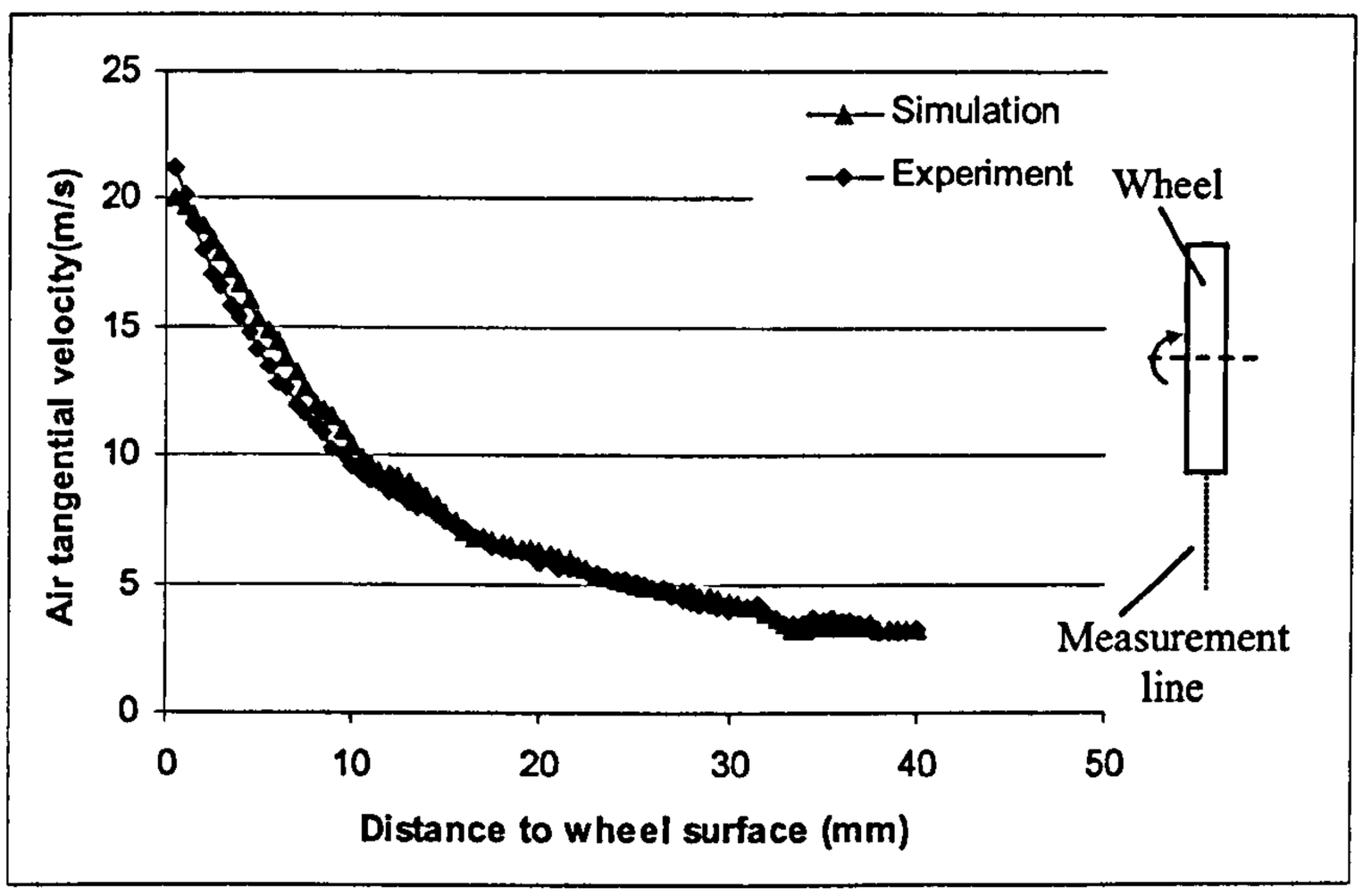

Figure 7-7 Comparison of results between simulation and experiment (tangential velocity)

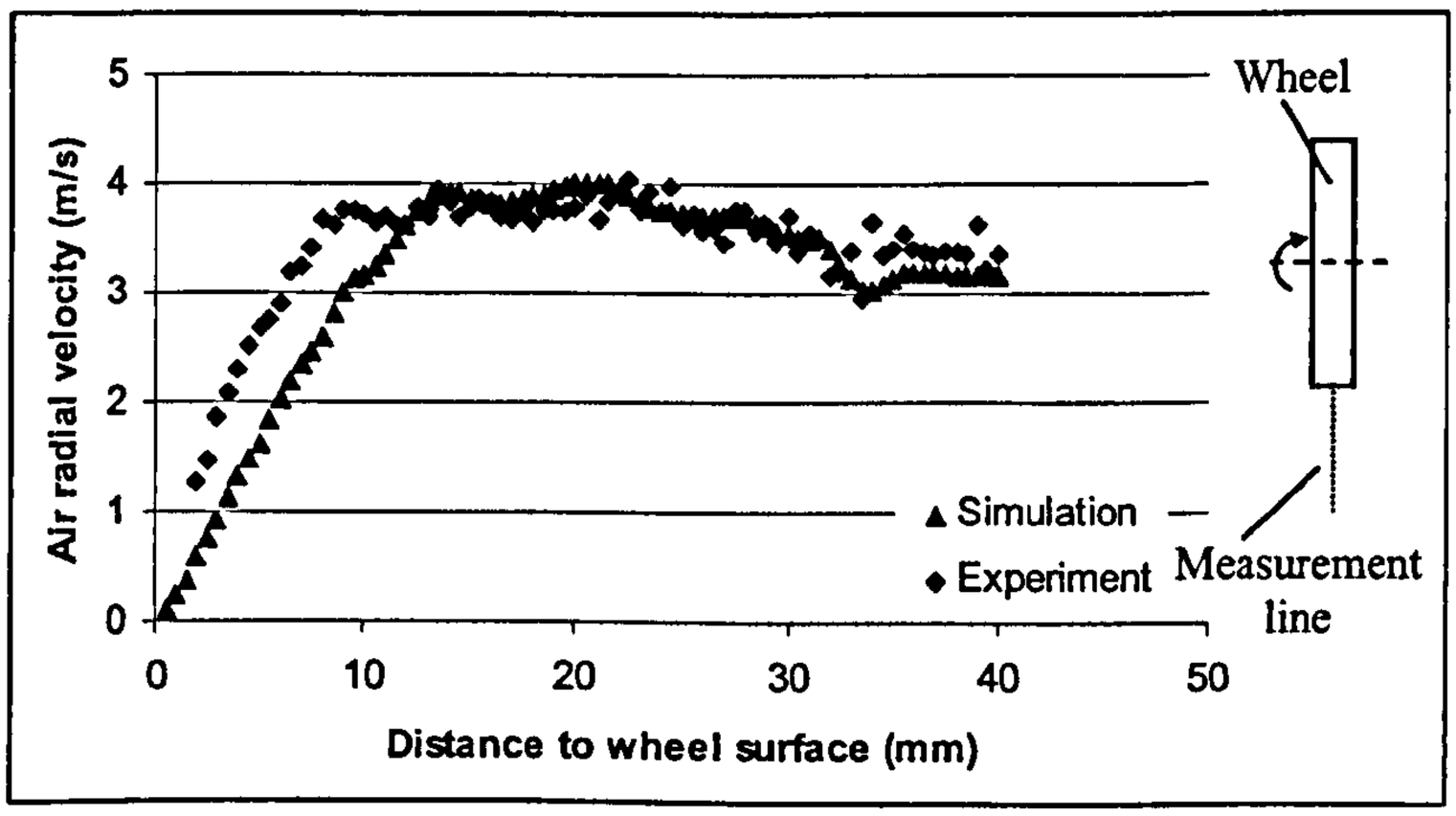

Figure 7-8 Comparison of results between simulation and experiment (radial velocity)

Figure 7-9 shows the air flow direction in the measurement area. Figure 7-9(a) is the experimental result and Figure 7-9 (b) is the simulation result. These give the air flow on a plane, through the wheel axis. Explanations about the air flow have been given in Section 6.4.3.

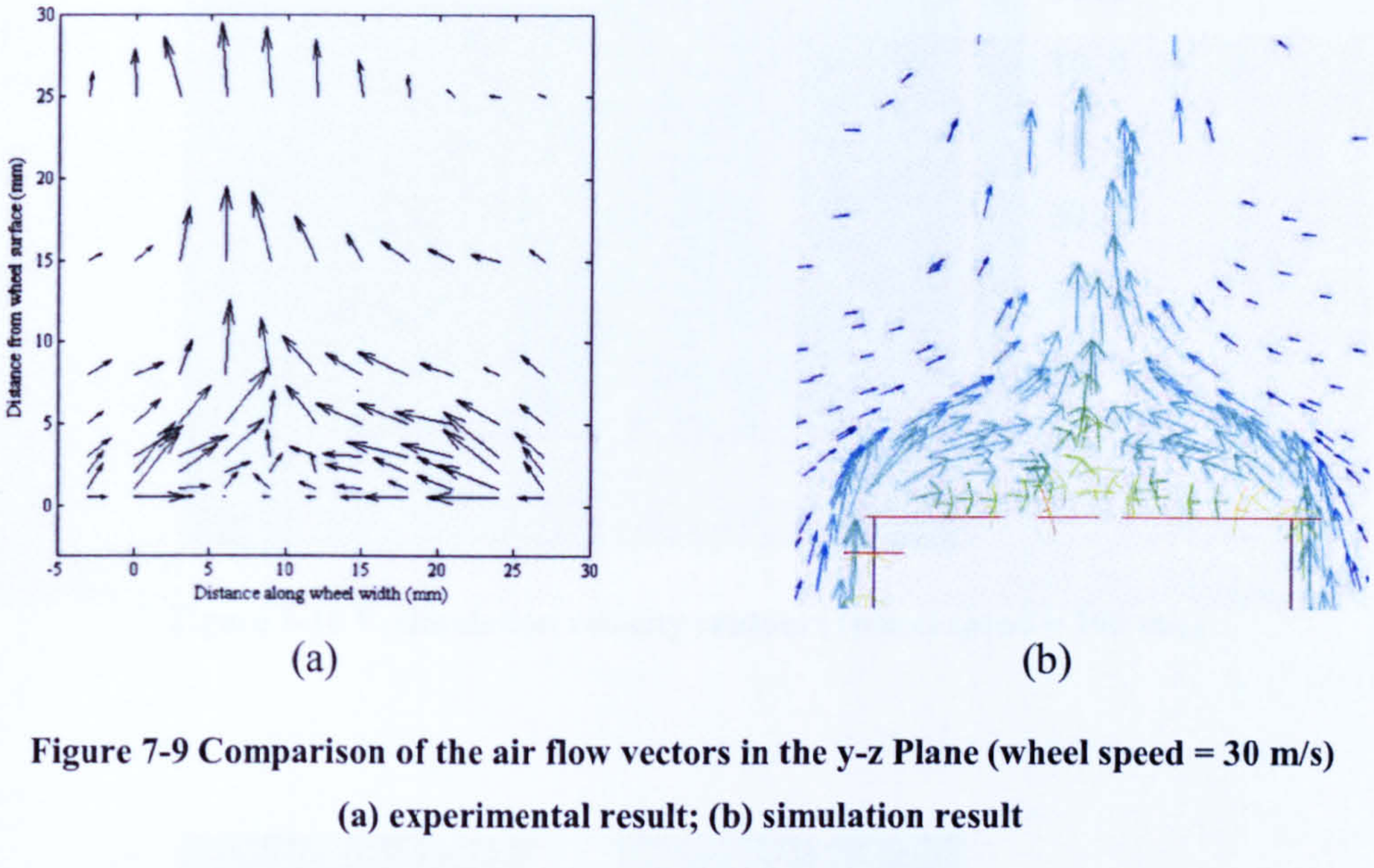

(a) (b)

Figure 7-9 Comparison of the air flow vectors in the y-z Plane (wheel speed = 30 m/s)

(a) experimental result; (b) simulation result

The above figures show that the simulation results agree very well with the experimental results. Therefore, the CFX simulation can confidently be used to investigate the air boundary layer in situations, where the experimental method cannot be applied.

7.4.2 Air velocity with high wheel speed

Figure 7-10 shows the air tangential velocity contours with the 100 m/s wheel speed. Comparison of Figure 7-10 with Figure 7-5, shows that the tangential velocity contours are similar but the velocity values are different, although the wheel speed increased from 30 m/s to 100 m/s.

The simulation results also show that the radial velocity distribution (Figure 7-11) and axial velocity distribution of air flow have the same characteristics.

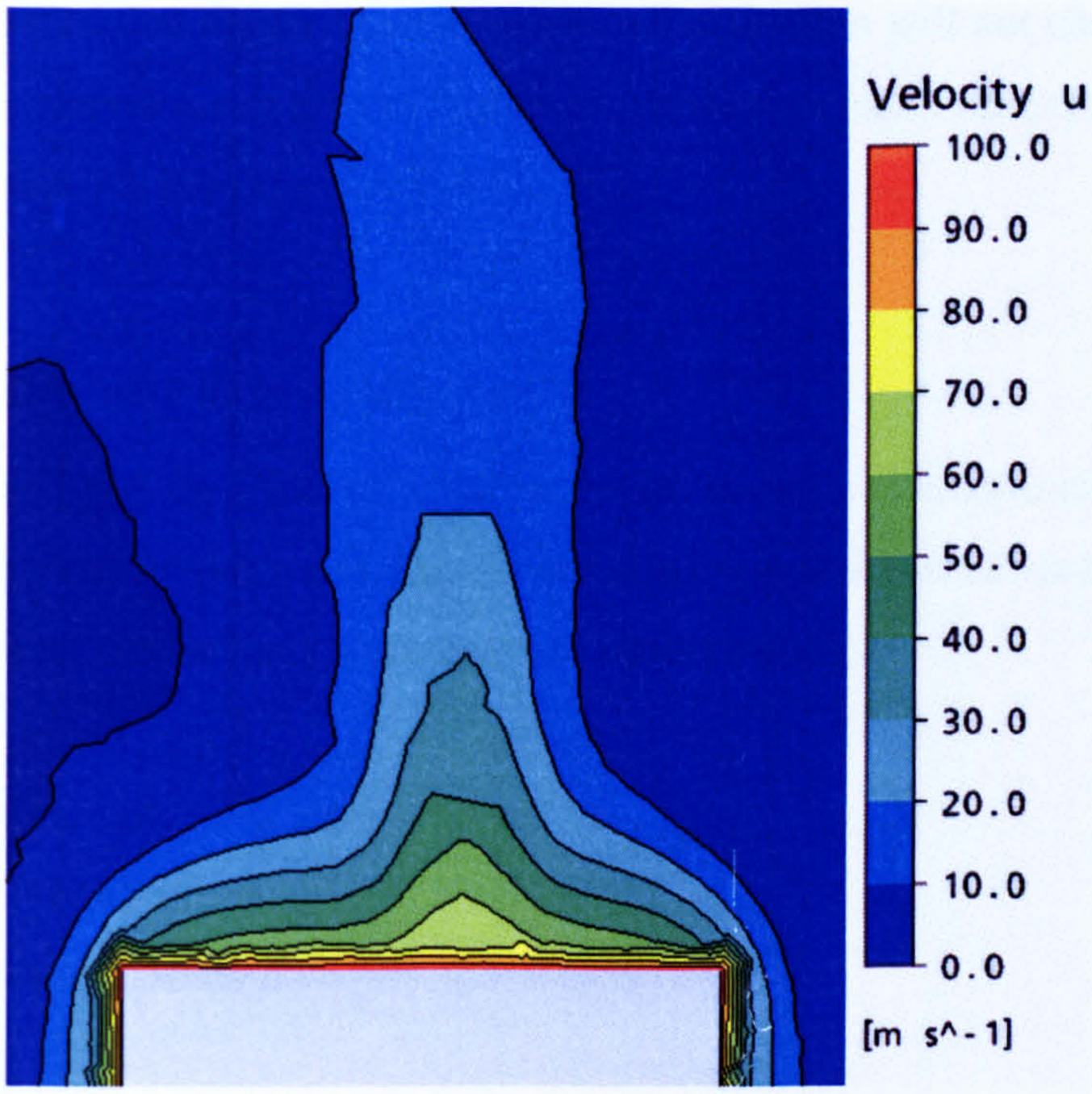

Figure 7-10 V_t simulation velocity contours (wheel speed = 100 m/s)

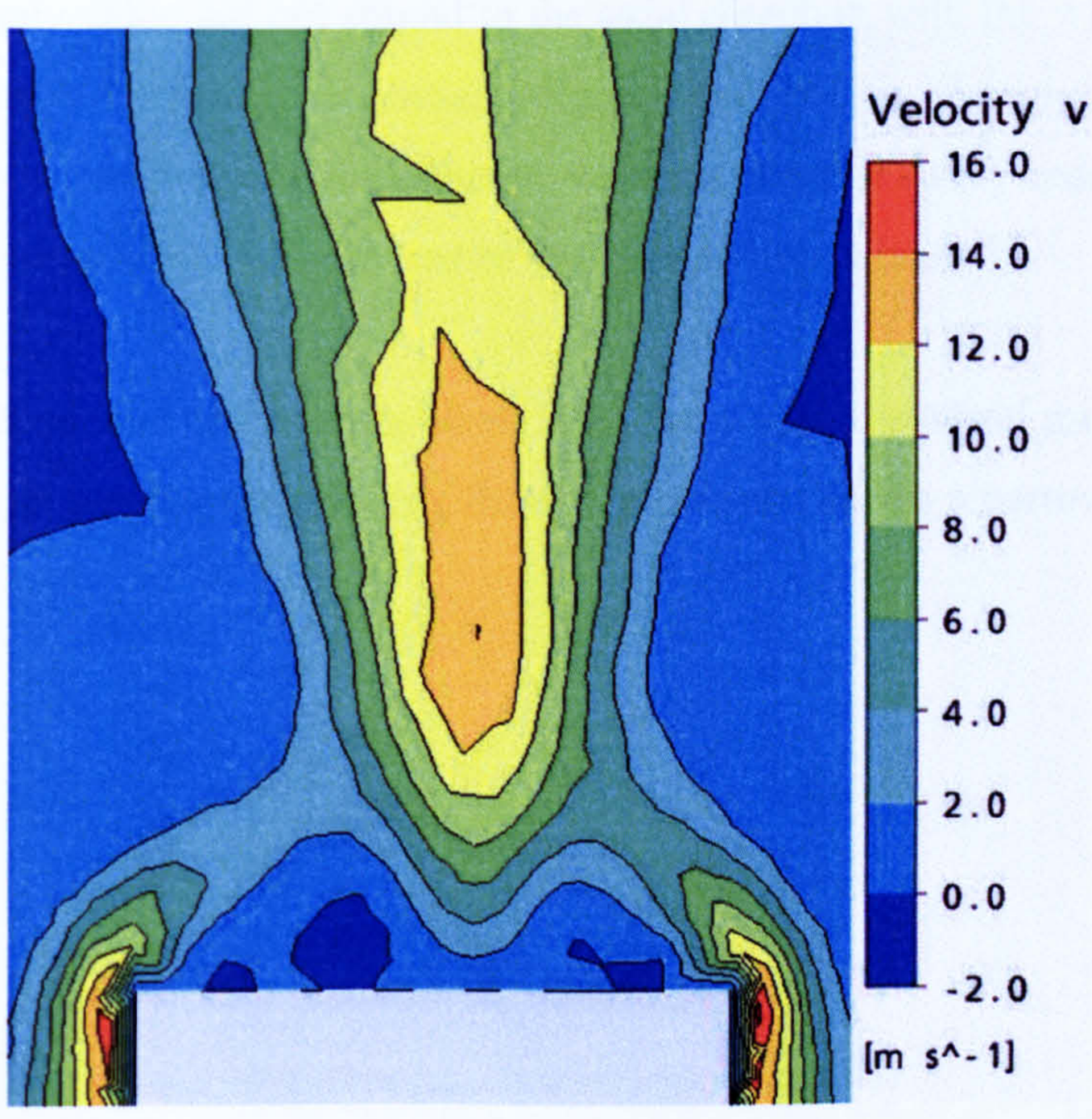

Figure 7-11 V_r simulation velocity contours (wheel speed = 100 m/s)

It can be concluded that the air velocity contour distribution will not change with wheel speed. This simulation result also validated the prediction based on experimental results shown in Figure 6-22. (See Chapter 6.4.5)

7.4.3 Air velocity with different wheel width

In order to investigate the affect of wheel width on air velocity distribution, a simulation with a different wheel width was carried out (this test was not carried out on the real grinding machine). The wheel parameters are shown below:

- Wheel Diameter: 180 mm;
- Wheel Width: 50 mm;
- Wheel Speed: 30 m/s.

The simulation results are shown in Figure 7-12 (air tangential velocity distribution) and Figure 7-13 (air radial velocity distribution). The air tangential velocity distribution is similar to the results of the simulation with the 25 mm wide wheel. However, the peak of the air velocity value did not spread in the axial direction with the wider wheel. This produced a much narrower tangential velocity distribution. Away from the wheel middle section to two wheel flanks, the air velocity decreases very quickly. The radial velocity distribution was similar to that of the 25 mm wide wheel.

This means that even if the grinding wheel becomes wider, the wheel middle area is still the most difficult area for the grinding fluid to penetrate. This is a narrow area whatever the wheel width.

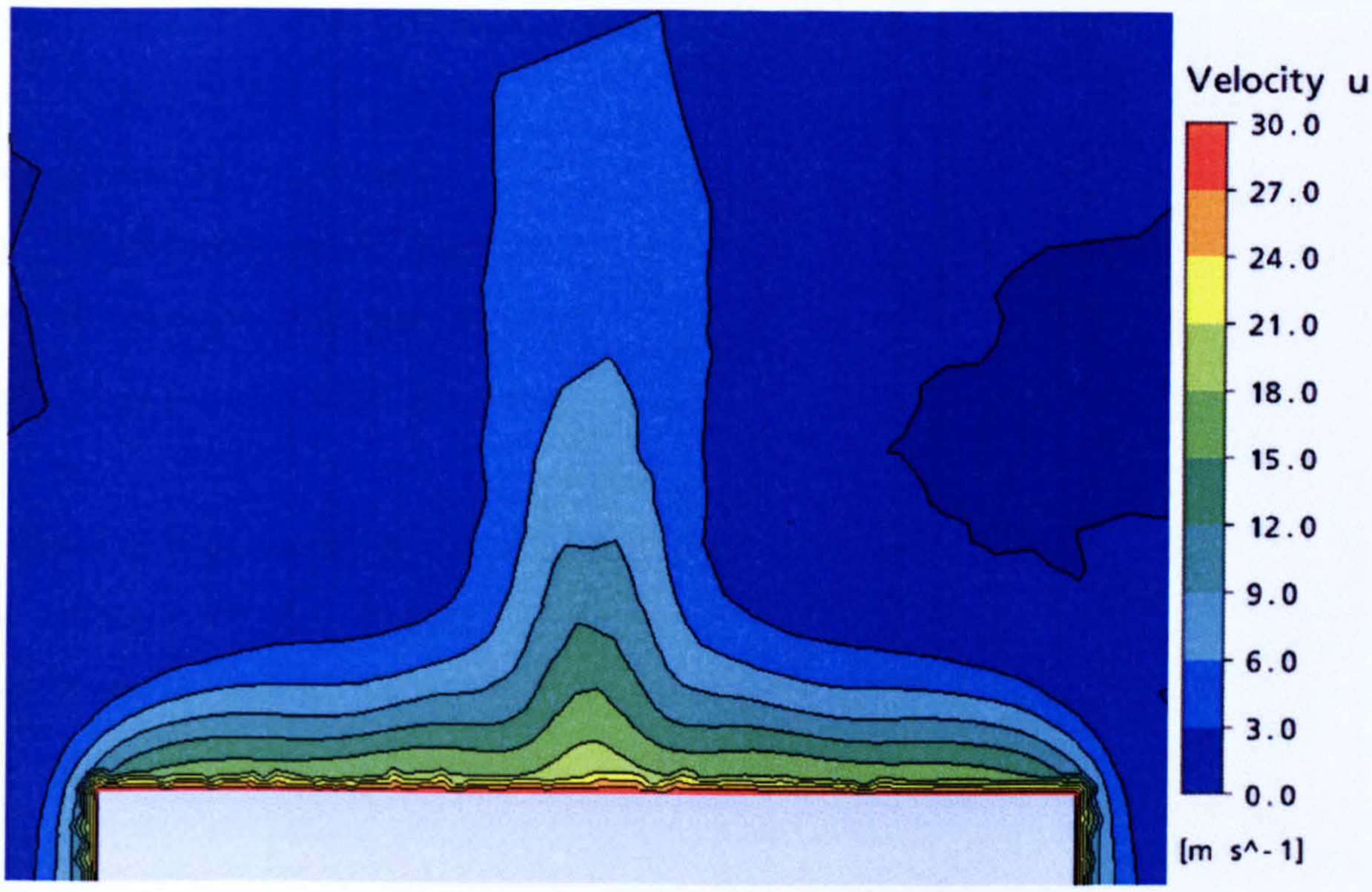

Figure 7-12 V_t simulation velocity contours (wheel width= 50 mm; wheel speed = 30 m/s)

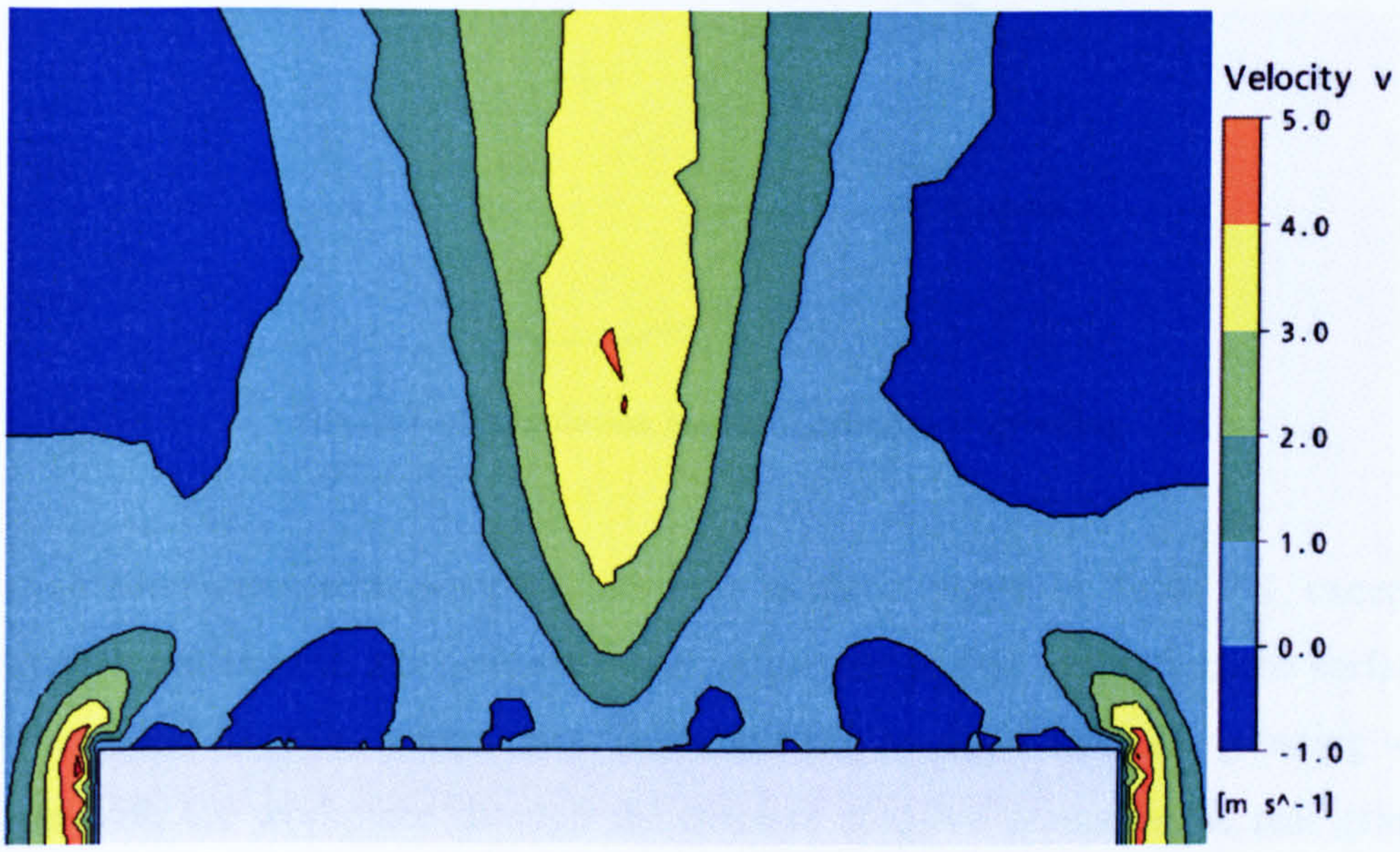

Figure 7-13 V_r simulation velocity contour (wheel speed = 30 m/s)

7.4.4 Air velocity distribution on cylindrical grinding

Another simulation was carried out within the cylindrical situation to investigate the air flow velocity and air pressure distribution around the grinding wheel and the workpiece. The simulation model is shown in Figure 7-14. The grinding parameters used in this simulation are shown below:

- Wheel Diameter: 400 mm
- Wheel Width: 50 mm
- Wheel Speed: 40 m/s
- Workpiece Speed: 15m/min
- Workpiece Diameter: 40 mm
- Workpiece Length: 80 mm

The simulation geometry is shown as follows:

- Cuboid Width: 150 mm
- Cuboid Length: 700 mm
- Cuboid Height: 600 mm

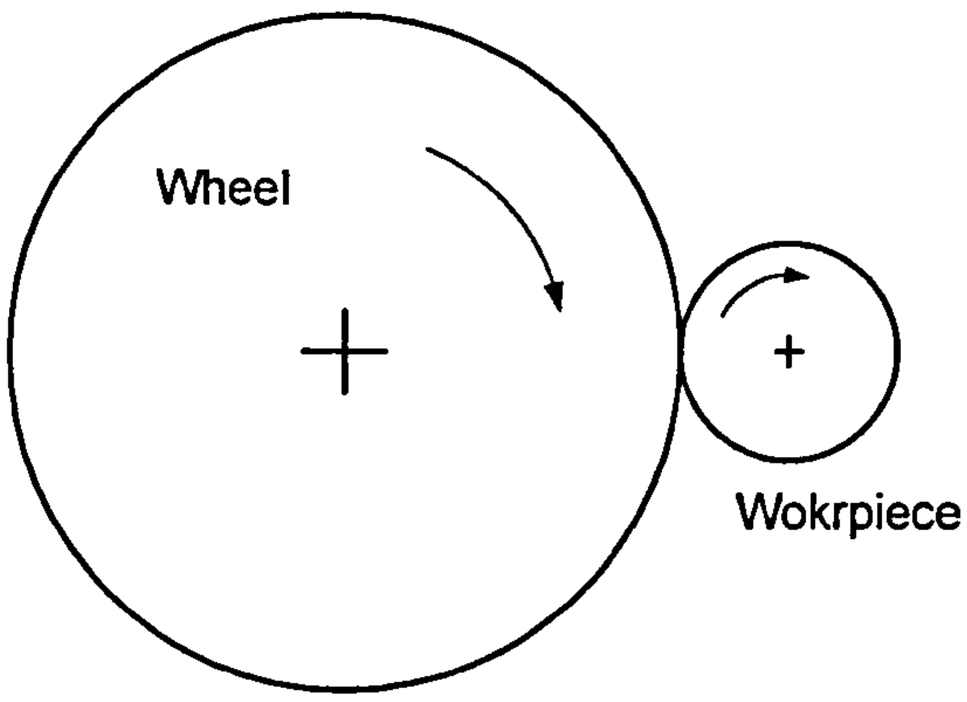

Figure 7-14 Simulation model of cylindrical grinding

The simulation parameters were set the same as those shown in Table 7-1, except for the wheel speed and the workpiece surface roughness. In this simulation, the surface of the workpiece was set as a smooth surface and with 'no slip'. Since the grinding wheel interacts with the workpiece through the discrete abrasive grains in the real grinding situation, the wheel and the workpiece cannot be set as touching in the simulation. There is a 0.1 mm gap between the wheel and the workpiece in this simulation.

Figure 7-15 gives the air velocity distribution around the grinding contact zone on a cross section through the middle of the wheel, where the air velocity is highest. The air velocity shown in Figure 7-15 is the air resultant velocity in this plane.

It is apparent that the air velocity is very high close to the wheel surface, but close to the grinding contact zone, the air velocity becomes very low relative to the wheel speed (40 m/s), no matter what the velocity is in the grinding entry zone or the grinding exit zone. There is no significant air flow around the workpiece because of the low speed, although it blocks the air flow on the wheel surface.

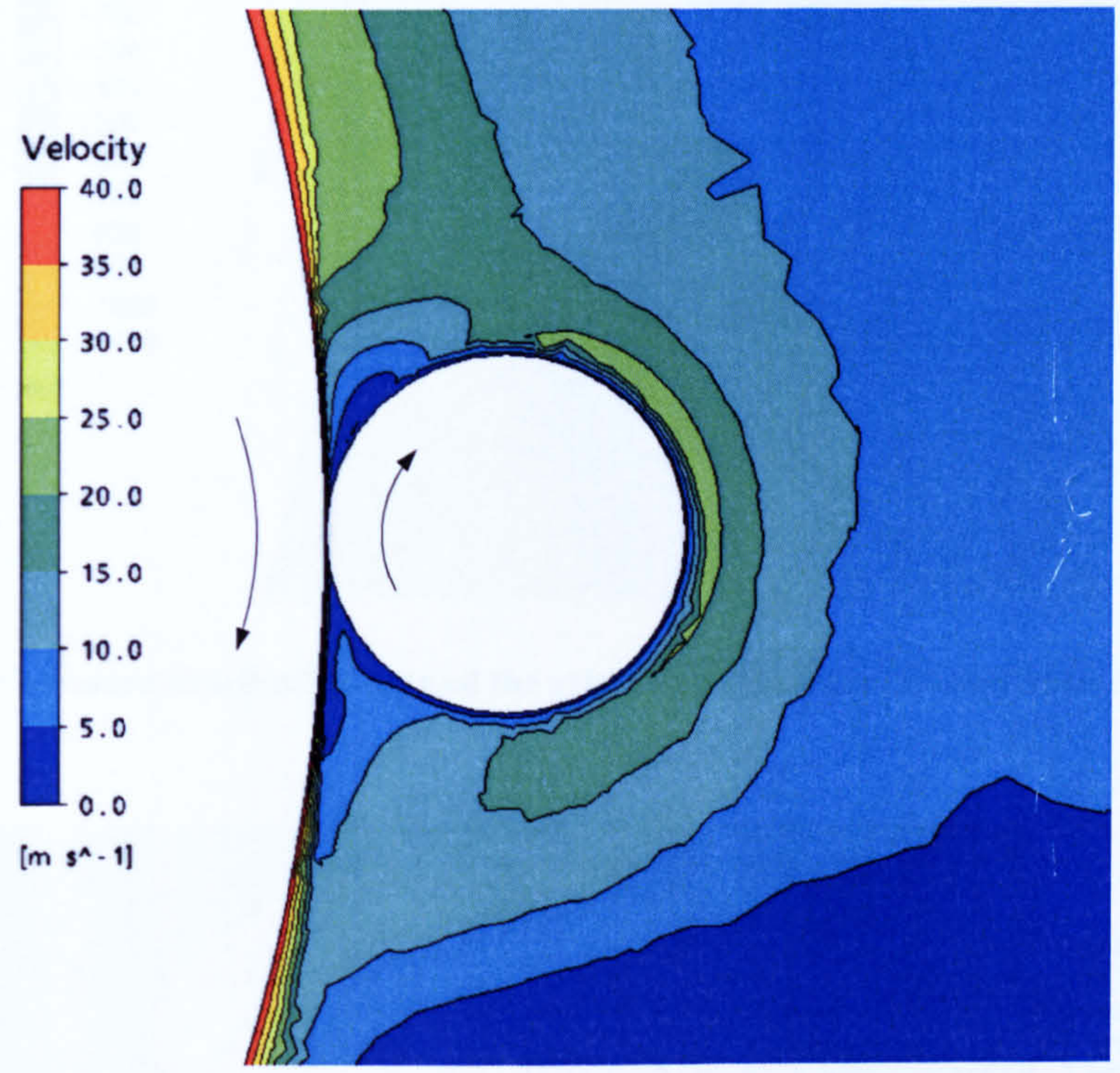

Figure 7-15 Air flow velocity distribution around grinding contact zone

However, it does not mean that the fluid flow can be delivered to the grinding zone when grinding. Figure 7-16 shows the air pressure distribution around the grinding contact zone, in the middle section in wheel axial direction. It can be seen that the pressure is very high in the grinding contact entry region and very low in the grinding exit region. This phenomenon is shown more clearly in Figure 7-17, it was viewed in the plane through grinding contact zone. It is the high-pressure area that prevents effective fluid delivery in cylindrical grinding. After the contact area, the pressure reduces to a negative value.

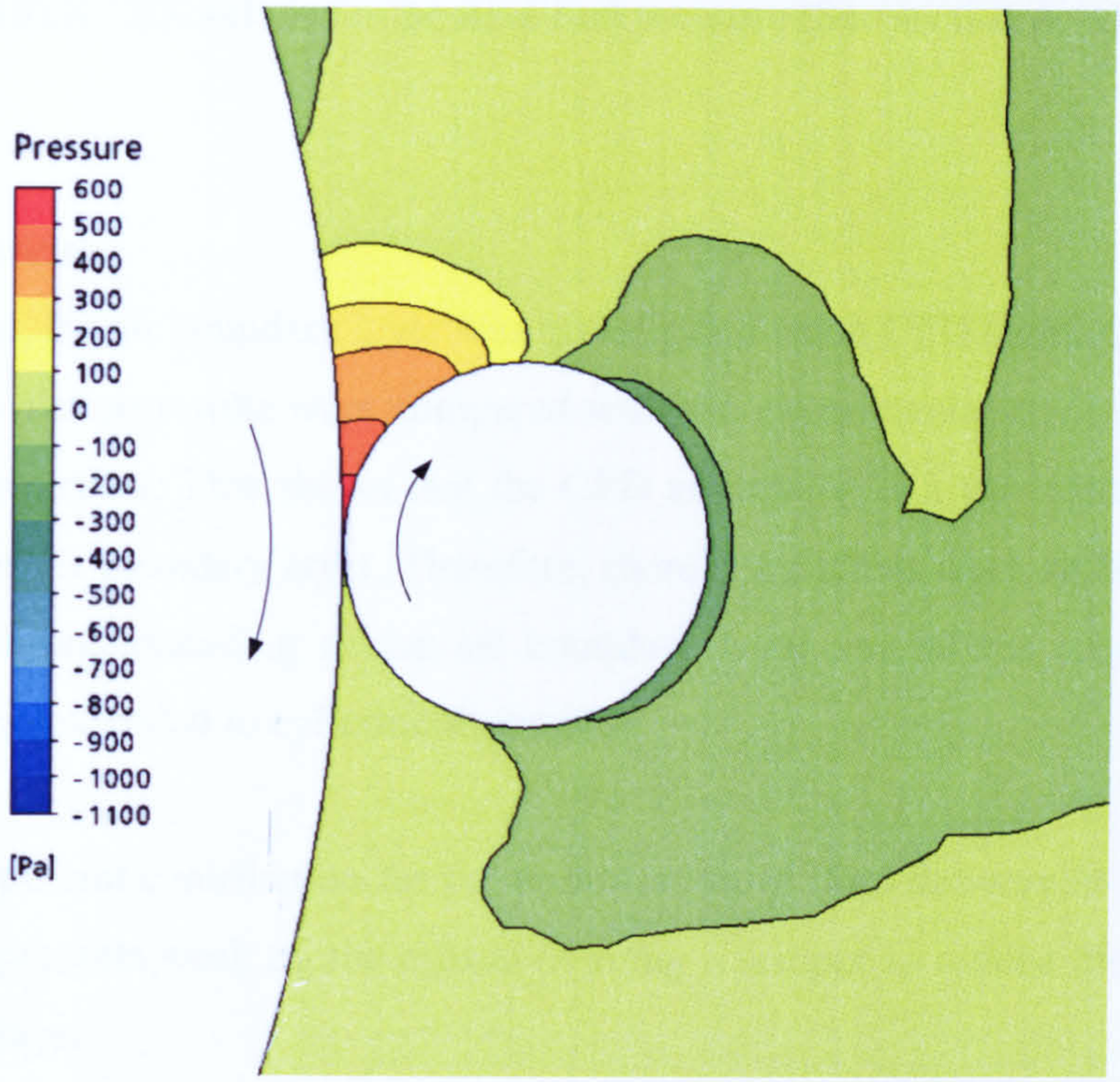

Figure 7-16 Air pressure distribution around the grinding contact zone (wheel axial direction view)

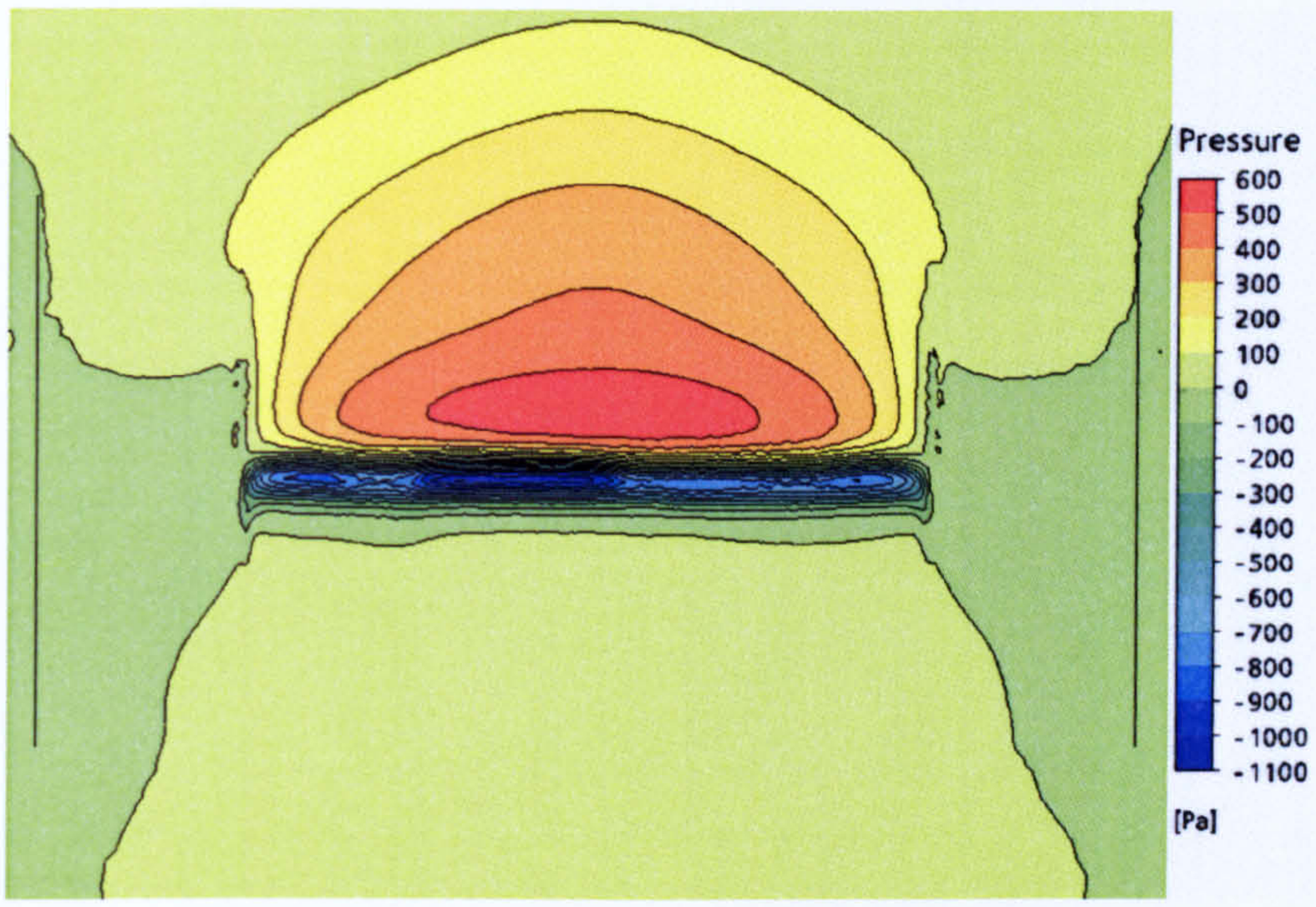

Figure 7-17 Air pressure distribution around the grinding contact zone (through grinding zone view)

The air pressure demonstrated here is the Modified Pressure (see equation 8.1) in ANSYS CFX. When the k-ε turbulence model is used, the fluctuating velocity components give rise to an additional pressure term to give the modified pressure. In

this case, ANSYS CFX solves for the modified pressure (See section 8.4.3 Pressure distribution).

7.5 Conclusions

In this chapter, the air boundary layer was investigated using CFD simulation. In section 7.4.1, the simulation results were compared with the experimental results in Chapter 6 with good agreement. This shows that the CFD simulation is a trustworthy method to investigate the air boundary layer. Therefore, more simulations were carried out further enhancing the understanding of the air boundary layer around the rotating grinding wheel; this was extended to cylindrical grinding.

This is an important contribution for the optimisation of fluid delivery in grinding. The next chapter presents work on the effects of suing a scraper to reduce the effect of the air boundary layer.

Chapter 8 Air Scraper Investigation in Grinding

8.1 Introduction

In Chapter 6 and Chapter 7, the air boundary layer around a rotating wheel without a workpiece boundary condition was investigated. The main work of the investigation was to obtain air velocity distributions for a range of conditions through experiment and simulations. The results of the work reported in the previous chapters help improve understanding of the nature of the flows so that requirements for effective penetration and minimising the effect of the air boundary layer effect could be established.

This chapter reports on the work concerned with the assessment of the ability of the air scraper to reduce the intensity of the air boundary layer. The difference from the work reported in the previous two chapters is that the experimental work includes a configuration with the workpiece in this chapter.

8.2 Air scraper application

Air scrapers of various shapes and dimensions have been used in industry and evaluated by various investigators.

Work by Trmal and Kaliszer (1976) showed some of the effects achieved when scraper plates are employed. They used a Pitot tube method to measure the velocity in the boundary layer. A decrease in air velocity was found to occur as the scraper plate was moved towards the wheel periphery. They concluded that the scraper plate could be used to effectively divert the air flow rotating with the wheel before the cutting fluid approaches the cutting zone, though issues with location and angle were identified.

This approach is supported by Campbell (1995) who investigated the hydrodynamic pressure at the wheel-workpiece interface caused by the passage of cutting fluid beneath the wheel. At a critical wheel speed, this pressure measured zero, i.e. the boundary layer of air was preventing cutting fluid from passing beneath the grinding wheel. Introducing a scraper plate allowed the grinding wheel speed to be increased by 20% before the hydrodynamic pressure again measured zero.

The use of a scraper plate to deflect the boundary layer reduces the effect of the air barrier, but does not completely overcome the problem even at low speeds. The boundary layer quickly re-establishes itself within a short distance of the scraper plate, so it is important to place the scraper in the boundary layer just upstream and as close as possible to the nozzle. Generally, cutting fluid distribution improves with reduction in the gap between the wheel and the scraper plate. At the same time, however a small gap may require frequent adjustments due to wheel wear and therefore may not be very practical in actual industrial conditions. This is particularly so in the case of high material removal operations with conventional abrasives.

Although previous research has presented results to show how the scraper can affect the air boundary layer and fluid delivery, it is still to be demonstrated how to apply the air scraper to obtain optimal fluid delivery. In this Chapter, the research will focus on the scraper application. Investigation of the effect of the scraper on the air velocity and pressure distribution is reported. A knowledge of these distributions provides the basis for strategies to ensure maximum penetration of the fluid.

8.3 Air scraper experiments (air velocity distribution)

The aim of the work presented in this section was to obtain velocity distributions of the air boundary layer in the grinding entry region using LDA for the real grinding situation under varying scraper configurations.

8.3.1 Experimental arrangements

The Abwood grinding machine (described previously in Chapter 6) was employed as the experimental test machine. The width of the workpiece was 40 mm. The air scraper was fixed on the wheel guard to break the air flow with facility to adjust the acraper position. The width of scraper was 30 mm, that is, 5 mm wider than wheel, and thickness was 1 mm. The scraper was set up parallel to the surface of the magnetic base, and the vertical height between scraper and the grinding contact zone was 43 mm (Figure 8-1). The position of the scraper could be adjusted in the horizontal direction and the gap (distance between the wheel surface and scraper) could be changed according to the demand of the experiment. The wheel speed was set to 30 m/s for all experiments reported in this chapter.

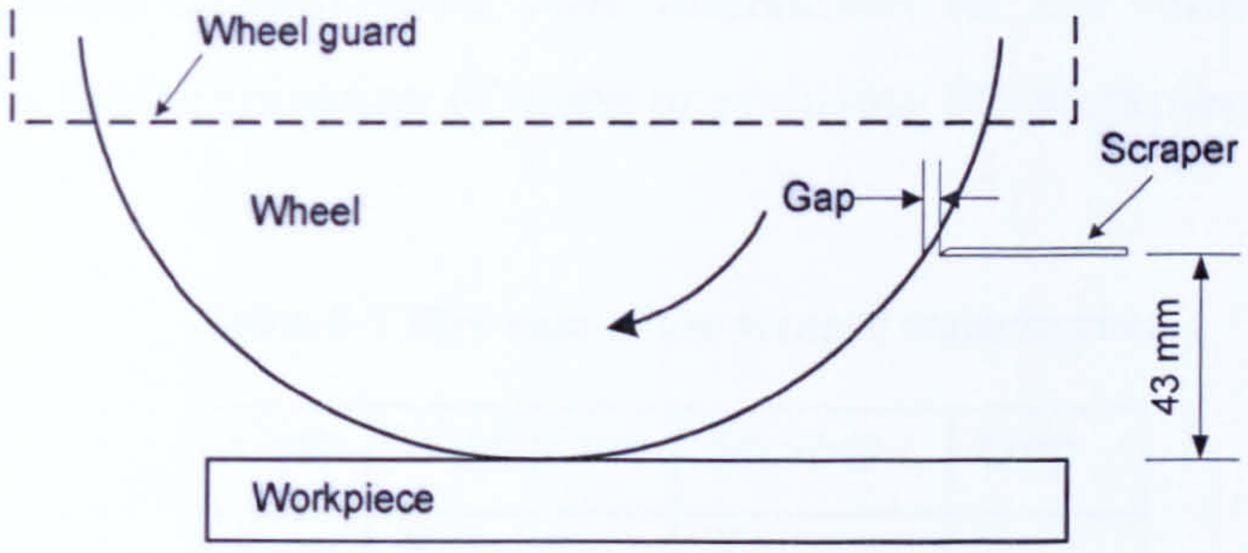

Figure 8-1 Position of the air scraper

The experimental arrangement is shown in Figure 8-2. The air velocity was measured in the area between the workpiece and scraper in the grinding entry region. The measurement plane was the middle section of the wheel since the highest air velocity occurs in this plane. The 2-D velocity was measured. The results were processed and the velocity vector distribution obtained.

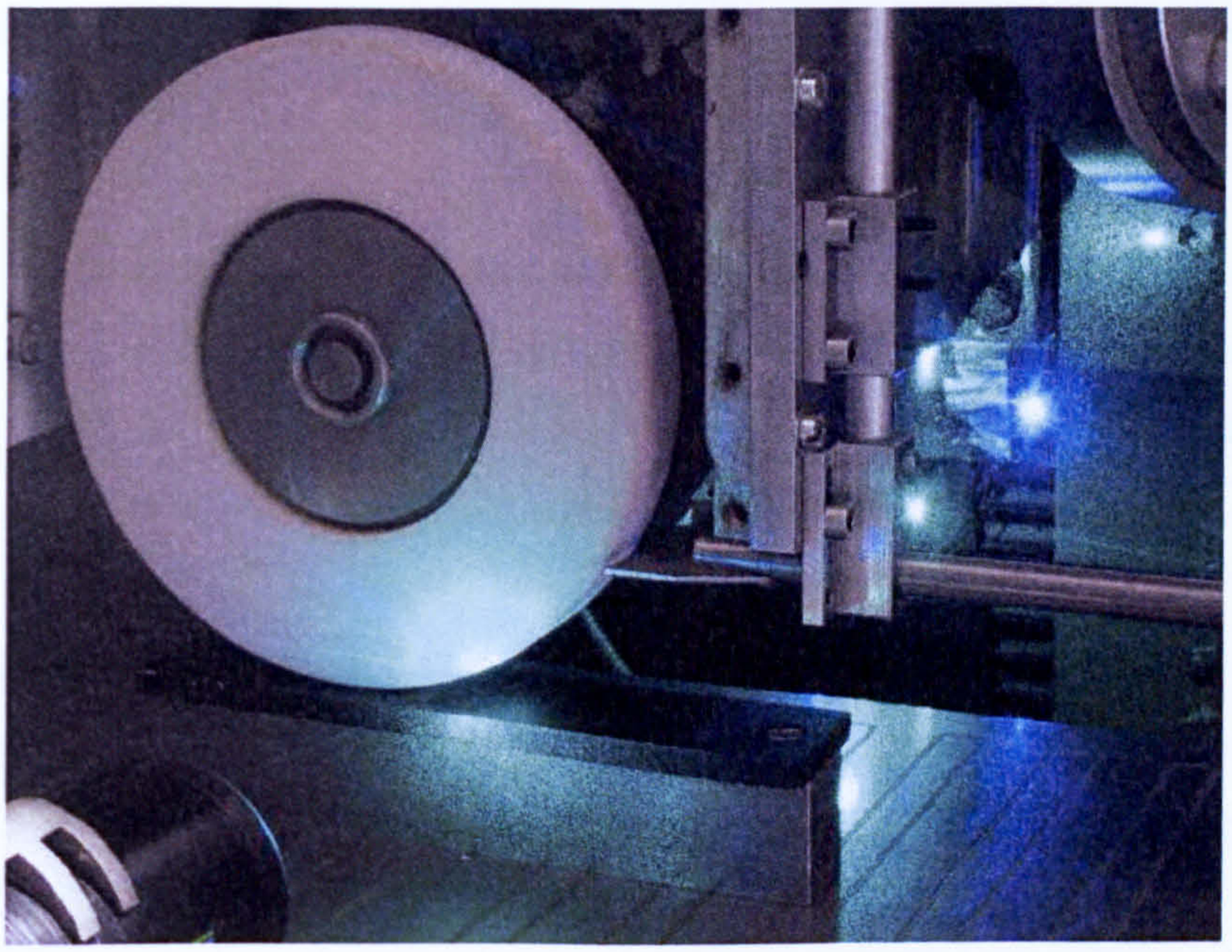

Figure 8-2 Experimental arrangement (air scraper tests)

8.3.2 Experimental results

Velocity distribution measurements were undertaken for the various cases (shown in Table 8-1, that is the combination of using or not using the workpiece and air scraper):

Table 8-1 Five case of the scraper experiments

Case	Workpiece	Scraper	Gap
1	X	X	
2	X	√	1 mm
3	√	X	
4	√	√	1 mm
5	√	√	3 mm

'X': not using; '√': using

The aim of measurement Case 1 was to obtain the velocity distribution without any external influences thus providing a benchmark for subsequent comparisons. When the scraper was used, its effect could be determined through a comparison of the two experimental results, Case 1 and Case 2.

The aim of measurement in Case 3 was to identify the air velocity distribution when the workpiece was put to use without the scraper (maintaining wheel and workpiece contact at the start of the measurement). When using the scraper, Case 4, the velocity distribution was measured in the real grinding situation.

The aim of measurement Case 5 was to determine the effect of the gap between the air scraper and the grinding wheel surface. A 1 mm gap was considered a safe distance to take account of the wheel expansion. It was also a practicable distance for experimental measurements.

Figure 8-3 to Figure 8-7 show the experimental results of Case 1 to Case 5 respectively. They are vector maps of the air velocity in the measurement area. In each figure, the lowest point of the wheel in the vertical direction was defined as the coordinate origin (0, 0). The x and y coordinates are distances from the origin. The vertical distance

between neighbouring measurement points is 2 mm, and the horizontal distance is 5 mm.

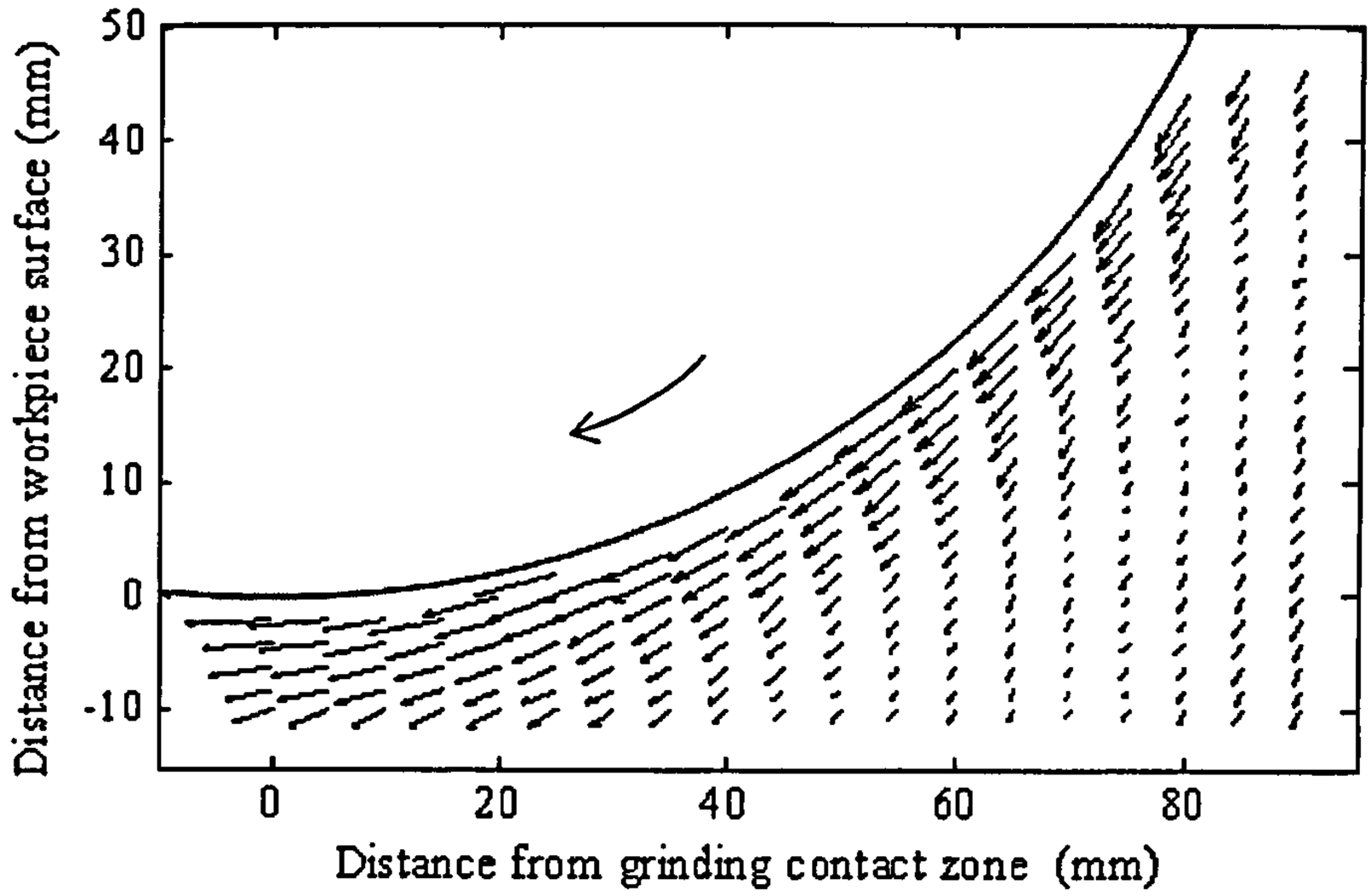

Figure 8-3 Air velocity vector map (Case 1: without workpiece and scraper)

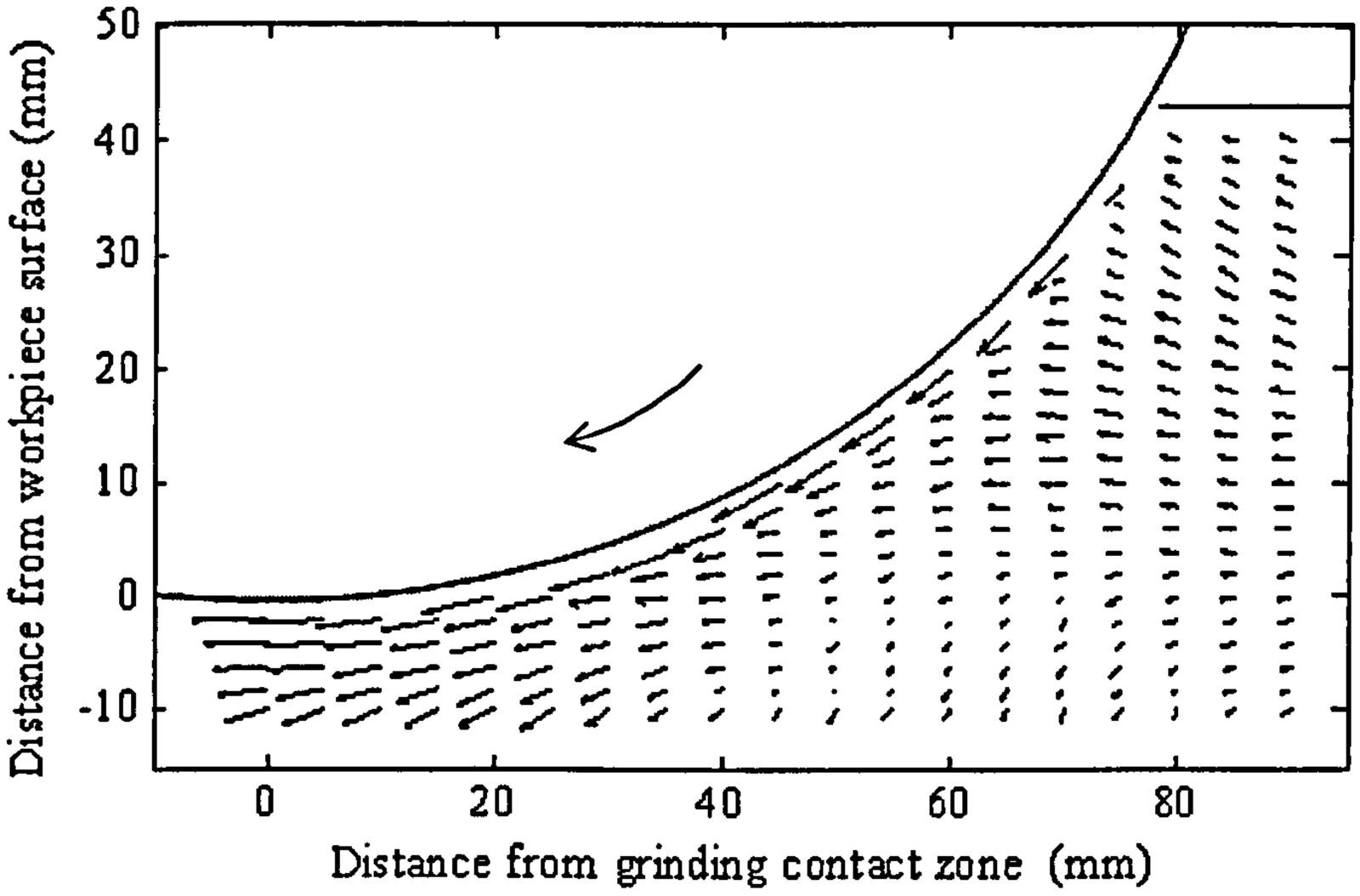

Figure 8-4 Air velocity vector map (Case 2: without workpiece but with scraper, Gap = 1 mm)

Figure 8-3 shows the velocity distribution around the rotating wheel without the workpiece or scraper. It is clear that the air velocity is much higher in the area approaching the wheel surface. In the direction away from the wheel surface, the air velocity steadily diminishes. This is the pure velocity distribution of the air boundary

layer, however, due to the effect of the wheel guard, the thickness of the air boundary layer does not have axial symmetry along the wheel surface.

Figure 8-4 shows the velocity distribution for the case when the air scraper was employed, and was placed 1 mm from wheel surface. The most significant difference from results of Figure 8-3 is that the velocity becomes very low in the area close to the air scraper, and the air boundary layer becomes much narrower compared to the case without the scraper. The direction of the air flow has also changed in the area below the scraper, from flow tangential to the wheel surface, to flow toward the wheel surface. Thus, the most apparent function of the air scraper - to break the air flow and weaken the air boundary layer is clearly identified using this technique.

One further point deserves to be mentioned: the velocity distributions are very similar in the area below the wheel surface, with or without the scraper (comparing Figure 8-3 and Figure 8-4). This implies that the air boundary layer can fully recover within some distance after the scraper. This issue is important for optimisation of fluid delivery and is discussed further later in this chapter.

From Figure 8-5 to Figure 8-7, the velocity of the boundary layer was measured in the real grinding situation. It was not necessary to make the workpiece moving because it usually moves with a very low speed relative to the wheel, that is: $v_w \ll v_s$.

Figure 8-5 shows the velocity distribution in the grinding contact zone without the scraper. The air boundary layer is still evident when the air flow is approaching the grinding contact zone. It is also noted that the air velocity distribution is similar to that in Figure 8-3, the introduction of the workpiece dose not have a strong effect, except in the immediate grinding contact zone.

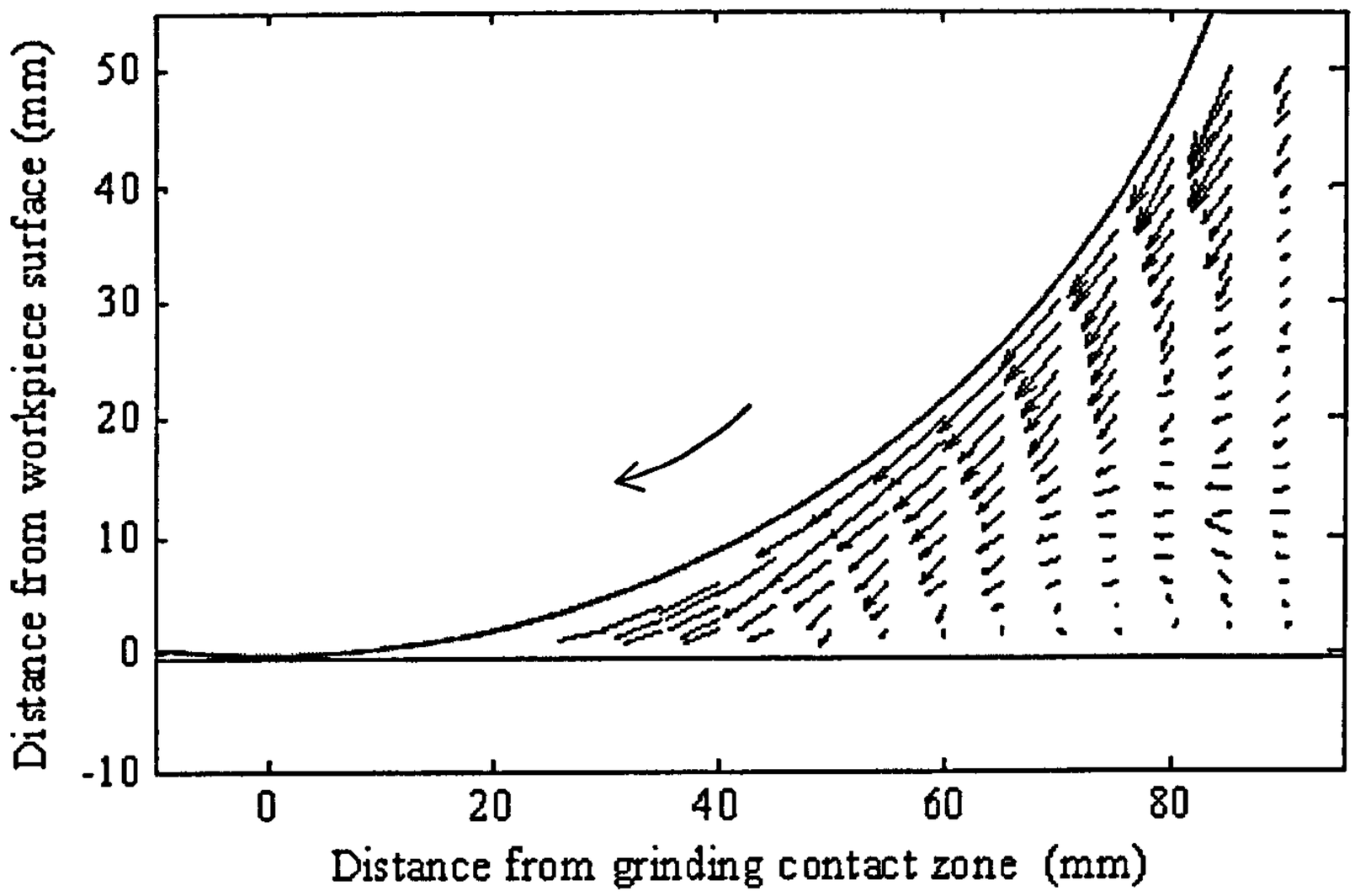

Figure 8-5 Air velocity vector map (Case 3: with workpiece but without scraper)

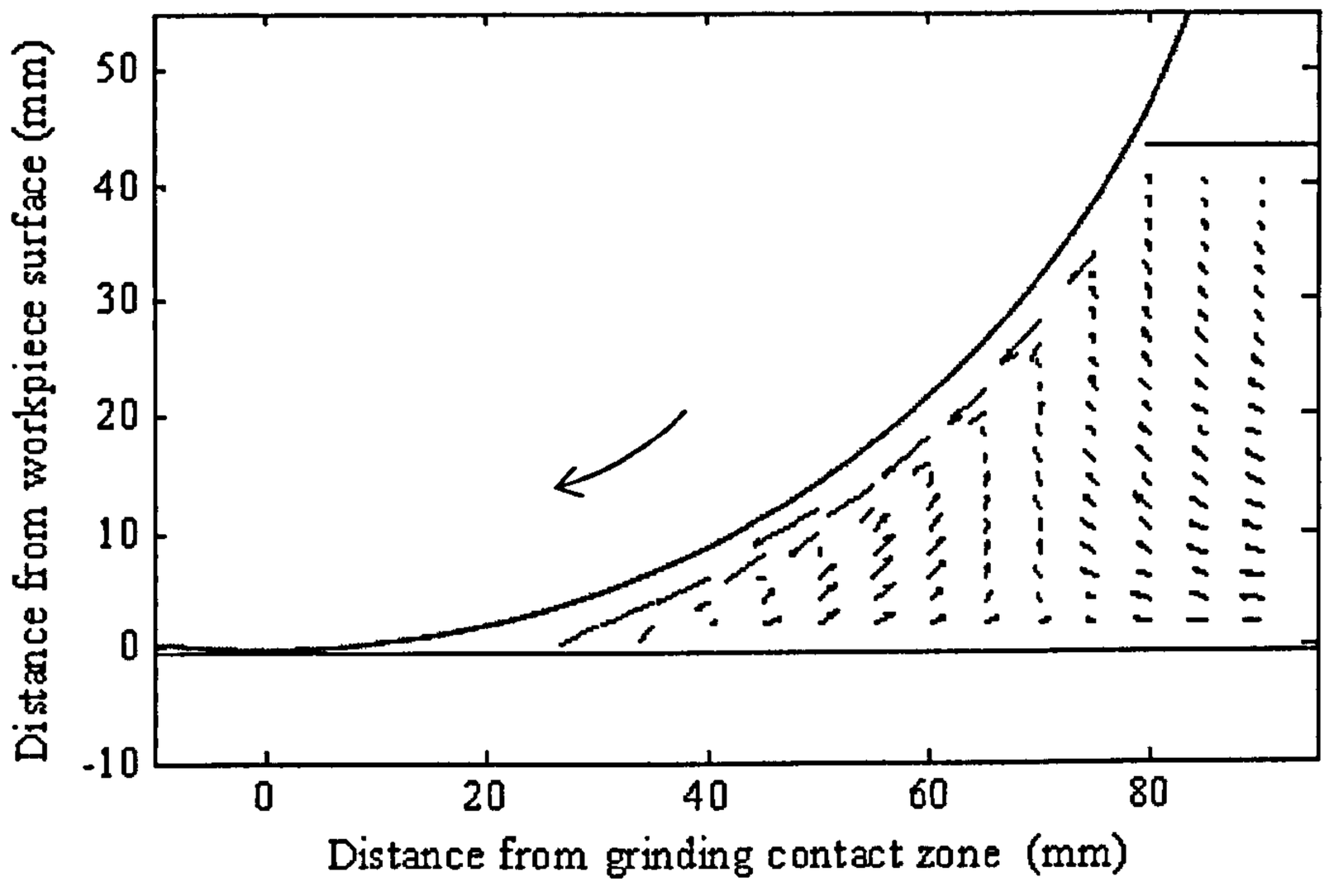

Figure 8-6 Air velocity vector map (Case 4: with workpiece and scraper, Gap = 1 mm)

However, when the air scraper was used with the gap of 1 mm from the wheel surface (Figure 8-6), the air flow was interrupted. The air boundary layer became quite narrow, and the air velocity decreased from the underbody of the scraper to the entry region. The air not close to the wheel surface flows with a low speed in the opposite direction back toward the scraper.

Figure 8-7 shows the air velocity distribution when the scraper is further from the wheel surface (the gap is 3 mm). The thickness of the air boundary layer increases when compared to the Case shown previously in Figure 8-6. It can be expected that the air boundary layer recovery will follow a similar pattern to that shown in Figure 8-5 with the gap increasing. Therefore, if the gap can be adjusted to a minimum within the practicable condition then the effect of the scraper on the air boundary layer will be maximised.

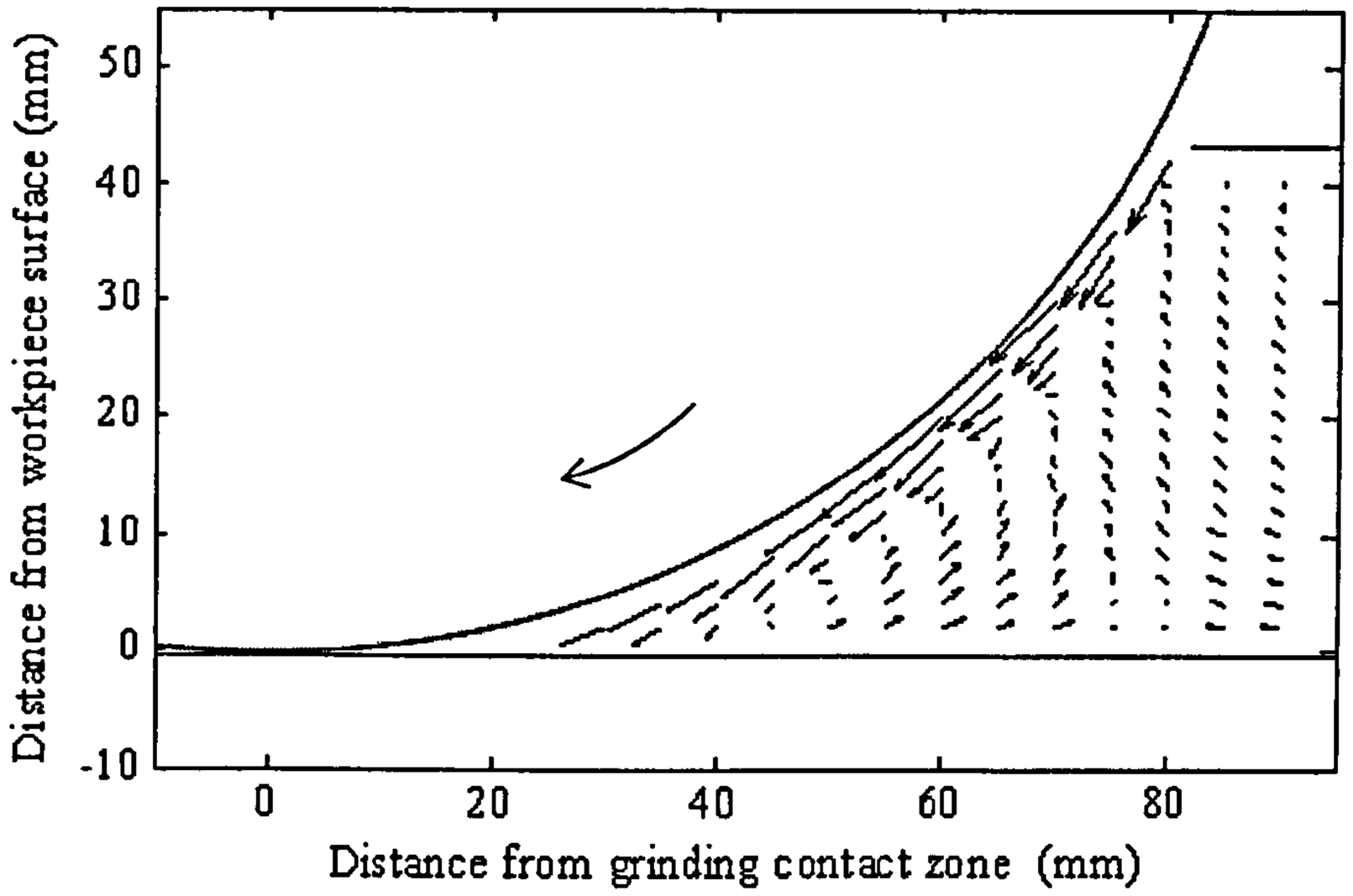

Figure 8-7 Air velocity vector map (Case 5: with workpiece and with scraper, Gap = 3 mm)

8.3.3 Discussion

Figure 8-3 and Figure 8-4 show the effect of the scraper on the air boundary layer in the case of not using a workpiece; Figure 8-5, Figure 8-6, and Figure 8-7 show the effect of the air scraper when using the workpiece). It is evident that the scraper can reduce the air velocity, thereby reducing the ability of the boundary layer to oppose fluid penetration. Thus, in order to ensure that the air boundary layer does not fully recover, the guidance is to position the nozzle close to the air scraper with conventional fluid delivery methods and use of a scraper. It can been concluded from Figure 8-6 and Figure 8-7 that the area immediately after the scraper would be a good position for the fluid to be directed as it is a region of low-pressure and fluid penetration should be eased. However, compliance with nozzle positioning theory would need to be observed.

In this section, the air velocity distributions were measured. The pressure distribution was obtained in the following section using the CFD simulation. This provided a more complete understanding of the requirements for optimal fluid penetration.

8.4 Air scraper simulation

With the help of the CFD simulation, the air velocity distribution can readily be obtained for the various situations described previously and additionally, for situations where the experiments cannot be undertaken. If the results obtained by CFD simulation are seen to correlate well with experimental results, the CFX-Post simulation can be used to extract other parametric data, for example, air pressure.

In this section, the air scraper application will be investigated using the simulation. The aim of the first simulation model was to establish the same velocity distribution as that obtained from experiment. The air pressure distribution could then be obtained for similar conditions. The air pressure distribution is a very important factor to help understand where to best position the scraper in order to achieve optimal fluid penetration. The pressure analysis is one of the main tasks of the simulation reported in this section.

8.4.1 Layout of the simulations

The simulation model is described by the configuration shown in Figure 8-1. The dimensions of the wheel and workpiece used in the simulation were the same as those used in the experiments. The value of other parameters of the simulation (including the geometry, dimensions and wheel speed) were also the same as those used in experiments.

The wheel and workpiece cannot be set as direct contacts due to the mesh problem; therefore, at the interface, the simulation employs a gap of 0.3 mm between the two surfaces. In practice, only a small percentage of the wheel surface, approximately 1 to 3 per cent is actually in contact with the workpiece. This contact area is the area of the wear flats on the abrasive grains. As a consequence, the approximation used for the

simulation is reasonable and this has been confirmed by the results from the simulation which have correlated well with results from experiment.

The initial simulations in this section were used to validate the experimental results, these include the Cases 1 to 4 (of the experiments shown in section 8.3). The pressure distribution is subsequently obtained from the simulation.

Further simulations were undertaken in order to investigate the effect of the scraper dimension on the velocity distribution and pressure distribution of the air boundary layer. The scraper dimensions include both width and length. This work will help to define the necessary width and length as well as the shape in scraper design.

The following simulations were undertaken to establish the effect of the scraper position, with reference to the gap between the wheel surface and the workpiece surface. The aim of the work was to aid the optimisation of scraper use, i.e. how best to locate the scraper to break the air boundary layer. In this section, the nozzle position will be introduced, since this is generally positioned close to the scraper. The air velocity and the pressure of the boundary layer are the main parameters in the analysis.

In conclusion, a definition of the air boundary layer recovery distance (or recovery degree to the wheel axis) will be proposed for use in subsequent simulations. This new work is important as all previous studies neglected to give a value to this parameter.

8.4.2 Experimental results validation

In this section, the velocity vector maps obtained by simulation are compared with the experimental results. The simulation results shown in Figure 8-8 to Figure 8-12 are compared with the experimental results, shown in Figure 8-3 to Figure 8-7 respectively.

- Simulation 1 and simulation 2, are compared with the experiments: case 1 and case 2, to show the scraper effect when not using workpiece.
- Simulation 3 and simulation 4, are compared with the experiments: case 3 and case 4, to show the scraper effect when using workpiece.

- Simulation 4 and simulation 5, are compared with the experiments: case 4 and case 5, to show the effect of the gap size.

Through comparing the velocity vectors obtained from the experiments and the simulations, it can be seen that, the simulation results correlated extremely well with experimental results and consequently the discussion concerning the changes in air velocity observed from these simulations would be very similar to that given for the experimental results. There are small differences due to the fact that in the simulation there was no wheel guard and the wheel was not porous.

The results indicate that the simulation model is an effective tool for modelling the behaviour of air flows under the circumstances considered.

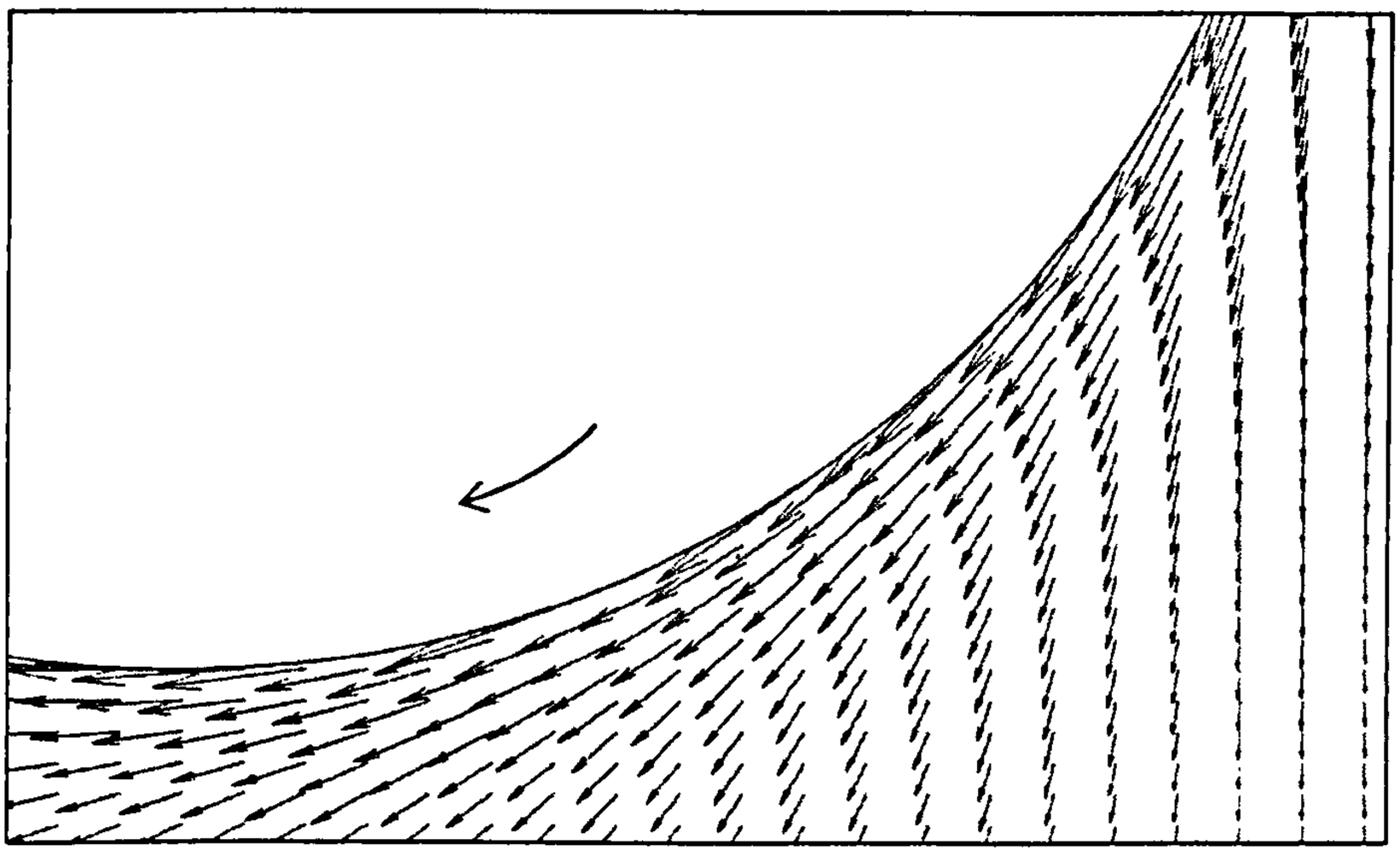

Figure 8-8 Air velocity vector map (Simulation 1: without workpiece and scraper)

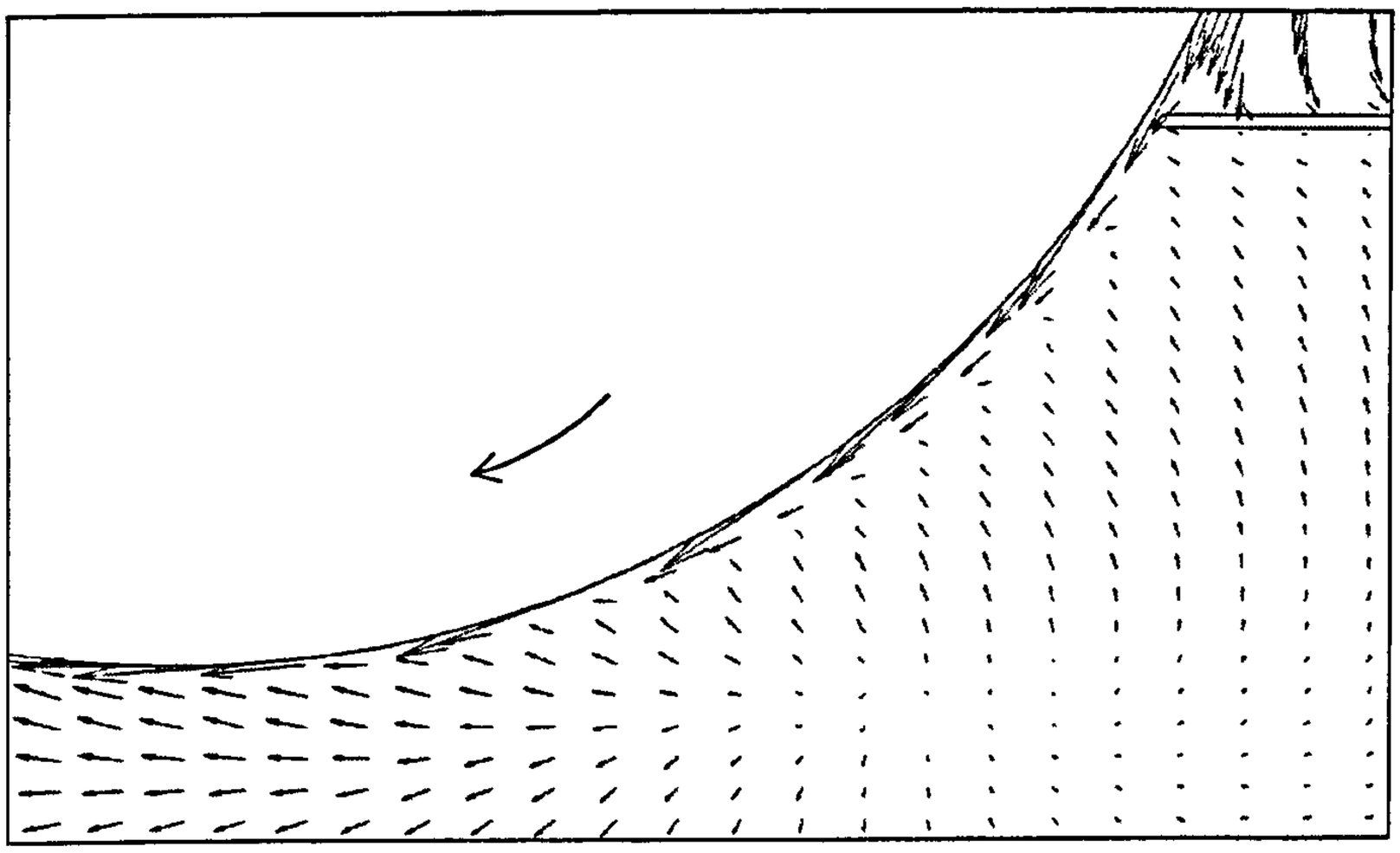

Figure 8-9 Air velocity vector map (simulation 2: without workpiece but with scraper, Gap = 1 mm)

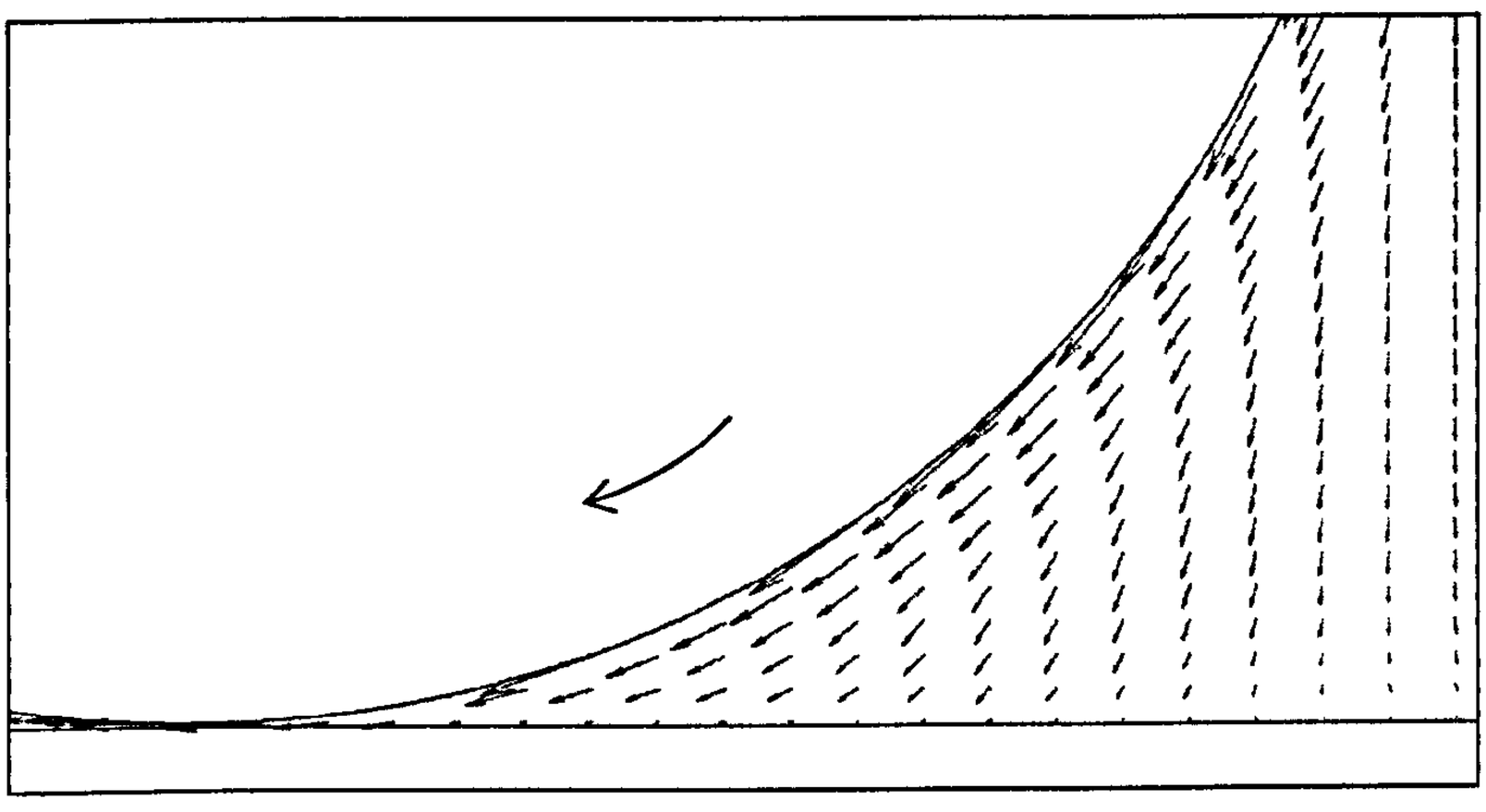

Figure 8-10 Air velocity vector map (simulation 3: with workpiece but without scraper)

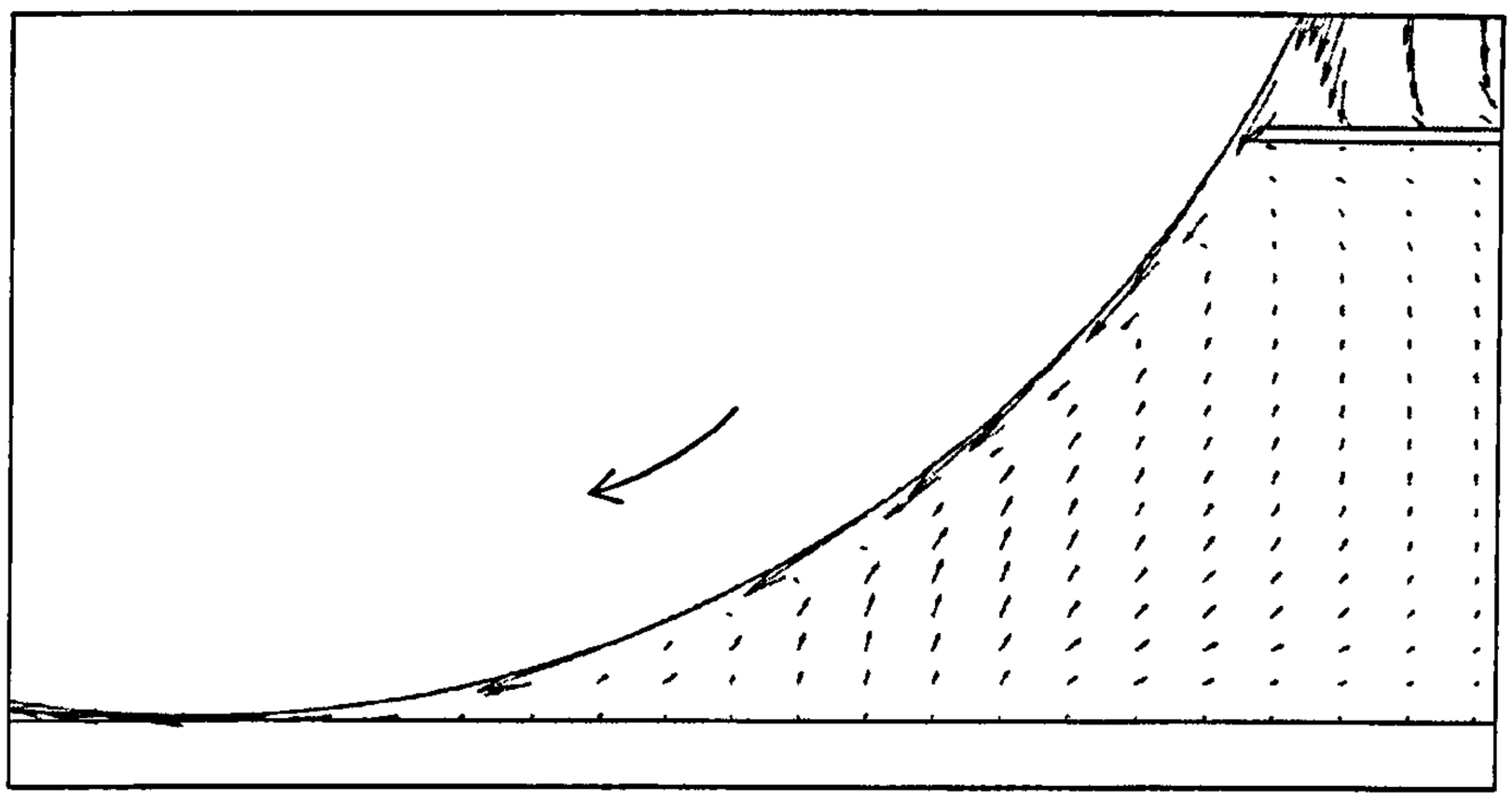

Figure 8-11 Air velocity vector map (simulation 4: with workpiece and scraper, Gap = 1 mm)

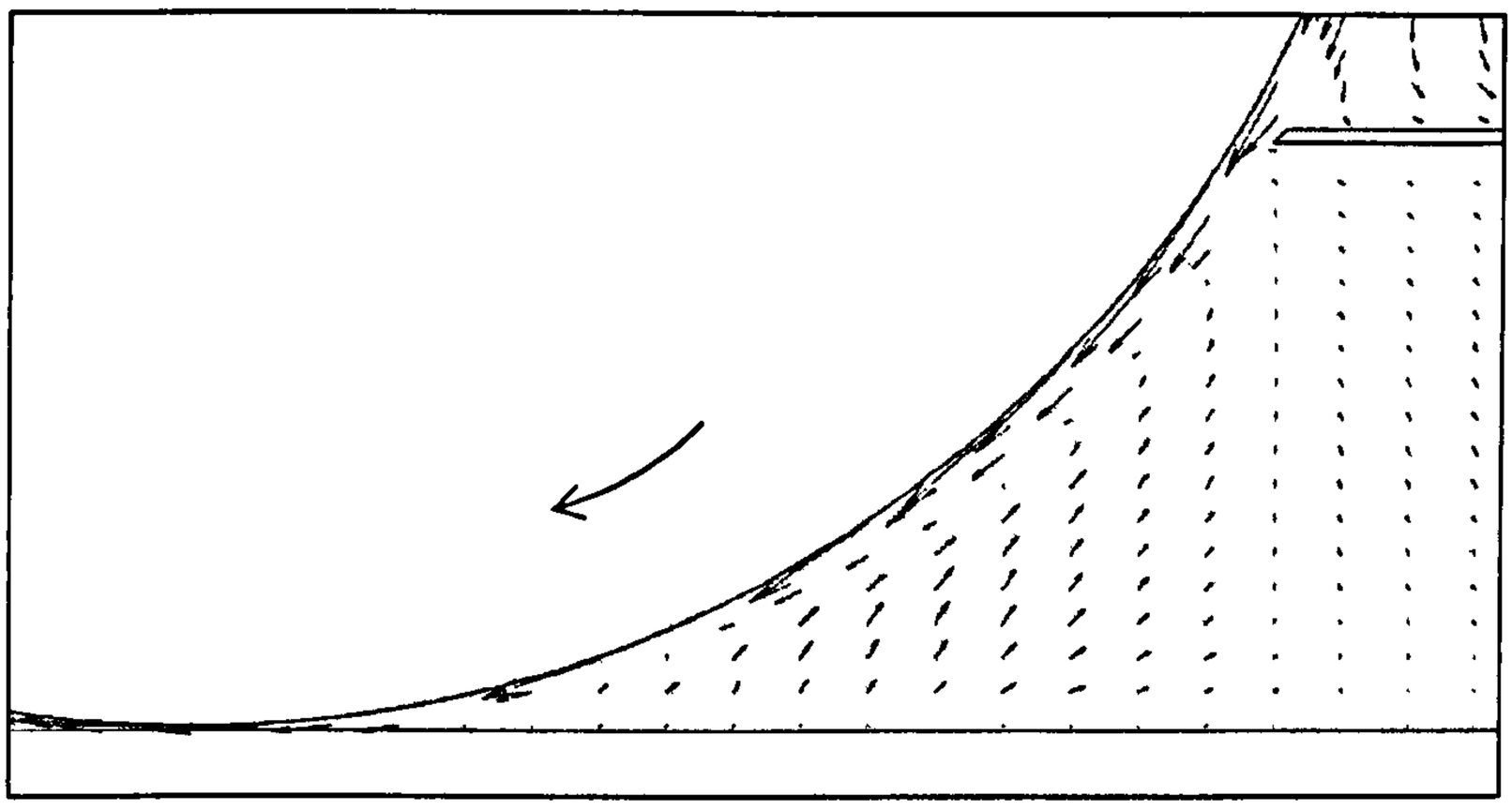

Figure 8-12 Air velocity vector map (simulation 5: with workpiece and scraper, Gap = 3 mm)

The simulation results also confirm that the CFD model is sufficiently developed and robust to provide extensive investigations without the need for large numbers of experimental tests.

Figure 8-13 shows the resultant velocity distribution in the grinding contact zone. When the scraper was put close to the wheel approximately 1 mm from the surface, the air flow was broken by the scraper. This phenomenon is shown in Figure 8-14.

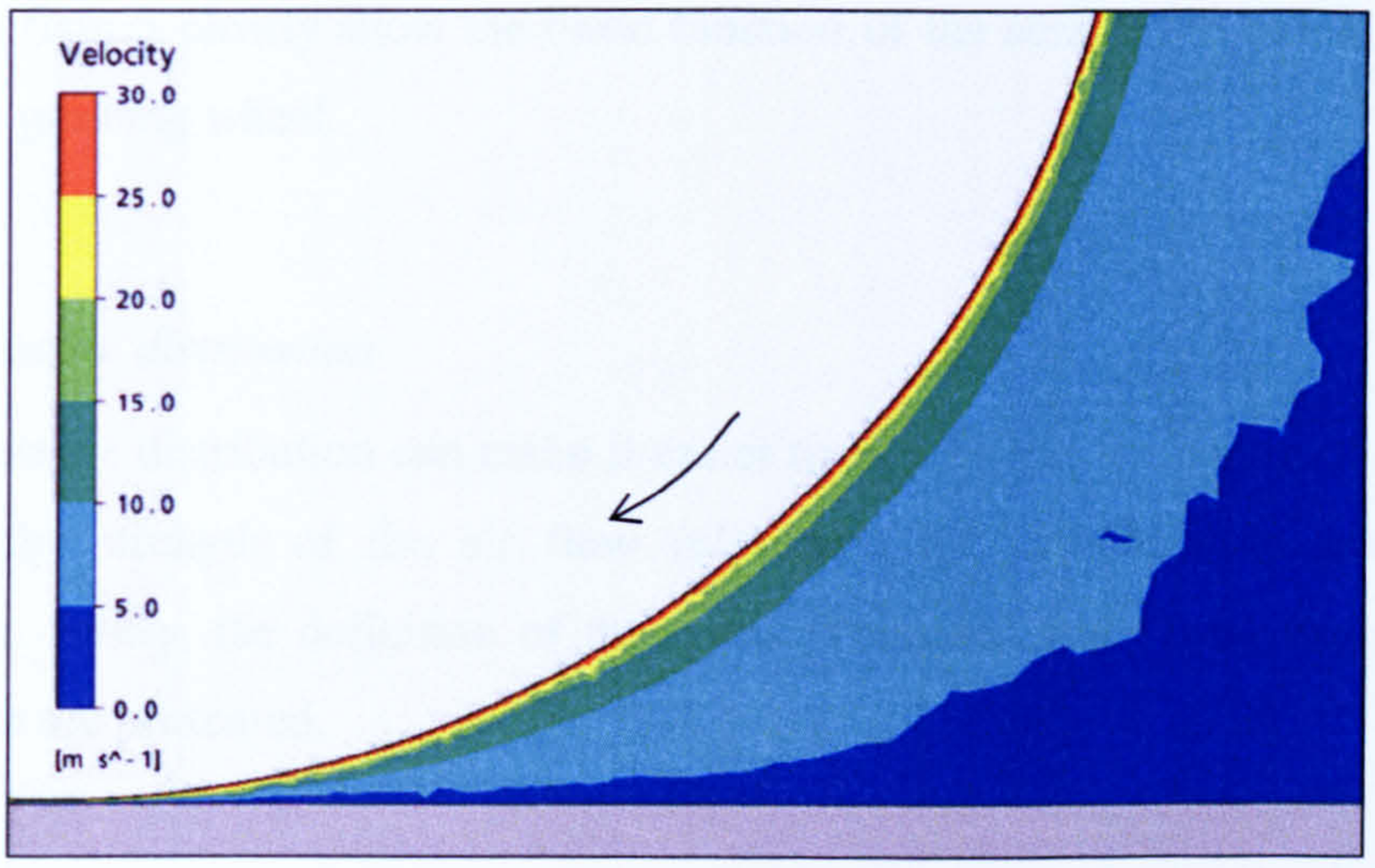

Figure 8-13 Contour of air velocity distribution in grinding entry region by simulation without a scraper

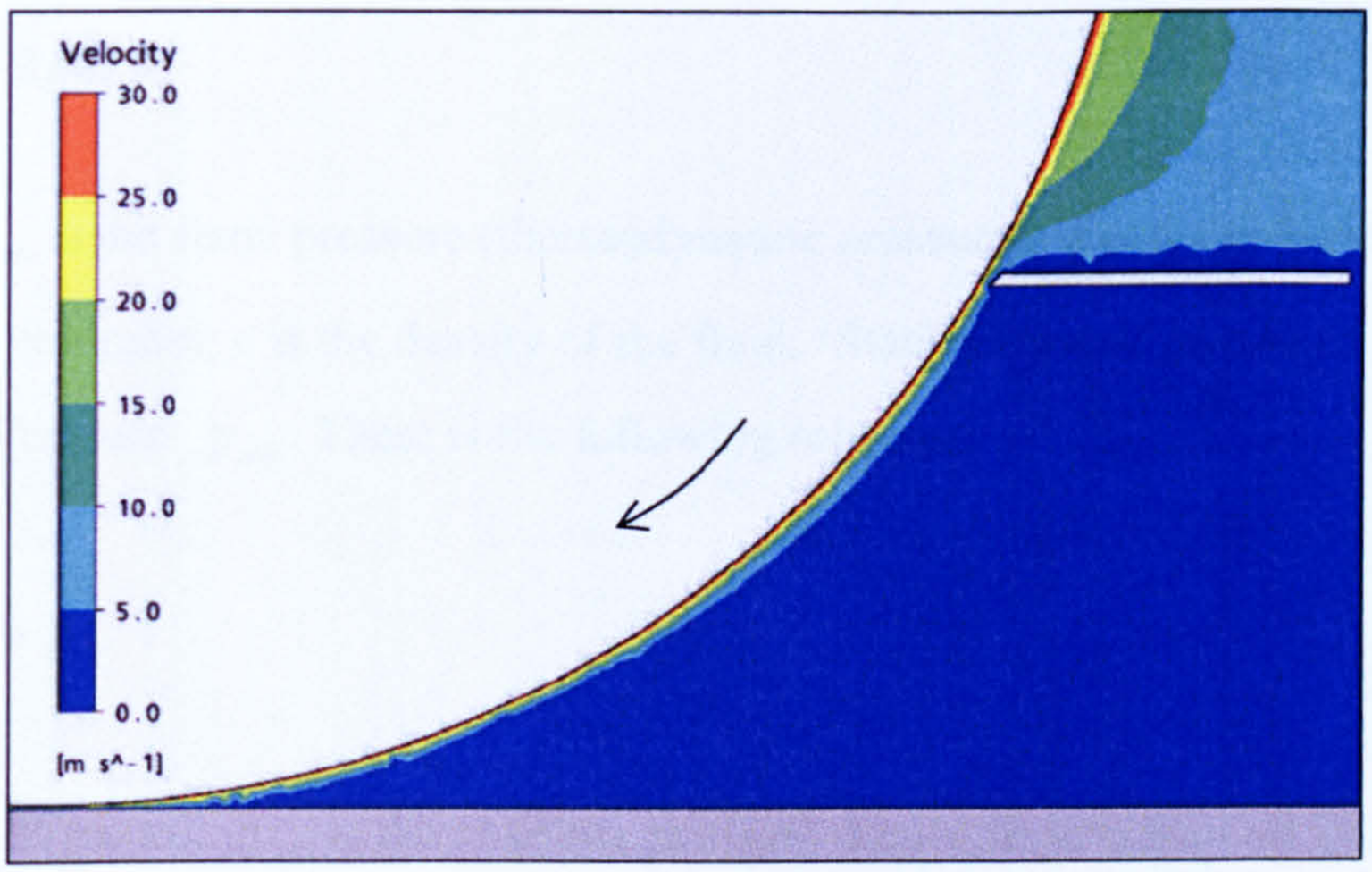

Figure 8-14 Effect of the scraper on the air velocity distribution contour in grinding entry region

The wheel speed was 30 m/s. It is observed that the air velocity decreases quickly to less than 5 m/s in most of the region beneath the scraper and a short distance from the wheel surface (Figure 8-14). Because the scraper is 1 mm from the wheel surface, there is still opportunity for the air boundary layer to adhere to the wheel, but the layer is very thin compared to the thickness prior to using the scraper. A reduced thickness layer would be more easily penetrated than a thicker layer.

These two figures clearly show the basic function of the scraper: to break the air flow around the grinding wheel.

8.4.3 Pressure distribution

The air pressure distribution can make it easier to understand the nature of the air flow and how the strength of the air flow influences the resistance to grinding fluid penetration. Firstly, the definition of the terms 'Pressure' and 'Total Pressure' in the CFX Solver are presented.

When the *k*-ε turbulence model (ANSYS CFX, ANSYS CFX-Solver Modelling Guide) is used, the fluctuating velocity components give rise to an additional pressure term. In this case, ANSYS CFX solves for the modified pressure. This variable is named 'Pressure' in ANSYS CFX.

$$p' = p_{stat} + 2\rho k/3 \tag{8.1}$$

Where, p_{stat} is the static pressure (thermodynamic pressure); k is the turbulent kinetic energy per unit mass; ρ is the density of the fluid. 'Static Pressure' is related to 'Absolute Pressure' p_{abs}. There is the following relative:

$$p_{abs} = p_{stat} + p_{ref} \tag{8.2}$$

'Reference Pressure' p_{ref} is the absolute pressure datum from which all other pressure values are taken. All relative pressure specification in ANSYS CFX are relative to the Reference Pressure p_{ref}. In the simulation in this chapter, the local atmospheric pressure of 100,000 Pa is suitable and used as the relative pressure.

'Total Pressure' is defined as the pressure that would exist at a point if the fluid was brought instantaneously to rest such that the dynamic energy of the flow converted to pressure without losses. For incompressible flows such as those of liquids and low speed gas flows, the total pressure is given by Bernoulli's equation:

$$p_{tot} = p_{stat} + \frac{1}{2}\rho(U \times U) \tag{8.3}$$

which is the sum of the static and dynamic pressure.

The value of the Pressure mainly rests with the fluctuating velocity components in the CFX simulation, so the pressure is higher in the area where the air flow is fluctuating most. The value of the Total Pressure in the CFX simulation is mainly determined by the value of the air velocity. Because the air velocity is very high close to the wheel surface, the Total Pressure is much larger than the Pressure, but in the grinding contact zone, the Pressure is also large due to the complex flows and consequent fluctuations.

Figure 8-15 gives the Pressure distribution in the plane just above the workpiece upper surface and through the grinding contact zone. In the grinding entry region, the Pressure is much higher, and in practice, it can push back the grinding fluid. The Pressure decreases greatly after the grinding contact zone. This pressure distribution also can explain the fluid flow phenomena described in Chapter 4.

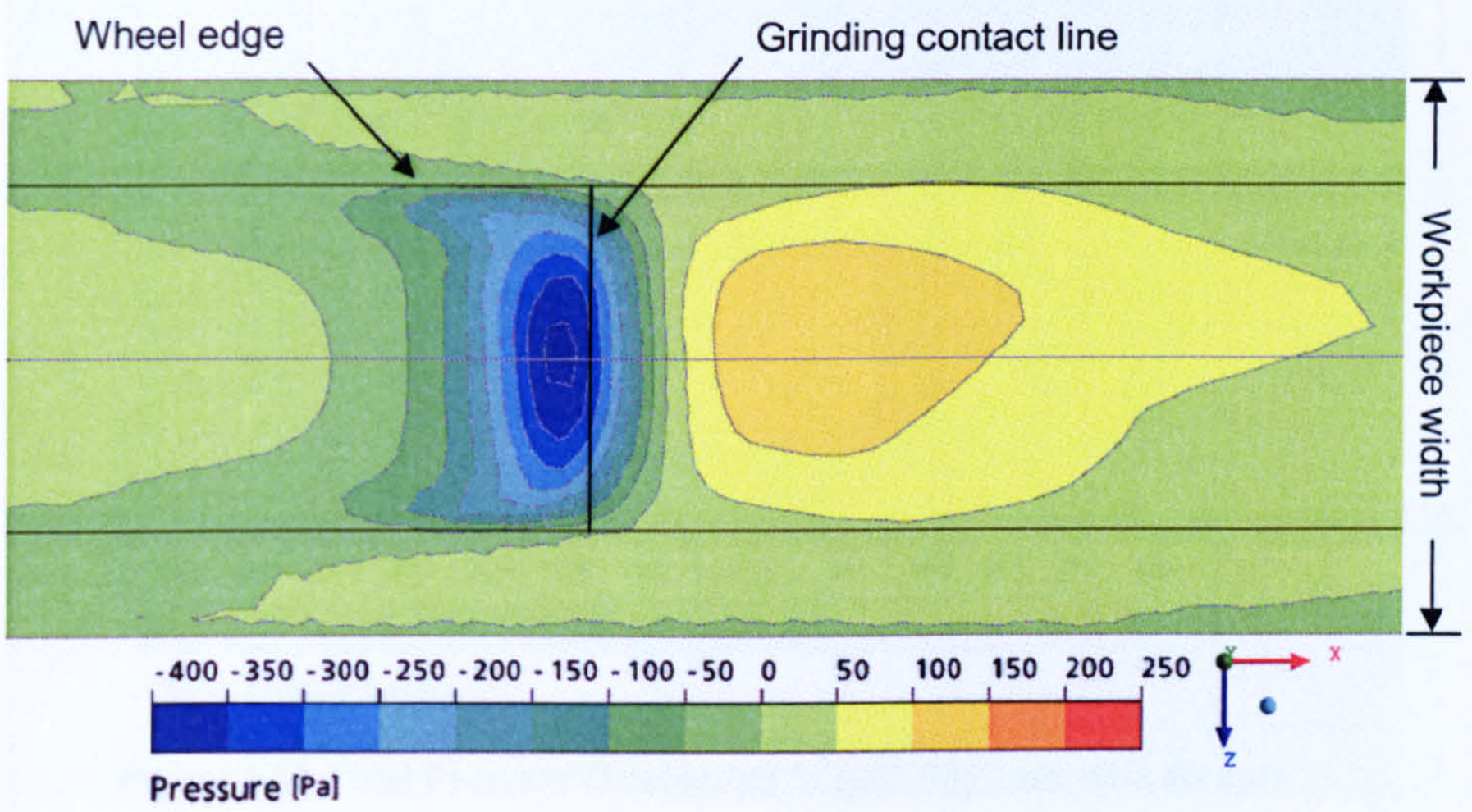

Figure 8-15 Pressure distribution in grinding zone

The Total pressure distribution along the workpiece upper surface is similar to the Pressure distribution (shown in Figure 8-16), but due to the value of the velocity, the Total Pressure is higher than the Pressure in grinding contact entry region. When the

scraper is applied, the value of the pressure reduces, but the distribution contour sees no great change (shown in Figure 8-17).

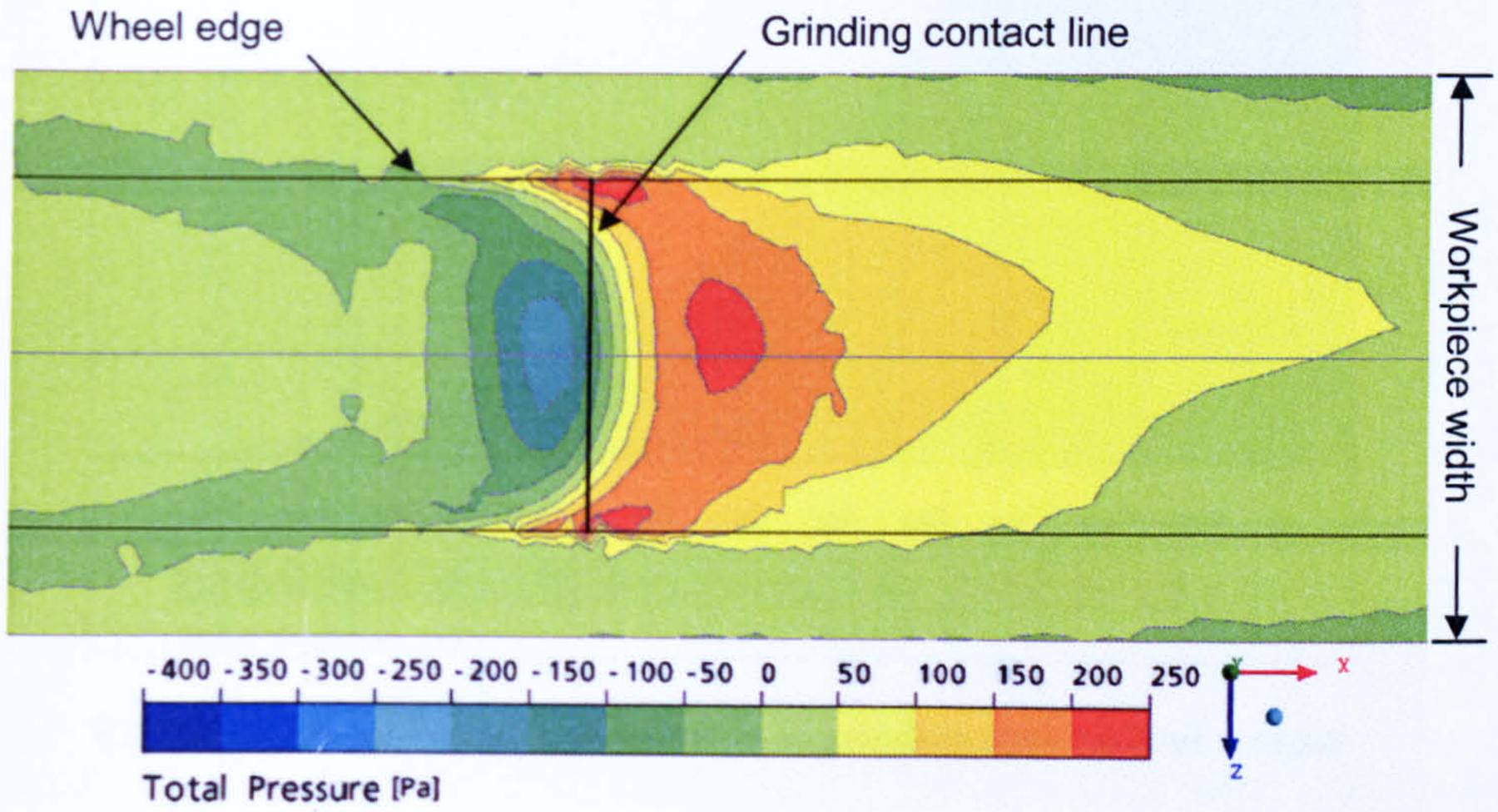

Figure 8-16 Total Pressure distribution in grinding zone without scraper

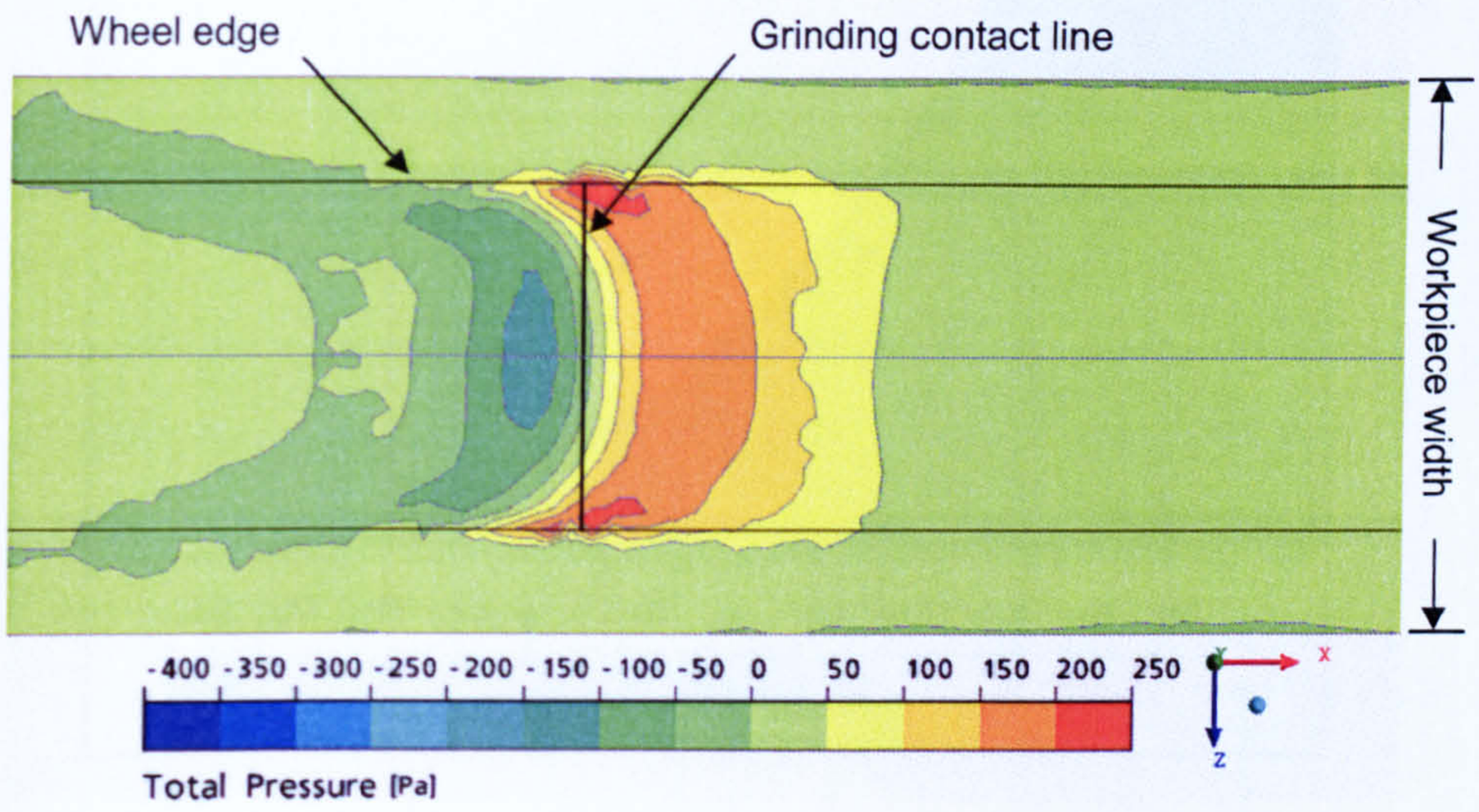

Figure 8-17 Total Pressure distribution in grinding zone with scraper

The Total Pressure distribution in the middle section of the wheel is shown in Figure 8-18. Close to the wheel surface, the Total pressure gradient is very large, and there is a thin high-pressure layer. However, when the scraper is used, the Total Pressure in the area just after the scraper becomes much smaller, although it recovers a little approaching the grinding contact zone (shown in Figure 8-19).

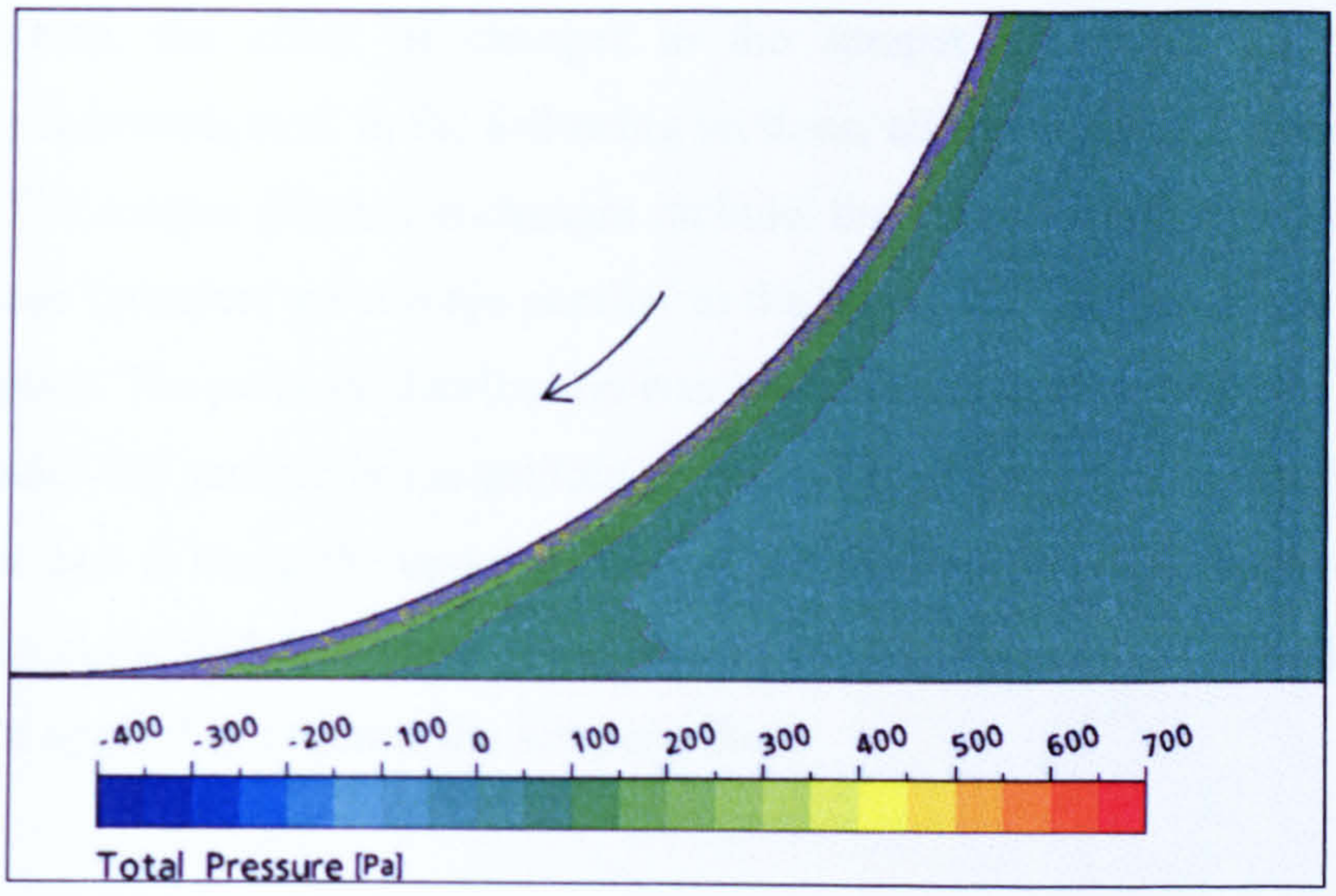

Figure 8-18 Total Pressure distribution in grinding zone without scraper

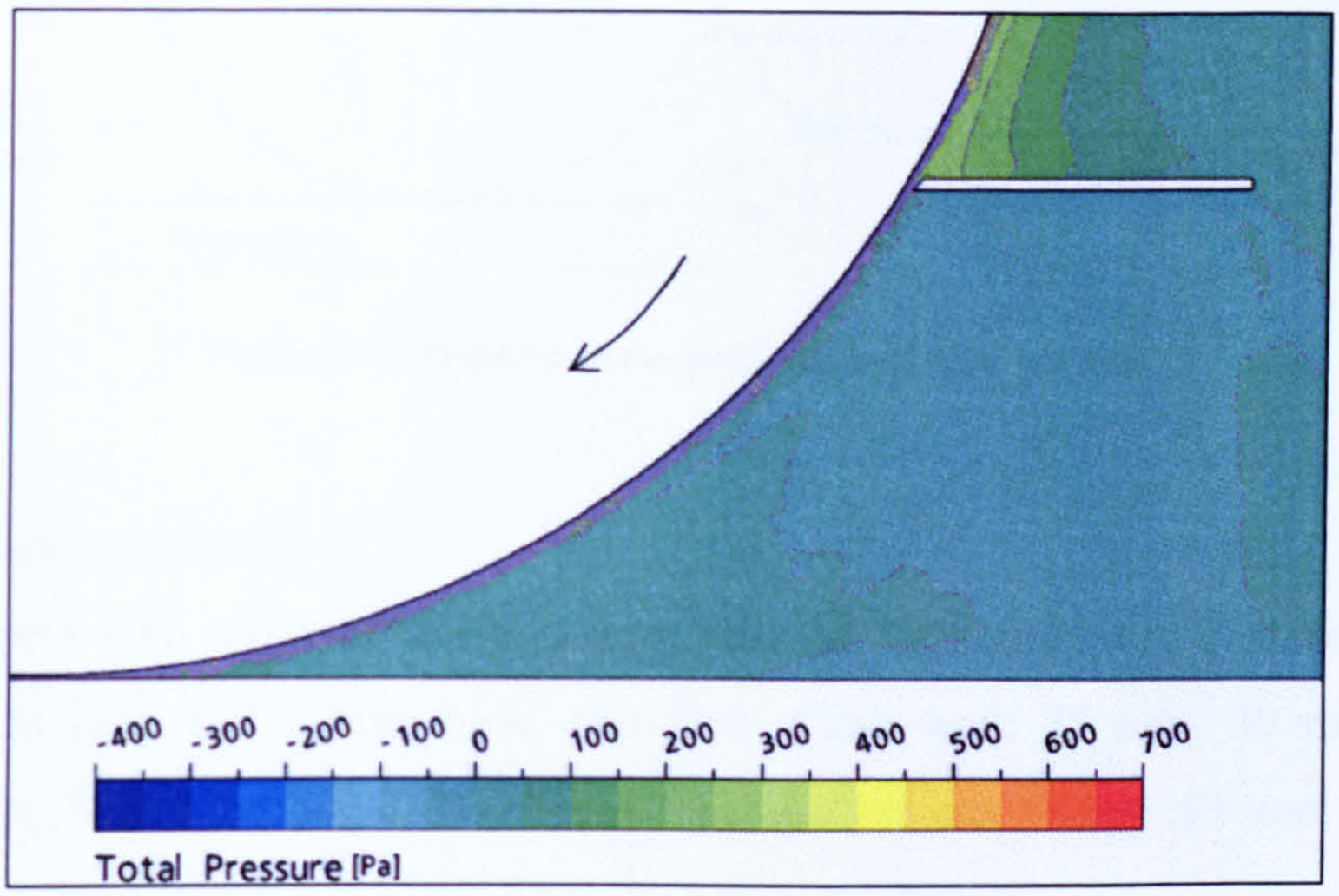

Figure 8-19 Total Pressure distribution in grinding zone with scraper

In this section, the pressure distribution was investigated both along the workpiece upper surface through the grinding contact zone and in the wheel middle section. The work provides a basic understanding of how the pressure distributes in each relative area. The function of the scraper was confirmed to reduce the pressure.

8.4.4 Effect of the scraper dimension to pressure

In this section, the effect of changes to the scraper dimension on the pressure distribution is investigated. In the following sections, all the 'pressure' means the 'Total Pressure'. The scraper dimension changes include: the scraper width change and scraper length change (scrapers are always parallel to the workpiece surface in the simulations in this chapter). The pressure distribution was analyzed along two axes: one is along the line just under the scraper in the middle section of the wheel (Shown in Figure 8-20) and another axis is along the upper surface of the workpiece and through the grinding contact zone in the middle section of the wheel (show in Figure 8-20). Total Pressure in CFX will be applied to estimate the scraper effect.

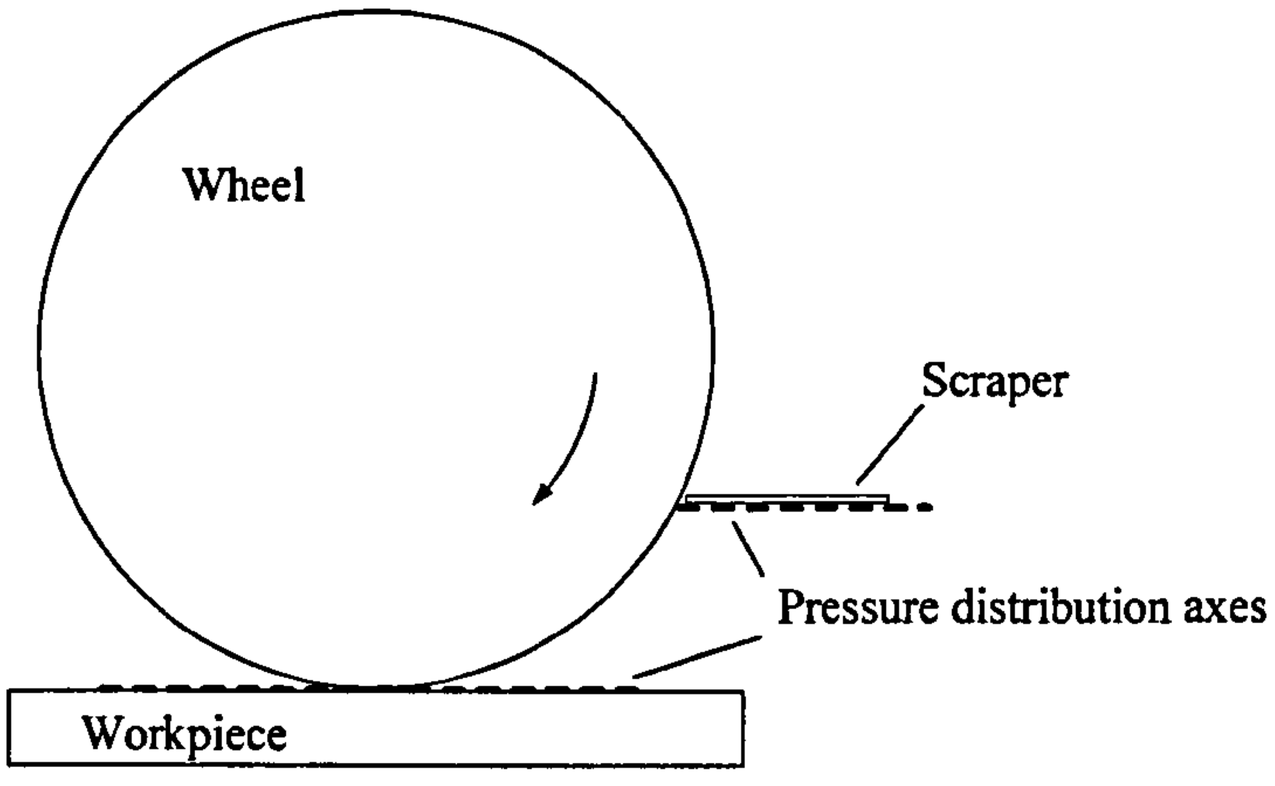

Figure 8-20 Position of the pressure distribution axes

Effect of scraper width:

Three scrapers with different width were applied in the simulation. The scrapers were each 30 mm long and 1 mm thick, and their width were 25 mm, 30 mm, 35 mm respectively (Shown in Figure 8-21). All scrapers were placed 43 mm above the workpiece upper surface and 1 mm from the wheel surface.

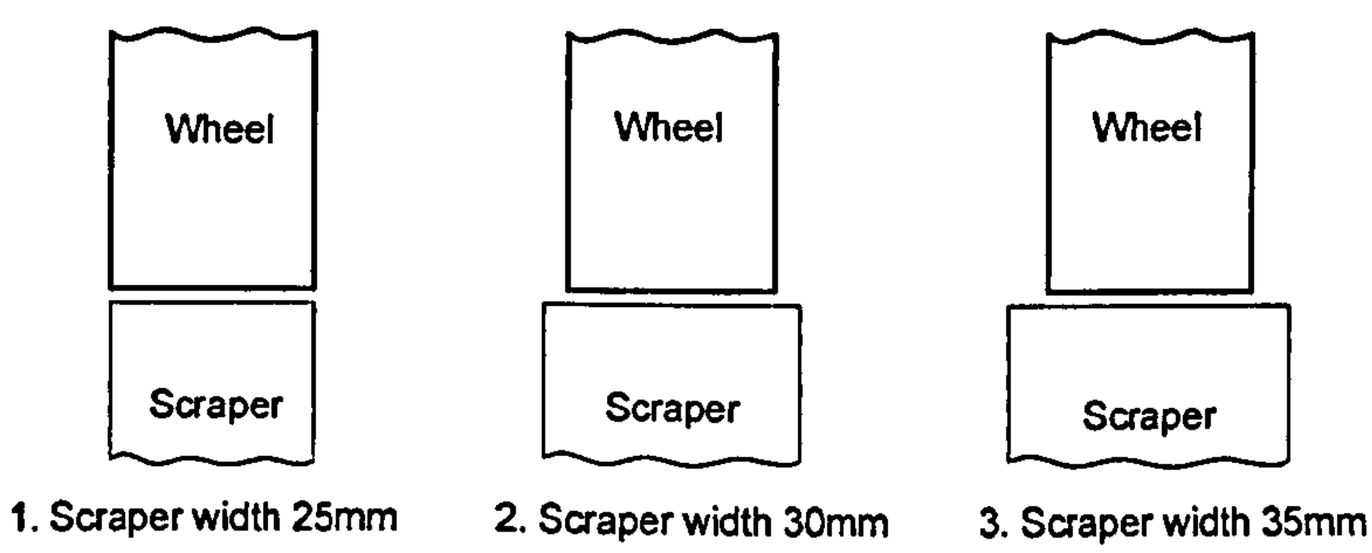

Figure 8-21 Three scrapers with different width

Total pressure distributions through the grinding contact zone using different width of scraper are shown in Figure 8-22 as well as the pressure distribution without the scraper. The figure shows that scrapers can reduce the pressure by more that 50% in the grinding entry region along the workpiece surface, compared to the situation not using a scraper. This pressure reduction is beneficial for effective fluid penetration. The pressure in the grinding exit region was not greatly affected by the use of a scraper.

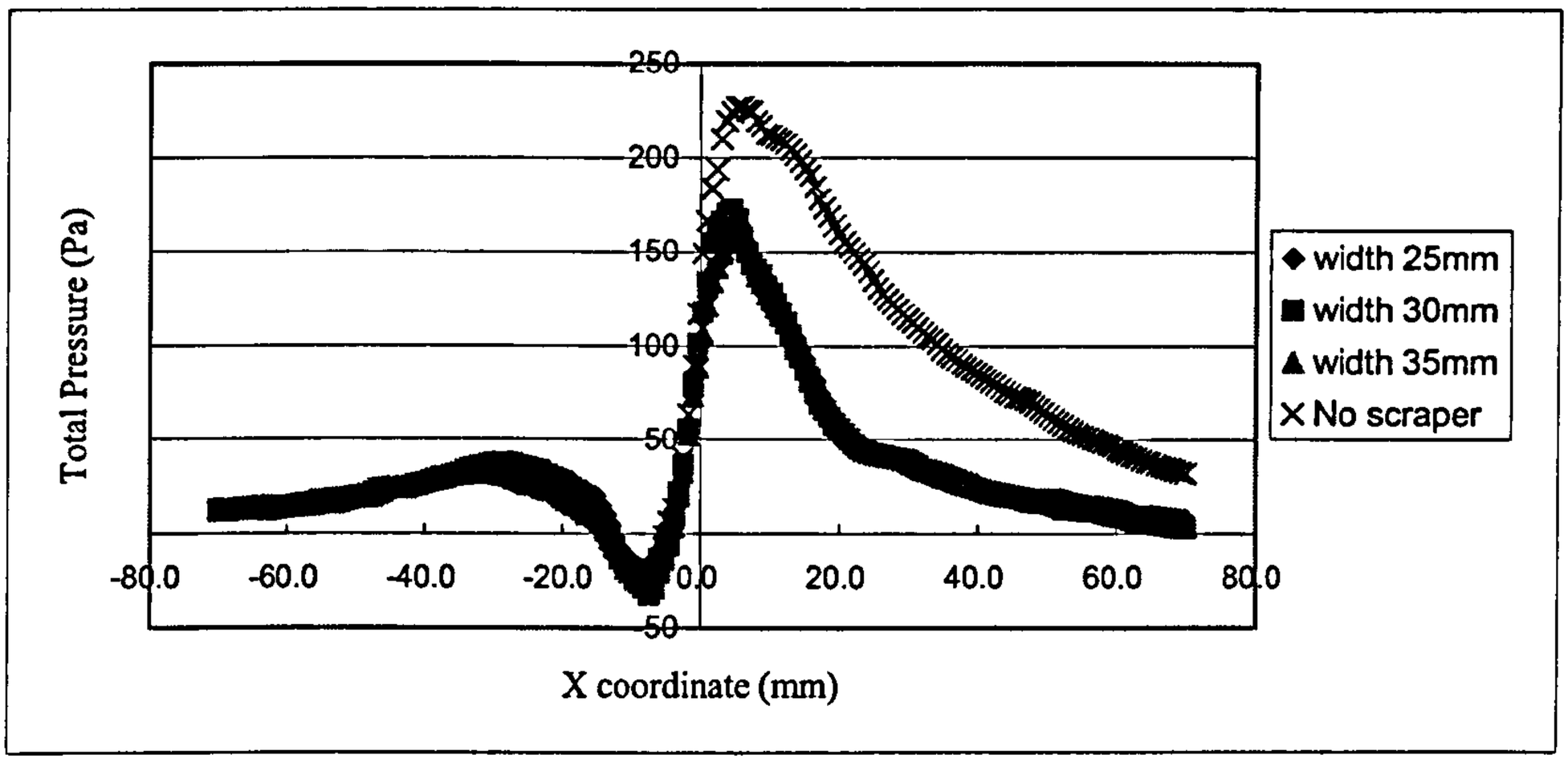

Figure 8-22 Pressure distribution through grinding contact zone (effect of the scraper width)

The pressure distributions under the scraper are shown in Figure 8-23 for the two cases: (i) scraper with gap1 mm and (ii) no scraper. The pressure is seen to decrease in the area close to the wheel surface. Immediately underneath the scraper, the pressure reduced nearly to zero. The pressure of the air at some distance from the wheel surface reduces more in the case (i) compared to the pressure with no scraper.

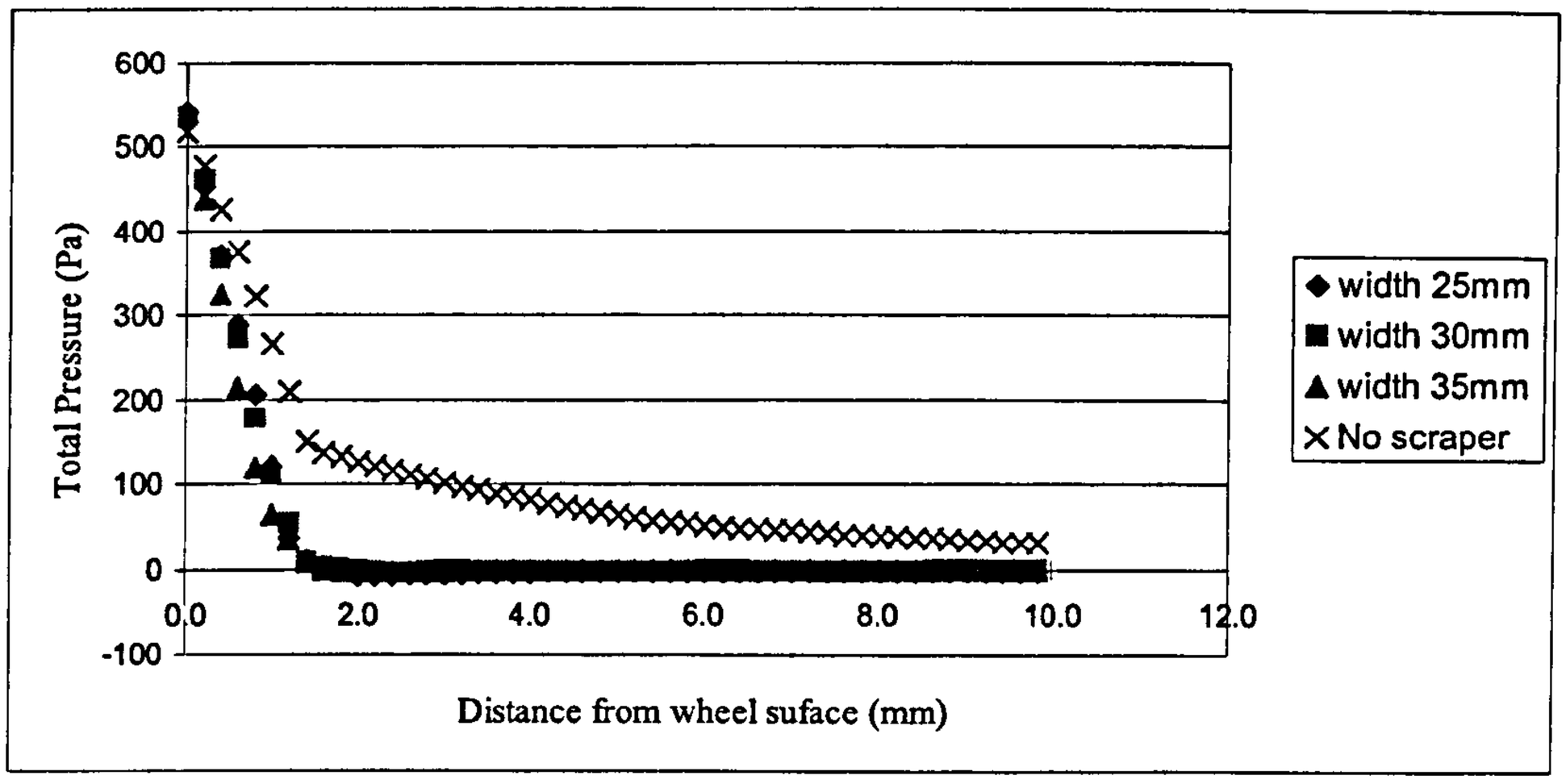

Figure 8-23 Pressure distribution under the scraper (effect of the scraper width)

Figure 8-22 and Figure 8-23 also indicate that the width of scraper does not have a strong effect on the pressure distribution along the measurement axes both in the grinding zone and underneath the scraper.

The effect of scraper length:

Two scrapers were used to research the effect the scraper length on the pressure. The length of the two scrapers was 10 mm and 30 mm respectively (Figure 8-24). Their width was 30 mm; thickness 1 mm. The vertical position of the scrapers was 43 mm measured from the workpiece upper surface and 1 mm from the wheel surface.

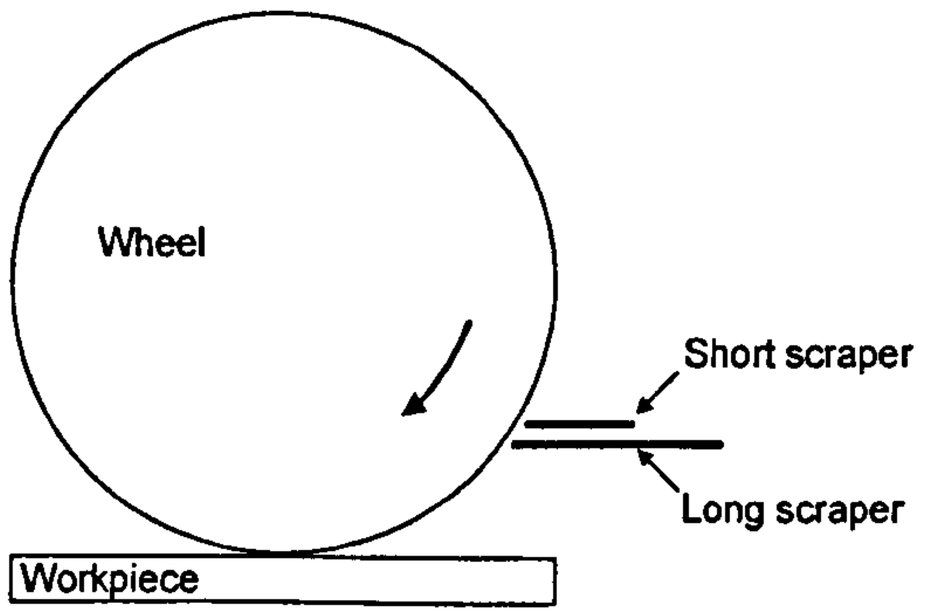

Figure 8-24 Two different length scraper

Figure 8-25 shows the pressure distribution in the grinding zone along the measurement axes with the different scrapers. It also clearly shows that the length of the scraper has no great effect on the pressure distribution in the grinding zone.

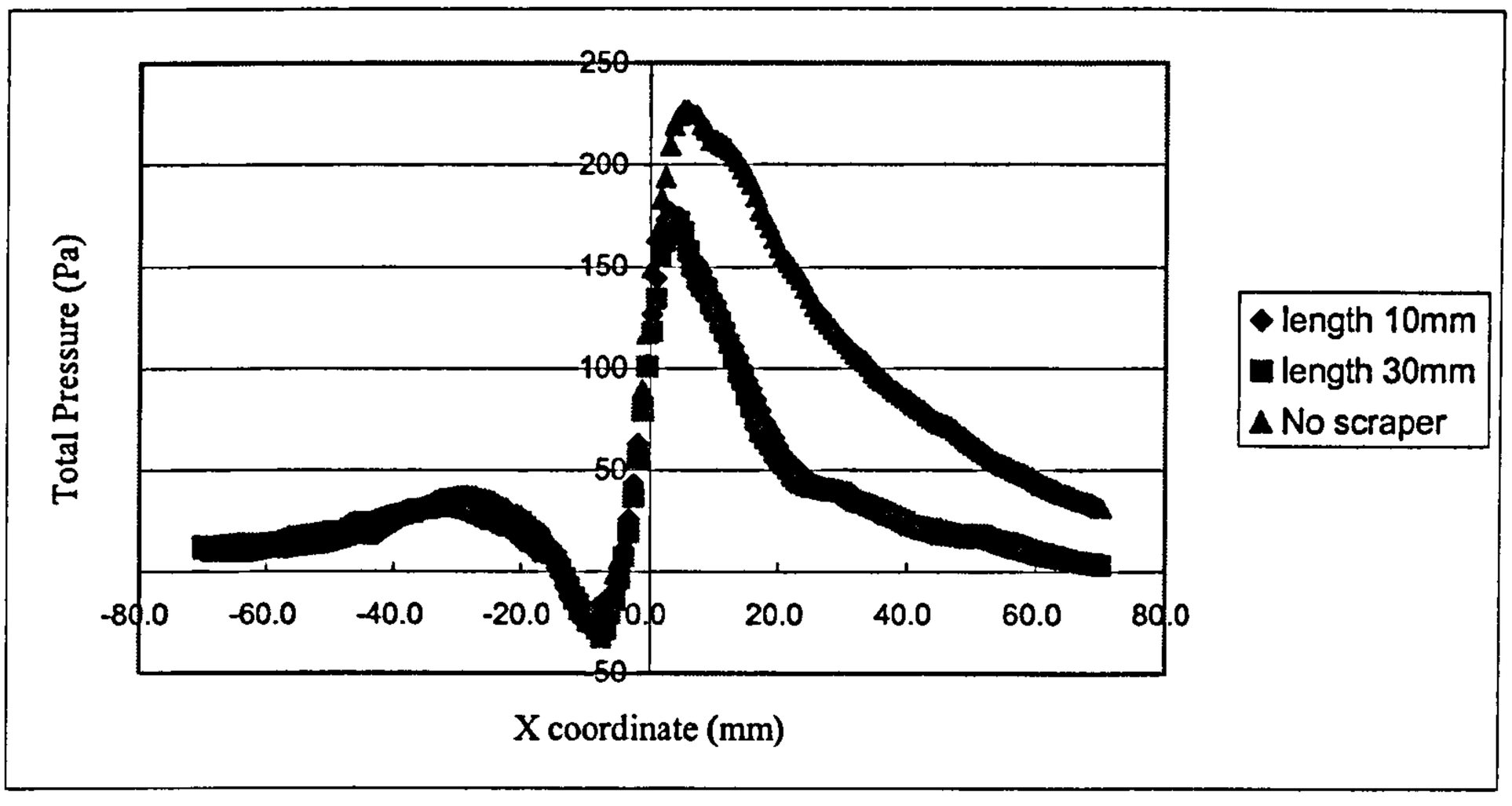

Figure 8-25 Pressure distribution in grinding contact zone (effect of the scraper length)

Figure 8-26 shows the pressure distribution under the scraper. Both scrapers could result in a pressure decrease to approximately zero immediately under the scraper, but when using a scraper, the pressure of the deflected air (in a direction away from the wheel) may be sufficient to interfere with fluid delivery if the nozzle is not positioned sufficiently close to the wheel. Therefore, for improved performance the nozzle should be sited under the scraper to avoid the effect of the deflected air flow. If the nozzle position is too difficult to change to ensure this condition is satisfied then the alternative is to increase the scraper length.

Figure 8-26 also illustrates that the change in the pressure of the deflected flow occurs much farther from the wheel surface with the long scraper than in the case of the short scraper and the pressure change is much smaller.

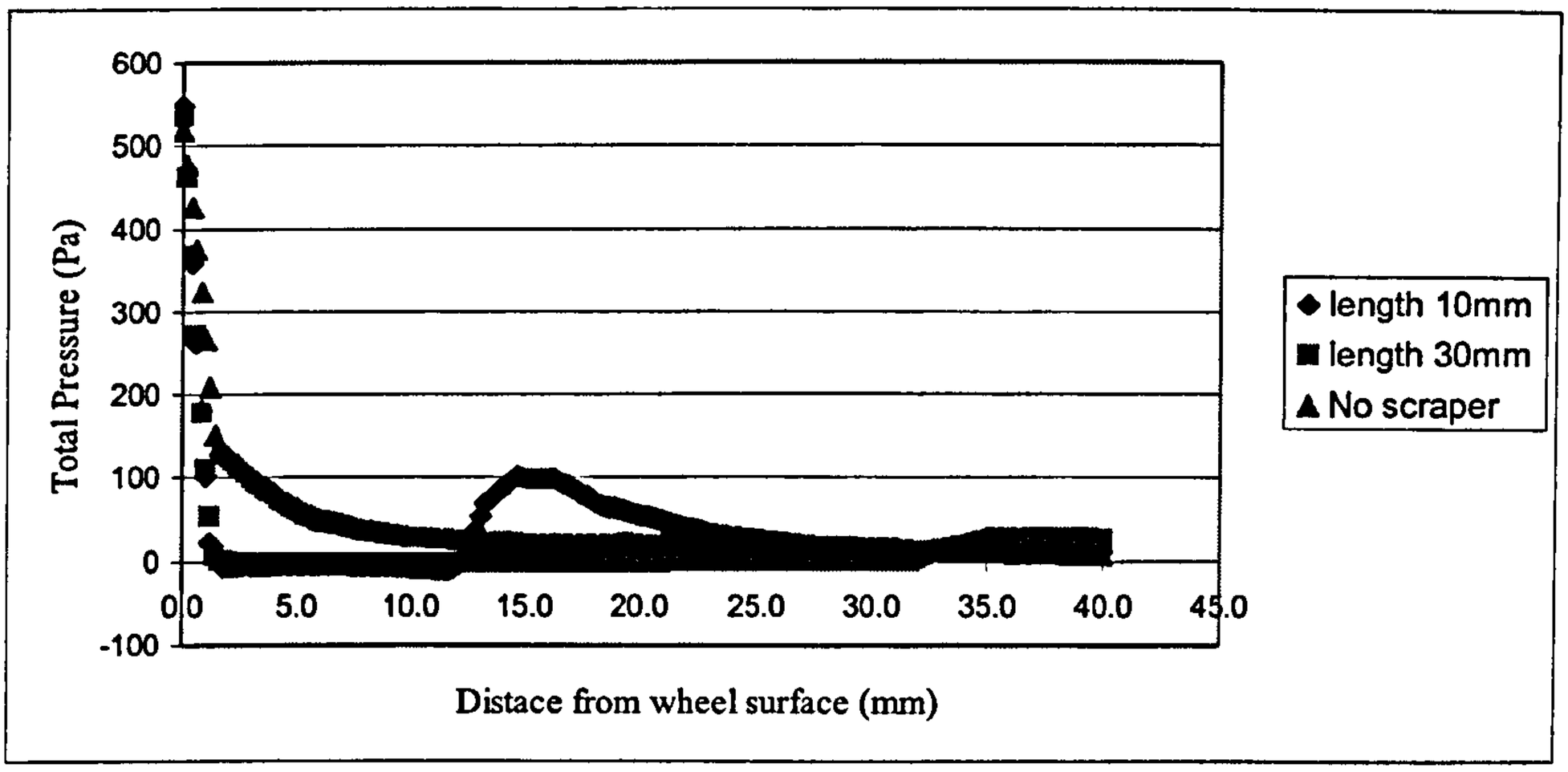

Figure 8-26 Pressure distribution under the scraper (effect of the scraper length)

The length and width of the scraper have been investigated in this section. The narrowest scraper used had a width equal to the wheel width, and this width of scraper functions very well compared to wider scrapers. It is therefore not necessary to use much wider scrapers. If the scraper length is too short the boundary layer recovers very shortly afterwards. It is strongly recommended that the nozzle orifice be sited just under the scraper in the case of short nozzles.

8.4.5 Effect of the scraper position on pressure

Using the same size scraper in different positions can produce different effects. In this section, the position of the scraper will be discussed, and this includes the gap between the scraper and the wheel surface, and the scraper height from the workpiece surface.

Effect of gap:

The dimension of the scraper used for the test was length 30 mm; width 30 mm; thickness 1 mm; height 43 mm from workpiece upper surface. Distances to wheel surface (gap size) of 1 mm, 2 mm, and 3 mm were applied.

Figure 8-27 shows the pressure distribution in the grinding contact zone. The use of a scraper is seen to decrease the pressure; however, the scraper gap has only a slight effect on the magnitude of the pressure. Figure 8-28 clearly shows that as the distance

between the scraper and the wheel surface increases, the pressure under the scraper becomes higher. Therefore, the scraper should be sited as close as possible to the wheel surface, if at all possible.

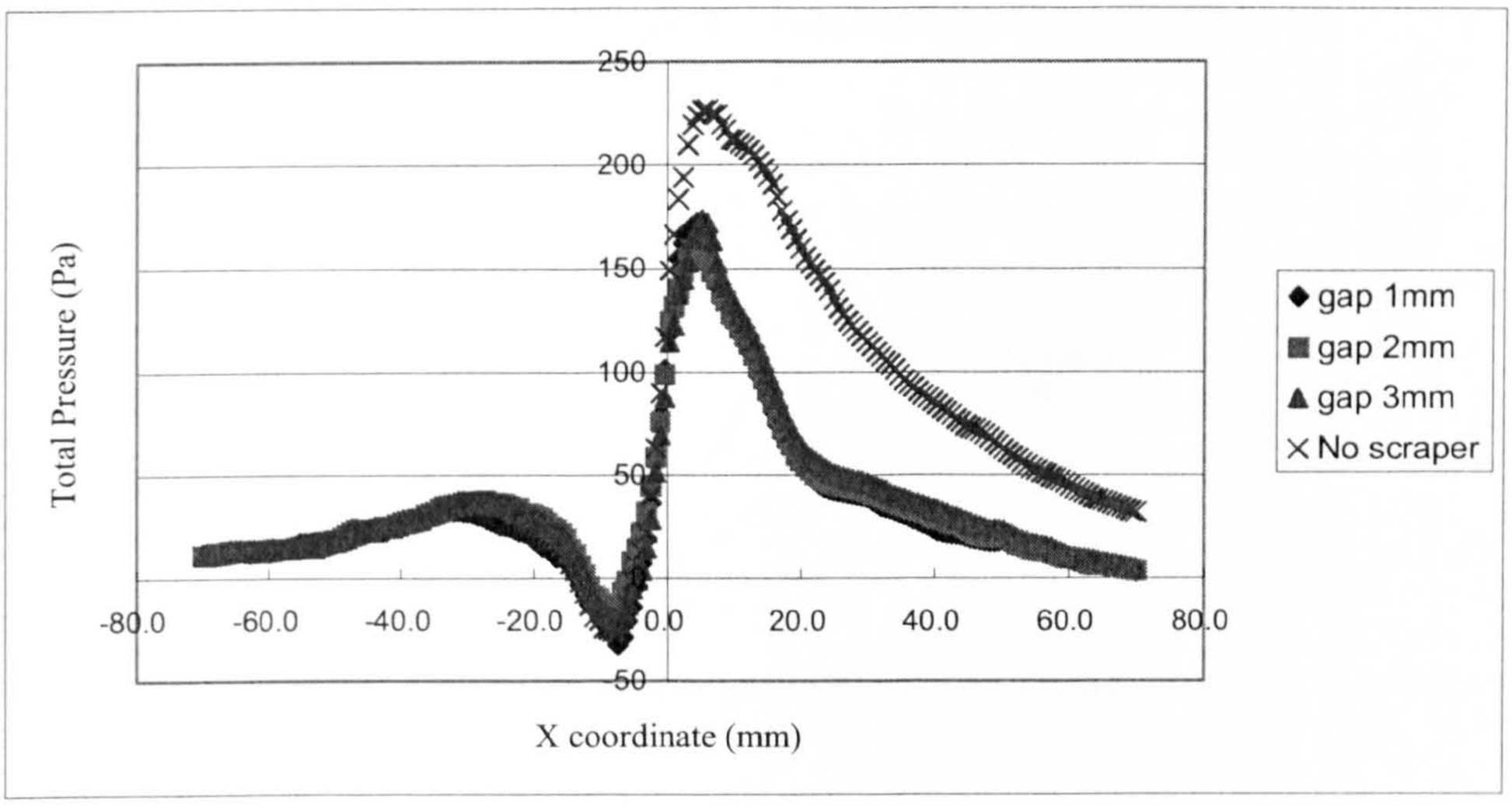

Figure 8-27 Pressure distribution in the grinding contact zone (effect of the gap between the scraper and wheel surface)

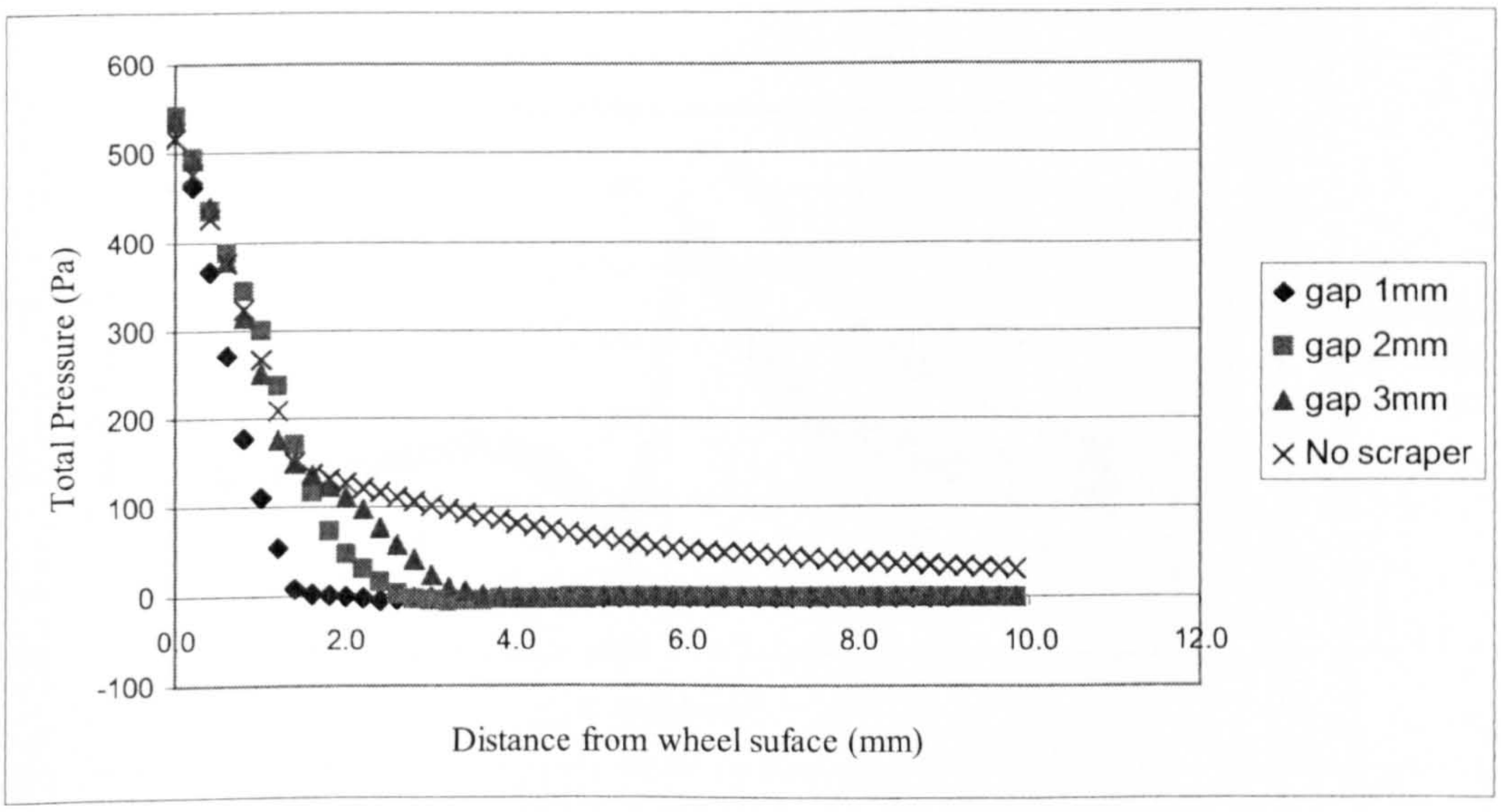

Figure 8-28 Pressure distribution in a horizontal direction immediately beneath the scraper (effect of the gap between the scraper and wheel surface)

Effect of height:

A scraper of dimensions similar to that above was used to test the effect of scraper distance above the workpiece surface (Figure 8-29). Three heights were investigated: 23 mm, 43 mm, and 90 mm. The measurement line was at 22.5 mm, just beneath the 23 mm high scraper. All scrapers were placed 1 mm from the wheel surface.

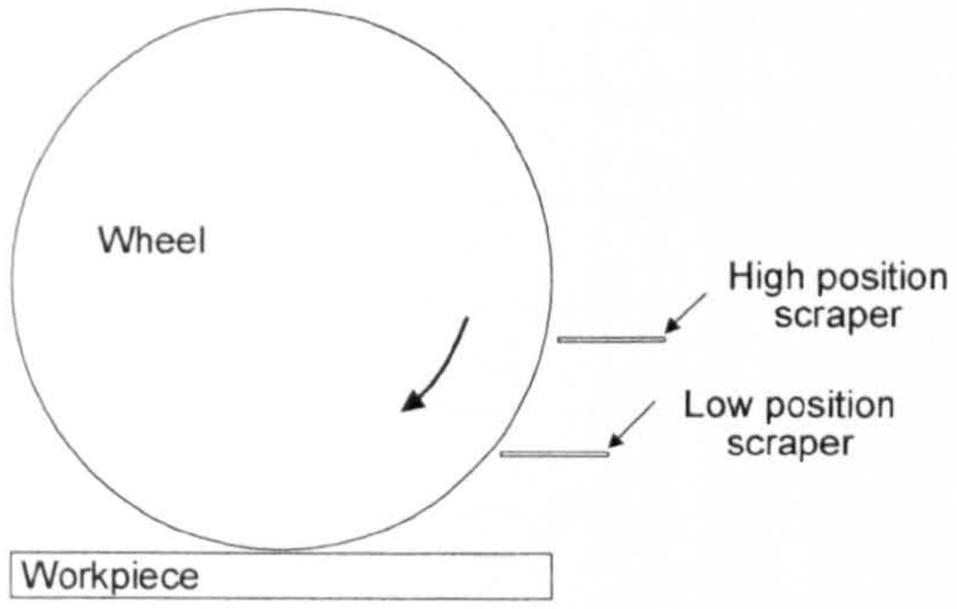

Figure 8-29 Scraper position above workpiece

Figure 8-30 shows that, in the grinding zone, the pressure is not strongly affected by the scraper height. However, the lower scraper position can result in a lower pressure on the workpiece, although it only occurs at a distance of more than 40 mm distance from the grinding contact zone.

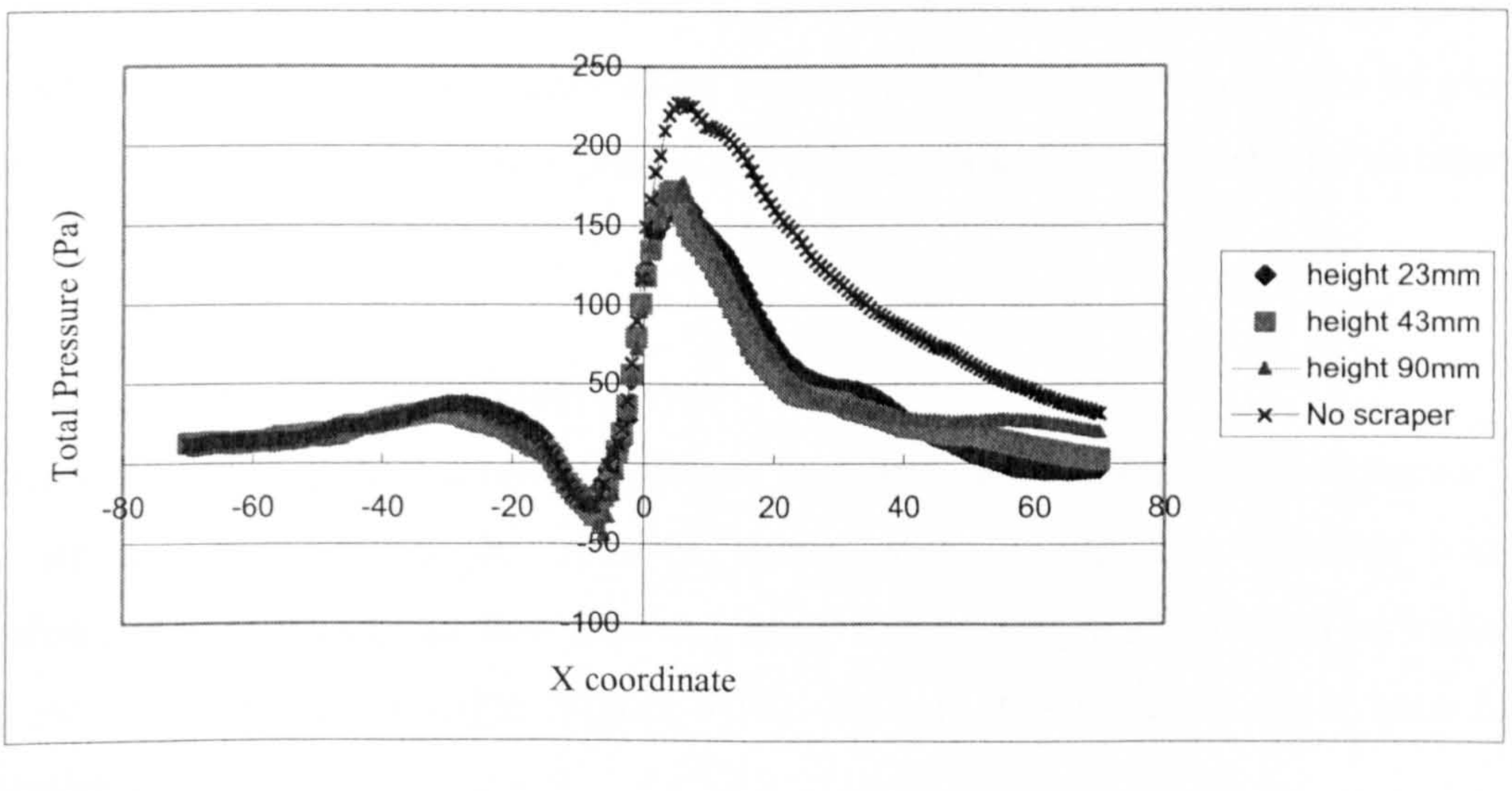

Figure 8-30 Total pressure distribution in the grinding contact zone (effect of scraper height)

When the scraper is further away from the measurement position, the measured pressure will be lower, and this is illustrated in Figure 8-31. This is due to the increased opportunity for the air boundary layer to recover when the scraper is higher. Therefore, the nozzle orifice should be put as close as possible to the scraper to minimise the air flow recovery.

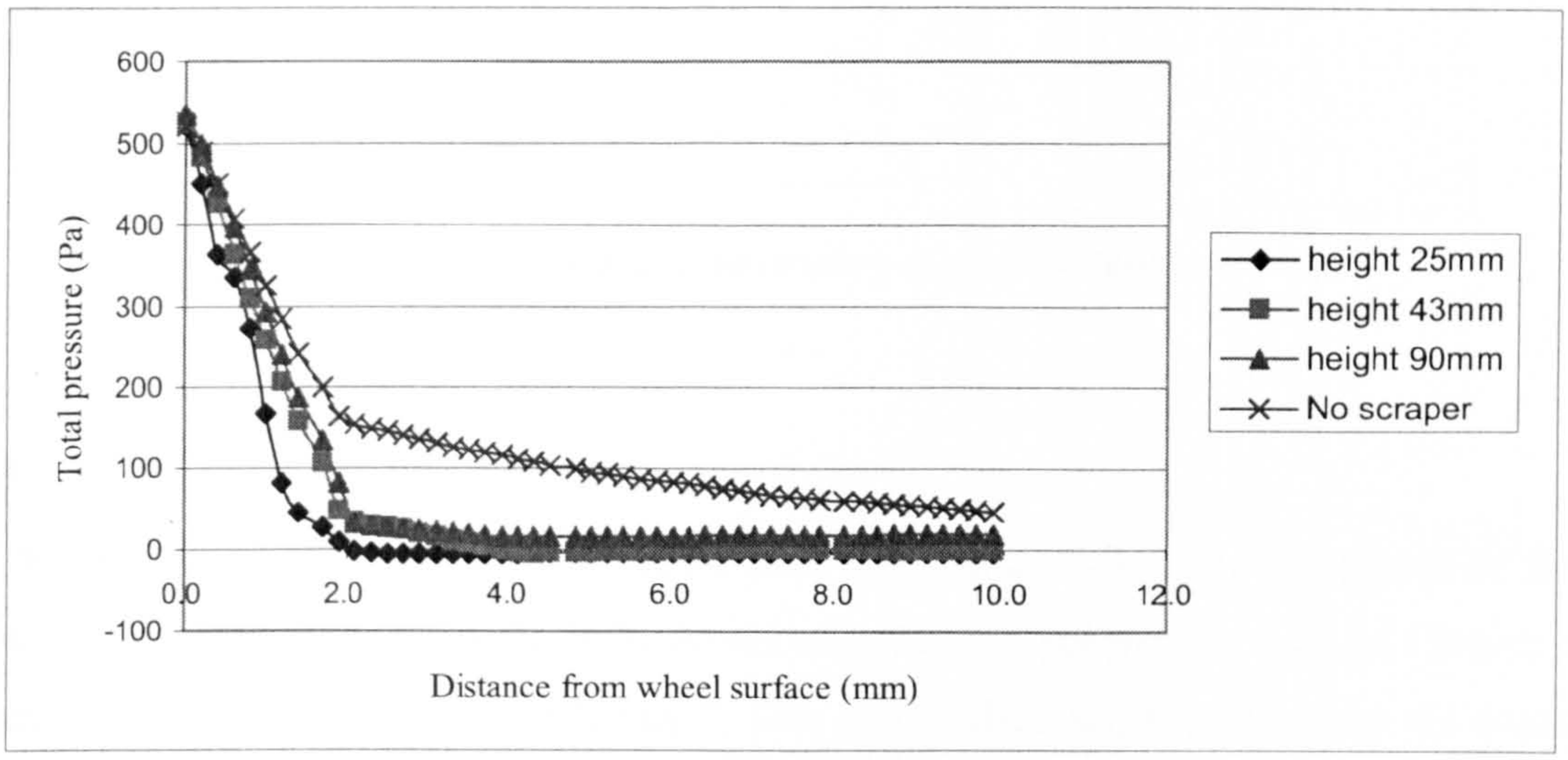

Figure 8-31 Total Pressure distribution in a horizontal direction immediately beneath the scraper (effect of the scraper height)

In this section, the effects on boundary layer flow for varying scraper positions were investigated. The simulation results show that if possible, the scraper should be placed as close to the wheel surface as is practicably possible, and the nozzle should be close to the scraper.

8.5 Recovery of the air boundary layer

When a scraper is applied to interrupt the air boundary layer in grinding, the recovery of the air boundary flow is the issue of interest and concern. For effective scraper application, the nature of air flow recovery needs to be clearly understood. This includes the recovery distance or angle (Figure 8-32). To date, this matter has not been fully investigated.

In this section, the recovery of the air boundary layer downstream of the scraper is investigated using CFD simulation.

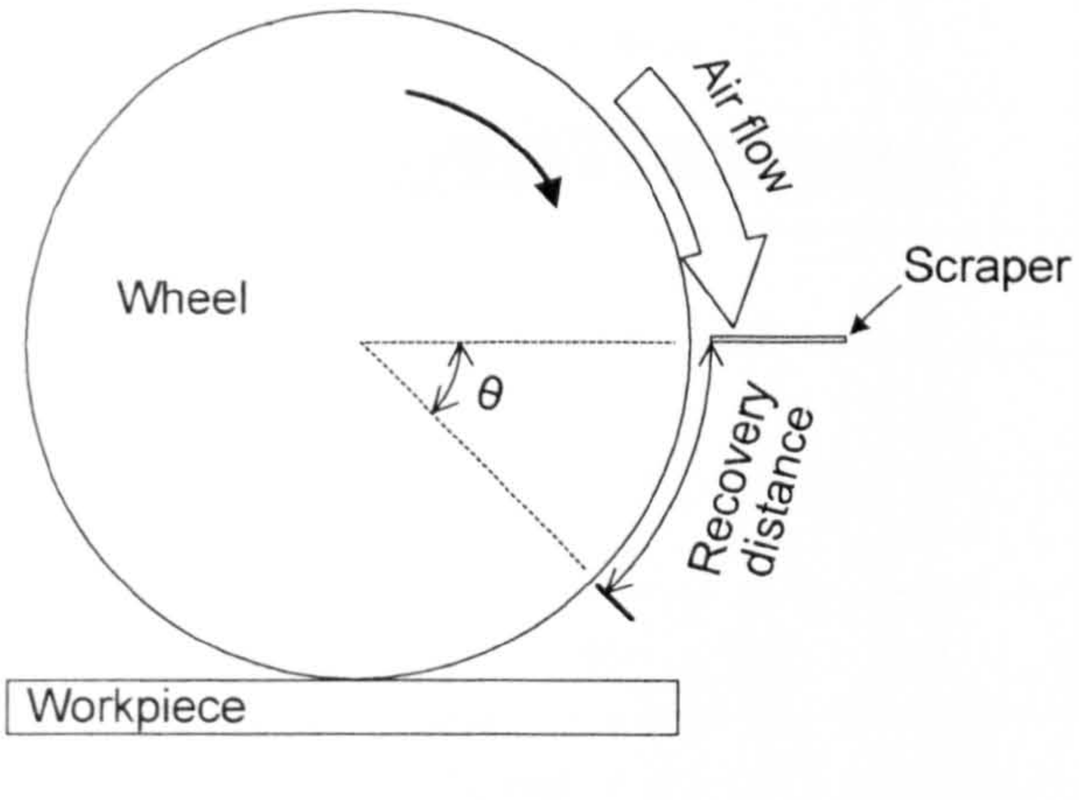

Figure 8-32 Schema of the recovery of air boundary layer

8.5.1 Recovery angle of the air boundary layer

The geometry of the simulation was as shown in Figure 8-32. The dimension of the wheel and scraper were similar to previous experimental parameters used in Chapter 6 and simulation parameters in Chapter 7. The wheel diameter was 180 mm, the wheel width was 25 mm, wheel surface roughness Rt was 1 mm; the scraper length was 30 mm, width was 30 mm, thickness was 1 mm, and the distance from the wheel surface was 1 mm.

The parameter 'Total Pressure' was used to identify the recovery angle. The pressure distribution was shown along a circular arc with radius 93 mm, i.e. 3 mm from the wheel surface. Figure 8-33 shows the recovery angle of the air boundary layer: there are two curves in this figure, one is the pressure distribution around the wheel without a scraper, and the other is the pressure distribution with a scraper. Pressures are shown from a position 30° upstream of the scraper. At a position immediately ahead of the scraper, the pressure increases a little, but immediately after the scraper, the pressure reduces sharply. At a small angle after this point, the pressure begins to increase steadily. This means that the air boundary layer is recovering. At the angle of 180 degrees, the pressure has fully recovered and it is approximately the same as that without the scraper.

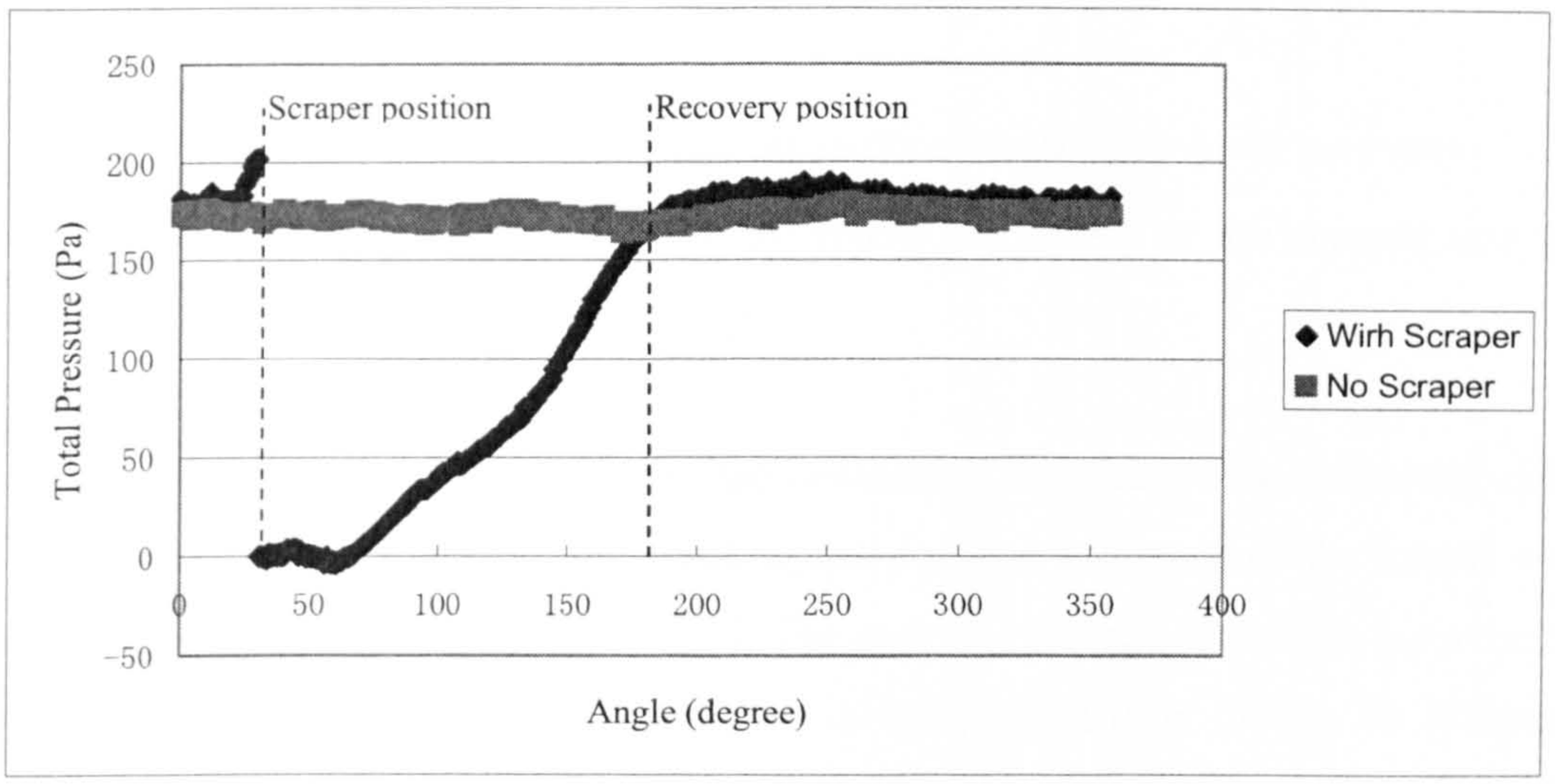

Figure 8-33 Recovery angle of air boundary layer without workpiece (pressure distribution)

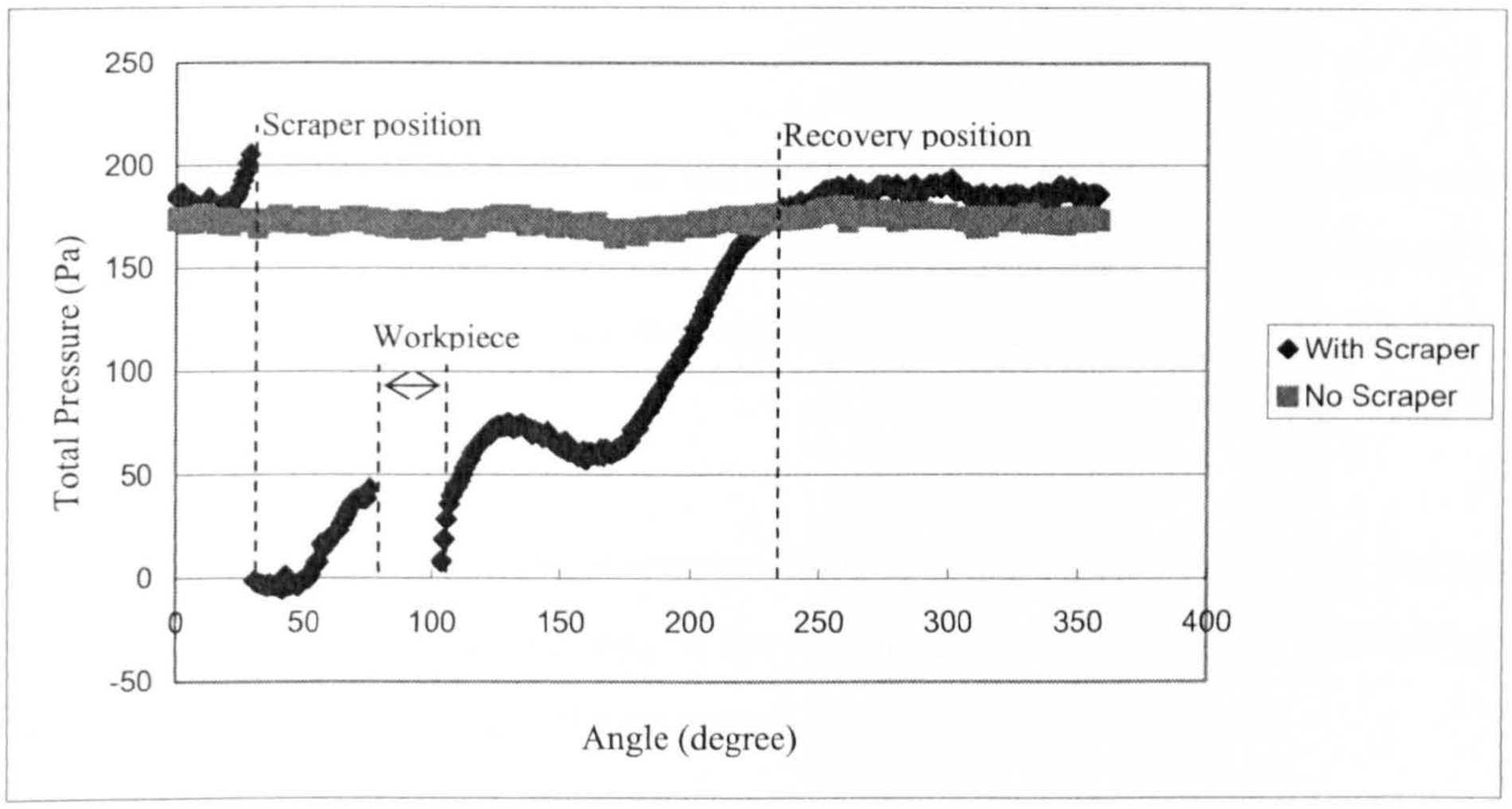

Figure 8-34 Recovery angle of air boundary layer with workpiece (pressure distribution)

The simulation results show that the air boundary layer completely re-establishes itself at an angle of 150 degrees after the scraper.

Figure 8-34 show the pressure distribution with a workpiece and the scraper positioned 43 mm above it. It can be seen that the pressure does not fully recover in the grinding entry region. When approaching the workpiece, the pressure only recovers to a value of approximately one third of the full pressure. After the workpiece, the air boundary layer begins to recover again.

8.5.2 Effect of the scraper size and position on the air boundary layer recovery

Further simulations were undertaken to investigate the effect of the scraper size and position on the air boundary later recovery.

In summary, the size of the scraper and the position of the scraper has no strong effect on the air boundary recovery in the grinding entry region and most of the results were very similar to those shown in Figure 8-33. The reason is that the arc length between the scraper and contact region is small and there is insufficient time for the air boundary layer to fully recover. However, the application of the scraper can improve the situation by reducing the air velocity and pressure.

8.6 Conclusions

In this chapter, the research focused on the scraper application. The effect of the scraper on the air velocity and pressure distribution was reported, and the knowledge of these distributions provides the basis for strategies to ensure maximum penetration by the fluid.

The air pressure distribution was illustrated both in the area just above the workpiece through the grinding contact zone and in the wheel middle section. The function of the scraper was confirmed to reduce the pressure.

The effect of the scraper size and position was also illustrated in this chapter. The results showed that for all size scrapers the pressure in the grinding entry region along the workpiece surface can be reduced by more that 50% compared to the situation not using a scraper. Immediately beneath the scraper, the pressure reduces to nearly zero. The different width of scrapers does not show any significant distinction on the pressure distribution along the measurement line both in the grinding zone and under the scraper. The narrowest width of scraper used was that equal to the wheel width, and this size scraper can function very well compared to wider scrapers, it is therefore not necessary to use a scraper much wider than the wheel in fluid delivery. If the scraper length is too short, it does not block the air flow very efficiently; therefore the nozzle orifice should

be placed just under the scraper or a longer scraper used. The scraper should be placed as close as possible to the wheel surface if the operation is practicable in grinding, since the pressure decreases more quickly as the scraper is positioned closer to the wheel surface.

The area immediately after the scraper would be a good position for the fluid to be directed as it is a region of lowest-pressure and fluid penetration should be easiest.

The air boundary layer recovery angle has also been investigated, and the results show that the angle at which the layer fully re-establishes itself is at an angle of 150 degrees after the scraper. Therefore, in the narrow arc between the scraper and grinding entry region, the air boundary layer is not able to fully recover.

The size of the scraper has no strong effect on the air boundary layer recovery in the grinding entry region. The air boundary layer recovers more with the longer distance after the scraper along the wheel surface, so the scraper should be positioned close to the workpiece surface if it is practicable.

Chapter 9 Shoe Nozzle Design and Application

9.1 Introduction

The adequate wetting of the grinding wheel and the workpiece is fundamental for the transport of the grinding fluid into the contact zone. In industrial practice, free jet nozzles are often used for supplying the grinding fluid. An efficient alternative, even for lower grinding fluid flowrate, are shoe nozzles. This type nozzle fits nearly exactly to the wheel profile and encloses the grinding wheel on one side or three sides (Wittmann, et al., 2002).

Due to the speciality of the shoe nozzle and its setting position, when it is employed in grinding fluid delivery, the upper surface of the shoe nozzle can be regarded as an air scraper, which can break the air flow. Therefore, the fluid will flow more easily under this "air scraper", the grinding wheel is wetted and the pores can be filled with coolant just before penetrating the grinding contact zone (Figure 9-1).

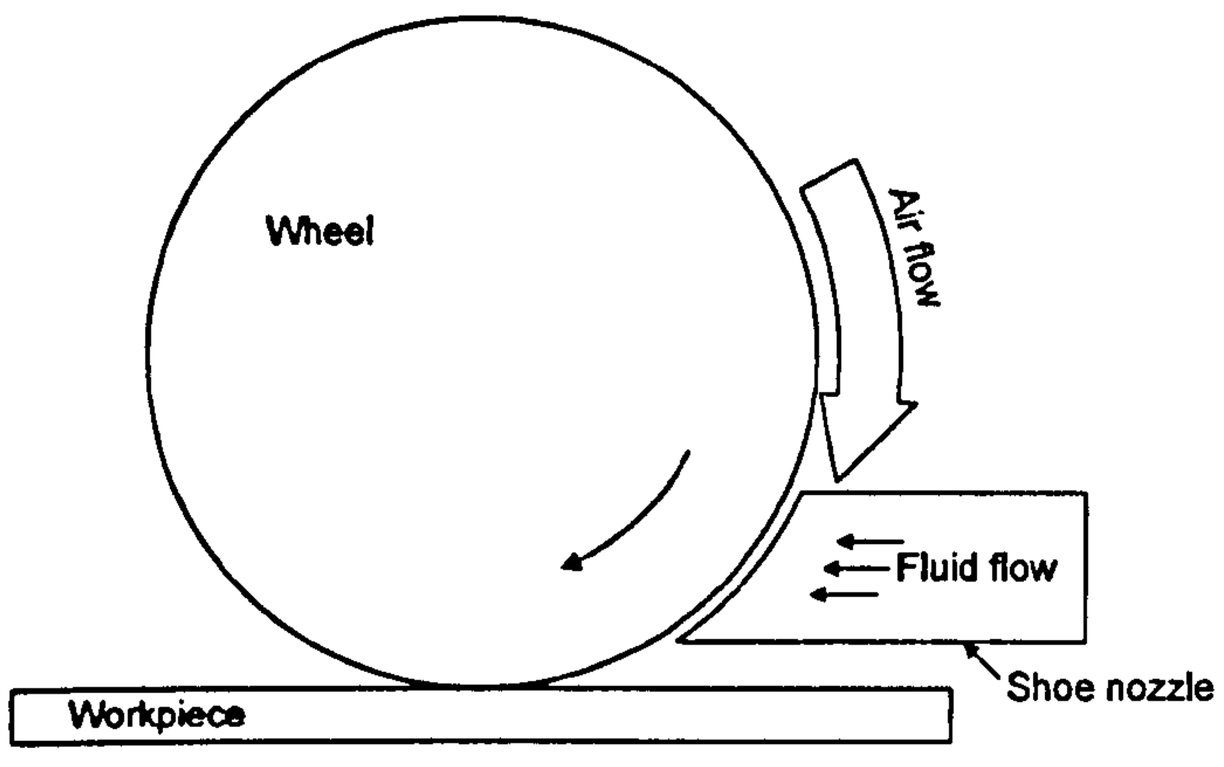

Figure 9-1 Illustration of a simple geometry shoe nozzle configuration

In this situation, the rotating grinding wheel accelerates the fluid to the wheel circumferential velocity. The total amount of coolant supplied can be limited to the volume necessary to fill the whole pore space of the wheel surface because a further supply shows an insignificant effect on the work result. The geometry of the shoe nozzle is determined by the grinding wheel profile and adjustment to a changing wheel

diameter is required; hence, there is only a limited flexibility in the application of the shoe nozzle.

In this chapter, the shoe nozzle application will be investigated using the CFD simulation. The character of flow in the shoe nozzle will be analyzed and the results used to aid in the design of a high-efficiency shoe nozzle. The effect of shoe nozzle position will also be simulated.

9.2 Review of the Shoe Nozzle

Several investigations deal with the comparison of different coolant nozzle types. Often, important characteristic issues such as coolant flowrate, the pressure directly in front of the nozzle or the outlet cross section are not reported, so that comparability of results is not always possible. However, in general, it is accepted that shoe nozzles can lead to lower tool wear and less burning with generally lower coolant flowrate and lower pressures in comparison to free jet nozzles. Moreover, the coolant flowrate can be reduced in comparison to external flooding, leading to a similar process quality with internal coolant supply strategies; a combination of internal and external supply leads to an enhancement of quality and economy. The use of a shoe nozzle leads to wetting of the grinding wheel directly in front of the contact zone over a comparably large area. By the rotation of the wheel and the resulting centrifugal force on the coolant in the porous layer, a part of this coolant leads to cooling and lubrication in the contact zone. This provides another transport mechanism for the coolant into the contact zone (internal coolant supply), in addition to the drag effect by the grinding wheel rotation (Brinksmeier, et al., 1999).

Prior work has also been published on jet nozzles, shoe nozzles and chambers, with regards their overall grinding performance. Shoe nozzles have been shown to be extremely effectively. Investigations prove the capability of this nozzle form to reduce the wheel wear as well as the thermal degradation of the workpiece with less required flowrate of the coolant (Marinescu, et al., 2007).

Brinksmeier, et al. (2000) stated that the immense benefit of using the shoe nozzle is the obvious reduction of the necessary coolant quantity. Because of the side cover of the grinding wheel, the huge flowrate normally used for an adequate coolant supply of the

contact area when using a free jet nozzle are avoided. This low quantity is sufficient for a coolant and lubrication effect in the contact zone and for swarf transport as well. In contrast to a shoe nozzle, for a specific material rate and a coolant flowrate, the coolant supply to the contact zone with a free jet nozzle cannot be considered to be adequate due to the sharp tensile residual stress profile measured in the subsurface layer. An additional advantage is a smaller coolant supply system with less energy and space consumption. The investigations show that the coolant flowrate can be minimized considerably when using a shoe nozzle.

Akiyama, et al. (1984) also thought a shoe nozzle was an excellent method for overcoming these limitations because the large contact area between wheel and the fluid allows good penetration into the wheel. According to the power flux rig (PFR) tests, it shows that the shoe nozzle can obtain a larger power flux compared with other nozzles, because shoe nozzles are always set-up very close to the wheel surface.

Klocke, et al. (2000) stated that the shoe nozzle is especially suitable for high-speed cBN grinding with oil. The nozzle tightly encloses the grinding wheel on three sides. The oil is fed under almost no pressure to a reservoir inside the nozzle. From here, it is accelerated by the grinding wheel to the circumferential wheel velocity, clinging to the surface of the grinding wheel. Because an increased coolant flowrate not only causes a rise in the total grinding normal force, but can also reduce friction only to the extent that the coolant actually penetrates into the grinding gap, it is advisable to avoid coolant flows which merely pass the grinding gap without being used. One means of meeting this requirement in the case of oil-cooled grinding processes is to employ a shoe nozzle. These can be used to feed the cooling lubricant almost directly into the grinding gap, not only reducing the cooling lubricant flow, using proper flowrate, also lowering the grinding normal force.

In practice, the disadvantage of shoe nozzles is that: they are difficult to adjust and re-adjust to the grinding wheel. Thus, it is difficult to keep them sealed against the wheel surface or to maintain a small enough gap between the wheel as the diameter reduces with wear (especially true with continuous dressing creep feed grinding) (Brinksmeier, et al. 2000, Webster, et al. 2002). Furthermore, the shoe is considered bulky for general purpose grinding and fixture. Nevertheless, due to the huge advantage of the shoe

nozzle method in grinding fluid delivery, some research was focused on how to optimise the application of the shoe nozzle.

Ramesh, et al. (2001) designed a coolant shoe nozzle. The coolant shoe nozzle covers nearly $1/6^{th}$ of the grinding wheel. The upper portion was built with a constantly loaded block for scraping the air curtain and the unit was designed with three orifices. The upper orifice was configured to break the built in air curtain, while the lower orifice was designed to give a coolant coating and a penetrating supply of coolant to the grinding zone. Ramesh's results shows that the coolant shoe method offered the following advantages:

1) Improvement to grinding efficiency: the power consumed per unit contact area was reduced by 4-5 times depending upon the grinding conditions, grain size, coolant type and grinding mode. Meanwhile, the grinding forces were reduced by 40-60%. The reduction in the ratio Ft/Fn was a clear indication of the lower friction in the rubbing and grinding region. The coolant shoe method passes the coolant between the layers and produces a ground surface that was free from thermal damage and strong burn.

2) Improvement to surface finish: The onset of localized grinding stress was less and the ground surface possessed streaks and grooves with a minimal amount of micro-voids. The roughness was reduced by nearly 10-20%. Foreign particle adherence to the grinding wheel is lessened due to the penetration of the coolant. This is due to the temperature reduction of the grinding region.

Powell (1979) stated that, to keep the penetration required at the shoe nozzle to a minimum, the shoe nozzle should be positioned as near to the workpiece as possible. The shoe nozzle should also be positioned as close to the wheel as possible to reduce the leakage gap between wheel and shoe. Leakage flow can be a significant portion of total flow and ensuring a minimum gap between the wheel and shoe is essential. Therefore, he gave the following suggestions on the design of shoe nozzles:

- Ascertain the minimum possible angle between the end of the shoe and the start of the cutting zone.
- Calculate the minimum expected saturation penetration for the expected conditions.
- Construct a graph of flowrate against shoe length for a range of shoe pressures spanning the pump characteristic.

- For each pressure used in the above calculation there will be a limiting flowrate, which may be determined from the pump characteristic.

Brinksmeier, et al. (2000) and Heinzel, et al. (2002) introduced the light sheet method for visualizing the flow in coolant nozzles and using this method for flow optimization of the nozzle geometry. To establish an optimum flow behaviour of the coolant on the grinding wheel/nozzle interface, they designed interior guiding elements to affect the flow inside the shoe nozzle. Shoe nozzles without guiding elements and with straight, tangential, and radial guides were investigated. The evaluation of the residual stress profiles made clear that when using shoe nozzle a comparatively low flowrate is sufficient to supply the grinding arc adequately with grinding fluid. In addition, the investigations verify that an increase of the grinding fluid flowrate does not lead automatically to a better cooling effect. The influence of guiding elements on the residual stress profile shows that the different types of shoe nozzles leading to an optimum process result at different coolant flowrate. Hence, the idea was derived to design a shoe nozzle with externally adjustable guiding elements. Different positions of the guiding elements depending on the coolant flowrate would be possible. This could be important for an optimization of a multistep grinding process with varying material removal and coolant flowrate.

Klocke, et al. (2002) investigated the coolant flow inside a shoe nozzle by using FE methods. The maximum speed of the lubricant inside the shoe nozzle was calculated. The necessary coolant flow to achieve a nearly laminar flow at the end of the nozzle was also estimated. The simulated flow conditions correlate closely with the results of practical tests using the plexiglass shoe nozzle. The FEM tool for this simulation was FLOTRAN, which is part of the software package ANSYS.

9.3 Shoe Nozzle Design

The advantages of shoe nozzle have been discussed, and some investigation on how to optimise the shoe nozzle application has been completed by previous research. However, the guidance on shoe nozzle designs, for example, the size of the shoe nozzle, the position of the shoe nozzle in grinding, is still not very clear.

Powell (1979) made good suggestions for shoe nozzle design, but some of them are difficult to be carried out in practice. For example, when the angle between the end of the shoe and the start of the cutting zone is too small, he proposed that the nozzle can work at the start of the grinding. However, with the wheel wearing and the wheel dressing, the start 'minimum angle' will disable the shoe nozzle due to the geometric configuration of the wheel and shoe nozzle. Taking into account the grinding process safety, the gap between the wheel and the shoe nozzle also cannot be minimized due to the rotating wheel expansion and the vibration of the system.

Heinzel, et al.'s (2002) light sheet method to visualize the flow in shoe nozzles and using this method to optimize the nozzle geometry are potentially useful tools to investigate the shoe nozzle design. However, their experiments were limited to the guide element design within the nozzle. An estimation of the performance of different guides was made by only comparing the residual stress of the workpiece surface.

Klocke, et al. (2002) showed that FE methods provided a means to investigate the coolant flow inside a shoe nozzle. This method helps to estimate the effect of the fluid flow condition on the fluid delivery.

In this chapter, the CFD simulation will be used to investigate the shoe nozzle flows. The analysis will include shoe nozzles of different geometry and dimension. The fluid pressure in the nozzle and at the wheel/nozzle interface is also analysed. When shoes nozzles are applied in practice, the depth of the fluid penetrating the wheel can be estimated using the model shown in Figure 9-2.

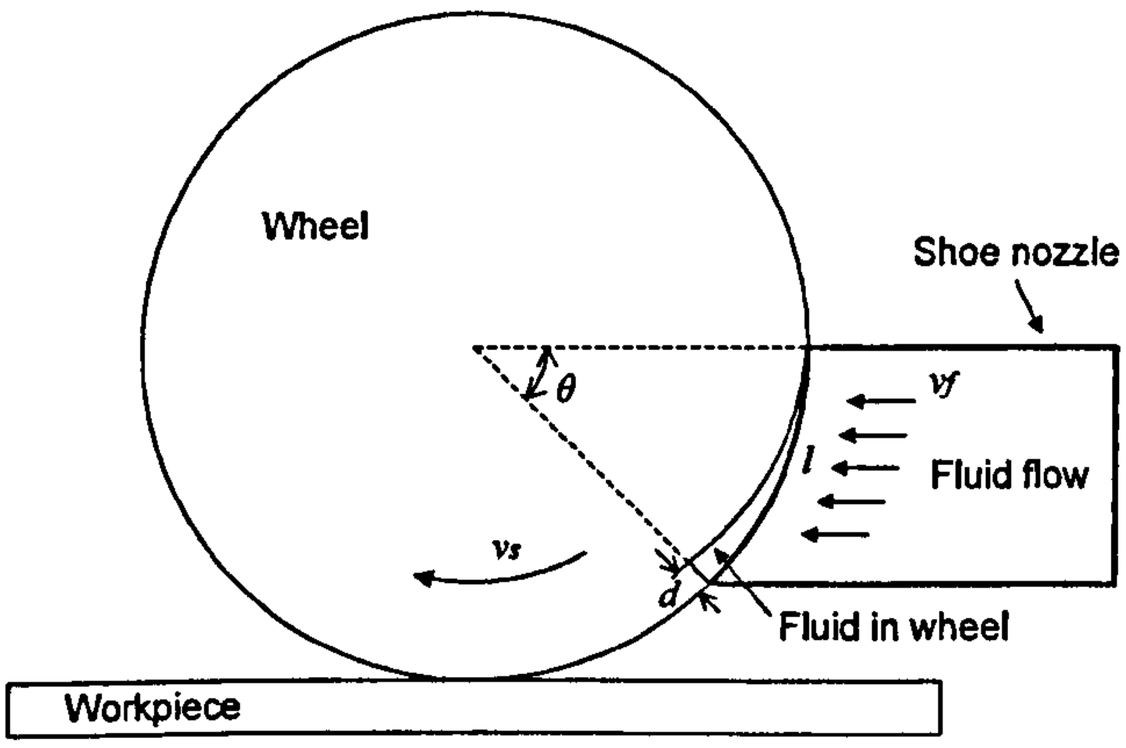

Figure 9-2 Penetration depth of the fluid in shoe nozzle application

The following assumptions should be made before the calculation: the shoe nozzle covers the grinding wheel completely (no gap between the nozzle and the wheel); the velocity of fluid penetrating into the wheel in wheel radial direction is same as the mean velocity of fluid in the shoe nozzle, i.e. if the wheel speed is v_s and the arc length of the interface of the wheel and the shoe nozzle is l, each point on the wheel surface will use l/v_s second to pass the interface. When one point on the wheel surface is in the interface zone, the fluid will enter the wheel with certain velocity v_f. Therefore, the penetration depth d of the fluid into the wheel can be calculated using the following equations:

$$d = \frac{l}{v_s} v_f = \frac{v_f}{v_s} l \tag{9.1}$$

Since $l = \pi D\theta$

$$d = \frac{v_f}{v_s} \pi D\theta \tag{9.2}$$

Where, D is wheel diameter, θ is the arc angle of the interface.

When using the shoe nozzle, $v_f << v_s$, so the fluid penetration depth $d << D$. For example, if

the wheel diameter is 200 mm;

the wheel speed v_s is 25 m/s;

the fluid velocity v_f is 1 m/s;

the θ is $\pi/8$,

the penetration depth is only d = 1 mm, moreover, this value is obtained in the ideal situation.

Actually, the true penetration depth should be less than 1 mm in practice because the shoe nozzle cannot 'seal' the wheel surface, and the fluid penetrating velocity is not same as the fluid velocity in the shoe nozzle taking account of the fluid leaking in the interface between the wheel and the nozzle.

Because the porous wheel module cannot be constructed, in the simulation, the solid wheel with a rough surface will be used to replace the porous grinding wheel. This has no strong effect on the fluid flow in the nozzle due to the fact that in practice very little fluid penetrates beneath a depth much greater than a single grain diameter in a porous wheel.

9.4 Simulation geometry of shoe nozzles

The size of the grinding wheel used in the simulation in this chapter is the same as that used in the experiments described in Chapter 6. The diameter of the grinding wheel was 180 mm, and its width was 25 mm. Water was used as the grinding fluid in the simulation.

There were three shoe nozzles applied in the simulation with different geometries: for simplicity these are labelled: shoe nozzle A; shoe nozzle B and shoe nozzle C. The thickness of the shoe nozzle walls was ignored in the simulation. Shoe nozzle width in the wheel axial direction was the same as the wheel width in each case. The dimensions and position of shoe nozzle A is shown in Figure 9-3. The vertical dimension of the nozzle was 30 mm. The diameter of pipe connected to the shoe nozzles was 21 mm. The gap between the nozzle orifice and the grinding wheel surface was either 1 mm or 2 mm depending on the simulations considered. The bottom surface of the nozzle was 10 mm from the workpiece upper surface.

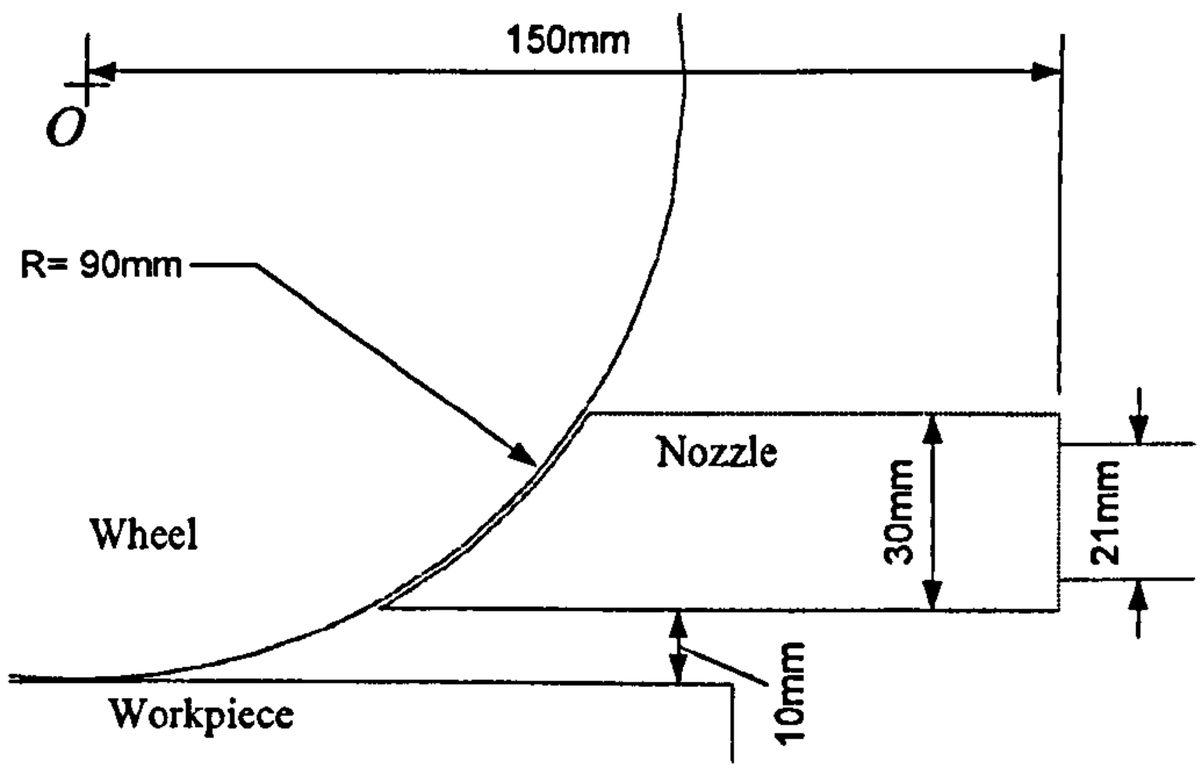

Figure 9-3 Dimension and position of shoe nozzle A

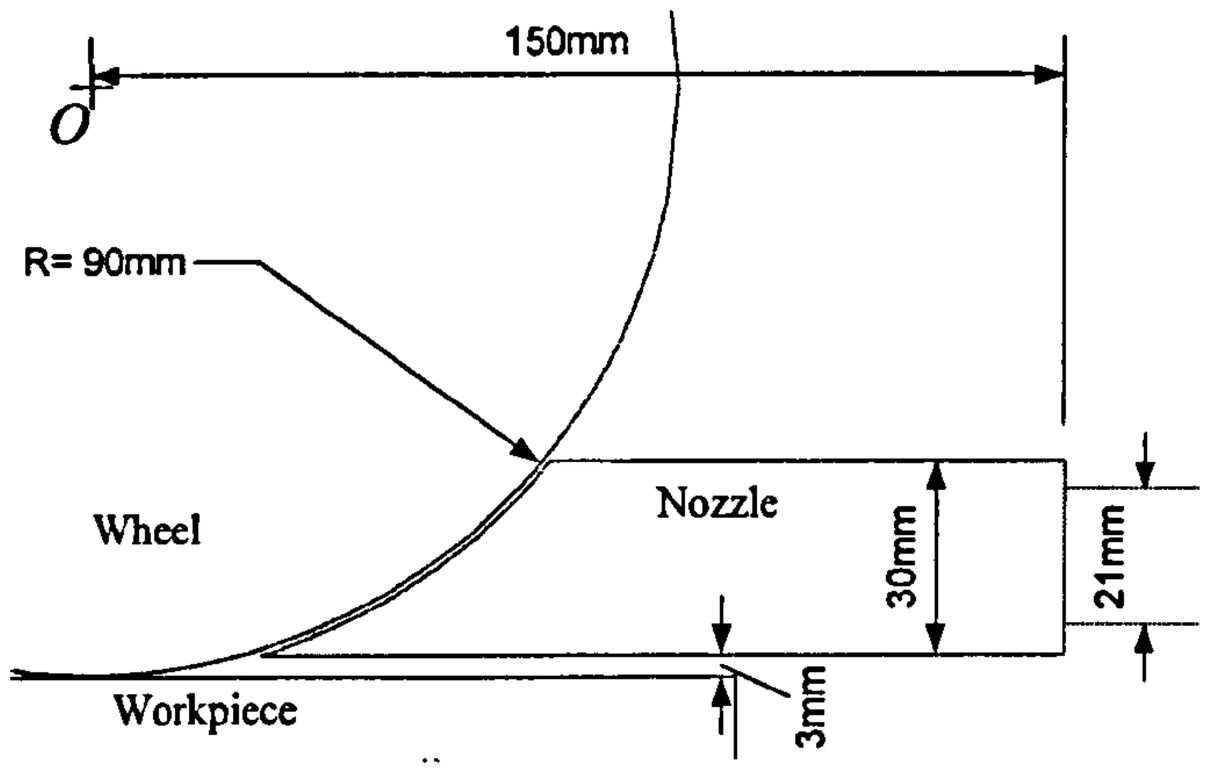

Figure 9-4 Dimension and position of shoe nozzle B

The dimension and position of nozzle B is shown in Figure 9-4. The basic dimension of nozzle B is the same as that of nozzle A. However, nozzle B is positioned closer to the workpiece surface, the distance to it being 3 mm. This change resulted in nozzle B having a larger arc of coverage over the wheel surface, since the nozzle orifice must surround and enclose the wheel surface. The larger arc of coverage would provide more time for fluid to penetrate into the wheel and be driven by the wheel. Meanwhile, the fluid is closer to the grinding contact zone when it exits the gap. This has the effect of reducing the volume of the fluid deviating from the wheel surface due to centrifugal forces.

Shoe nozzle C is shown in Figure 9-5. Its arc length of coverage is larger than that of nozzle B. The diameter of the pipe connected to the nozzle was 21 mm.

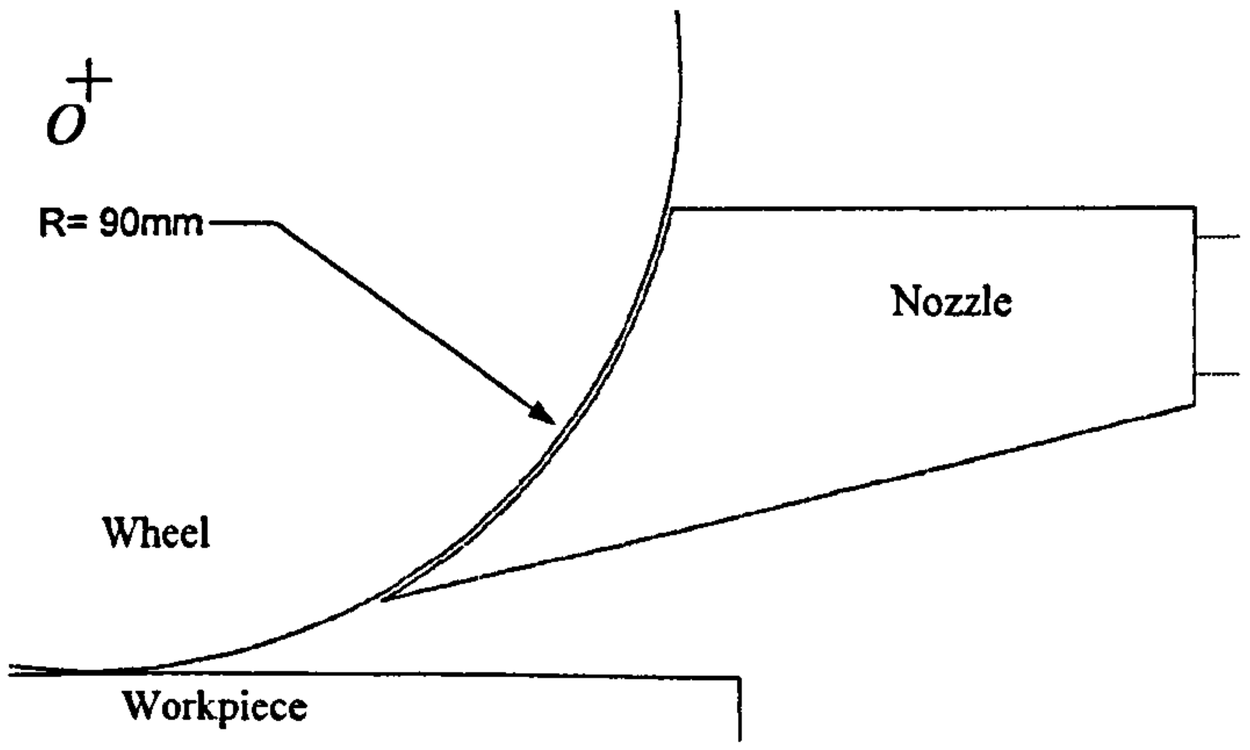

Figure 9-5 Dimension and position of shoe nozzle C

The effect of shoe nozzle geometry on nozzle interior fluid flow is investigated comparing simulation results of these three different shoe nozzles.

9.5 Air flow around the shoe nozzle

An advantage of the shoe nozzle is that it prevents the air boundary layer affecting fluid flow at the wheel surface. This phenomenon is shown in Figure 9-6: the air velocity distribution around the wheel and shoe nozzle is shown as vector plots. It is observed that in the case of a small gap (gap=1 mm) between the nozzle and wheel surface, and wheel speed of 30 m/s air flow was disturbed by the nozzle upper wall and did not penetrate the gap. Therefore, a high fluid velocity is not essential, because the fluid inside the nozzle may flow to the wheel surface quite readily. This design can save on electrical power and improve the economics of the fluid delivery system.

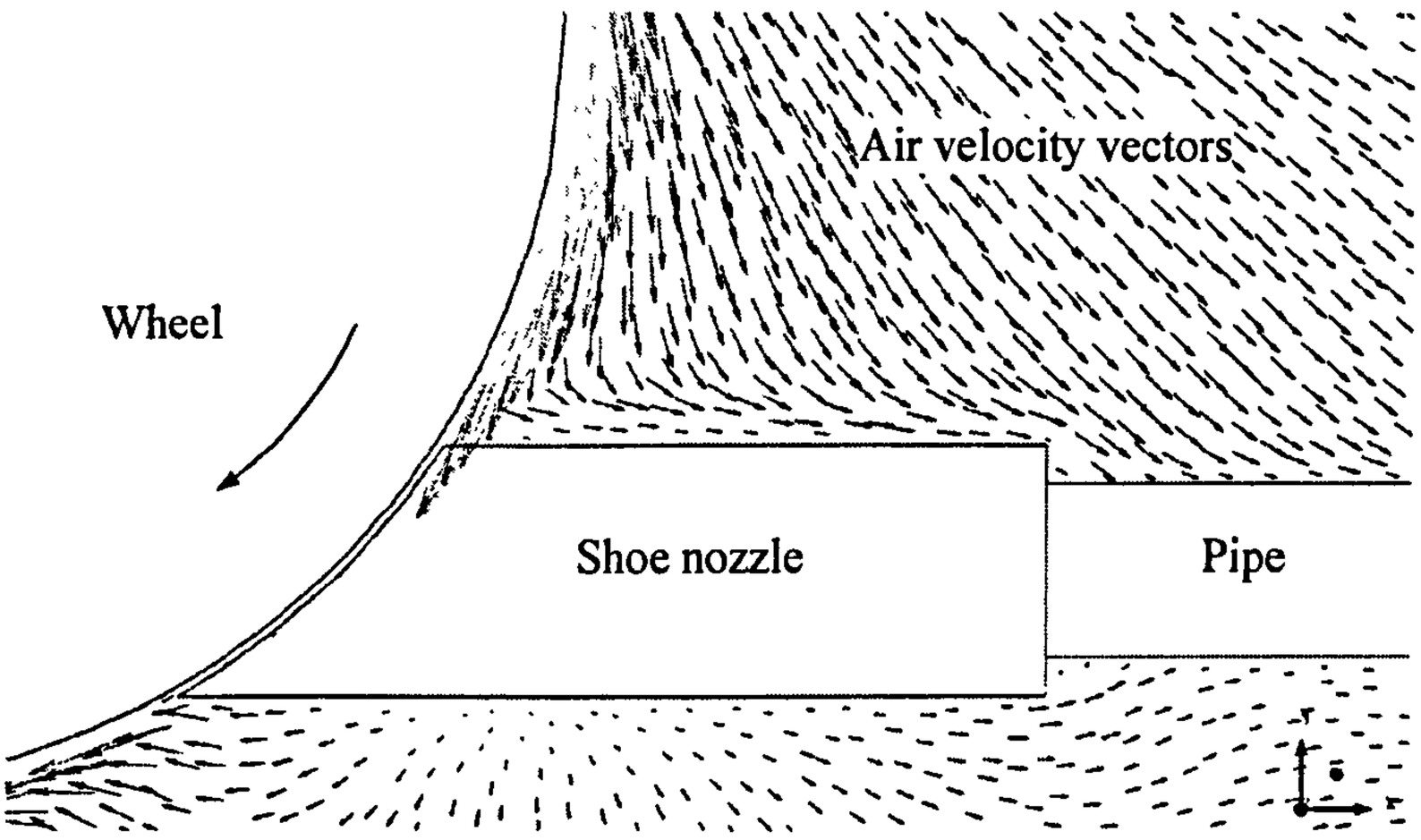

Figure 9-6 Air flow around the shoe nozzle

In the area beneath the nozzle, the boundary layer cannot recover due to the short distance before the grinding contact zone. In such a case it can be reasoned that the fluid would cover the entire wheel surface immediately after exiting the nozzle orifice and much of this is retained up to the point of the contact zone. This is supported by results in Figure 9-6.

9.6 Fluid flow in different shoe nozzles

Figure 9-7 shows the fluid flow in shoe nozzle A. Wheel speed is 30 m/s, input fluid velocity (fluid pipe velocity) is 3 m/s and gap size is 1 mm. The fluid travels through the pipe and then flows forward to the wheel directly. At the gap area between the wheel and nozzle orifice, the fluid was directed and driven by the rotating wheel surface, and out from the gap with a higher velocity approaching the wheel speed. Inside the shoe nozzle, the flow has no directional change until it approaches the wheel surface. The velocity of the flow close to nozzle bottom surface was lower than in other areas. This is due to wall shear stresses and to the high pressure zone at the leading edge of the lower surface.

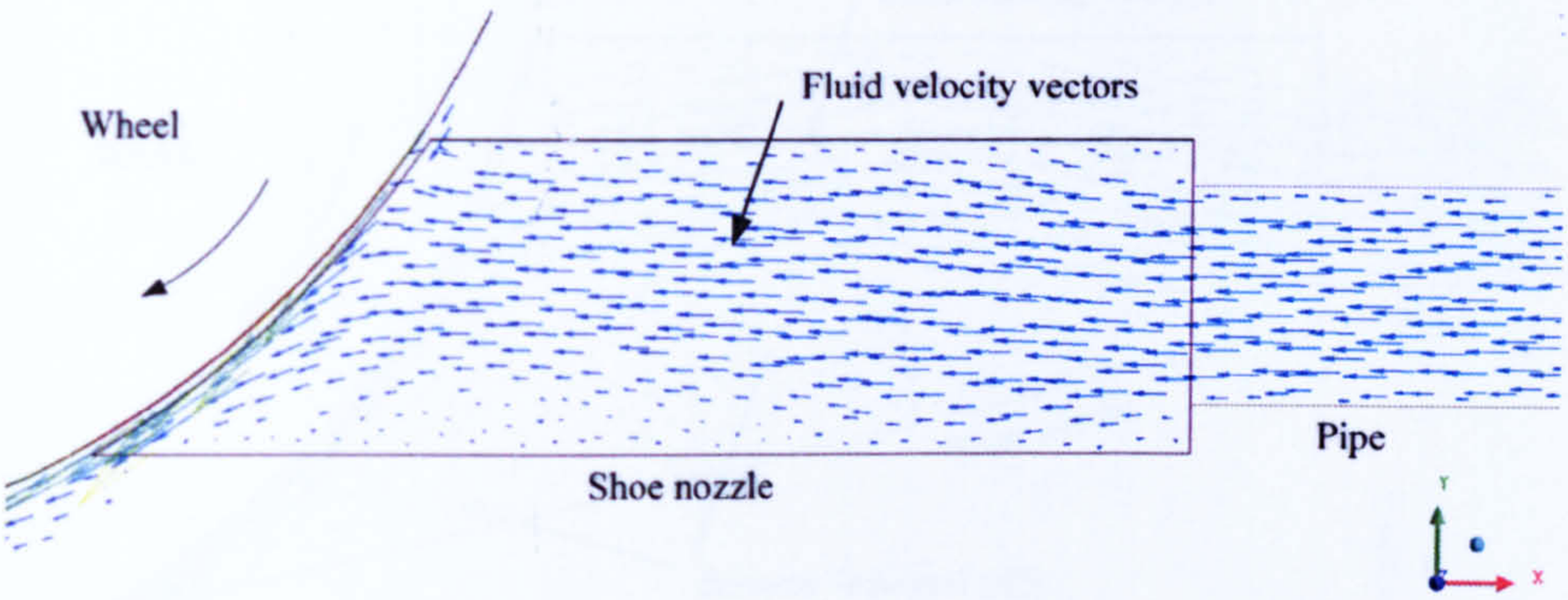

Figure 9-7 Fluid flow in the shoe nozzle A (v_s=30 m/s, pipe velocity =3 m/s)

The situation of fluid flow in shoe nozzle B is similar to that of fluid flow in nozzle A, except for the longer arc of coverage (Figure 9-8).

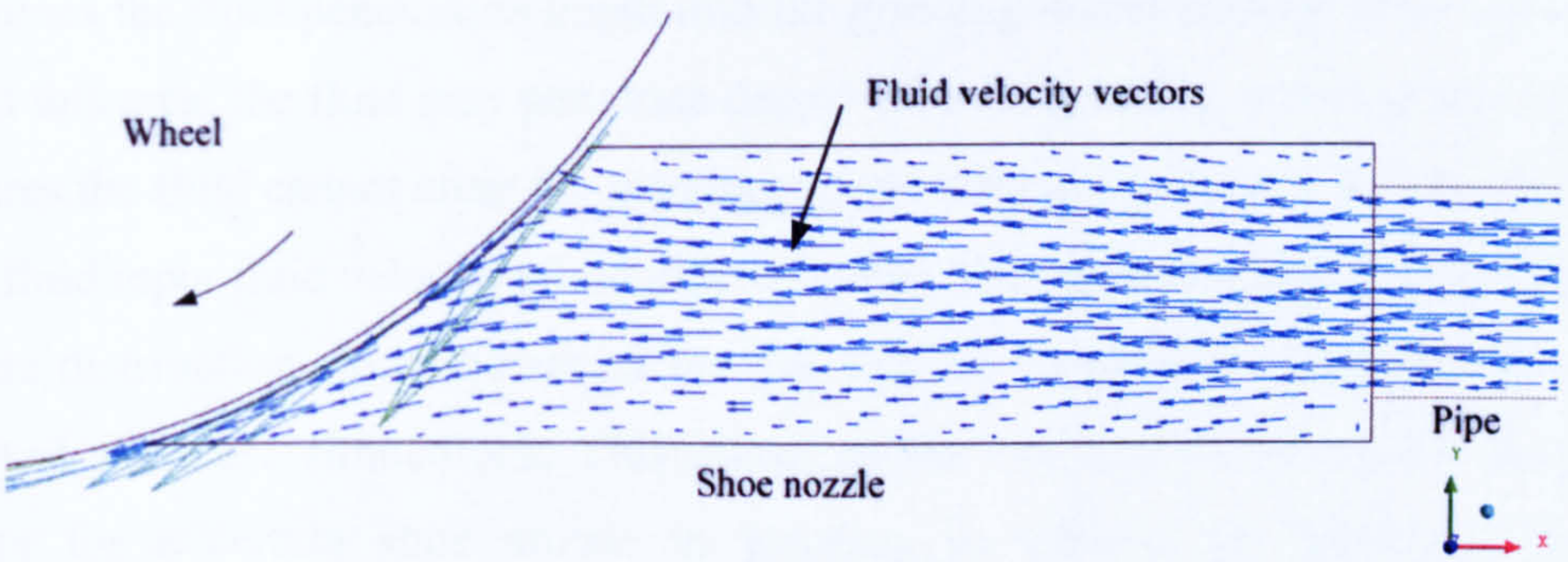

Figure 9-8 Fluid flow in the shoe nozzle B (v_s=30 m/s, pipe velocity =3 m/s)

In shoe nozzle C (Figure 9-9), the reverse flow and eddy flow is evident. The reason for this is that due to the longer arc of coverage a greater volume of fluid was accelerated by the wheel to a higher velocity. It is observed that as the fluid flow approaches the nozzle exit in the lower section it is unable to discharge because of the high pressure area in that region. As a result fluid is forced to return to the centre of the nozzle along the nozzle lower surface resulting in eddy flows. As a result turbulent flow appears within the nozzle. For optimal fluid delivery, turbulent flow should be avoided; hence reverse flow should also be prevented.

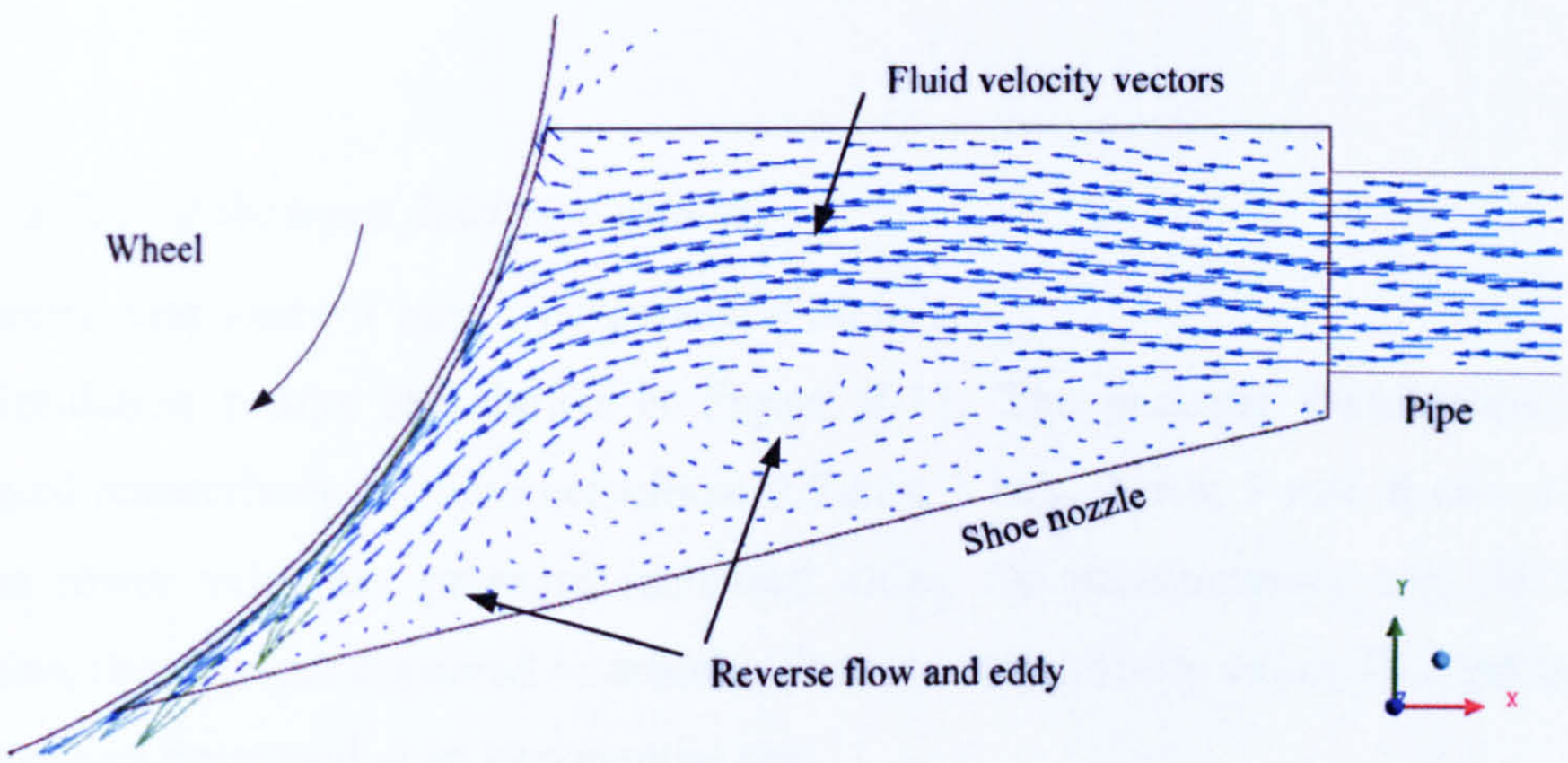

Figure 9-9 Fluid flow in the shoe nozzle C (v_s=30 m/s, pipe velocity =3 m/s)

9.7 Fluid pressure on wheel surface in the gap

The fluid pressure in the gap between the shoe nozzle and the grinding wheel determines the fluid penetration depth into the grinding wheel surface. If the pressure is high in this area, the fluid may penetrate deeply into the grinding wheel, whereas at low pressures the fluid cannot enter the grinding wheel effectively. In this section, the effect of the fluid input fluid velocity (fluid pipe velocity), the gap size and wheel speed on the pressure distribution along the arc of the gap will be investigated. Shoe nozzle A was employed for these simulations. This investigation can help to define the fluid pipe velocity for a certain shoe nozzle in grinding to achieve an optimized pressure distribution on the wheel surface along the arc of the gap.

Pressure measurements where obtained from the middle section of the wheel surface in the arc gap as shown in Figure 9-10.

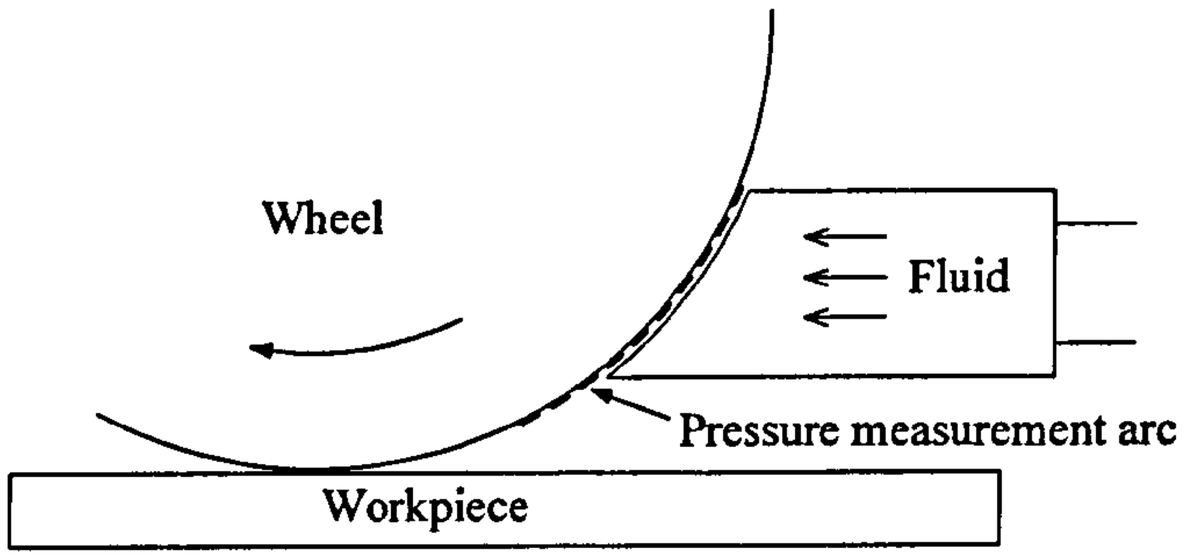

Figure 9-10 Position of the pressure measurement arc

9.7.1 Effect of the input fluid pipe velocity

Parameters: Gap size = 1 mm, wheel speed = 30 m/s.

The simulation results are shown in Figure 9-11. The pressure distributions were calculated respectively for pipe velocities: 0.5 m/s, 1 m/s, 2 m/s, 3 m/s, 6 m/s, 12 m/s. For the lower velocities pressure increased along the measurement arc. At higher velocities, the pressure appeared to achieve a constant maximum value. Beyond the gap fluid pressure decreased at an exponential rate.

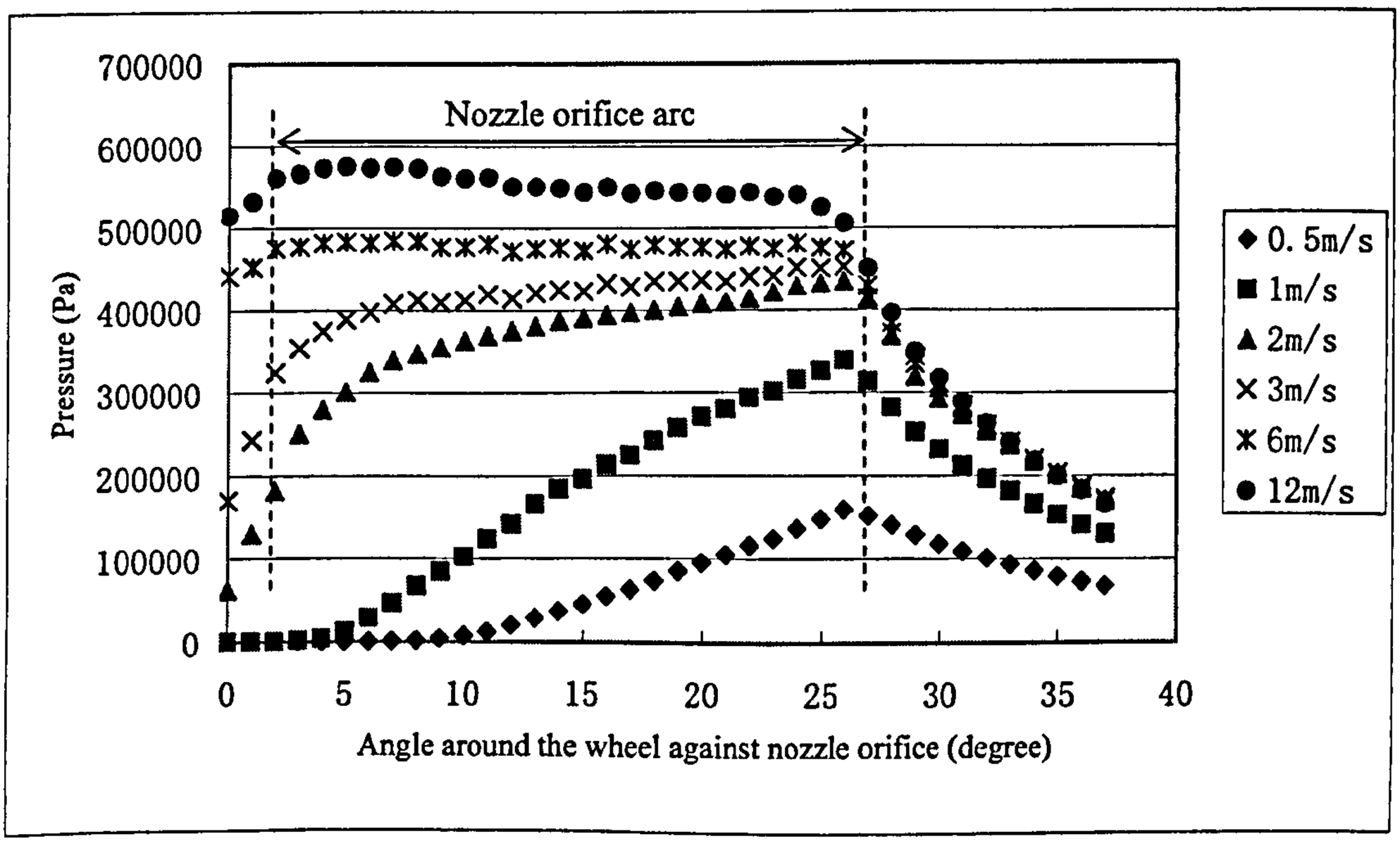

Figure 9-11 Pressure distribution with different pipe input fluid velocities

In general, the pressure on the wheel surface in the gap increased with increased fluid pipe velocity. One can reason therefore, that if the aim is to increase fluid penetration pressure on the wheel surface, then one method is to enhance the fluid pipe velocity. However, the pressure increase is not linear with the pipe velocity increase. Such a relationship points to a value of fluid pipe velocity and penetration pressure optimised for energy efficiency.

Further, the fluid pipe velocity should not be too low, or the fluid cannot fill the nozzle, and in such a case, fluid penetration pressure is almost zero. Such an effect is shown in Figure 9-11, at a pipe velocity of 0.5 m/s or 1 m/s. This phenomenon can also be observed in Figure 9-12 and Figure 9-13. When the fluid pipe velocity is 3 m/s (Figure 9-13), the fluid is seen to fill the nozzle. In order to satisfy the requirement of fluid penetration, the fluid pressure along the gap should approximate to a constant maximum value.

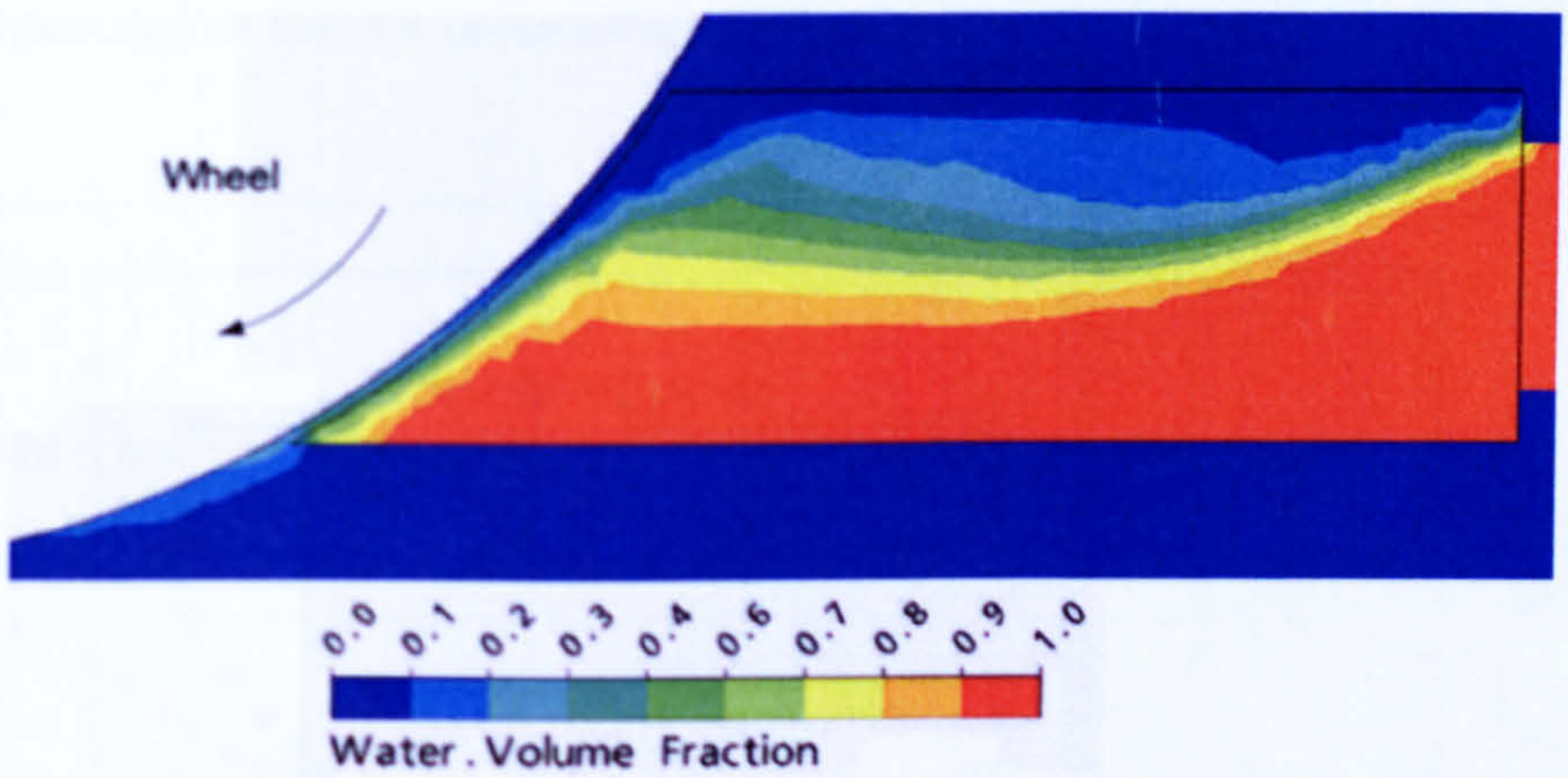

Figure 9-12 Water volume fraction distribution (Fluid pipe velocity 0.5 m/s)

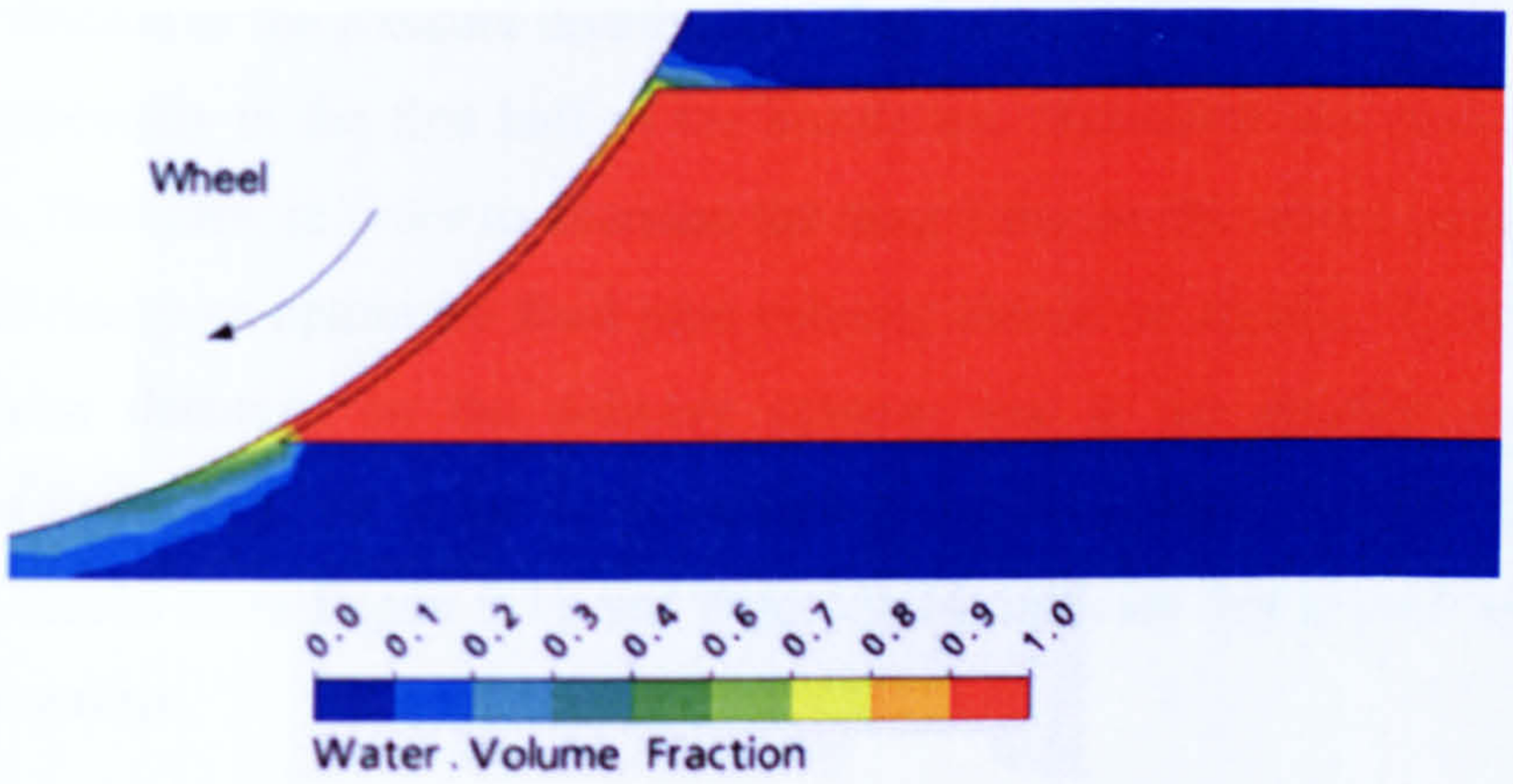

Figure 9-13 Water volume fraction distribution (Fluid pipe velocity 3 m/s)

When fluid pipe velocity is increased, the shear stresses on the fluid at the wheel surface increases. The magnitude of the shear stress will determine the drag force on the wheel, and the drag force will increase the grinding power required to ensure a constant rotational speed. Figure 9-14 shows the relationship between shear stress on the wheel surface with varying fluid pipe velocity. The value of shear stress was extracted from the same position as that for pressure measurements.

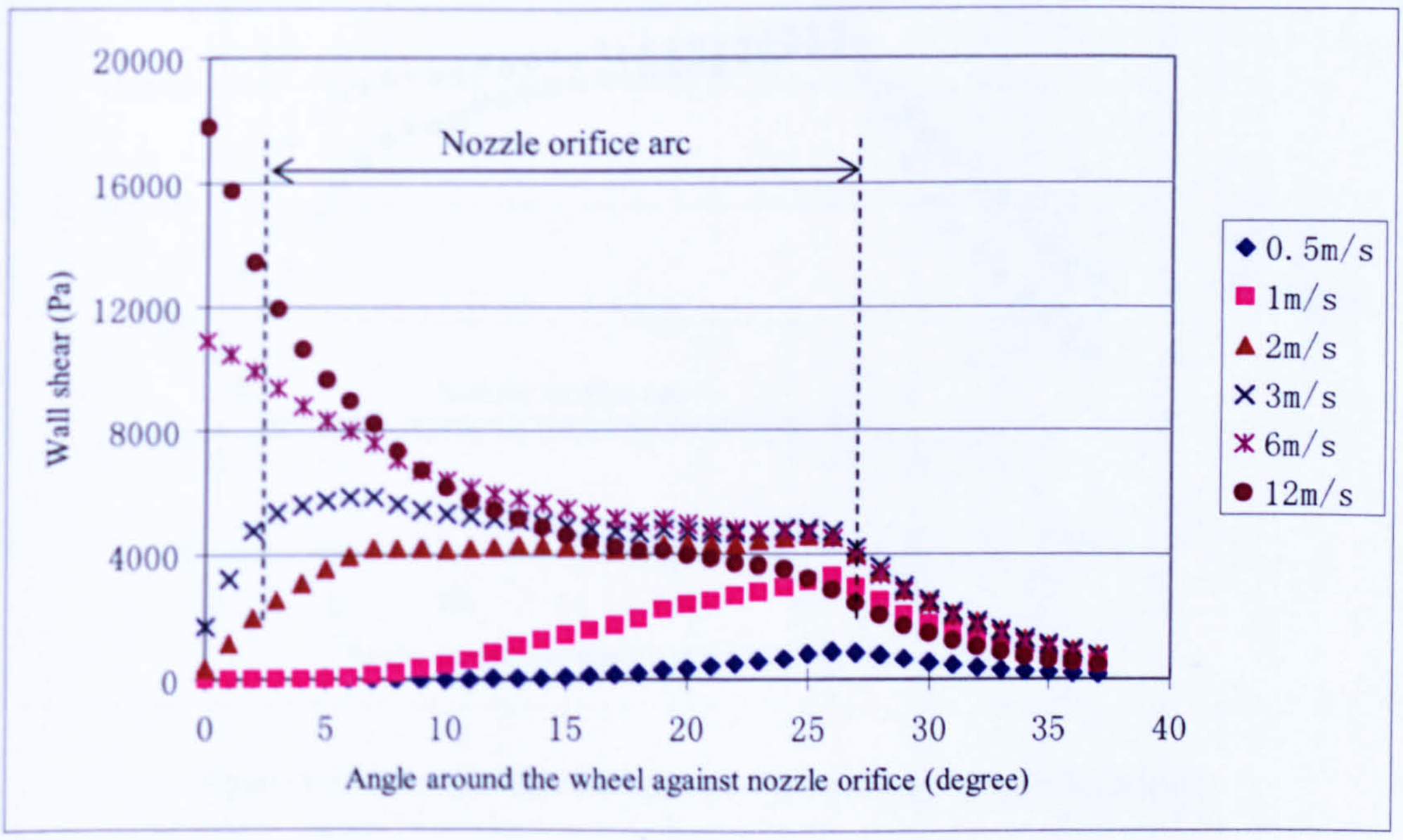

Figure 9-14 Wall shear distribution with different input fluid velocities

In similar fashion to the pressure distribution, shear stress increased with increased pipe velocity, especially in the first half of the nozzle arc. Moreover, the rate of change is quite high. Therefore, in order to decrease the drag force on the wheel and improve the process efficiency an optimized fluid pipe velocity should be chosen. There are clearly two opposing demands on the delivery system: one is the requirement for fluid penetration to be met; the other is to minimise the drag force. For the shoe nozzle examined, results from Figure 9-11 and Figure 9-14, indicate that a fluid pipe velocity of 3 m/s is optimal.

9.7.2 Effect the gap size

Parameters: Fluid pipe velocity = 3 m/s, wheel speed = 30 m/s.

It has been shown that the shoe nozzle orifice should be as close to the wheel surface as possible and that the geometry of the nozzle orifice should accord with the wheel. Simulation results such as those in Figure 9-15 further demonstrate that when such criteria is met fluid penetration and fluid flows are optimized.

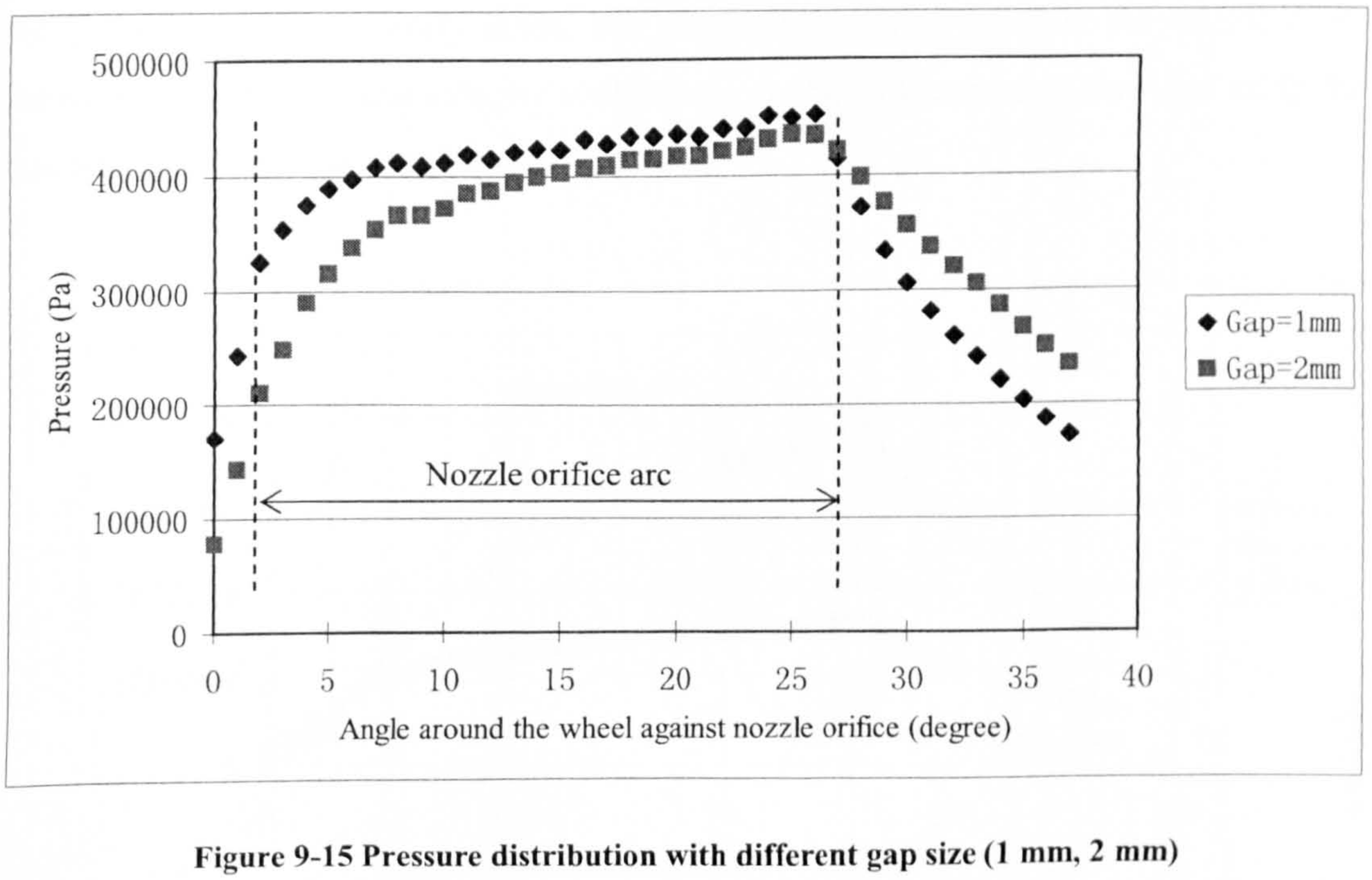

Figure 9-15 Pressure distribution with different gap size (1 mm, 2 mm)

Thus the small gap between nozzle and wheel surface serves not only to reduce losses through leakage but also to improve the pressure distribution and hence fluid penetration into the wheel.

9.7.3 Effect of wheel speed

Parameters: Gap size = 1 mm, fluid pipe velocity = 3 m/s.

The pressure distributions in the gap with three different wheel speeds, is shown in Figure 9-16.

It can be seen that the fluid pressure distribution in the gap did not show a 'flat' curve (constant maximum value) at the higher wheel speeds and in these cases the pressure distribution did not satisfy the requirement for effective fluid penetration. The reason was that the fluid did not fill the nozzle. Figure 9-17 shows the water fraction distribution in the shoe nozzle: the gap was not completely filled with water. The high surface speed of the wheel resulted in air being carried into the gap, and subsequently mixing with the water from the nozzle. The fraction of water increased with distance along the arc from the entry point. The fluid flow situation inside the nozzle is also shown in Figure 9-18 as a velocity vector map. It shows the reverse flow and eddy flow that appear at the higher wheel speeds.

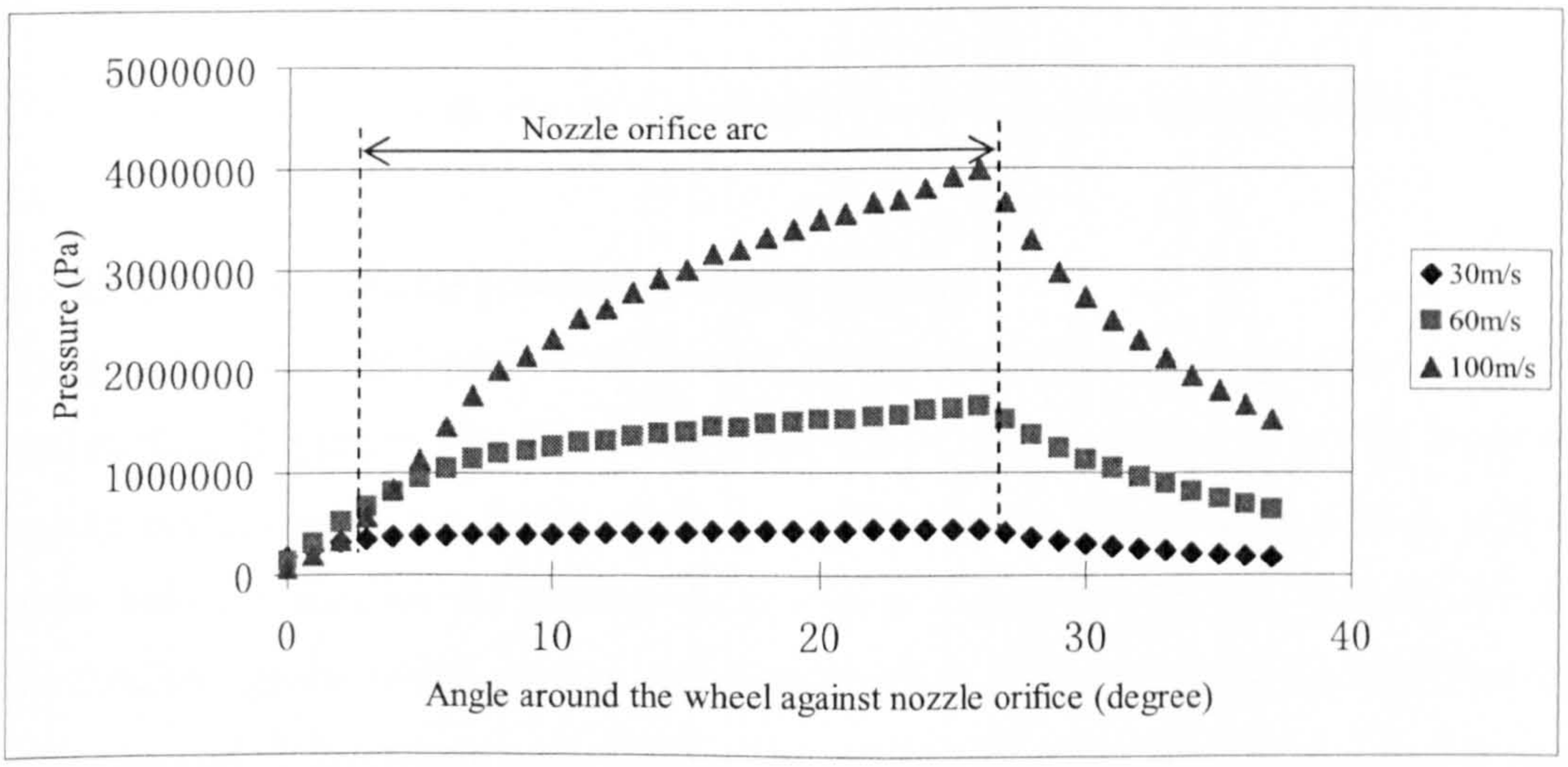

Figure 9-16 Pressure distribution with different wheel speeds (30 m/s, 60 m/s, 100 m/s)

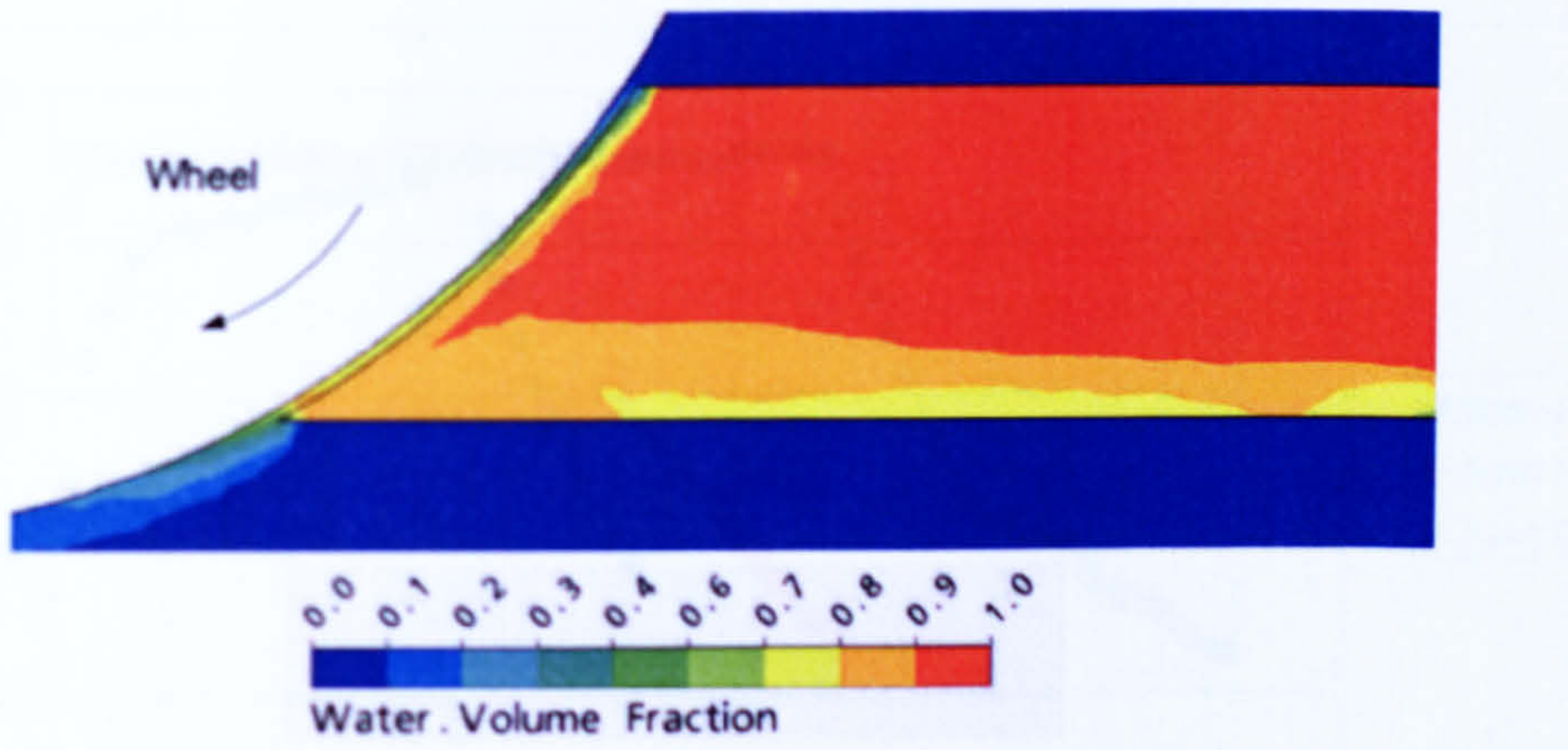

Figure 9-17 Water volume fraction distribution (Fluid pipe velocity 3 m/s)

It can be concluded that, when using a shoe nozzle the fluid pipe velocity needs to be increased if high wheel speeds are employed, due to the requirement for fluid penetration.

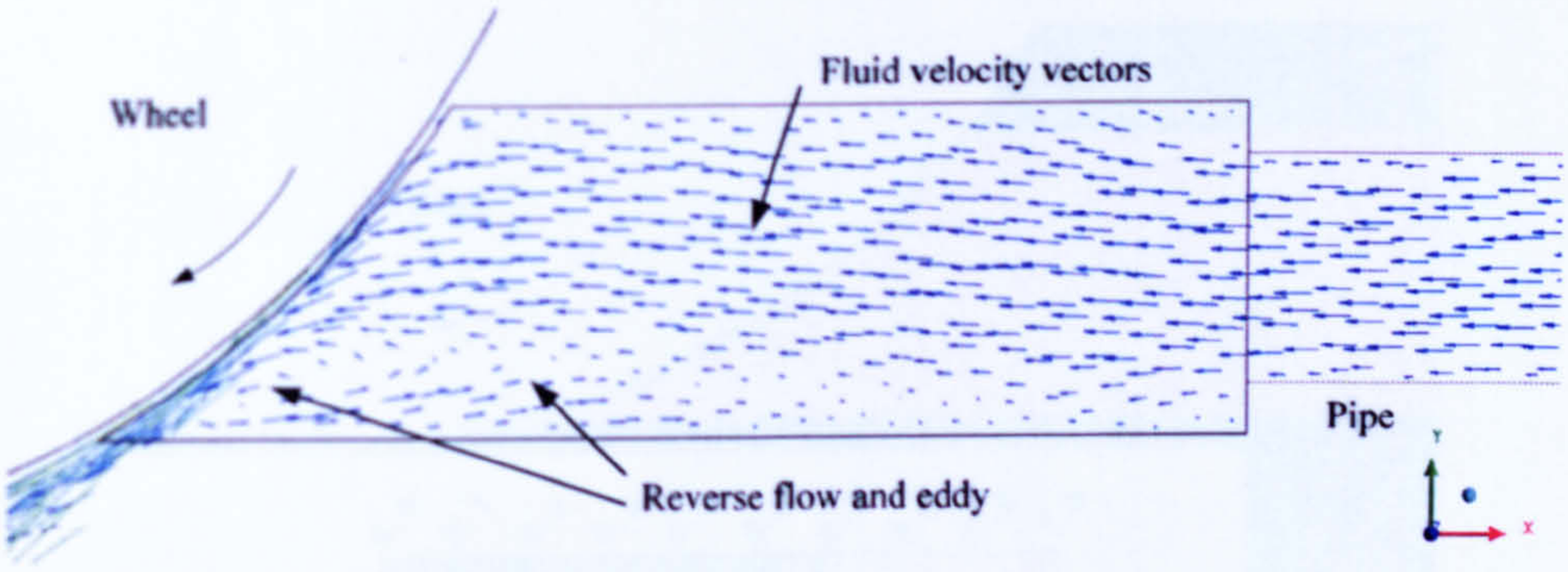

Figure 9-18 Fluid flow in the shoe nozzle A (vs=100 m/s, pipe velocity =3 m/s)

9.8 Effect of shoe nozzle geometry on fluid delivery

A long nozzle arc can improve the length along which fluid may penetrate into the wheel surface (Figure 9-19). However, if the end of nozzle orifice is too far from the grinding contact zone, the fluid, which has penetrated in the grinding wheel, will be ejected before it reaches the contact zone, due to centrifugal forces. Meanwhile, the fluid attached on the wheel surface will also disperse from the wheel surface. For this reason, the end of the nozzle orifice should be sited as close to the grinding contact zone as is reasonably practicable.

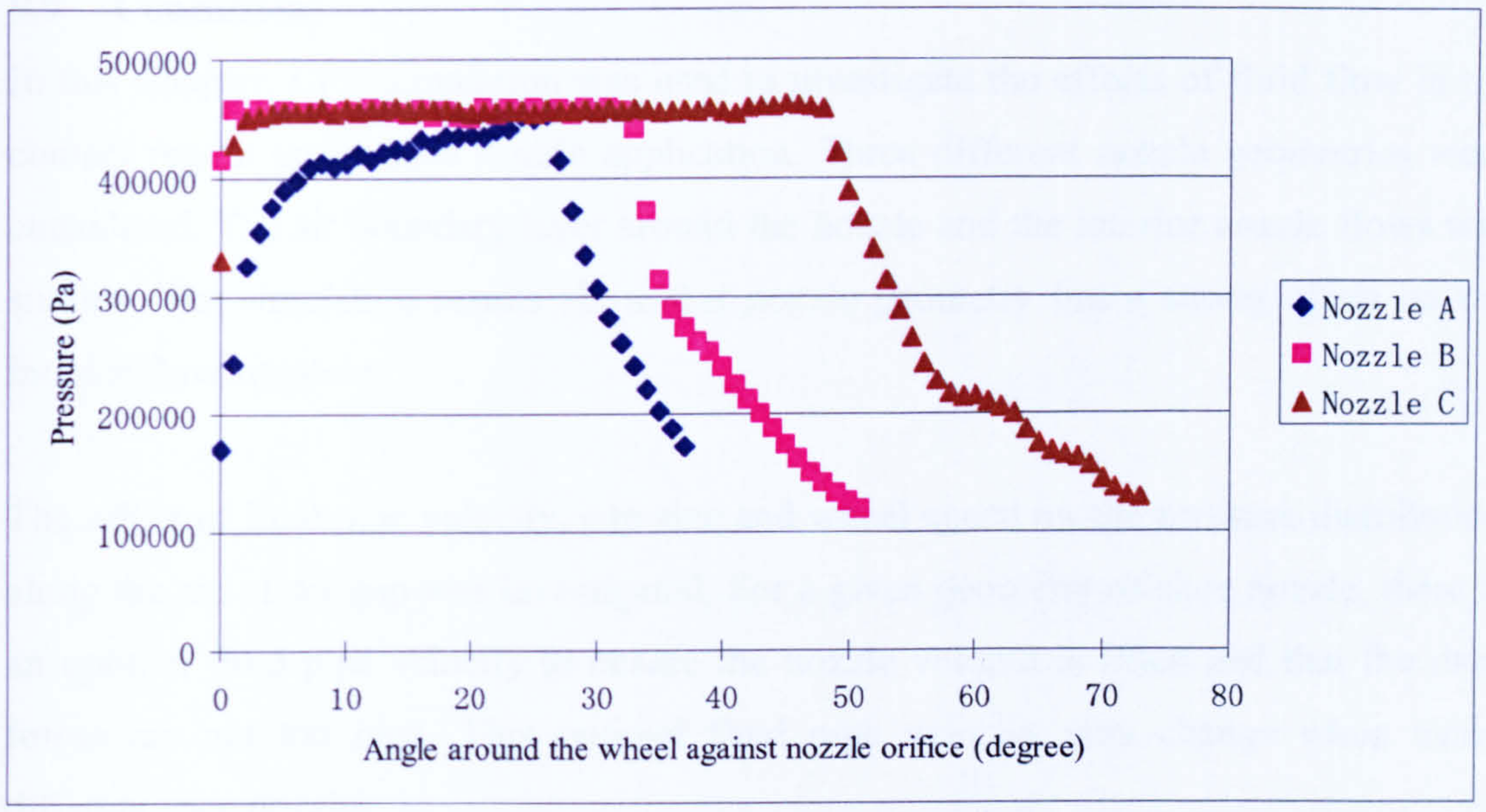

Figure 9-19 Pressure distribution along the nozzle arc for different nozzle geometries (position, arc length)

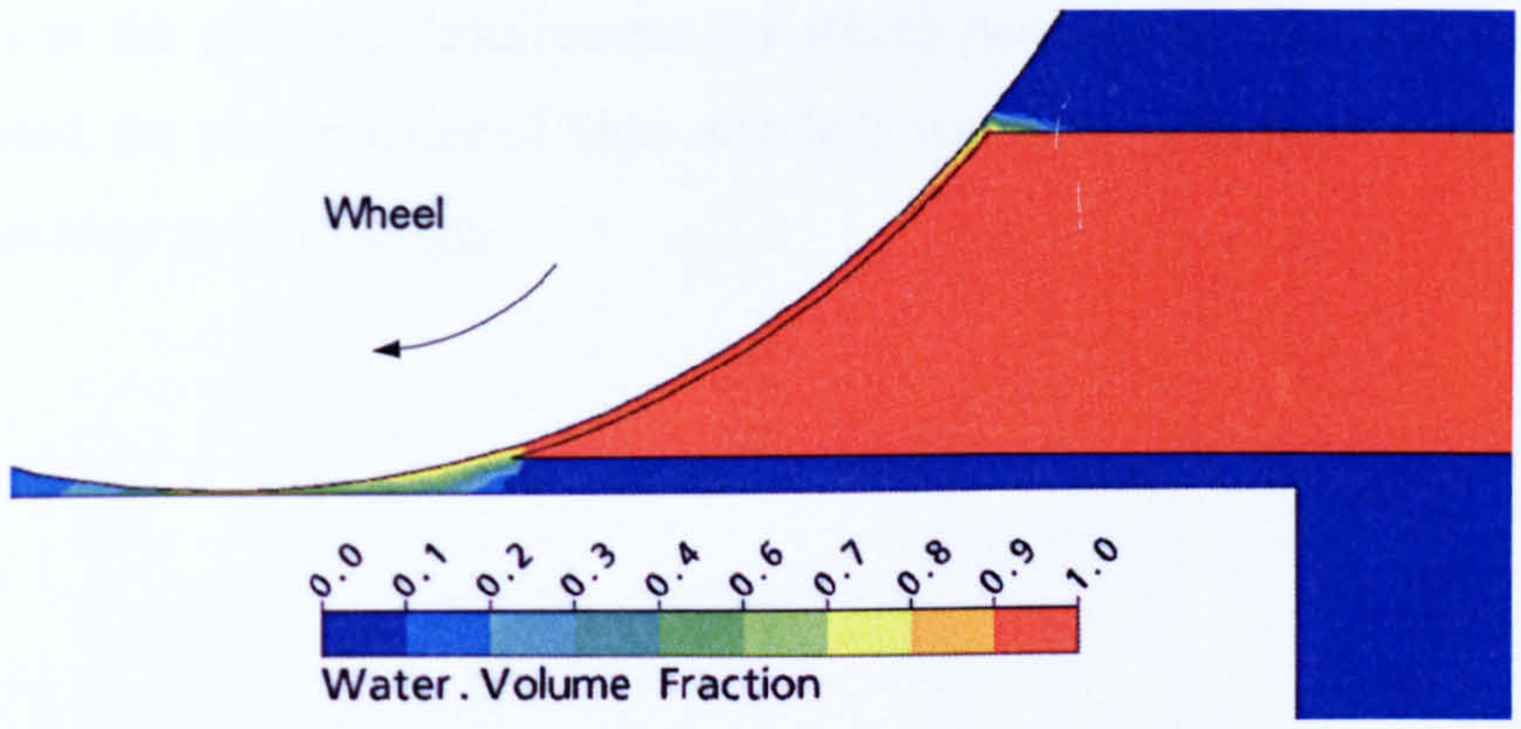

Figure 9-20 Water volume fraction distribution in Shoe nozzle B and grinding zone

Figure 9-20 shows the situation of the fluid distribution in the nozzle and close to the grinding contact zone for shoe nozzle B. Since the nozzle orifice is close to the grinding contact zone, the fluid reaches the grinding contact zone without disruption to the flow, as occurs with nozzle A and nozzle C. Shoe nozzle C has the largest orifice, but it tends to cause reverse and eddy flow at the same fluid pipe velocity. Therefore, Nozzle B is the better choice of the three nozzles for the case considered.

9.9 Conclusions

In this Chapter, CFD simulation was used to investigate the effects of fluid flow in the contact region under shoe nozzle application. Three different nozzle geometries were considered. The air boundary layer around the nozzle and the interior nozzle flows was studied. The simulation results show that nozzle geometry has a strong effect on the interior flow situation.

The effect of fluid pipe velocity, gap size and wheel speed on the pressure distribution along the arc of the gap was investigated. For a given geometry of shoe nozzle, there is an optimal fluid pipe velocity to ensure the nozzle volume is filled and that the drag forces are not too high. This optimal fluid pipe velocity may change when using different shoe nozzles.

In practice, the shoe should be set as close to the wheel surface as is practicably possible. When increasing the wheel speed, the fluid pipe velocity should also be increased in order to meet the pressure requirement for wheel penetration. Among the three shoe nozzles tested, the performance of Shoe nozzle B was best. The work is appropriate for guidance on shoe nozzle design.

Chapter 10 Conclusions

Laser Doppler Anemometry (LDA) was employed to obtain velocity distribution maps in the region close to the grinding contact zone in a low-speed grinding setup under varying conditions. This experimental work identified the key characteristics of fluid flow in this region and in close proximity. The work also showed that current two-dimensional analyses are inadequate to describe and explain the flow phenomena in the grinding zone.

The mathematical formulae describing the air velocity distribution around the wheel was derived from theory based on Newton's laws. The velocity distribution of the air boundary layer flow around the rotating wheel was fully investigated using LDA measurement and CFD simulation. This is the first time such research has been completed. The CFD simulation results correlated well with the experimental results. It was demonstrated that the CFD simulation, which was developed, provided a reliable method for the investigation of the air boundary layer and can be used in future studies.

New findings include:

(i) The highest tangential air velocity occurred in the central section of the wheel.

(ii) The air velocity was found to increase linearly with increasing wheel speed.

(iii) The lowest value of turbulent tangential velocity occurred in the centre of the wheel close to the wheel surface.

The air velocity increased with increasing wheel surface roughness. The roughness of the rotating cylindrical surface was found to be the main factor affecting the nature of the air flow. In summary, the experimental findings and conclusions gave a full understanding of the air boundary layer behaviour. It is hoped that this research will aid users in the setting up of their fluid delivery systems so as to achieve optimal cooling and lubrication in grinding through overcoming the air boundary layer effect.

The effect of the size and position of a scraper on the air flow velocity and pressure distribution was investigated. The knowledge gained concerning flow distribution

provides the basis for strategies to ensure maximum penetration by the grinding fluid. The results showed that use of scrapers of all sizes reduced the pressure in the grinding entry region along the workpiece surface by more than 50%. Immediately beneath the scraper, the air flow stream was broken and the pressure reduced to nearly zero. The width of the scrapers did not have any significant affect on the pressure distribution. It is not necessary to use a scraper much wider than the grinding wheel. The nozzle orifice should be placed just beneath the scraper, and as close as possible to the wheel surface as is practicable. The air boundary layer fully re-establishes at the position, which is at an angle of 150 degrees after the scraper. This work provides clear guidance for scraper application.

Three different nozzle geometries were considered in the investigation of the effects of fluid flow using CFD simulation. The results show that nozzle geometry has a strong effect on the interior flow situation. The effect of fluid pipe velocity, gap size and wheel speed on the pressure distribution along the arc of the gap was investigated. For a given shoe nozzle geometry, there is an optimal fluid pipe velocity that ensures the nozzle volume is filled and that the drag forces are not too high. This optimal fluid pipe velocity may change when using different shoe nozzles. In practice, the shoe should be set as close to the wheel surface as is practicably possible. When increasing the wheel speed, the fluid pipe velocity should also be increased in order to meet the pressure requirement for wheel penetration.

Chapter 11 Recommendations for Future Work

An investigation of the air boundary layer and air scraper application is described in this thesis. Research on shoe nozzle application has also been completed using CFD simulation. The ultimate aim of this work was to improve the efficiency of fluid delivery in grinding, and to obtain maximum useful flow though the grinding contact zone. The following suggestions are made for further investigations:

1. The air boundary layer around the rotating wheel surface can be blocked by a scraper. However, the air within the interior of the wheel below the wheel cutting surface may be under high pressure at high rotational speeds. This may prevent fluid penetrating into the wheel. The factors influencing this phenomenon need to be explored.

2. Scraper function may be identified in a quantitative manner by collecting useful flow, i.e. flow passing through the grinding contact zone.

3. The simulation work on shoe nozzles described in this thesis must be matched by experimental work. The spindle power should be measured before and after coolant application in order to obtain the drag force on the wheel resulting from using different nozzles. The effect of fluid supply direction and nozzle shape could be examined due to the fluid recirculation within the shoe nozzle. The quality of the workpiece surface should also be assessed to determine the effect of different shoe nozzles on grinding performance.

4. Further work is recommended on non-rigid scrapers including air- and water-jet systems. Such systems are increasingly employed in practice. The CFD developed will accommodate analysis of non-rigid scrapers without extensive further development.

References

Ainsworth, R.W., Thorpe, S.J., Manners, R.J., (1997) A new approach to flow-field measurement - a view of Doppler global velocimetry techniques, *International Journal of Heat and Fluid Flow*, 18(1) pp.116-130.

Akiyama, T., Shibata, J., Yonetsu, S., (1984) Behavior of grinding fluid in the gap of the contact area between a grinding wheel and a workpiece - a study on delivery of the grinding fluid, *Proceedings of the 5th international conference on Production Engineering, Japan Society of Precision Engineering*, pp.52-57.

Anon, (1974) Grinding fluid can break the air barrier, *Metalworking Production*, 118(1) pp.68-69, 71, 73.

ANSYS CFX, *ANSYS CFX-Solver Modelling Guide*, Release 11.0

Axinte, D., Axinte, M., Tannock, J.D.T., (2003) A multicriteria model for cutting fluid evaluation, *Proceedings of the Institution of Mechanical Engineers, Part B: Journal of Engineering Manufacture*, 217(10) pp.1341-1353.

Babic, D., Murray, D.B., Torrance, A.A., (2005) Mist jet cooling of grinding processes, *International Journal of Machine Tools and Manufacture*, 45(10) pp.1171-1177.

Bauer, R.J., Irani, R.A., Warkentin, A., (2005) A review of cutting fluid application in the grinding process, *International Journal of Machine Tools & Manufacture*, 45(15) pp.1696-1705.

Bradshaw, P., Huang, G.P., (1995), The law of the wall in turbulent flow, *Proceedings - Royal Society of London, Series A (Mathematical and Physical Sciences)*, 451(1941) pp.165-188.

Brinksmeier, E., Heinzel, C., Wittmann, M., (1999) Friction, cooling and lubrication in grinding, *CIRP Annals - Manufacturing Technology*, 48(2) pp.581-598.

Brinksmeier, E., Heinzel, C., Wittmann, M., (2000) Visualization of coolant flow in shoe nozzles and their effect on the residual grinding stresses, *Annals of the WGP*, VII/I pp.9-12.

Brinksmeier, E., Minke, E., (1993) High-performance surface grinding - the influence of coolant on the abrasive process, *CIRP Annals*, 42(1) pp.367-370.

Campbell, J.D., (1995) Optimized coolant application, *Society of Manufacturing Engineers*, MR95-211, pp.895-904.

Campbell, J.D., (1997) Tools to measure and improve coolant application effectiveness, *2nd international machining & grinding conference,* Dearborn, Michigan, 8-11 September 1997, SME

Catai, R.E., Bianchi, E.C., Zilio, F.M., Valarelli, I.D., Alves, M.C.S., Silva, L.R., Aguiar, P.R., (2006) Global analysis of aerodynamics deflectors efficiency in the

grinding process, *Journal of the Brazilian Society of Mechanical Sciences and Engineering*, 28(2) pp.140-145.

Chang, C.C., (1997) An application of lubrication theory to predict useful flow-rate of coolant on grinding porous media, *Tribology International*, 30(8) pp.575-581.

Chang, C.C., Wang, S.H., Szeri, A.Z., (1996) On the mechanism of fluid transport across the grinding zone, *Transactions of the ASME, Journal of Manufacturing Science and Engineering*, 118, pp.332-338.

Choi, H.Z., Lee, S.W., Jeong, H.D., (2001) A comparison of the cooling effects of compressed cold air and coolant for cylindrical grinding with a CBN wheel, *Journal of Materials Processing Technology*, 111(1-3) pp.265-268.

Dantec Dynamics, *Laser Doppler Anemometry*, [online] Available at: http://www.dantecdynamics.com/lda/Princip/Index.html [Accessed April 2005]

Dantec Elektronik, *BURSTware™ 2.0 Installation & User's guide*, 1991.

Dantec Elektronik, *User's guide, 57N10/57N14/57N25 Burst Spectrum Analyzer*.

Davies, T.P., Jackson, R.G., (1981) Air flow around grinding wheels, *Precision Engineering*, 3(4) pp.225-228.

Devenport, W.J., 2002. *Experiment 4 - Laser Doppler Anemometry*, [online] Available at: http://www.aoe.vt.edu/~devenpor/aoe3054/manual/expt4/index.html [Accessed May 2005]

Dierich, M., Gersten, K., Schlottmann, F., (1998) Turbulent flow around a rotating cylinder in a quiescent fluid, *Experiments in Fluids*, 25(5-6) pp.455-460.

Douglas, J.F., Gasiorek, J.M., Swaffield, J.A., Jack, L.B., (2005) *Fluid mechanics*. 5th ed. Prentice Hall.

Ebbrell, S., Woolley, N.H, Tridimas,Y.D., Allanson, D.R., Rowe, W.B., (2000) Effects of cutting fluid application methods on the grinding process, *International Journal of Machine Tools and Manufacture*, 40(2) pp.209-223.

Engineer, F., Guo, C., Malkin, S. (1992) Experimental measurement of fluid flow through the grinding zone, *Transactions of the ASME, Journal of Engineering for Industry*, 114, pp.61-66.

Gao, Y., Tse, S., Mak, H., (2003) An active coolant cooling system for applications in surface grinding, *Applied Thermal Engineering*, 23(5) pp.523-537.

Gong, Y.D., Li, H., Cai, G.Q., (2004) The Effect of Wheel Velocity and Shape on Rotating Airflow in Super-high-speed Grinding, *Key Engineering Materials*, 258-259 pp.282-286.

Gong, Y.D., Li, H., Cai, G.Q., (2006) Analysis and study of the influence factor on the airflow of ultra-speed grinding wheel, *Key Engineering Materials*, 304-305 pp.136-140.

Gong, Y.D., Li, H., Cai, G.Q., (2007) Theoretical analysis and simulation of airflow of super high-speed grinding wheel, *Key Engineering Materials*, 329 pp.507-510.

Graham, W., Whiston, M.G., (1978) Some observations of through-wheel coolant application in grinding, *International Journal of Machine Tool Design & Research*, 18(1) pp.9-18.

Guo, C., Malkin, S., (1992 A) Analysis of fluid flow through the grinding zone, *Transactions of the ASME, Journal of Engineering for Industry*, 114, pp.427-434.

Guo, C., Malkin, S., (1992 B) Heat transfer in grinding, *Journal of Materials Processings and Manufacturing Science*, 1(1) pp.16-27.

Guo, C., Malkin, S., (1994) Analytical and experimental investigation of burnout in creep-feed grinding, *CIRP Annals*, 43(1) pp.283-286.

Gviniashvili, V.K., Morgan, M.N., Woolley, N.H., Rowe, W.B., (2004) Modelling of the useful flowrate in grinding based on spindle power, *Key Engineering Material*, 257-258, pp.333-338.

Gviniashvili, V.K., Webster, J., Rowe, B., (2005) Fluid flow and pressure in the grinding wheel-workpiece interface, *Transactions of the ASME, Journal of Manufacturing Science and Engineering*, 127(1) pp.198-205.

Gviniashvili, V.K., Woolley, N.H., Rowe, W.B., (2004) Useful coolant flowrate in grinding, *International Journal of Machine Tools & Manufacture*, 44(6) pp.629-636.

Hamrock, B.J., (1994) *Fundamentals of fluid film lubrication*, McGraw Hill.

Howes, T., (1990) Assessment of the cooling and lubricative properties of grinding fluids, CIRP Annals, 39(1) pp.313-316.

Howes, T.D., Toenshoff, H.K., Heuer, W., (1991) Environmental aspects of grinding fluids, *CIRP Annals*, 40(2) pp.623-630.

Hryniewicz, P., Szeri, A.Z., Jahanmir, S., (2000) Coolant flow in surface grinding with non-porous wheels, *International Journal of Mechanical Sciences*, 42(12) pp.2347-2367.

Hryniewicz, P., Szeri, A.Z., Jahanmir, S., (2001) Application of lubrication theory to fluid flow in grinding: Part I - Flow between smooth surfaces, *Journal of Tribology*, 123(1) pp.94-100.

Hryniewicz, P., Szeri, A.Z., Jahanmir, S., (2001) Application of lubrication theory to fluid flow in grinding: Part II - Influence of wheel and workpiece roughness, *Journal of Tribology*, 123(1) pp.101-107.

Inasaki, I., Tonshoff, H.K., Howes, T.D., (1993) Abrasive machining in the future, *CIRP Annals*, 42(2) pp.723-732.

Jin, T., Stephenson, D.J., Corbett, J., (2002) Burn threshold of high-carbon steel in high-efficiency deep grinding, *Proceedings of the Institution of Mechanical Engineers. Part B. Journal of engineering manufacture*, 216(3) pp.357-364.

Jin, T., Stephenson, D.J., Rowe, W.B., (2003) Estimation of the convection heat transfer coefficient of coolant within the grinding zone, *Proceedings of the Institution of Mechanical Engineers, Part B: Journal of Engineering Manufacture*, 217(3) pp.397-407.

Kaliszer, H., Trmal, G., (1975) Mechanics of grinding fluid delivery, *Technical Paper - Society of Manufacturing Engineers*, MR75-614 pp.1-17.

Kim, N.K., Guo, C., Malkin, S., (1997) Heat flux distribution and energy partition in creep-feed grinding, *CIRP Annals - Manufacturing Technology*, 46(1) pp.227-232.

Klocke, F., Baus, A., Beck, T., (2000) Coolant induced forces in CBN high speed grinding with shoe nozzles, *CIRP Annals - Manufacturing Technology*, 49(1) pp.241-244.

Klocke, F., Beck, T., Hoppe, S., Krieg, T., Muller, N., Nothe, T., Raedt, H.W., Sweeney, K., (2002) Examples of FEM application in manufacturing technology, *Journal of Materials Processing Technology*, 120(1-3) pp.450-457.

Klocke, F., Brinksmeier, E., Evans, C., Howes, T., Inasaki, I., Minke, E., Toenshoff, H.K., Webster, J.A., Stuff, D., (1997) High-speed grinding - fundamentals and state of the art in Europe, Japan, and the USA, *CIRP Annals - Manufacturing Technology*, 46(2) pp.715-724.

Kovacevic, R., Beardsley, H.E., (1997) High-speed water jet as a coolant/lubricant in grinding, *Abrasives*, pp.10-11, 18, 22, 27, 31, 34.

Kovacevic, R., Mohan, R., (1995) Effect of high speed grinding fluid on surface grinding performance, *Society of Manufacturing Engineers*, MR95-213, pp.918-931.

Krishnan, N., Malkin, S., Guo, C., (1995) Fluid flow through the grinding zone in creep feed grinding, *Society of Manufacturing Engineers*, MR95-212, pp.906-916.

Kundu, P.K., Cohen, I.M., (2001) *Fluid mechanics*. 2nd ed. Academic Press.

Li, Y.Y., Chen, Y., (1989) Simulation of surface grinding, *Journal of Engineering Materials and Technology, Transactions of the ASME*, 111(1) pp.46-53.

Malkin, S., (1989) *Grinding Technology: Theory and applications of machining with abrasives*, Ellis Horwood.

Marinescu, J.D., Hitchiner, M., Marinescu, M.D., Inasaki, I., Uhlmann, E., Rowe, W.B., (2007) *Handbook of machining with grinding wheels*, CRC Press.

Marinescu, J.D., Rowe,W.B., Dimitrov, B., Inasaki, I., (2004) *Tribology of abrasive machining processes*, William Andrew Publishing.

Massey, B.S., (1989) *Mechanics of fluids*. 6th ed. Chapman & Hall.

Monici, R.D., Bianchi, E.C., Catai, R.E., Aguiar, P.R. (2006) Analysis of the different forms of application and types of cutting fluid used in plunge cylindrical grinding using conventional and superabrasive CBN grinding wheels, *International Journal of Machine Tools and Manufacture*, 46(2) pp.122-131.

Nguyen, T., Zhang, L.C., (2003) An assessment of the applicability of cold air and oil mist in surface grinding *Journal of Materials Processing Technology*, 140(1-3) pp.224-230.

O'Donovan, T.S., Murray, D.B., Torrance, A.A., (2006) Jet heat transfer in the vicinity of a rotating grinding wheel, *Proceedings of the Institution of Mechanical Engineers, Part C, Journal of Mechanical Engineering Science*, 220(C6) pp.837-845.

Oliveira, J.F.G., Alves, S.M., (2006) Development of environmentally friendly fluid for CBN grinding, *CIRP Annals - Manufacturing Technology*, 55(1) pp.343-346.

Osman, M., Malkin, S., (1972) Lubrication by grinding fluids at normal and high wheel speed, *ASLE Transactions*, 15(4) pp.261-268.

Powell, J.W., (1979), Application of grinding fluid in creep feed grinding, PhD Dissertation, Univ. of Bristol.

Qi, H.S., Rowe, W.B., Mills, B., (1997) Experimental investigation of contact behaviour in grinding, *Tribology International*, 30(4) pp.283-294.

Radhakrishnan, V.J., Rahman, J.F., (1977) A preliminary investigation on the condition of the grinding wheel surface by air flow measurements, *Annals of the CIRP*, 26(1-2) pp.147-150.

Rahman, J.F., Radhakrishnan, V., (1980) Measurement of grinding wheel surface topography using electro-pneumatic turbulence amplifier system, *International Journal of Machine Tool Design & Research*, 20(3-4) pp.189-196.

Ramesh, K., Huang, H., Yin, L., (2004) Analytical and experimental investigation of coolant velocity in high speed grinding, *International Journal of Machine Tools and Manufacture*, 44 (10) pp.1069-1076.

Ramesh, K., Yeo, S.H., Zhong, Z.W., Sim, K.C., (2001) Coolant shoe development for high efficiency grinding, *Journal of Materials Processing Technology*, 114(3) pp.240-245.

Schumack, M.R., Chung, J, Schultz, W.W., Kannatey-Asibu, E.Jr., (1991) Analysis of fluid flow under a grinding wheel, *Transactions of the ASME, Journal of Engineering for Industry*, 113, pp.190-197.

Shibata, J., Goto, T., Yamamoto M., Tsuwa, H., (1982) Characteristics of air flow around a grinding wheel and their availability for assessing the wheel wear, *Annals of the CIRP*, 31(1) pp.233-238.

Stephenson, D.J., (2005) Trends in fluid application strategy for grinding processes, *Key Engineering Materials*, 291-292 pp.245-250.

Sven, A., Johansson, J., (1996) Air flows and particle distribution around a rotating grinding wheel, *Aerosol Science and Technology*, 25(2) pp.121-133.

Tomita, Y., Eda, H., (1997) Influence of grinding fluid on ultra precision processing of high purity aluminum alloy by grinding stone, *Wear*, 212(2) pp.183-187.

Tonshoff, H.K., Friemuth, T., Becker, J.C., (2002) Process monitoring in grinding, *CIRP Annals - Manufacturing Technology*, 51(2) pp.551-571.

Tonshoff, H.K., Peters, J., Inasaki, I., Paul, T., (1992) Modelling and simulation of grinding processes, *CIRP Annals*, 41(2) pp.677-688.

Trmal, G., Kaliszer, H., (1976) Delivery of grinding fluids in grinding, *Chartered Mechanical Engineer*, 23(8) pp.95, 97-98, 100.

Vestnik M., (1980) Grinding fluid flow in the wheel/workpiece contact zone, Russian Engineering Journal, 60(11) pp.51-52.

Vries, W.R., Murray, F.S., (1994) Tribology at the cutting edge: cutting and grinding fluids, *American Society of Mechanical Engineers, Petroleum Division (Publication), Tribology Symposium*, 61 pp.23-33.

Wager, J.G., Gu, D.Y., (1991) Influence of up-grinding and down-grinding on the contact zone, *CIRP Annals*, 40(1) pp.323-326.

Wang, S.B., Kou, H.S., (1997) Cooling effectiveness of cutting fluid in creep feed grinding, *International Communications in Heat and Mass Transfer*, 24(6) pp.771-783.

Webster, J.A., Brinksmeier, E., Heinzel, C., Wittmann, M., Thoens, K., (2002) Assessment of grinding fluid effectiveness in continuous-dress creep feed grinding, *CIRP Annals - Manufacturing Technology*, 51(1) pp.235-240.

Webster, J.A., Cui, C., Mindek R.B.Jr., (1995) Grinding fluid application system design, *CIRP Annals - Manufacturing Technology*, 44 (1), pp.333–338.

Webster, J.A., Cui, C.L., (1995) Flow rate and jet velocity determination for design of a grinding coolant system, *1st International Machining & Grinding conference*, Dearborn, MI , 12-14 September 1995.

Weinerta, K., Inasakib, I., Sutherlandc, J.W., Wakabayashid, T., (2004) Dry Machining and Minimum Quantity Lubrication, *CIRP Annals - Manufacturing Technology*, 53(2) pp.511-537.

Williams, J., (2005) *Engineering tribology*, Cambridge University Press.

Wittmann, M., Meyer, L., Walter, A., Heinzel, C., (2002) Approaches to improve grinding fluid application, *Grinding and Abrasives*, June/July pp.16-22.

Bibliography

Douglas, J.F., Gasiorek, J.M., Swaffield, J.A., Jack, L.B., (2005) *Fluid mechanics. 5th ed*, Prentice Hall.

Hamrock, B.J., (1994) *Fundamentals of fluid film lubrication*, McGraw Hill.

Kundu, P.K., Cohen, I.M., (2001) *Fluid mechanics. 2nd ed*, Academic Press.

Malkin, S., (1989) *Grinding Technology: Theory and applications of machining with abrasives*, Ellis Horwood.

Marinescu, J.D., Hitchiner, M., Marinescu, M.D., Inasaki, I., Uhlmann, E., Rowe, W.B., (2007) *Handbook of machining with grinding wheels*, CRC Press.

Marinescu, J.D., Rowe,W.B., Dimitrov, B., Inasaki, I., (2004) *Tribology of abrasive machining processes*, William Andrew Publishing.

Massey, B.S., (1989) *Mechanics of fluids. 6th ed*, Chapman & Hall.

Powell, J.W., (1979), *Application of Grinding Fluid in Creep Feed Grinding*, PhD Dissertation, Univ. of Bristol.

Schlichting, H., Gersten, K., (1979) *Boundary-Layer Theory*, McGraw Hill, New York

Tridimas, Y.D., (1981), *Development and application of Laser Doppler Anemometer instrumentation for the study of gas-solid suspension flows*, PhD Dissertation, Liverpool Polytechnic (Liverpool John Moores University).

Watrasiewicz, B. M., Rudd, M. J., (1976) *Laser Doppler measurements*, Butterworths.

Webster, J.A., (2005), *Current global research projects in fixed abrasive grinding - A review of 353 current and recently completed grinding projects, being researched at 175 universities around the world*, Cool-Grinding Technologies USA

Williams, J., (2005) Engineering tribology, Cambridge University Press.

Appendix A. Experimental and simulation Figures

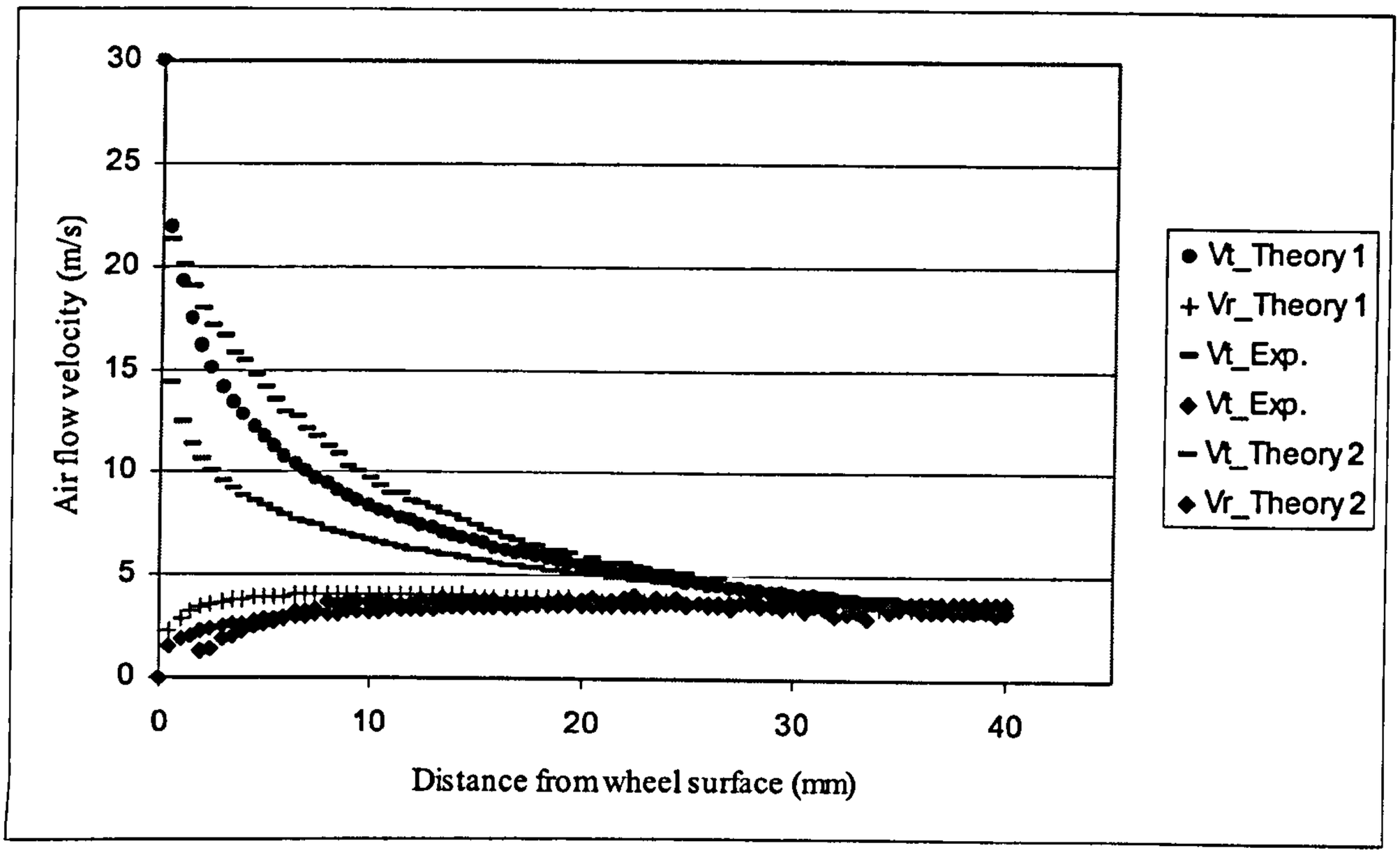

Comparison of experimental results and two theories results (*Vt and Vr* distribution)

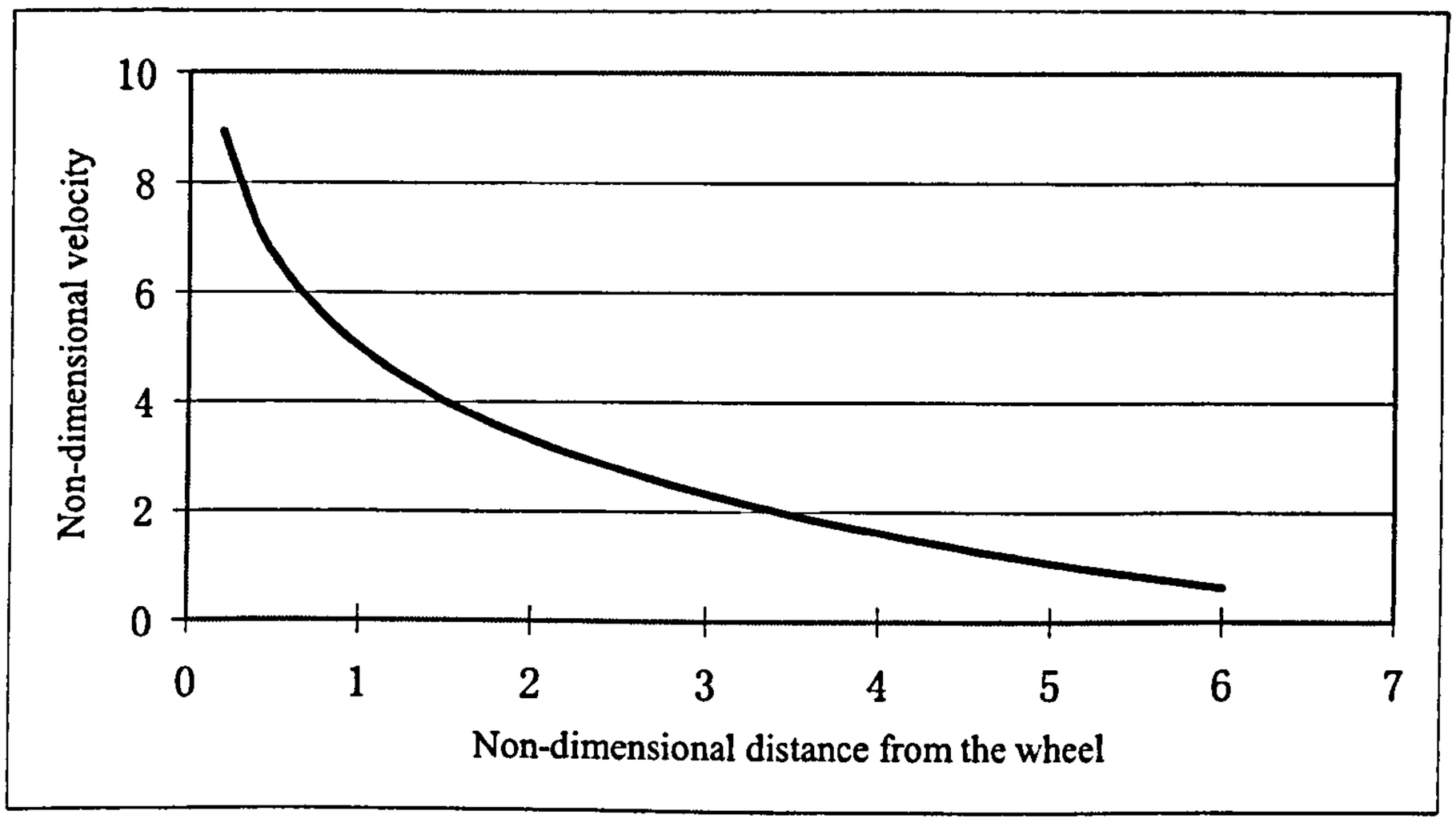

Tangential velocity distribution obtained from 'law of the wall'

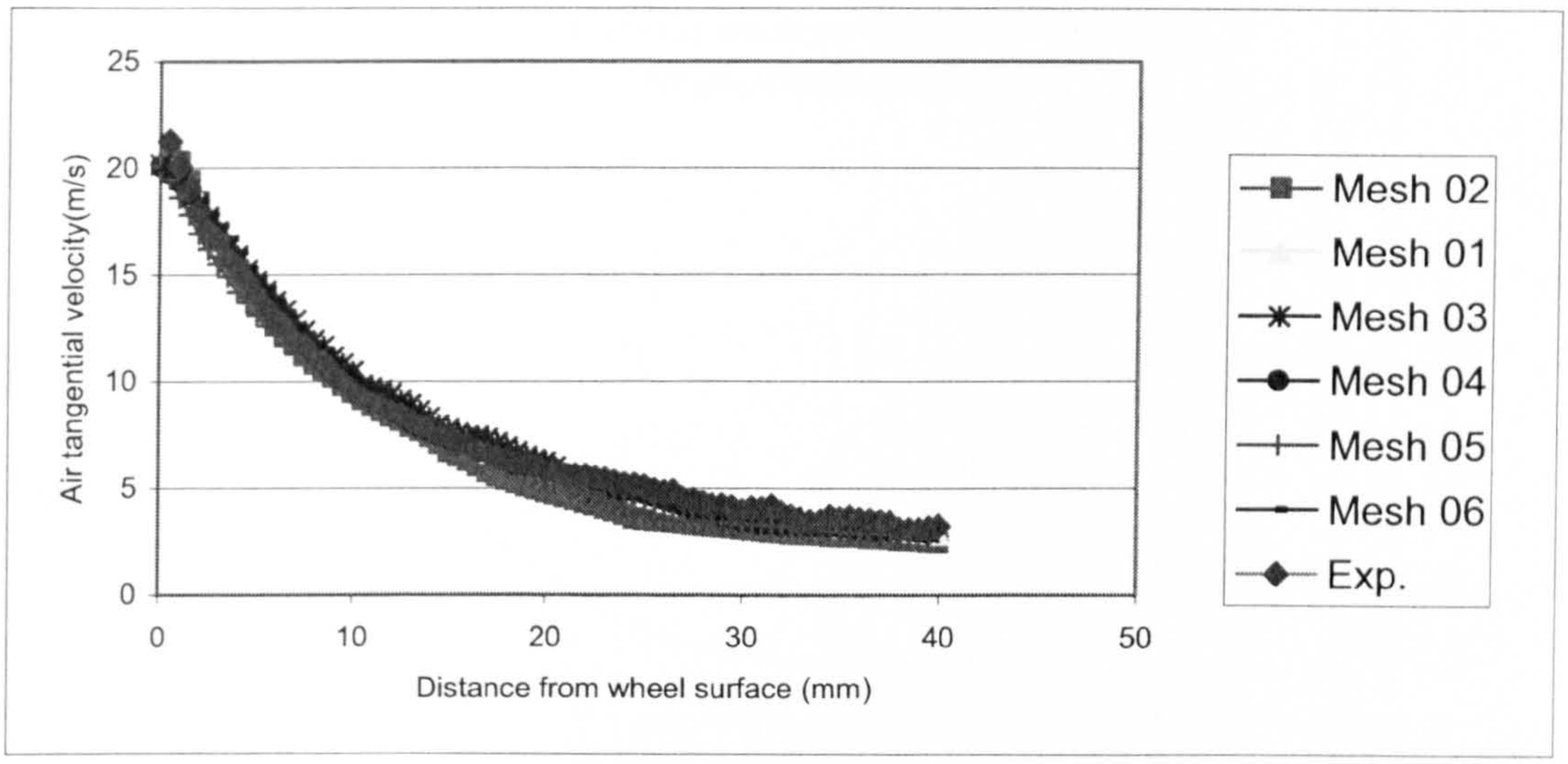

Comparison of experimental result and simulation results with different meshes (air tangential velocity)

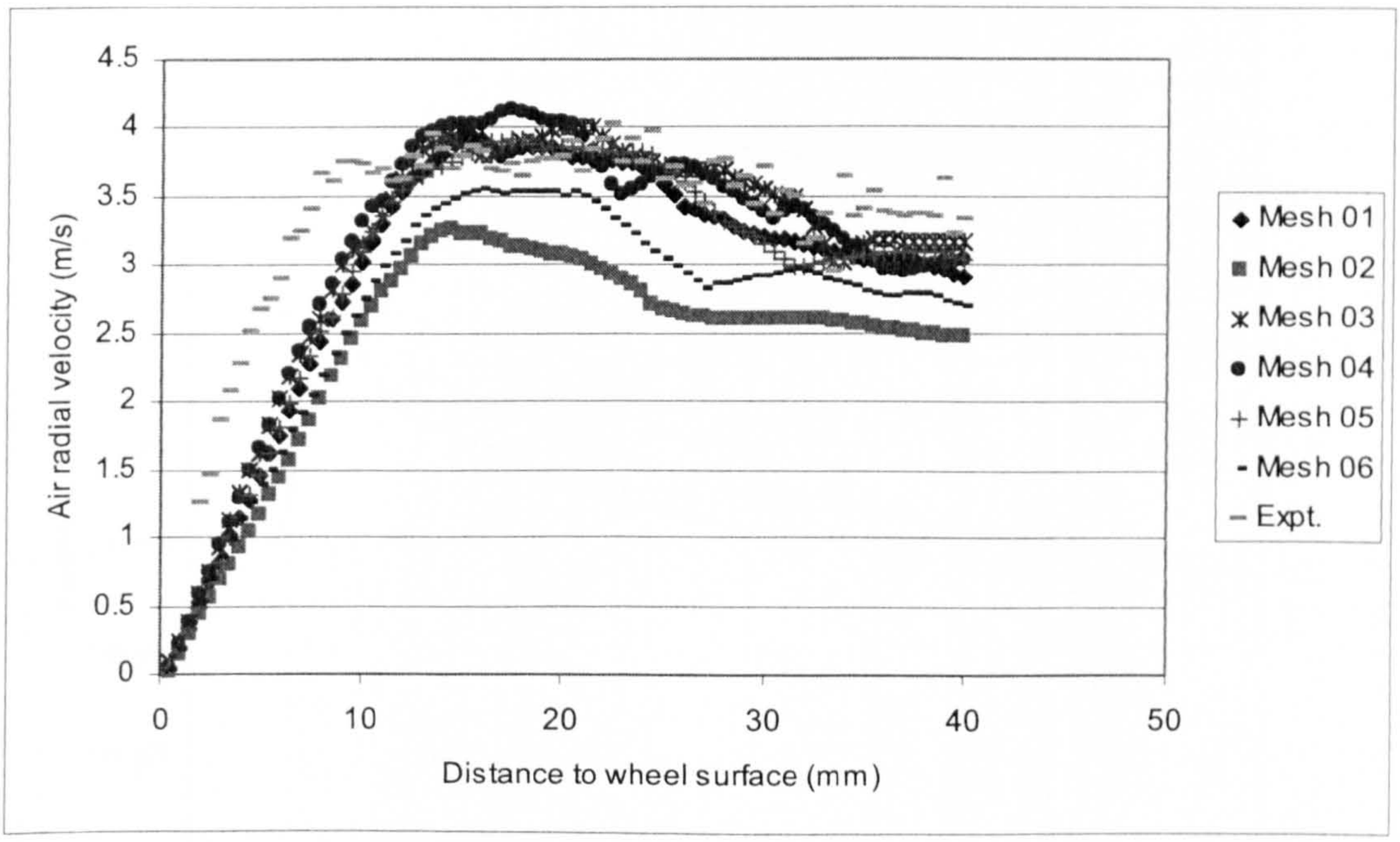

Comparison of experimental result and simulation results with different meshes (air radial velocity)

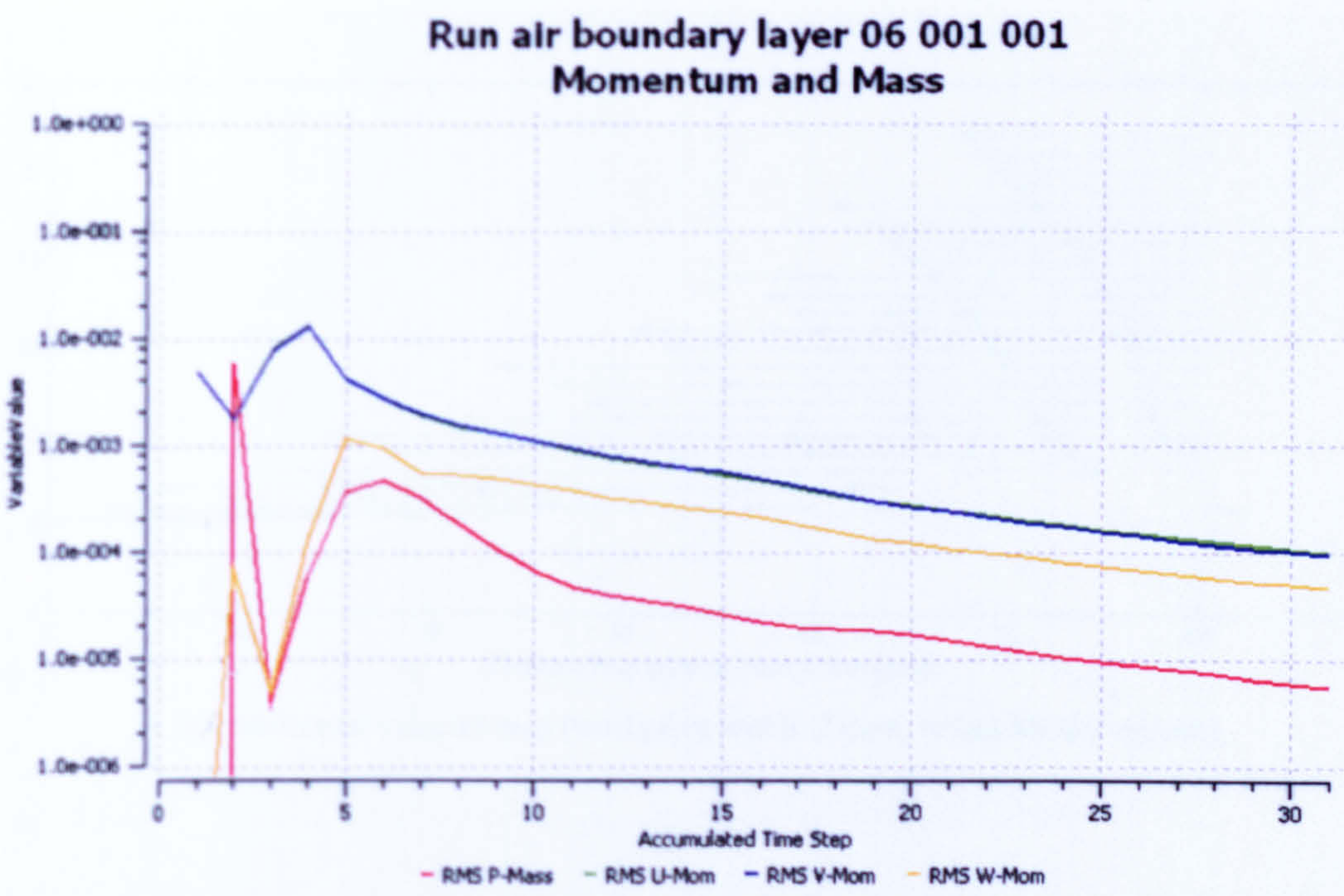

Sample of RMS Residuals Turbulent (KE) convergent in simulation

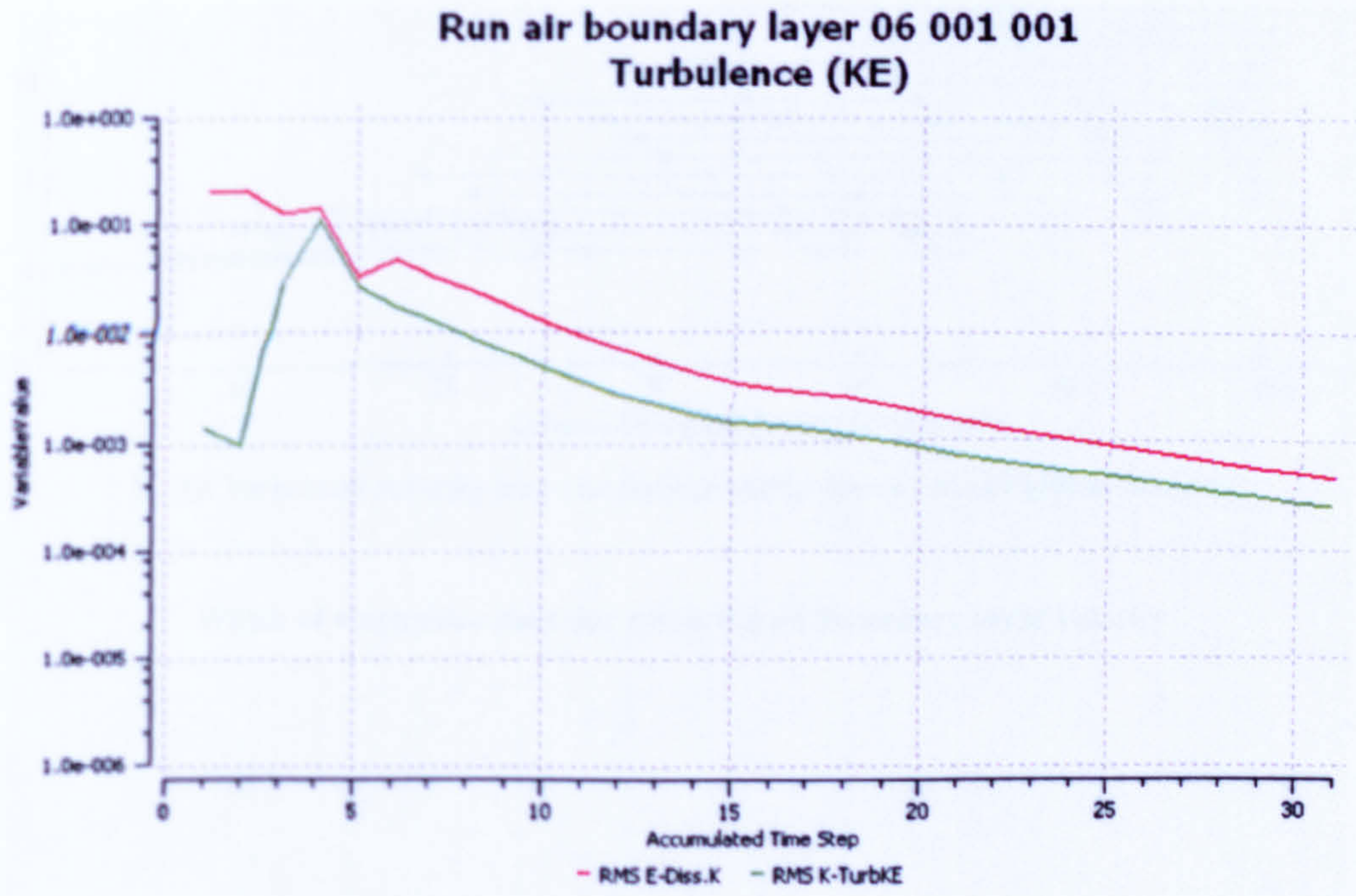

Sample of RMS Residuals Momentum and Mass convergent in simulation

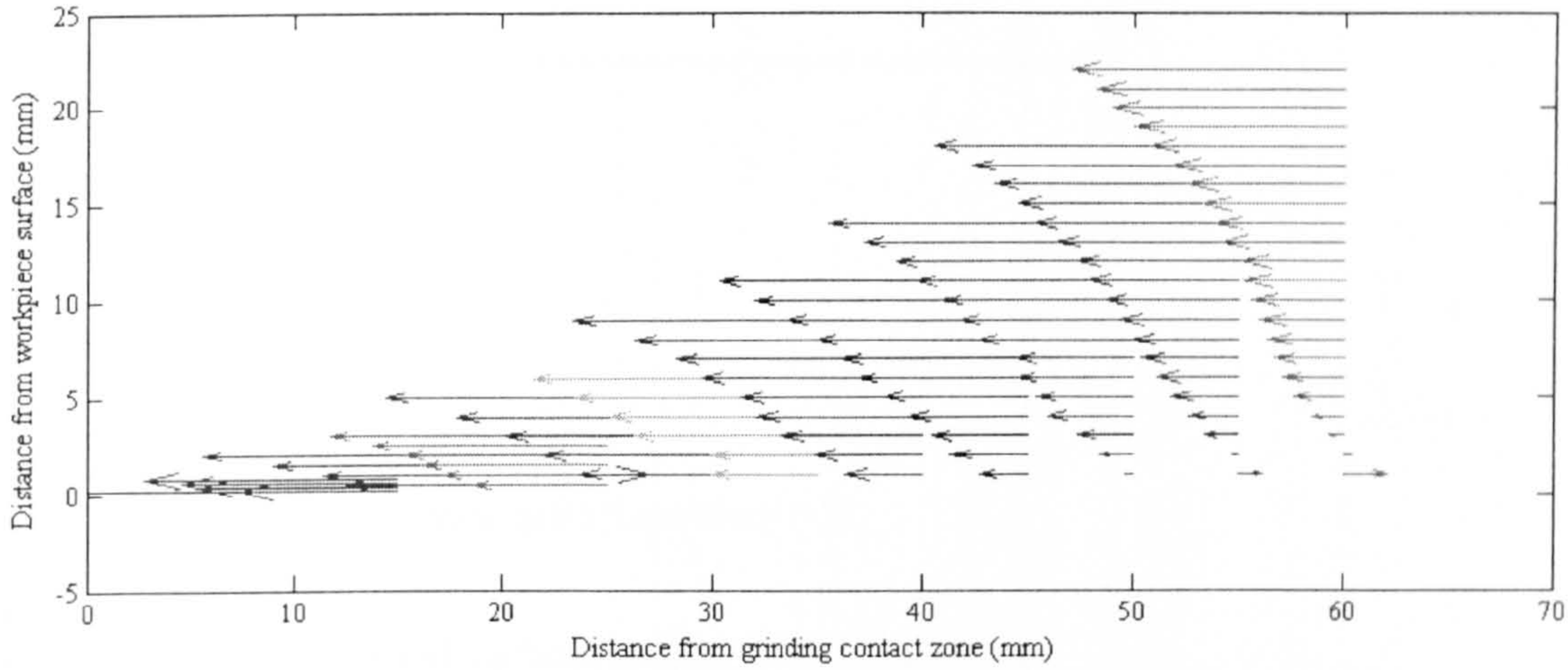

A. Air horizontal velocity map (workpiece width: 25mm; wheel Middle section)

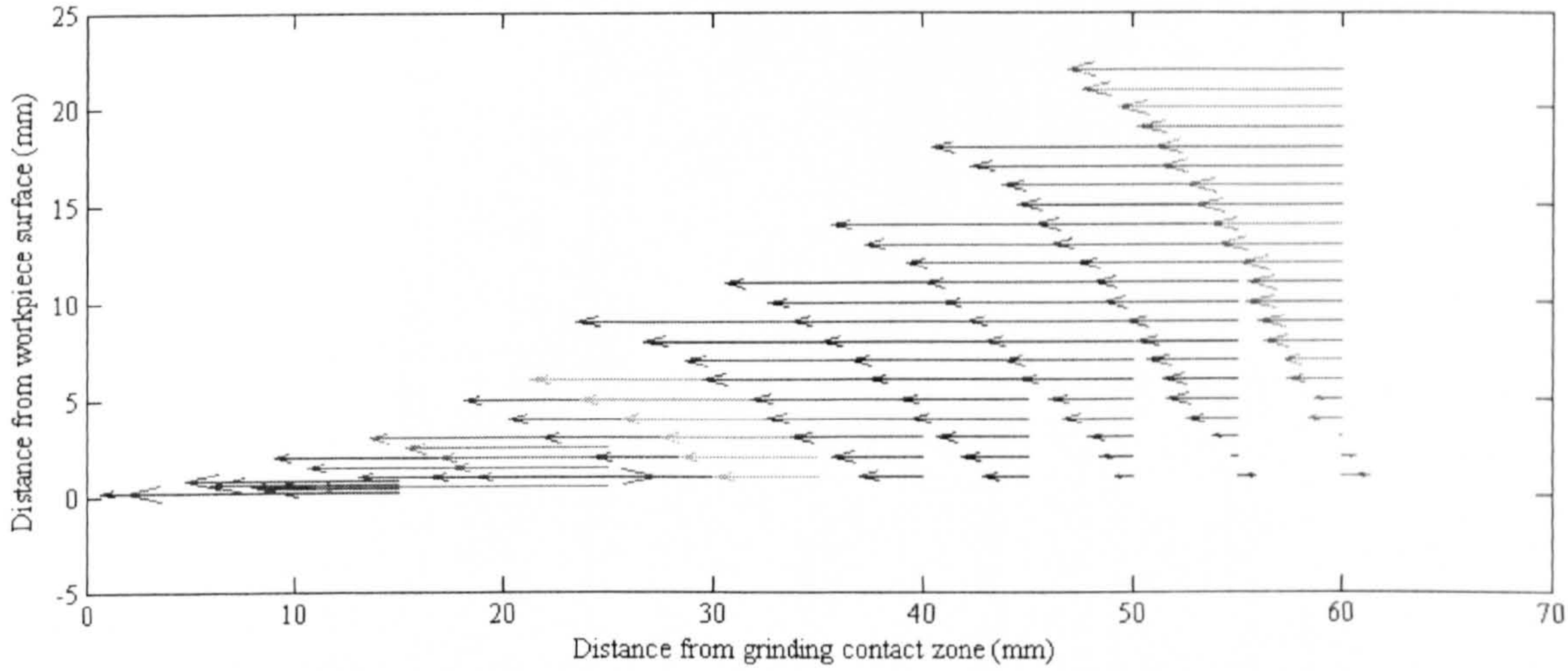

B. Air horizontal velocity map (workpiece width: 40mm; wheel Middle section)

Width of workpiece does not affect the air boundary layer velocity

Appendix B. Matlab programs

1. Sample of Matbab code to generate the velocity contour map

****

```
load velocity.dat
x=[-4:1:23]
y=[0.5,1.5,3,5,8,15,25,40]'
z=velocity
z=z'

[C,h] = contour(x,y,z)
set(h,'ShowText','on','TextStep',get(h,'LevelStep')*2)

axis ([-4 23 0 40]);
ylabel('Distance from wheel surface (mm)');  % Give y axis title
xlabel('Wheel width (mm)');
```

****

2. Sample of Matbab code to generate the fluid velocity map

****

```
load entryR_M_without_wp.dat
[A,B] = meshgrid(0,-10:2:-2);
b=entryR_M_without_wp(1:5,1)
a=entryR_M_without_wp(1:5,2)
quiver(A,B,a,b,0)
hold on

[C,D] = meshgrid(5,-10:2:-2);
d=entryR_M_without_wp(6:10,1)
c=entryR_M_without_wp(6:10,2)
quiver(C,D,c,d,0)

[E,F] = meshgrid(10,-10:2:-2);
f=entryR_M_without_wp(11:15,1)
e=entryR_M_without_wp(11:15,2)
quiver(E,F,e,f,0)

[G,H] = meshgrid(15,-10:2:-2);
h=entryR_M_without_wp(16:20,1)
g=entryR_M_without_wp(16:20,2)
quiver(G,H,g,h,0)

[I,J] = meshgrid(20,-10:2:0);
j=entryR_M_without_wp(21:26,1)
i=entryR_M_without_wp(21:26,2)
quiver(I,J,i,j,0)

[K,L] = meshgrid(25,-10:2:2);
l=entryR_M_without_wp(27:33,1)
k=entryR_M_without_wp(27:33,2)
quiver(K,L,k,l,0)

[M,N] = meshgrid(30,-10:2:2);
n=entryR_M_without_wp(34:40,1)
m=entryR_M_without_wp(34:40,2)
quiver(M,N,m,n,0)

[O,P] = meshgrid(35,-10:2:4);
p=entryR_M_without_wp(41:48,1)
o=entryR_M_without_wp(41:48,2)
quiver(O,P,o,p,0)

[Q,R] = meshgrid(40,-10:2:6);
r=entryR_M_without_wp(49:57,1)
q=entryR_M_without_wp(49:57,2)
quiver(Q,R,q,r,0)

[S,T] = meshgrid(45,-10:2:8);
t=entryR_M_without_wp(58:67,1)
s=entryR_M_without_wp(58:67,2)
quiver(S,T,s,t,0)

[U,V] = meshgrid(50,-10:2:12);
v=entryR_M_without_wp(68:79,1)
u=entryR_M_without_wp(68:79,2)
quiver(U,V,u,v,0)

[W,X] = meshgrid(55,-10:2:16);
x=entryR_M_without_wp(80:93,1)
w=entryR_M_without_wp(80:93,2)
quiver(W,X,w,x,0)

[Y,Z] = meshgrid(60,-10:2:20);
z=entryR_M_without_wp(94:109,1)
y=entryR_M_without_wp(94:109,2)
quiver(Y,Z,y,z,0)

[AA,BB] = meshgrid(65,-10:2:24);
bb=entryR_M_without_wp(110:127,1)
aa=entryR_M_without_wp(110:127,2)
quiver(AA,BB,aa,bb,0)

[CC,DD] = meshgrid(70,-10:2:30);
dd=entryR_M_without_wp(128:148,1)
cc=entryR_M_without_wp(128:148,2)
quiver(CC,DD,cc,dd,0)

[EE,FF] = meshgrid(75,-10:2:36);
ff=entryR_M_without_wp(149:172,1)
ee=entryR_M_without_wp(149:172,2)
quiver(EE,FF,ee,ff,0)

[GG,HH] = meshgrid(80,-10:2:44);
hh=entryR_M_without_wp(173:200,1)
gg=entryR_M_without_wp(173:200,2)
quiver(GG,HH,gg,hh,0)

[II,JJ] = meshgrid(85,-10:2:46);
jj=entryR_M_without_wp(201:229,1)
ii=entryR_M_without_wp(201:229,2)
quiver(II,JJ,ii,jj,0)

[KK,LL] = meshgrid(90,-10:2:46);
ll=entryR_M_without_wp(230:258,1)
kk=entryR_M_without_wp(230:258,2)
quiver(KK,LL,kk,ll,0)

axis ([-10 95 -15 50]);
ylabel('Distance from workpiece surface (mm)'); % Give y axis title
xlabel('Distance from grinding contact zone (mm)');
```

****

Appendix C. Experimental arrangement pictures

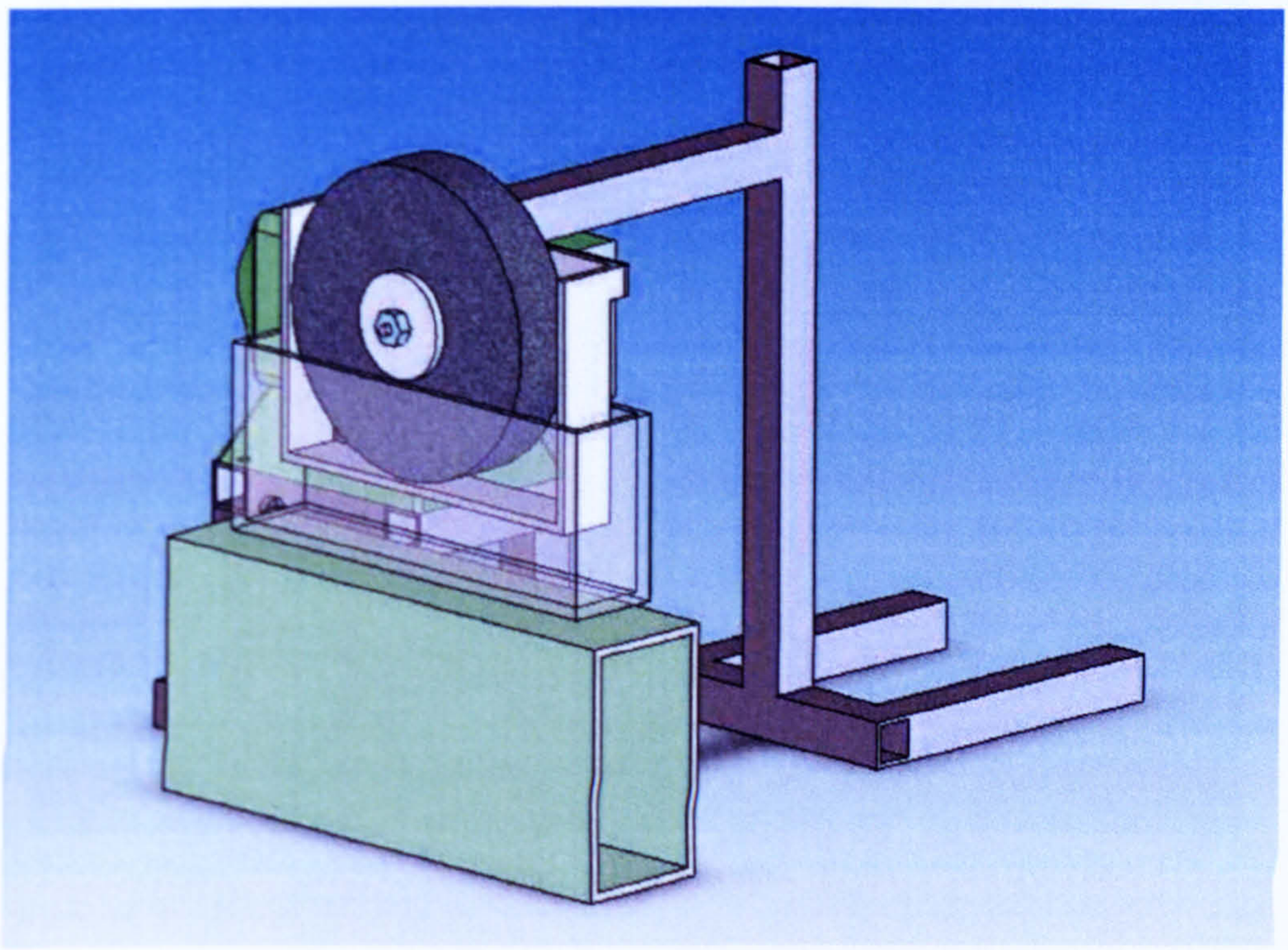

Modified grinding system for fluid velocity mapping using LDA

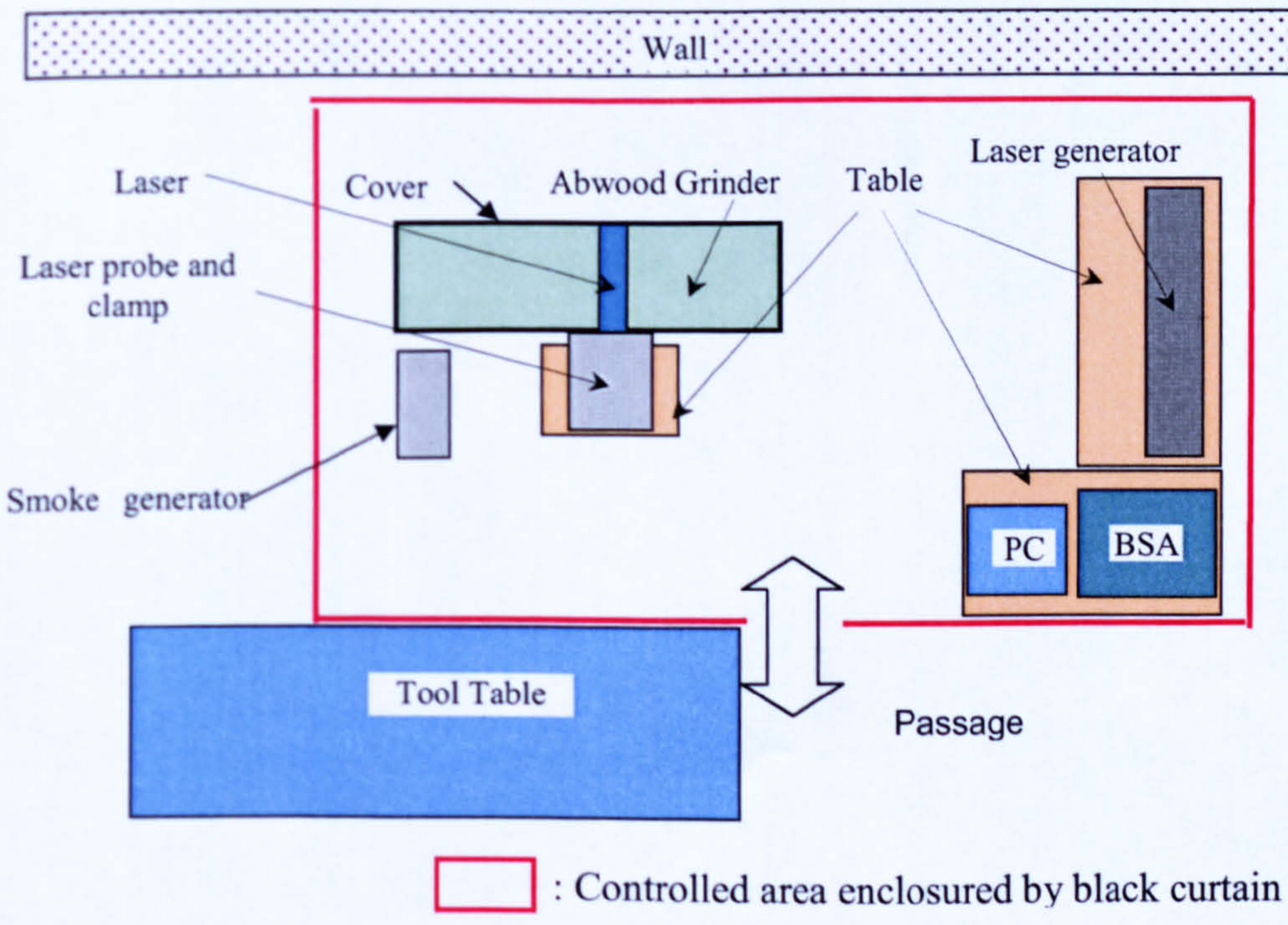

Position of the controlled area for the Laser safe

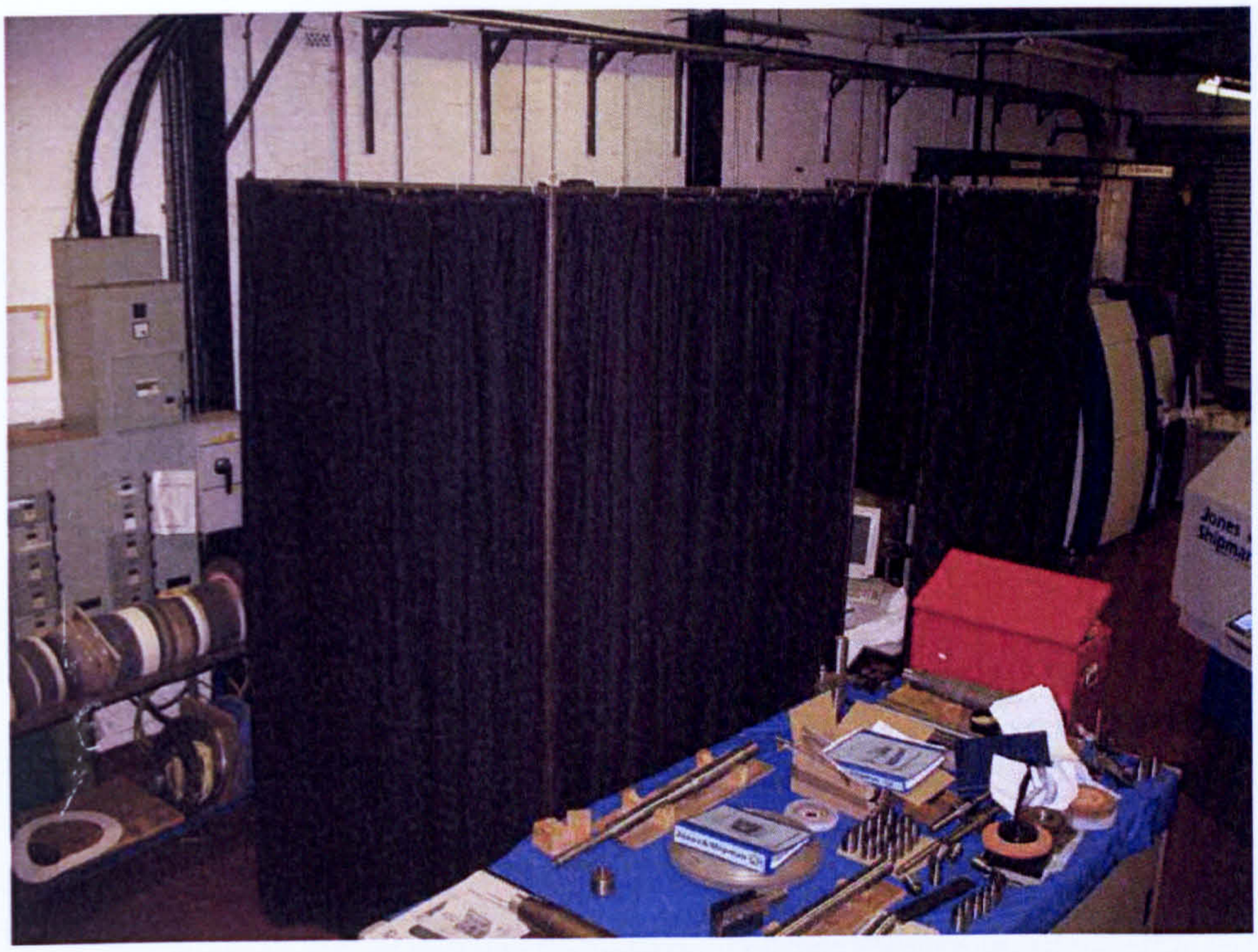

Laser safety curtain

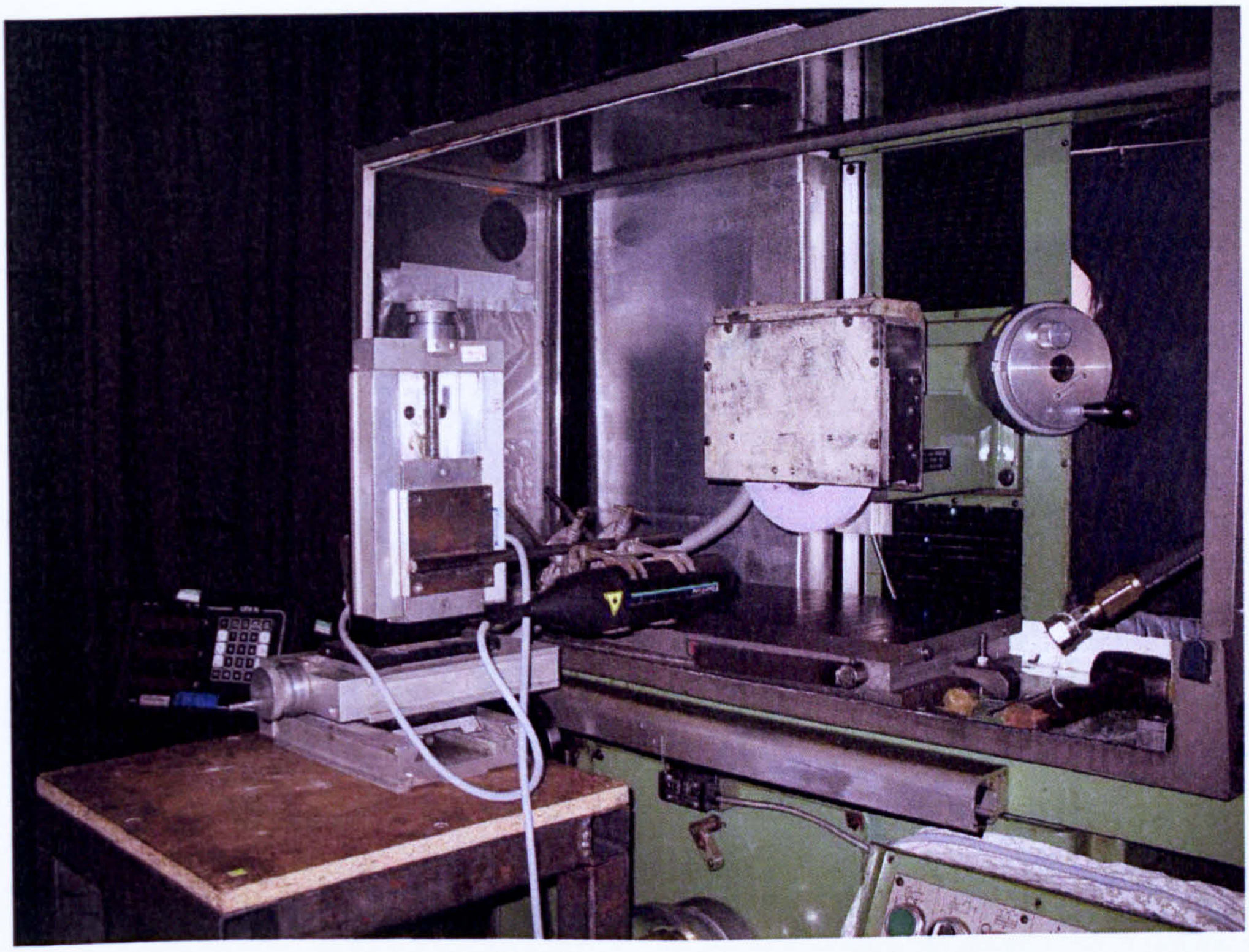

Abwood grinding machine

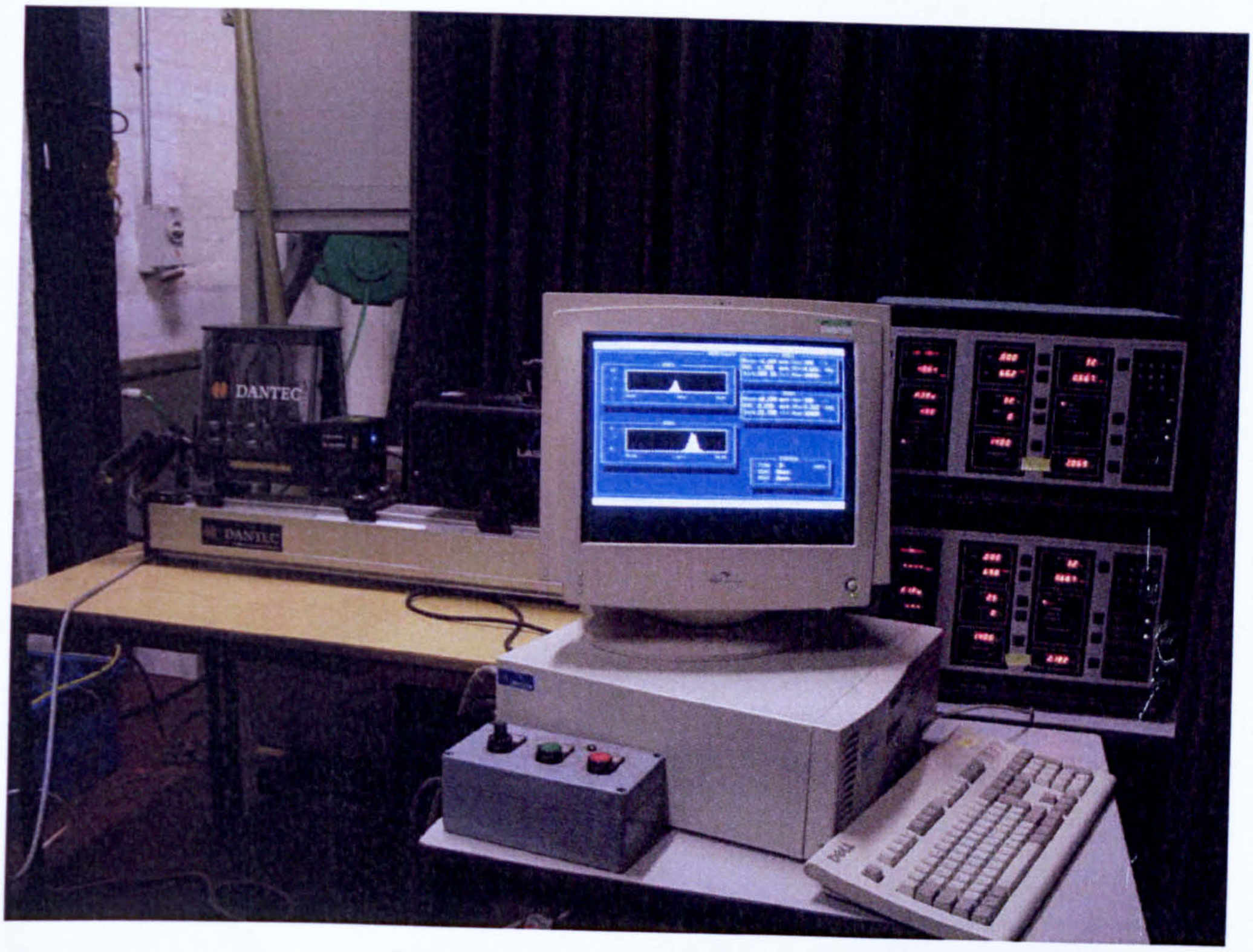

LDA arrangement in working place

Appendix D. Simulation results

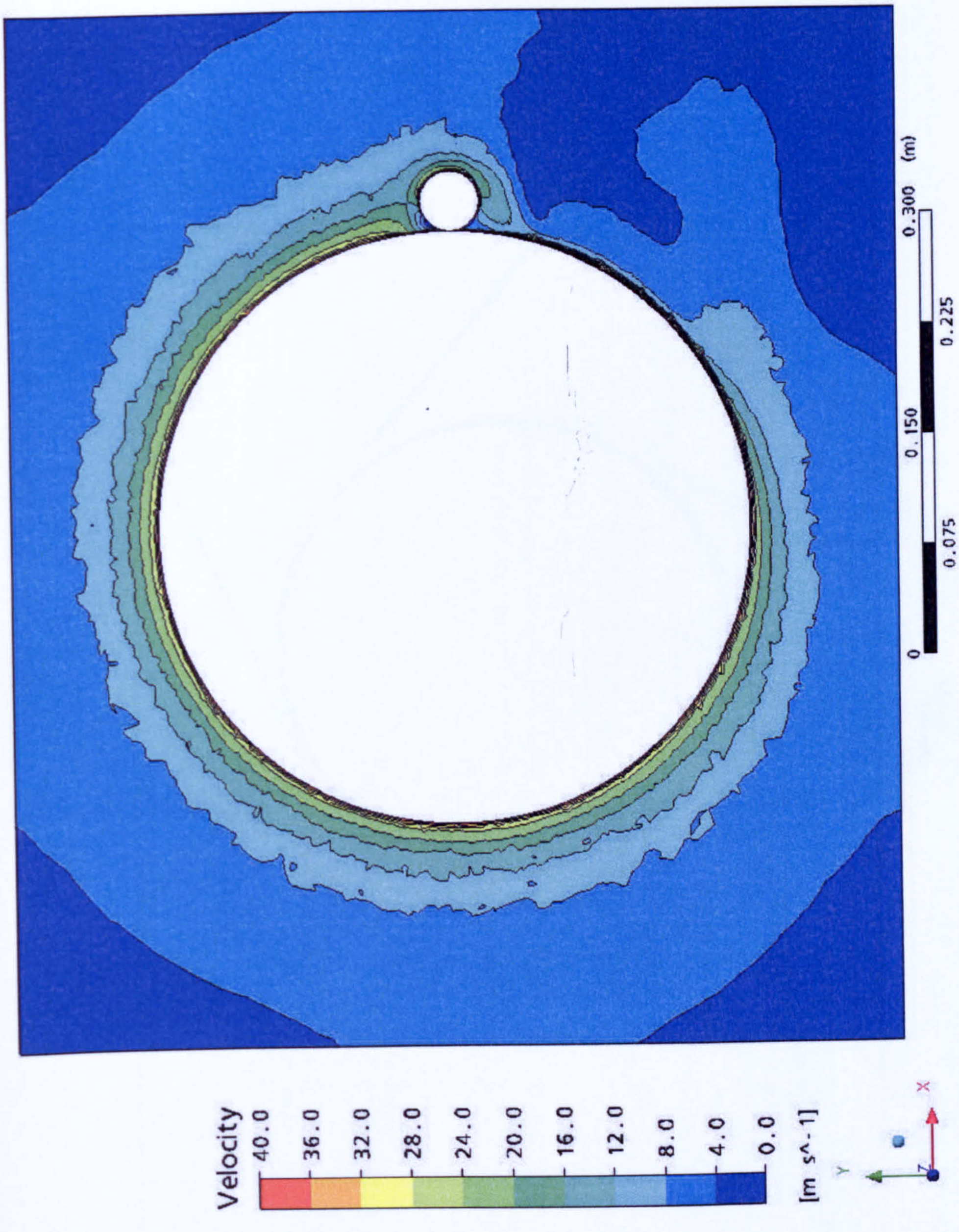

Air velocity distribution in cylindrical grinding

Air velocity stream line around the wheel

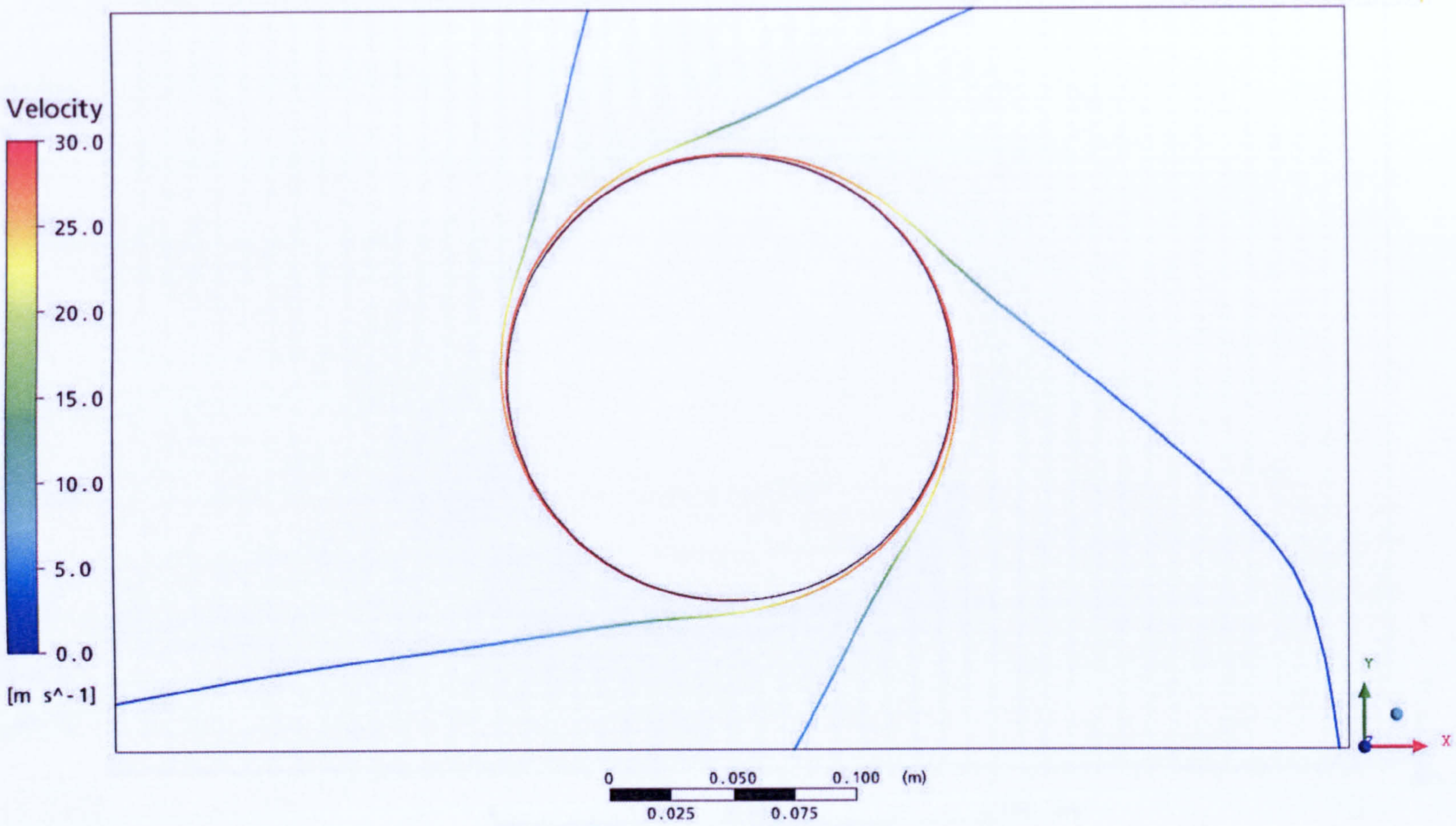

Velocity vector distribution around the wheel (without workpiece)

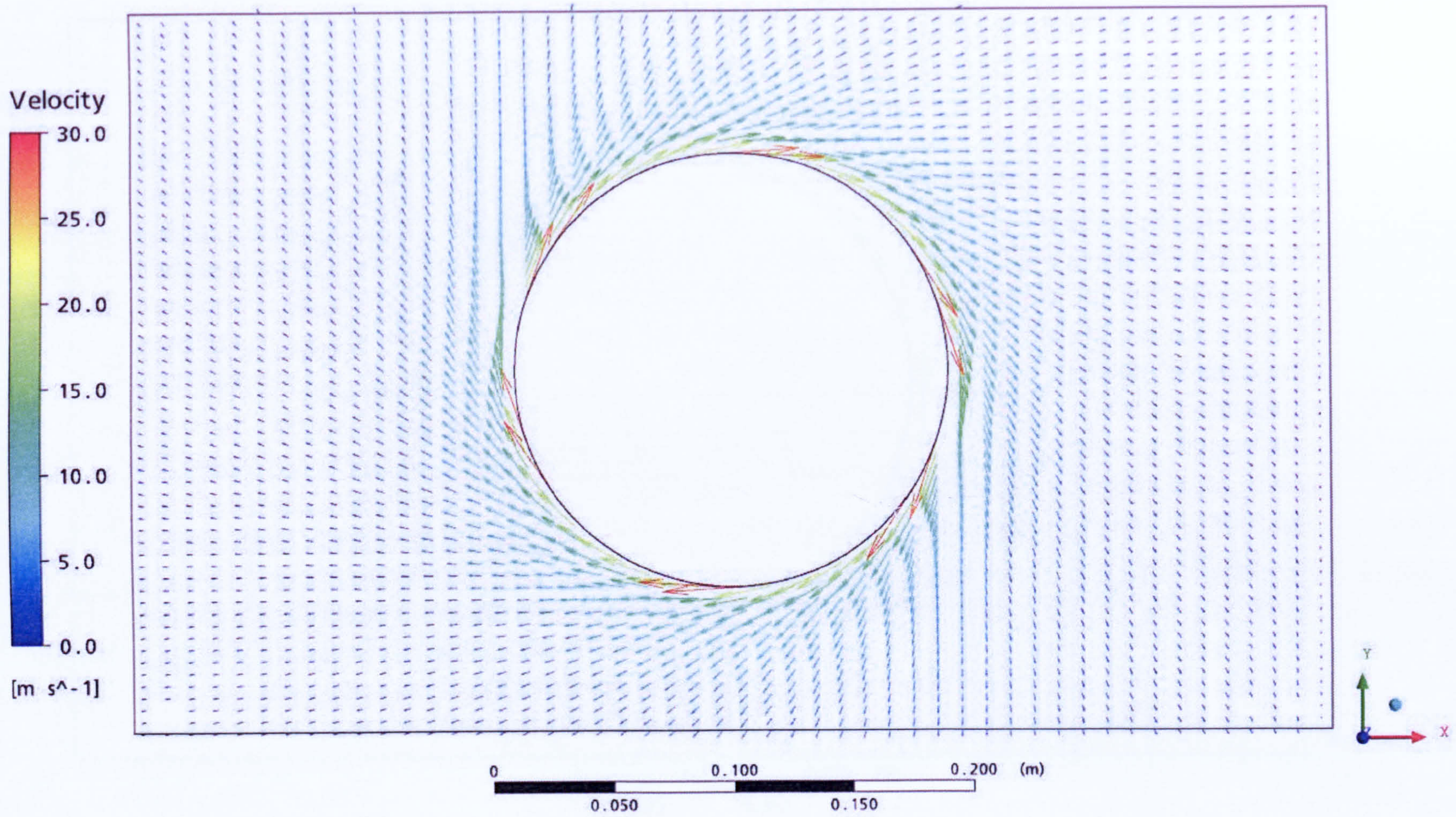

Velocity vector distribution around the wheel (with workpiece)

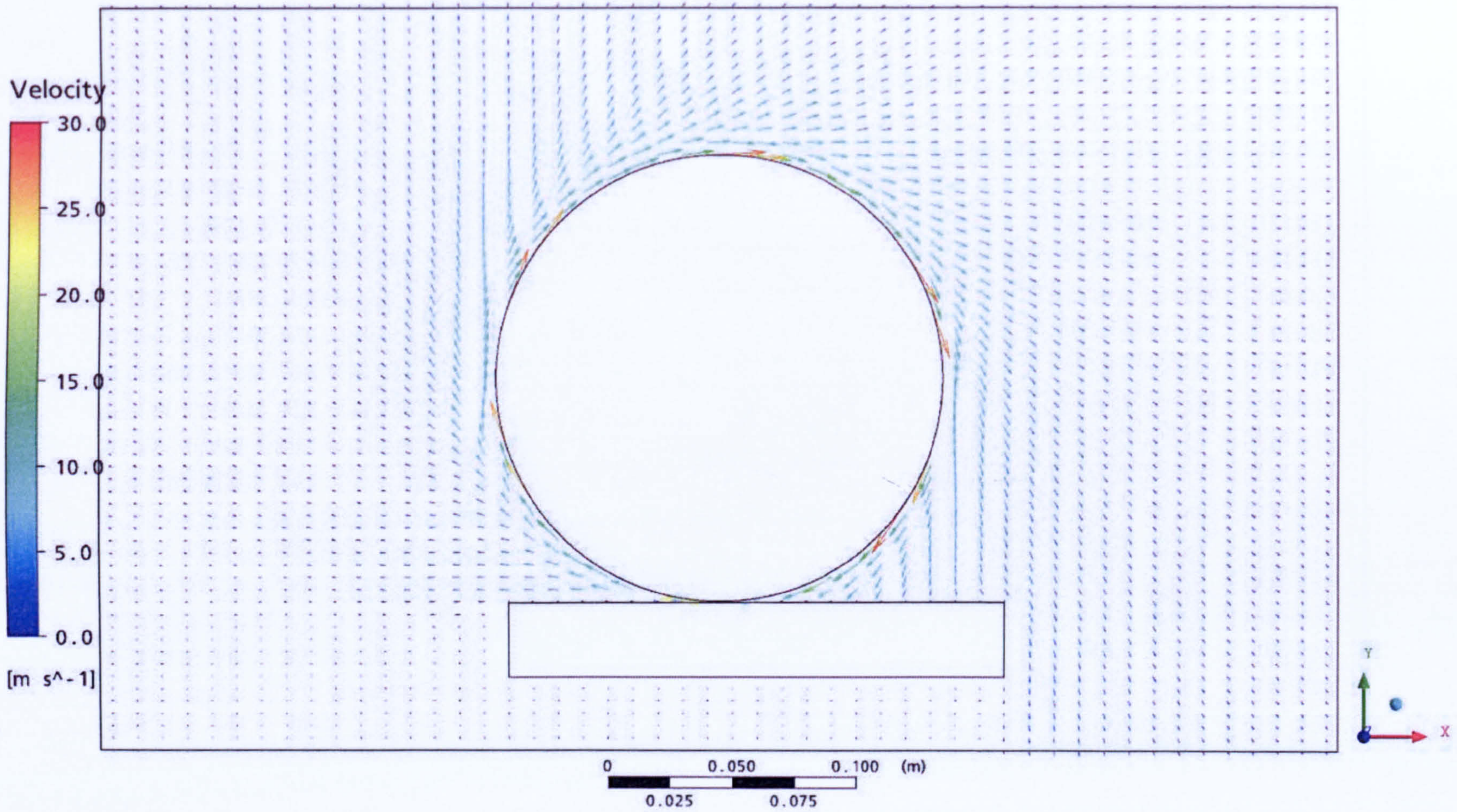

Velocity distribution with workpiece and scraper

Velocity
30.0
25.0
20.0
15.0
10.0
5.0
0.0
[m s^-1]

0 0.050 0.100 (m)
0.025 0.075

Y
X

Contour of velocity distribution with workpiece and scraper

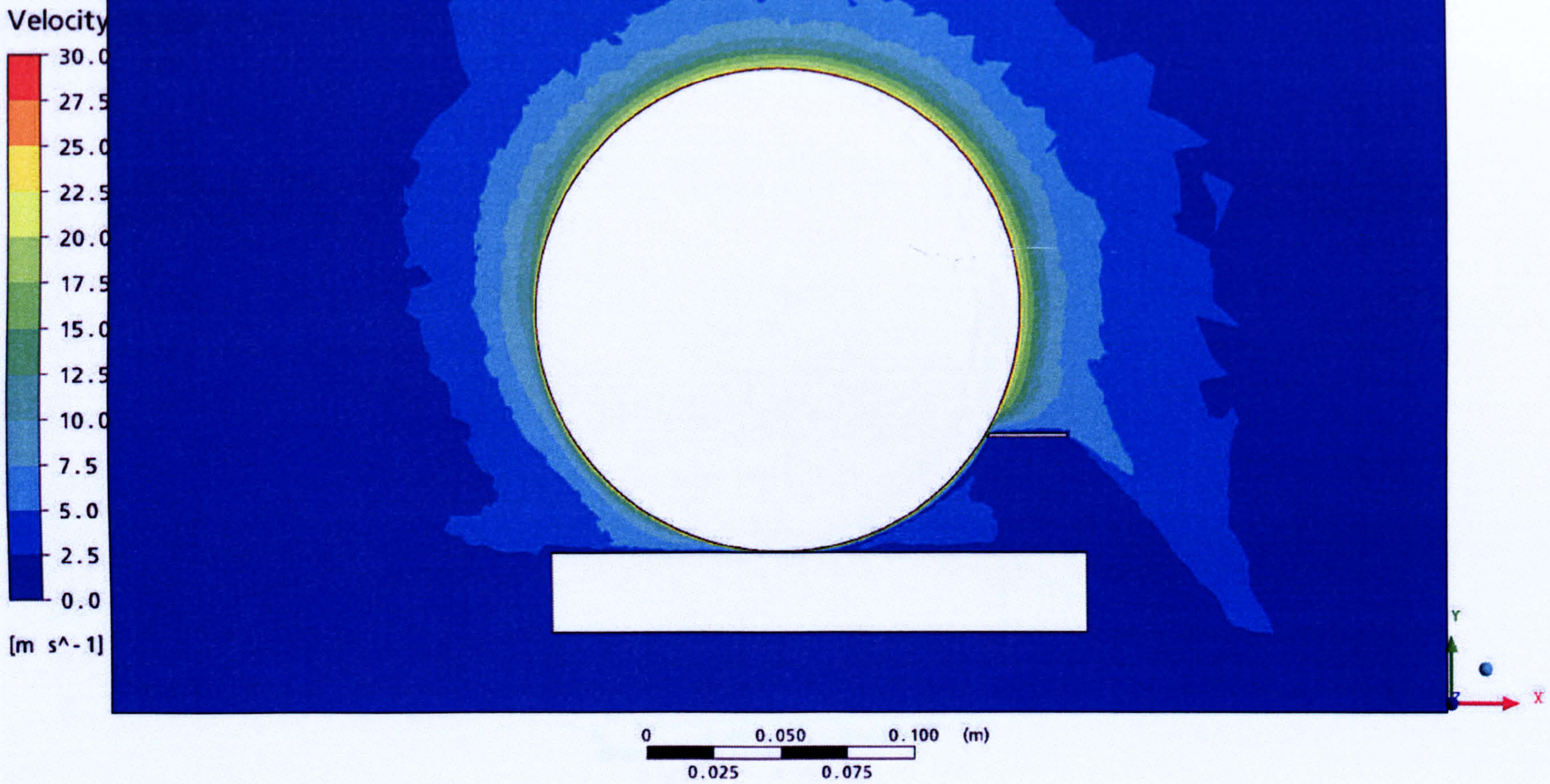

Air velocity vector with workpiece and shoe nozzle

Air at 25 C Superficial Velocity

30.0
25.0
20.0
15.0
10.0
5.0
0.0
[m s^-1]

0 0.050 0.100 (m)
0.025 0.075

Y
X
Z

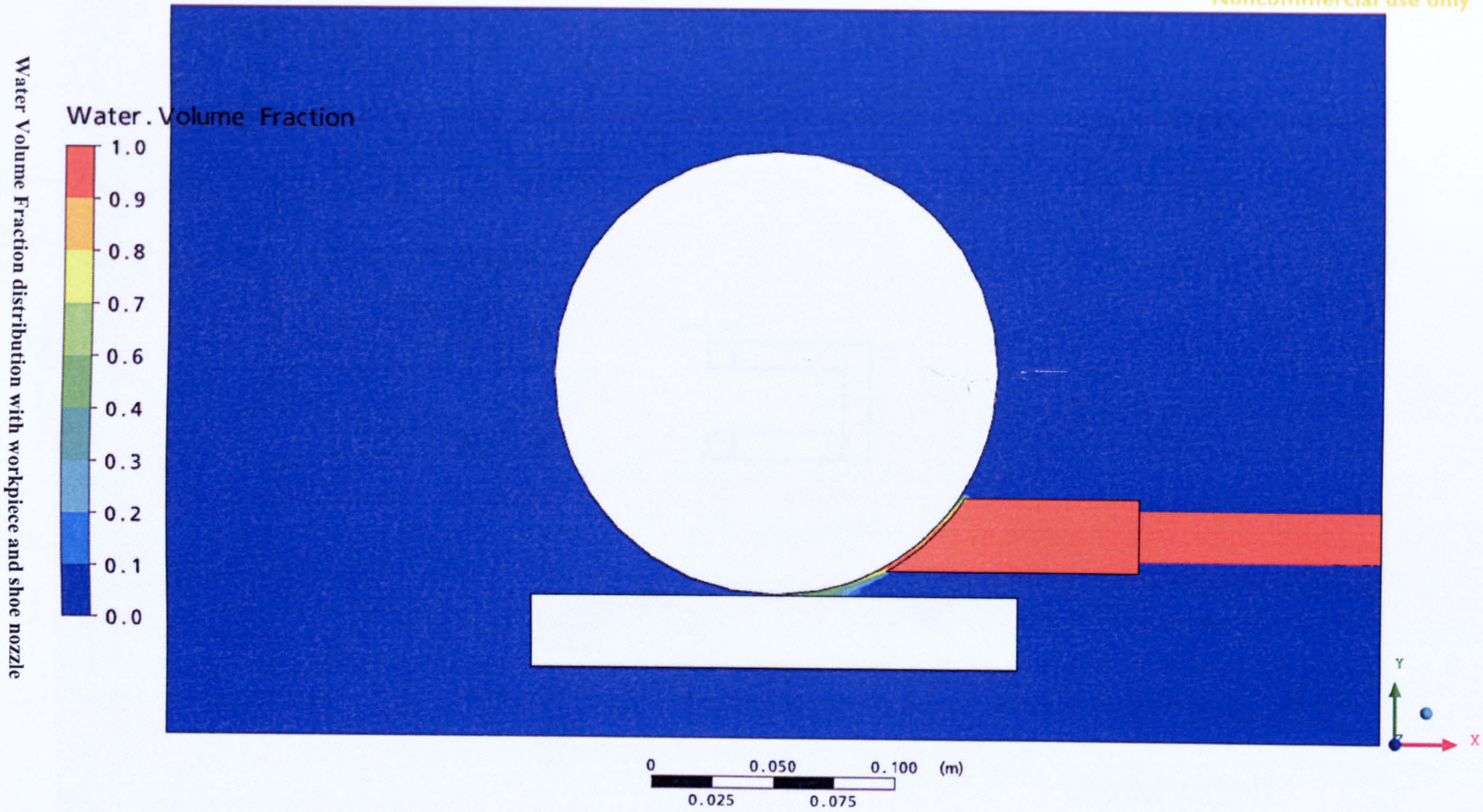

Water Volume Fraction distribution with workpiece and shoe nozzle

Appendix E. Engineering drawings

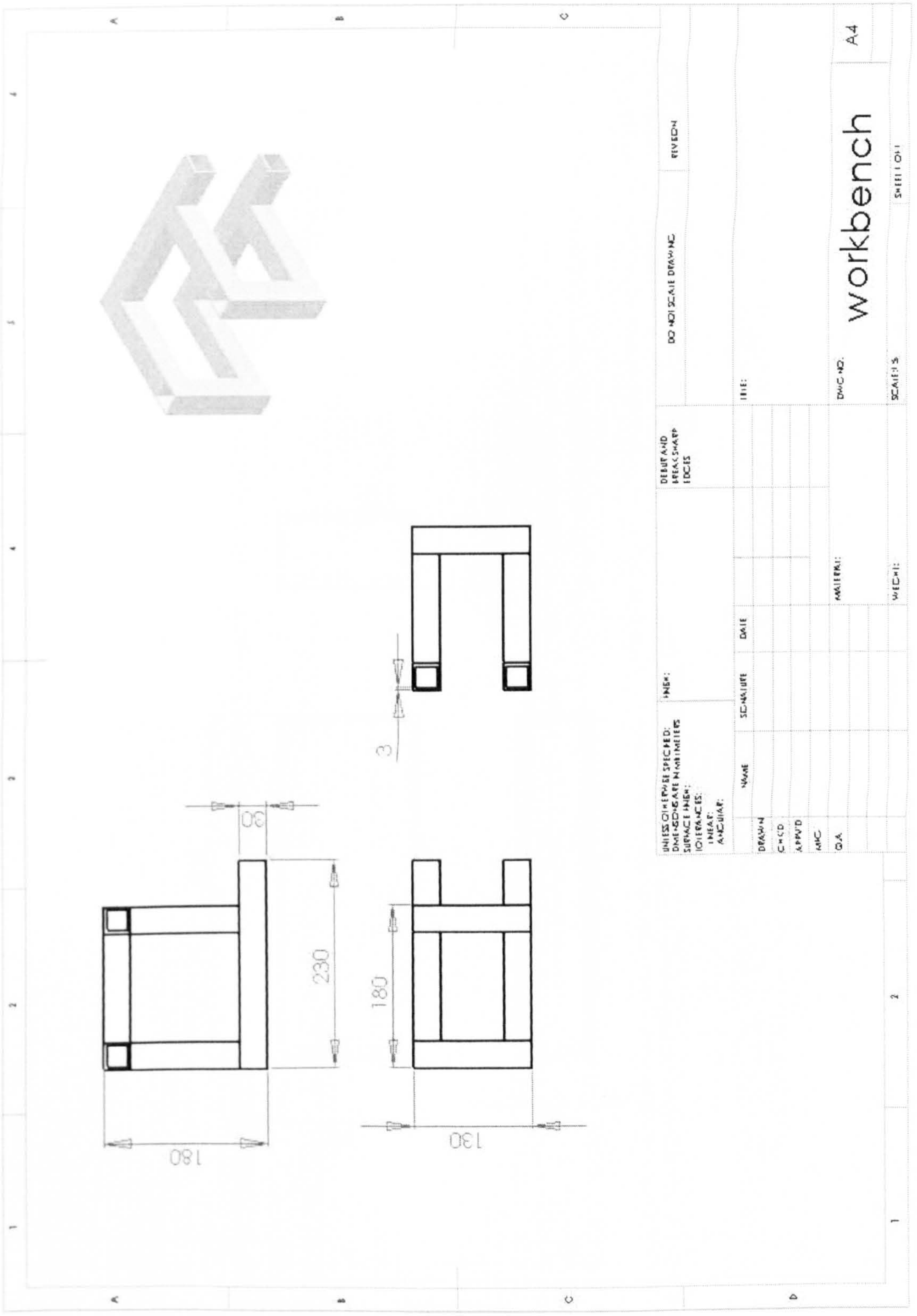

Grinder support

Fluid tank

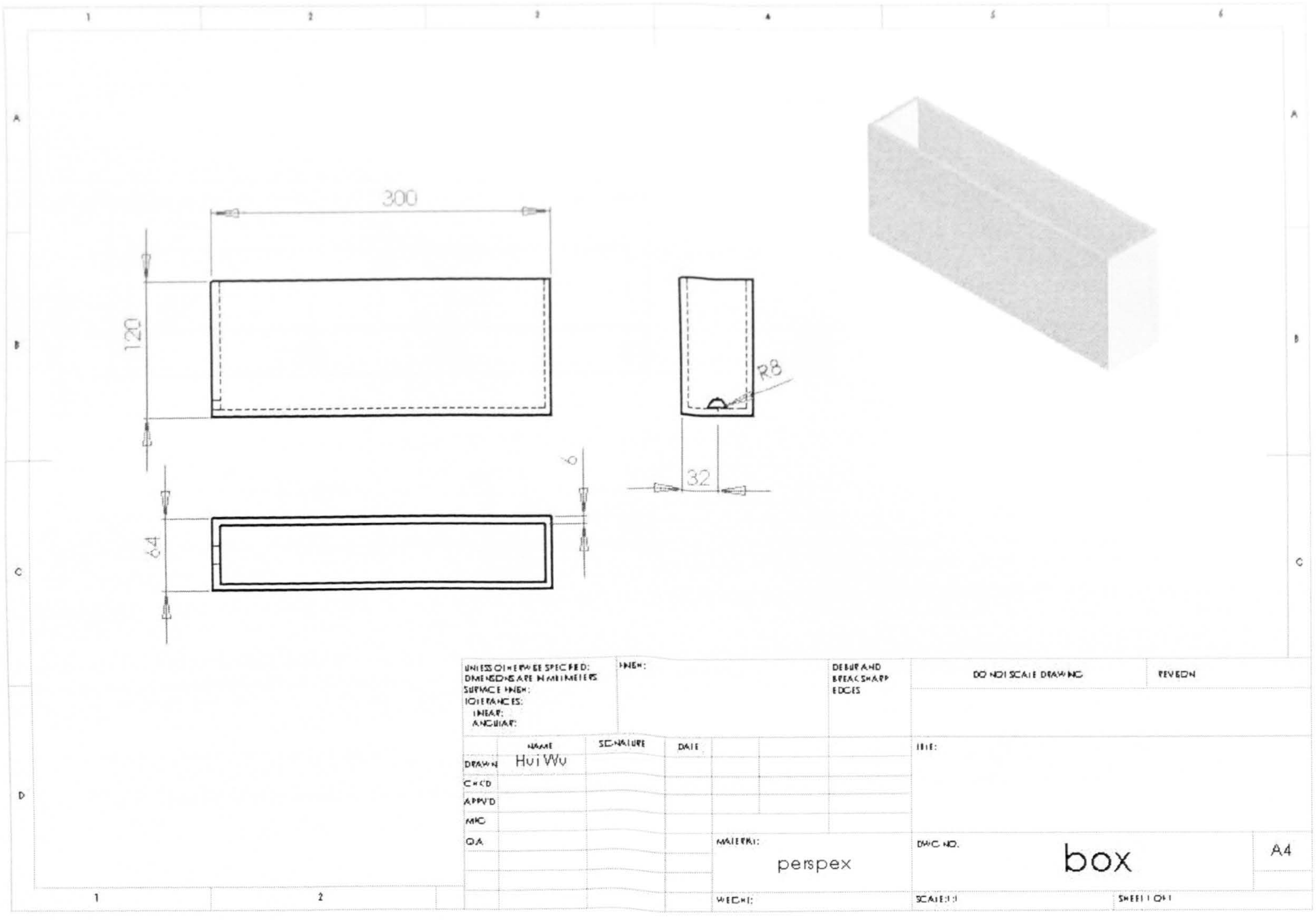

UNLESS OTHERWISE SPECIFIED: DIMENSIONS ARE IN MILLIMETERS SURFACE FINISH: TOLERANCES: LINEAR: ANGULAR:	FINISH:					DEBUR AND BREAK SHARP EDGES	DO NOT SCALE DRAWING	REVISION
	NAME	SIGNATURE	DATE				TITLE:	
DRAWN	Hui Wu							
CHK'D								
APPV'D								
MFG								
Q.A								
				MATERIAL: perspex			DWG NO. box	A4
				WEIGHT:			SCALE:1:1	SHEET 1 OF 1

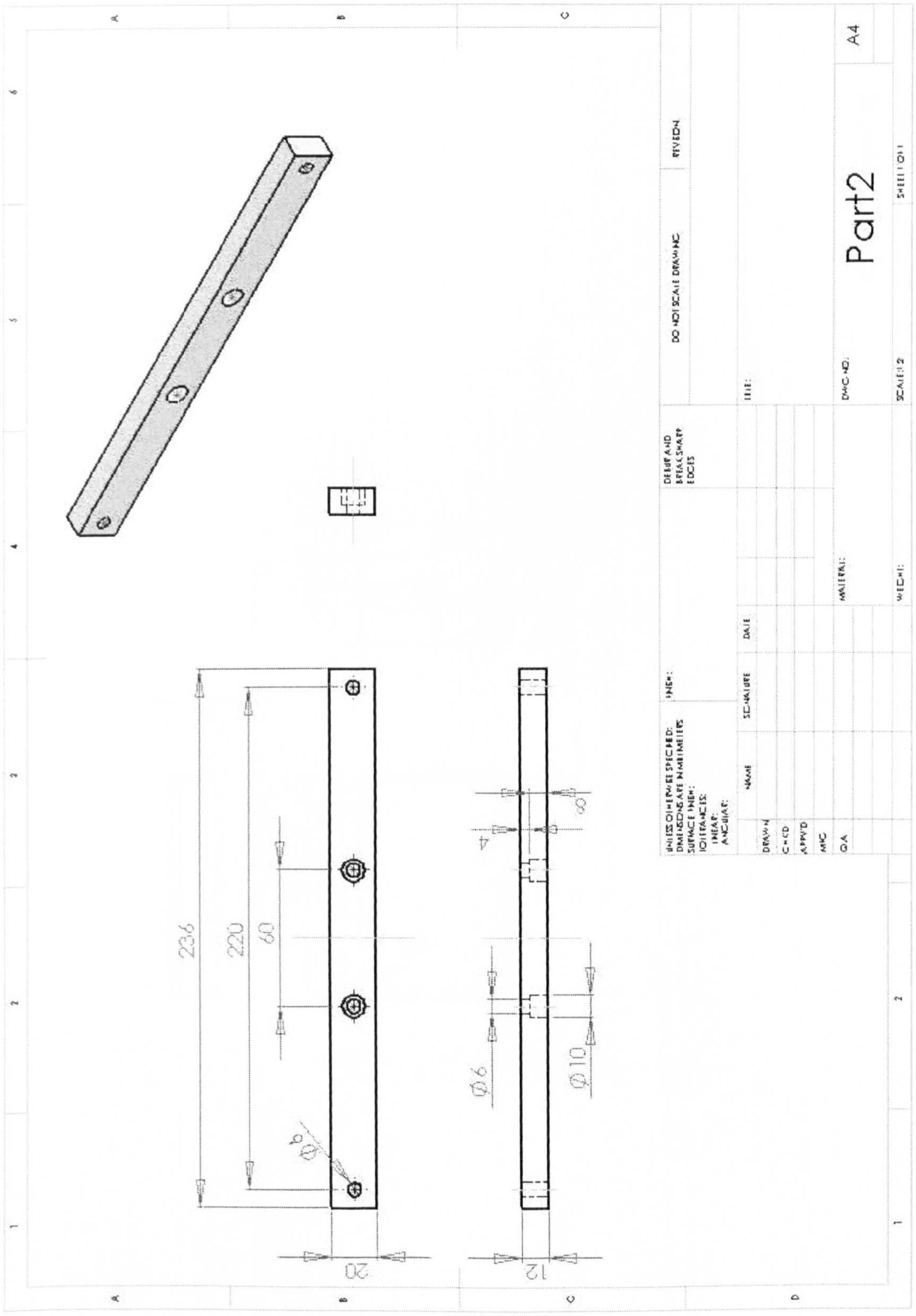

Connector of the workpiece and traverse

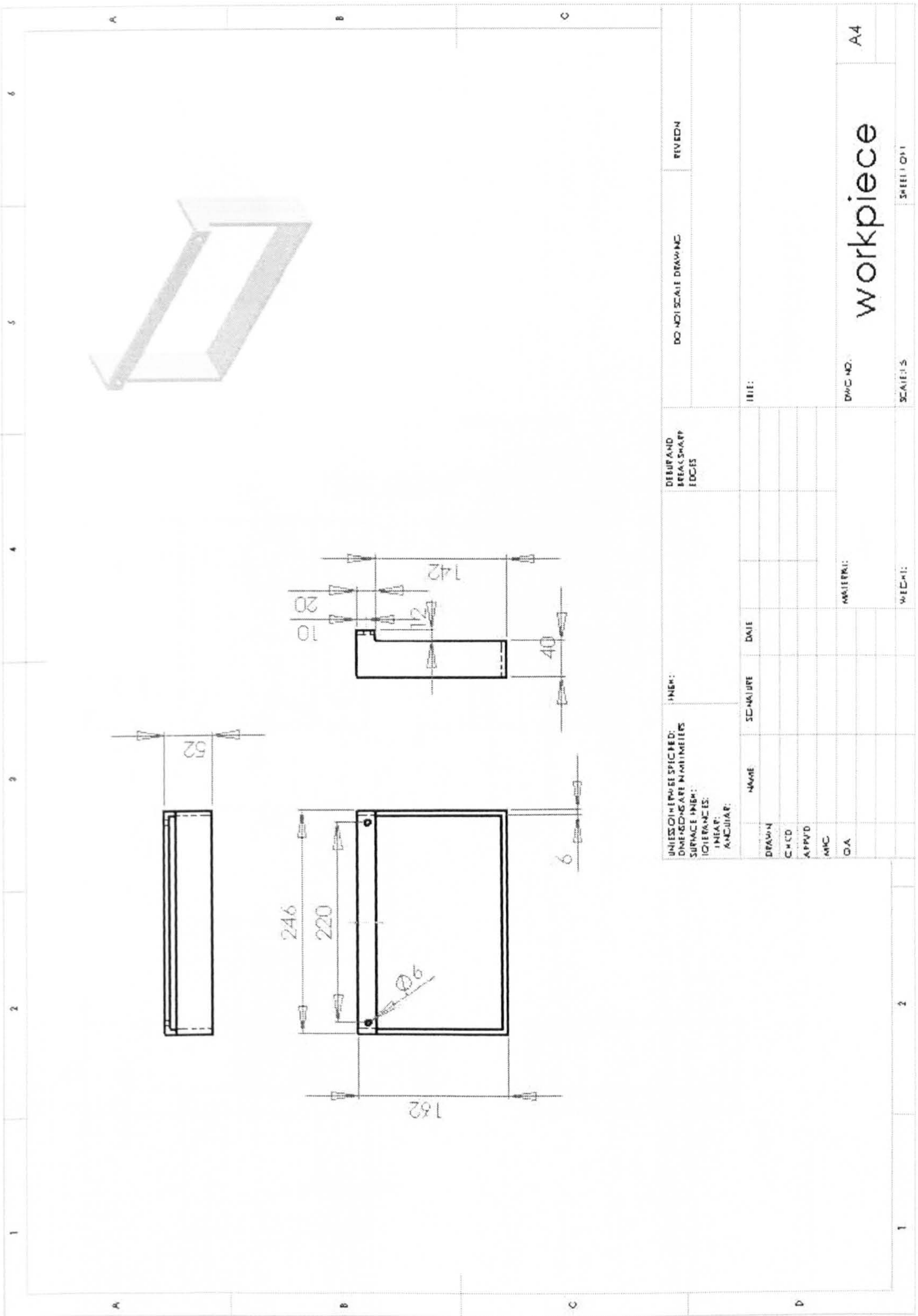

Workpiece support

Scraper clamp connector part 1

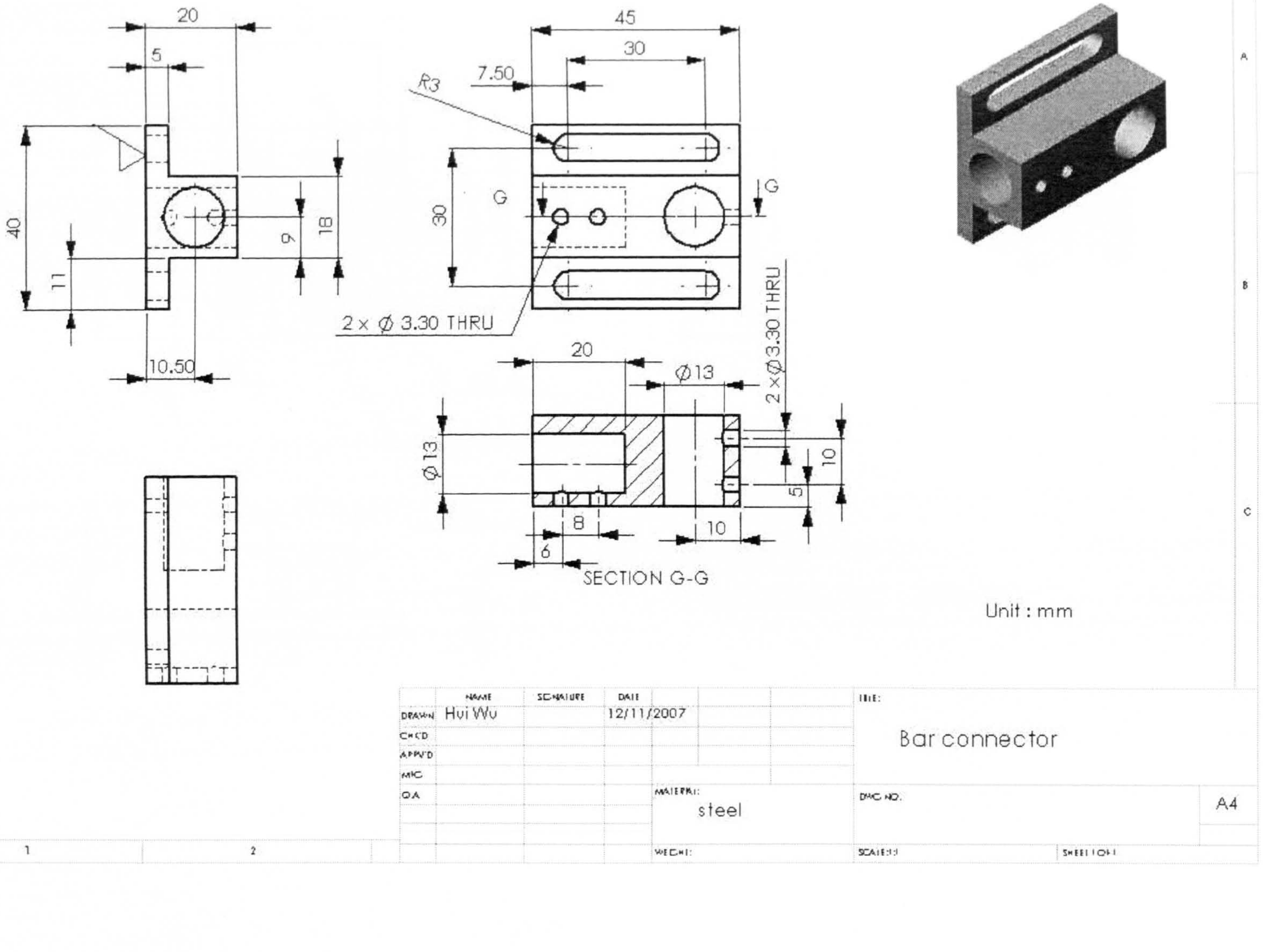

Scraper clamp connector part 2

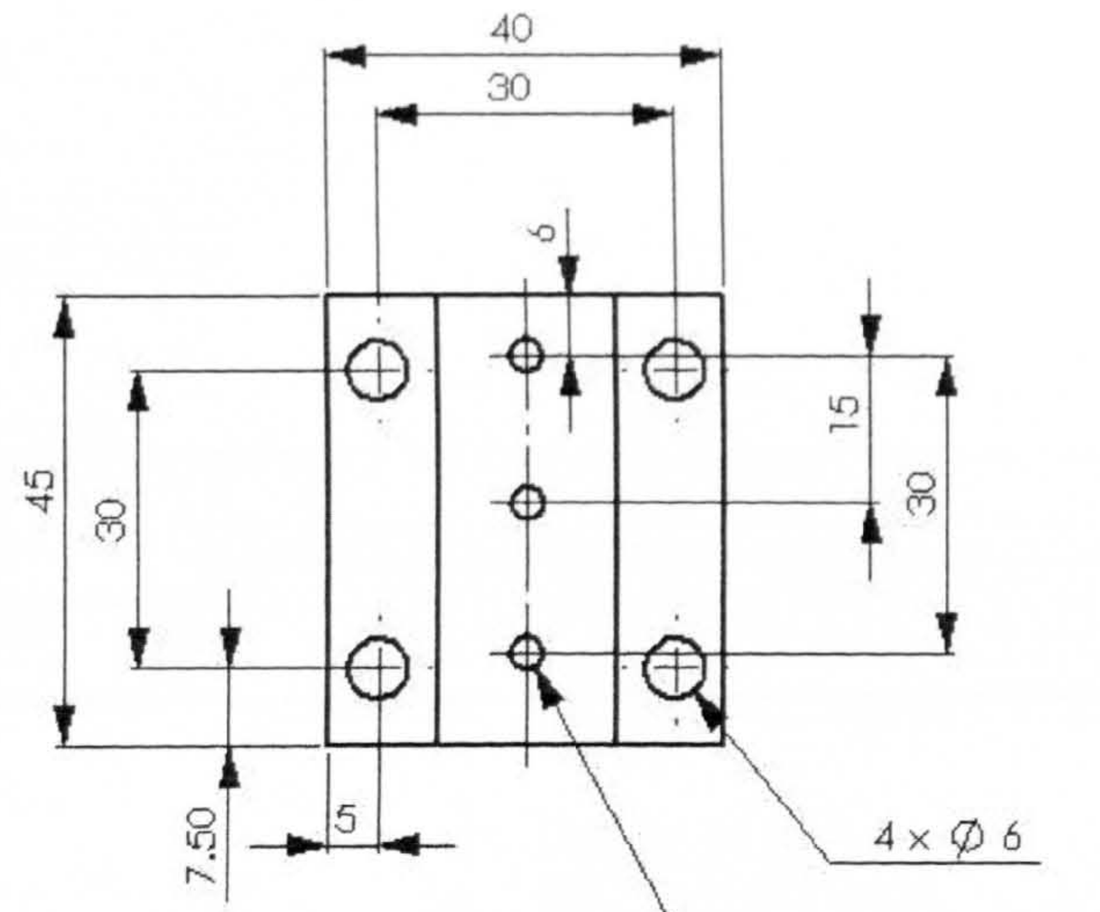

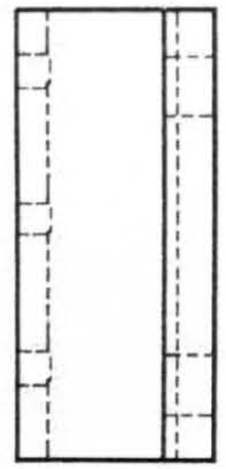

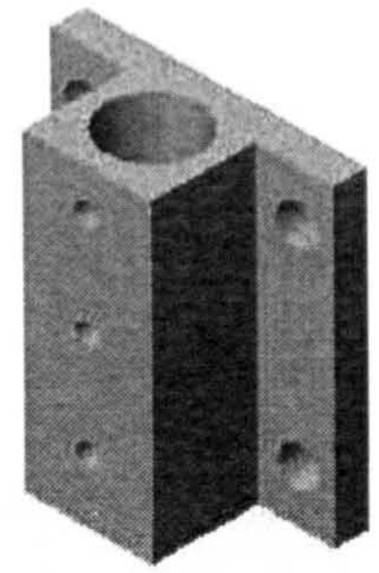

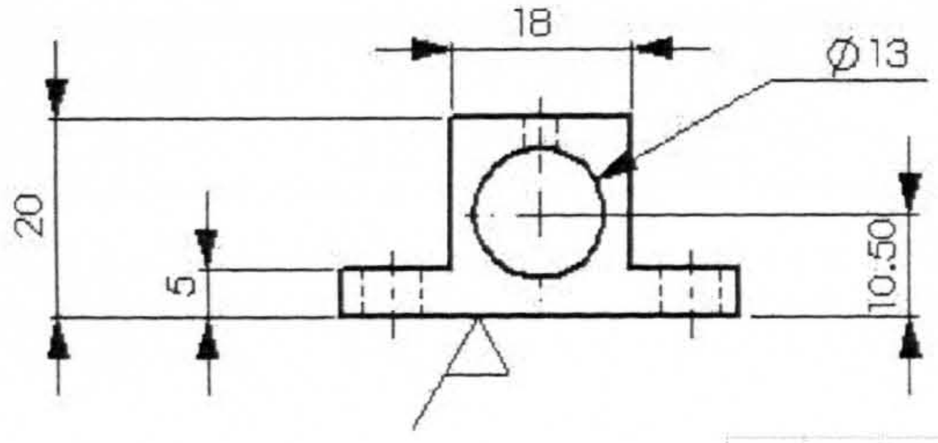

Unit : mm

	NAME	SIGNATURE	DATE	TITLE
DRAWN	Hui Wu		12/11/2007	Structure
CHK'D				
APP'D				
MFG				
Q.A			MATERIAL: Steel	DWG NO. A4
			WEIGHT:	SCALE: 1:1 SHEET 1 OF 1

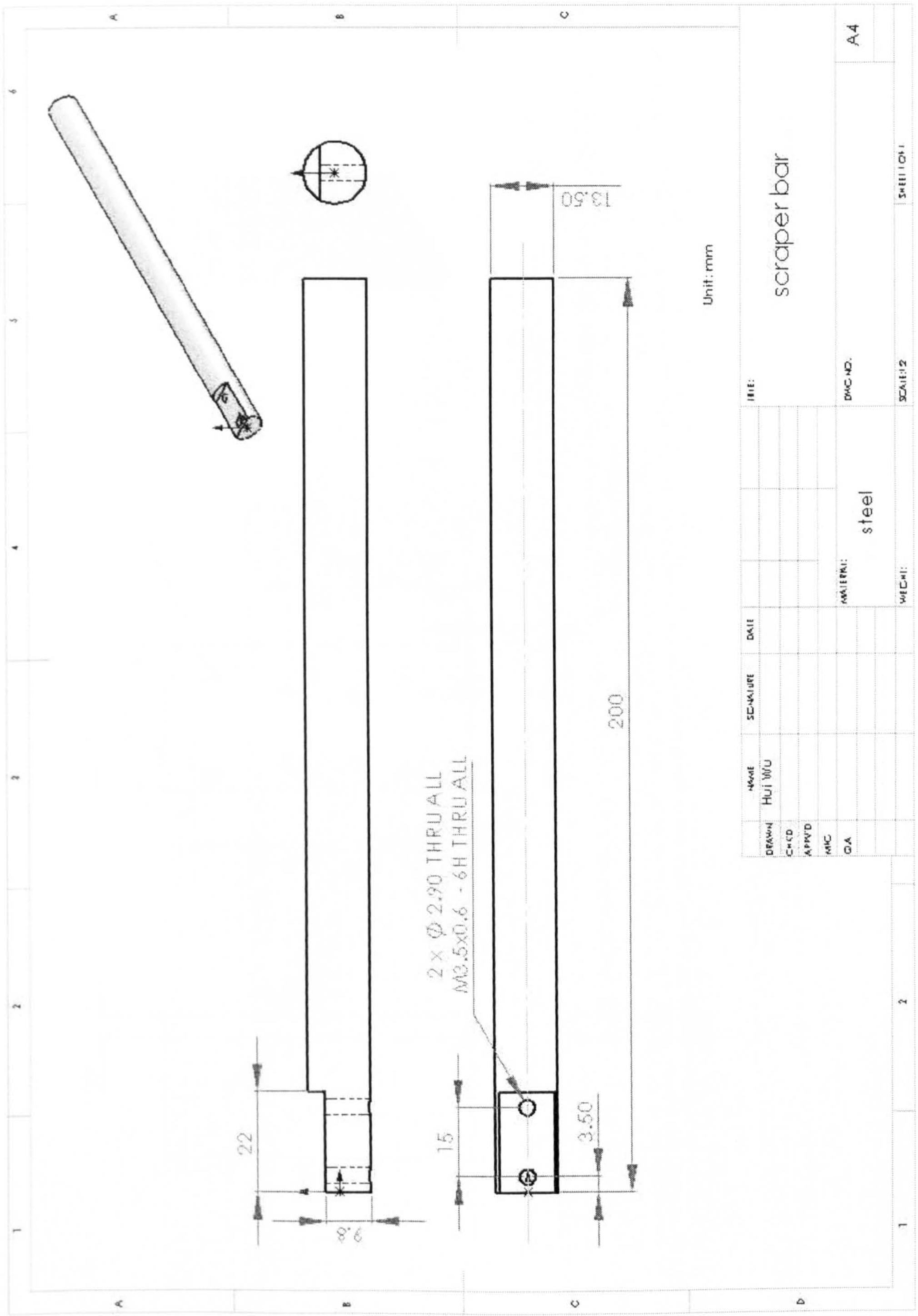
A4
SHEET 1 OF 1
scraper bar
Unit: mm
NAME
DRAWN Hui WU
CHK'D
APPV'D
MFG
QA
DATE:
DWG NO.
SCALE: 2
WEIGHT:
MATERIAL:
steel
SIGNATURE
DATE
13.50
200
2 X Ø 2.90 THRU ALL
M3.5x0.6 - 6H THRU ALL
22
15
3.50
8.6

Scraper bar

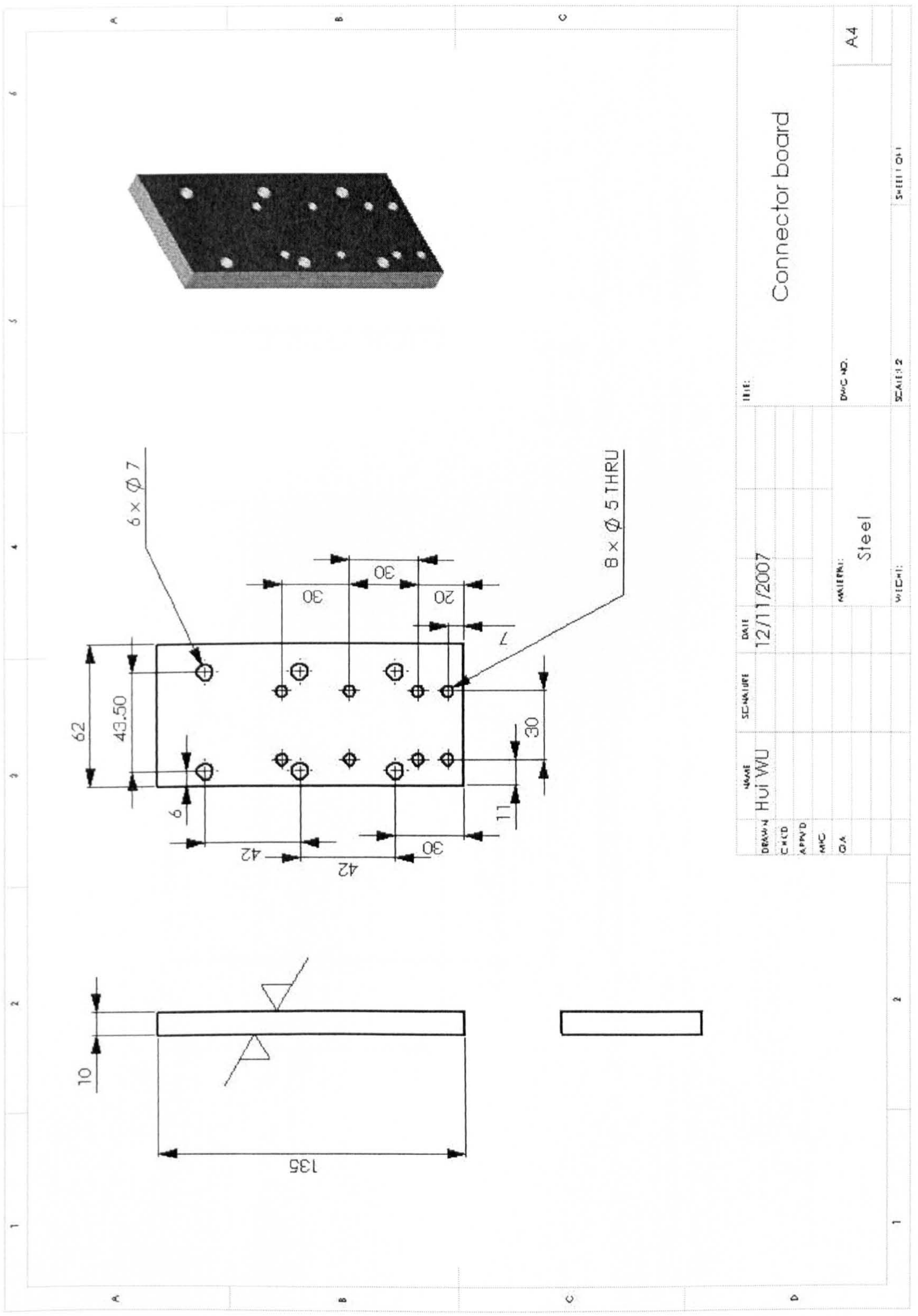

Scraper clamp connector board

Scraper (width: 30mm)

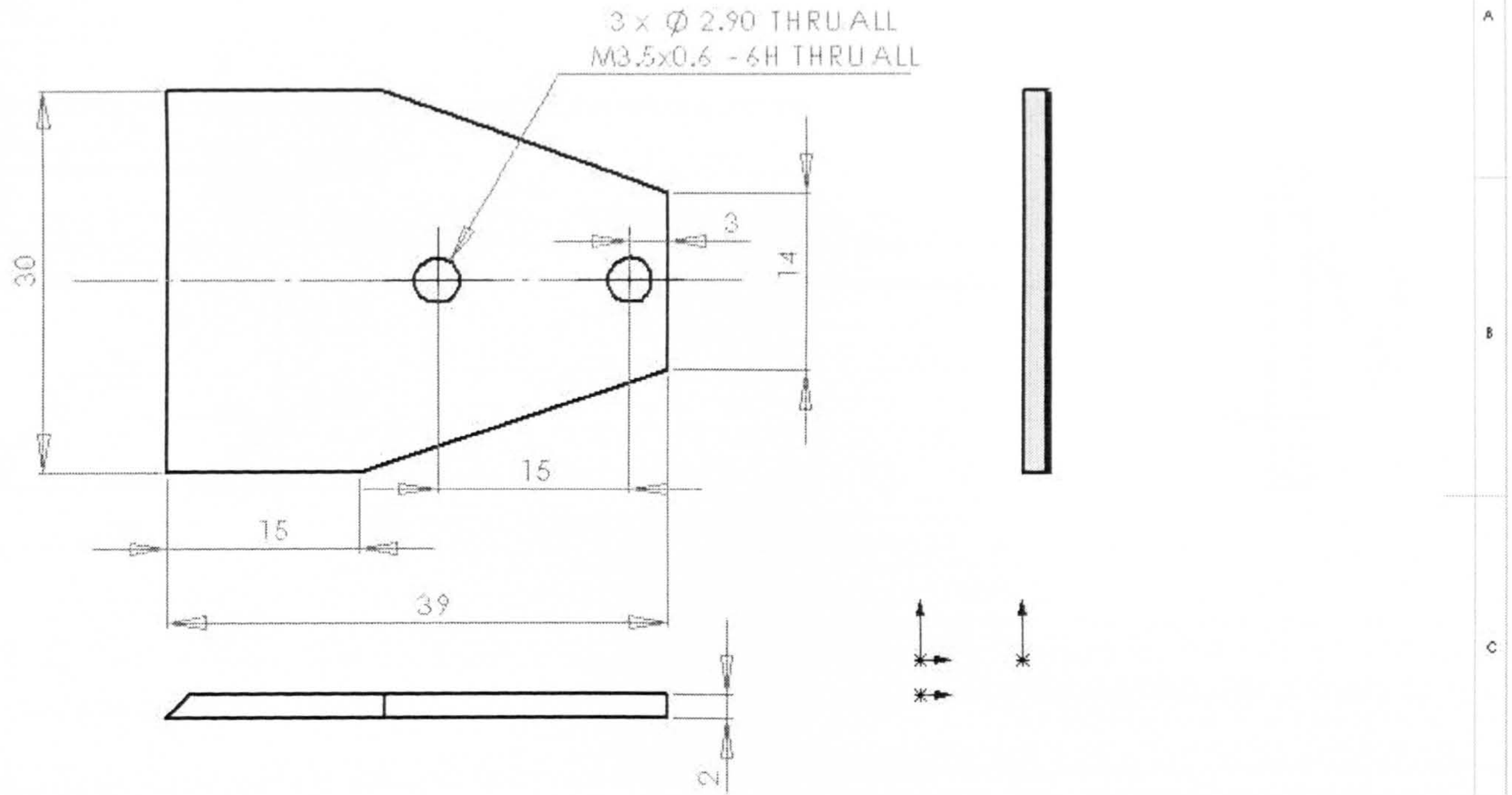

unit: mm

	NAME	SIGNATURE	DATE		
DRAWN	Hui Wu				
CHK'D					
APPV'D					
MFG					
Q.A.					

TITLE: Scraper

MATERIAL: Steel

DWG NO. A4

WEIGHT: SCALE:2:1 SHEET 1 OF 1

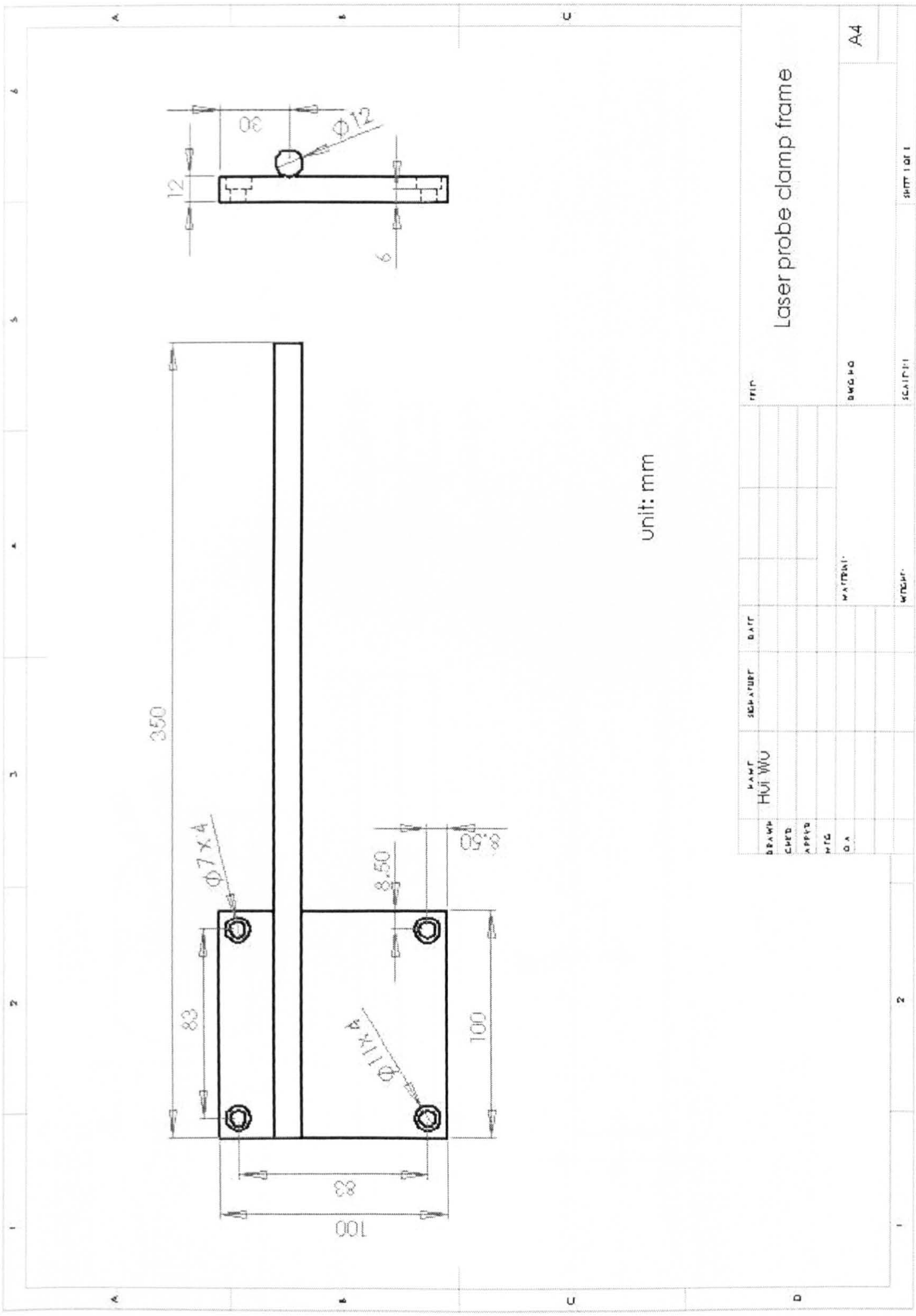

Clamp bar for Laser probe fixing

Workpiece for pressure measurement using Pitot tube